

Electronic Structure of Functionalized Semiconductor Surfaces and Interfaces for Photoelectrochemical Water Splitting

Zur Erlangung des akademischen Grades Doktor-Ingenieur (Dr.-Ing.)
Genehmigte Dissertation von Dominik Christian Moritz aus Frankfurt am Main
Tag der Einreichung: 21.12.2023, Tag der Prüfung: 14.03.2024

1. Gutachten: Prof. Dr. Wolfram Jaegermann
2. Gutachten: Prof. Dr. Andreas Klein
Darmstadt, Technische Universität Darmstadt



TECHNISCHE
UNIVERSITÄT
DARMSTADT



Materials and Earth
Sciences Department
Surface Science Laboratory

Electronic Structure of Functionalized Semiconductor Surfaces and Interfaces for Photoelectrochemical Water Splitting

Accepted doctoral thesis by Dominik Christian Moritz

Date of submission: 21.12.2023

Date of thesis defense: 14.03.2024

Darmstadt, Technische Universität Darmstadt

Bitte zitieren Sie dieses Dokument als:

URN: urn:nbn:de:tuda-tuprints-269531

URL: <http://tuprints.ulb.tu-darmstadt.de/26953>

Jahr der Veröffentlichung auf TUprints: 2024

Dieses Dokument wird bereitgestellt von tuprints,

E-Publishing-Service der TU Darmstadt

<http://tuprints.ulb.tu-darmstadt.de>

tuprints@ulb.tu-darmstadt.de

Die Veröffentlichung steht unter folgender Creative Commons Lizenz:

Namensnennung – Weitergabe unter gleichen Bedingungen 4.0 International

<https://creativecommons.org/licenses/by-sa/4.0/>

This work is licensed under a Creative Commons License:

Attribution–ShareAlike 4.0 International

<https://creativecommons.org/licenses/by-sa/4.0/>

“God made solids, but surfaces
are the work of the devil”

*Wolfgang Ernst Pauli (*1900 – †1958)*

Erklärungen laut Promotionsordnung

§ 8 Abs. 1 lit. c PromO

Ich versichere hiermit, dass die elektronische Version meiner Dissertation mit der schriftlichen Version übereinstimmt.

§ 8 Abs. 1 lit. d PromO

Ich versichere hiermit, dass zu einem vorherigen Zeitpunkt noch keine Promotion versucht wurde. In diesem Fall sind nähere Angaben über Zeitpunkt, Hochschule, Dissertationsthema und Ergebnis dieses Versuchs mitzuteilen.

§ 9 Abs. 1 PromO

Ich versichere hiermit, dass die vorliegende Dissertation selbstständig und nur unter Verwendung der angegebenen Quellen verfasst wurde.

§ 9 Abs. 2 PromO

Die Arbeit hat bisher noch nicht zu Prüfungszwecken gedient.

Darmstadt, 21.12.2023

D. C. Moritz

Abstract

Photoelectrochemical multi-junction devices for direct solar energy conversion have been highly improved during the last decade with solar to hydrogen efficiencies reaching almost up to 20 %.

However, these efficiencies are still below their expected physical limits, which requires a deeper understanding of band energy diagrams along the functional device interfaces in the vicinity of a liquid electrolyte in order to identify potential and charge transfer losses, that will limit the conversion efficiency of the overall device.

For this purpose, model surfaces of classical elemental (Si) and binary (InP) semiconductors were prepared and characterized by photoemission spectroscopy with respect to their electronic structure and electronic surface state formation. The interaction of these surfaces with water was investigated by modeling the electrochemical interface in ultra-high vacuum using a “frozen electrolyte” approach. Depending on surface termination and surface state concentration, the surfaces showed a shift in Fermi level towards the vacuum level, indicating an electron injection upon water adsorption by the interaction with unsaturated dangling surface bonds.

The contact formation of the photoabsorber to the noble-metal catalyst results in an electron depletion layer acting as a barrier for the charge transfer and therefore preventing considerable conversion efficiencies.

Using TiO_2 as buffer layer in between the photoabsorber and catalyst seemed to prevent the strong depletion of the photoabsorber. However, this effect strongly depends on the TiO_2 film properties, which results from the preparation process. This has to be optimized in order to guarantee a loss-free charge transfer from the photoabsorber to the catalyst.

The deduced energy band diagrams from modeled interface experiments help to understand the electrochemical performance when using the layer arrangement in a device-like setup. However, when method-related microstructural effects like lateral inhomogeneities or mechanical and structural stability come into play, the performance prediction solely derived from the energy band diagrams of model interfaces seem to fail and cannot fully describe the energetic device complexity at operation conditions.

Zusammenfassung

Photoelektrochemische Multisubstrat-Schichtverbindungen zur direkten Energieumwandlung der Sonnenenergie wurden im letzten Jahrzehnt erheblich verbessert, wobei Solar-zu-Wasserstoff-Wandlungseffizienzen von beinahe 20 % erreicht wurden. Dennoch liegen diese Effizienzen immer noch weit unter ihrem zu erwartendem physikalischen Potential. Daher ist ein tieferes Verständnis der Bandenergiendiagramme entlang der funktionalen Grenzflächen gerade im Kontakt zum flüssigen Elektrolyten erforderlich, um Potential- und Ladungsübertragungsverluste zu identifizieren, die die Umwandlungseffizienz der gesamten photoelektrochemischen Zelle begrenzen.

Zu diesem Zweck wurden Modelloberflächen aus klassischen elementaren (Si) und binären (InP) Halbleitern präpariert und hinsichtlich ihrer elektronischen Struktur sowie der Bildung elektronischer Oberflächenzustände mittels Photoelektronenspektroskopie charakterisiert. Die Wechselwirkung dieser Oberflächen mit Wasser wurde durch die Modellierung der elektrochemischen Grenzflächen im Ultrahochvakuum mithilfe eines gefrorenen Elektrolyt-Ansatzes bei Tieftemperaturadsorptionsexperimenten untersucht. Abhängig von der Oberflächenterminierung und der Oberflächenzustandsdichte zeigten die Oberflächen eine Verschiebung des Fermi-Niveaus in Richtung des Vakuumniveaus, was auf eine Elektroneninjektion im Kontakt mit den Wassermolekülen durch die Wechselwirkung mit ungesättigten Oberflächenbindungen hinweist.

Die Kontaktbildung des Photoabsorbers zum Edelmetallkatalysator führte zu einer Elektronenverarmungsschicht, die als Barriere für die Ladungsübertragung wirkt und somit nennenswerte Umwandlungseffizienzen verhindert.

Die Verwendung von TiO_2 als Pufferschicht zwischen dem Photoabsorber und dem Katalysator schien hingegen die starke Elektronenverarmung des Photoabsorbers teilweise zu verhindern. Dieser Effekt hängt jedoch stark von den Eigenschaften der TiO_2 -Schicht ab, die sich aus dem verwendeten Herstellungsprozess ergeben. Um eine verlustfreie Ladungsübertragung vom Photoabsorber zum Katalysator zu gewährleisten, müssen diese weiter optimiert werden.

Die abgeleiteten Energiebanddiagramme aus den modellierten Grenzflächenexperimenten helfen, die elektrochemische Leistungsfähigkeit der Zelle unter Anwendung zu verstehen. Wenn jedoch präparationsbedingte mikrostrukturelle Effekte wie laterale Inhomogenitäten oder die mechanische und strukturelle Stabilität berücksichtigt werden, scheinen die abgeleiteten Energiebanddiagramme die elektrochemische Leistungsfähigkeit nicht mehr genau vorhersagen zu können. Dies lässt vermuten, dass die energetische Komplexität des Multi-Schichtabsorbers unter Betriebsbedingungen nicht vollständig mit den hier präsentierten Modellexperimenten beschrieben werden kann.

Contents

List of abbreviations	xv
List of symbols	xvii
1 Introduction	1
2 Theoretical background	5
2.1 Fundamental properties of semiconductors	5
2.1.1 Solid state material classes: Metals / semiconductors / insulators	5
2.1.2 Semiconductor doping	6
2.1.3 Contact formation at semiconductor interfaces and potential distribution	7
2.1.4 Semiconductor surfaces	8
2.1.5 Optical properties of semiconductor junctions	9
2.2 Working principle of photoelectrochemical cells	10
2.2.1 Fundamentals of electrolysis	10
2.2.2 Butler-Volmer equation and charge transfer kinetics	11
2.2.3 The semiconductor / electrolyte interface	11
2.3 Investigated materials	13
2.3.1 Photoabsorber: Si and InP	13
2.3.2 Electrochemical buffer layer: TiO ₂	15
2.3.3 Electrocatalyst: Pt	16
3 Analytical methods	17
3.1 Photoemission spectroscopy (PES)	17
3.1.1 XP-spectra	18
3.1.2 Ultraviolet photoemission spectroscopy (UPS)	20
3.2 Near edge X-ray absorption fine structure (NEXAFS)	20
3.3 Low-energy electron diffraction (LEED)	20
3.4 Electrochemical performance	21
3.4.1 Reference electrodes	22
3.4.2 (Photo)current voltage curves	22
3.5 4-point Hall measurements	23
3.6 UV-Vis-NIR	24
3.7 Thin film deposition techniques	24
3.7.1 Magnetron sputtering	24
3.7.2 Atomic layer deposition (ALD)	25
3.7.3 Electrodeposition	26

4	Sample preparation and experimental setup	27
4.1	Photoemission spectroscopy (PES) analysis	28
4.1.1	Surface oxide thickness and stoichiometry	28
4.1.2	Potential corrected line shapes	29
4.1.3	Synchrotron XPS and NEXAFS	31
4.2	Semiconductor surface preparations	31
4.2.1	Si surface preparation	31
4.2.2	InP surface preparation	32
4.3	Water adsorption	33
4.4	Thin film deposition	33
4.4.1	Magnetron sputtering	33
4.4.2	Atomic layer deposition of TiO ₂	34
4.4.3	Thermal evaporation of Pt	35
4.4.4	Interface experiments	35
4.5	Electrochemical characterization	35
4.5.1	Chopped light open circuit potential (OCP)	36
4.5.2	Chopped light voltammetry	36
4.5.3	Galvanostatic Pt deposition	36
4.6	Other techniques	36
4.6.1	LEED setup	36
4.6.2	Hall measurements	36
4.6.3	UV/vis spectroscopy	36
4.6.4	Profilometry	37
4.6.5	External measurements	37
5	Silicon surfaces	39
5.1	Dangling bond defects on Si surfaces	39
5.1.1	Surface band bending and surface defects	40
5.1.2	The intrinsic dangling bond states at Si surfaces	42
5.1.3	Oxide specification and oxygen-related dangling bond defects	45
5.1.4	Dangling bond passivation by hydrogen termination	47
5.1.5	Source-induced photovoltages at cryogenic temperatures	50
5.1.6	Conclusion on Si surface defects	53
5.2	Surface reactivity of Si dangling bonds	54
5.2.1	Reactivity of Si (100)	54
5.2.2	Reactivity of Si (111)	56
5.3	Low-temperature water adsorption on Si surfaces	59
5.3.1	Model experiment at the example of H-terminated p-Si(100) / H ₂ O	59
5.3.2	H ₂ O adsorption on treated Si surfaces	62
5.3.3	Origin of electron injection into Si substrates	66
5.3.4	Conclusion and energy band diagrams	69
5.4	Contact formation of Si with Pt catalyst	71
5.4.1	The Si/Pt interface energetics	71
5.4.2	Water adsorption on Pt covered Si	77
5.4.3	Electrochemical performance of the n-Si/Pt hetero contact	82

6	InP surfaces	85
6.1	P-rich p-InP (100)	85
6.1.1	Electronic structure and surface states of P-rich p-InP (100)	85
6.1.2	Reactivity of P-rich p-InP (100) with water	89
6.2	In-rich p-InP (100)	94
6.2.1	Electronic structure and surface states of In-rich p-InP (100)	94
6.2.2	Reactivity of In-rich InP with water	98
6.3	O-rich InP	102
6.3.1	Surface composition of native oxide terminated InP (100)	102
6.3.2	Electronic interaction of O-rich InP with water	103
6.4	Final conclusion on InP surfaces in contact to water	105
7	TiO₂ as electrochemical buffer layer	107
7.1	Interfaces to ALD-TiO ₂	107
7.1.1	The p-Si/SiO ₂ /TiO ₂ interface formation	107
7.2	Band alignment of p-InP/ALD-TiO ₂	110
7.2.1	Initial ALD growth of TiO ₂ P-rich InP (100)	110
7.2.2	Partially oxidized InP (100) as substrate for ALD-TiO ₂	112
7.3	Low-temperature water adsorption on the p-InP/TiO ₂ interface	116
7.4	Sputter deposition of TiO ₂	119
8	pn⁺-Si model device structures	123
8.1	Charge separation of the pn ⁺ -Si photoelectrode	124
8.2	The Pt covered pn ⁺ photocathode	125
8.2.1	Electrochemical cell tests of pn ⁺ -Si/Pt photocathodes	129
8.3	The impact of TiO ₂ on the device performance	131
8.3.1	Electrochemical cell tests of pn ⁺ -Si/TiO ₂ photocathodes	133
8.4	Conclusions on pn ⁺ -Si device structure performances	135
9	Conclusions and outlook	137
	Bibliography	141
	Appendix	163
1	Prepared Si surfaces	163
2	Water adsorption on Si(100)-H	165
3	Impact of bias light on low-temperature adsorption experiment	166
4	n-Si/SiO ₂ /Pt interface	167
5	Water adsorption on Pt and Pd foil	168
6	HeII spectra of p-Si/SiO ₂ /Pt interfaces upon water adsorption	169
7	Chopped light current voltage scans of p-Si/SiO ₂ /Pt	170
8	Photoreduction of p-Si/SiO ₂ /TiO ₂ interfaces	171
9	InP (100) after ALD treatment	173
10	Low-temperature water adsorption on p-InP/ALD-TiO ₂ interface	174
11	Current-voltage curves of p-Si and pn ⁺ -Si	176
12	Sputter-deposited TiO ₂	177

List of abbreviations

Acronym	Description
AFM	atomic force microscopy
ALD	atomic layer deposition
CB	conduction band
CBM	conduction band minimum
CE	counter electrode
CNL	charge neutrality level
CV profiling	electrochemical capacitance–voltage profiling
CVD	chemical vapour deposition
DAISY-FUN	D armstadt I ntegrated S ystem for F undamental research
DC	direct current
DEZn	diethylzinc
DFT	density functional theory
DGS	deep gap state
DI water	deionized water
DOS	density of states
ESR	electron spin resonance spectroscopy
fcc	face-centered cubic
FTO	fluorine doped tin oxide
FWHM	full width at half maximum
HER	hydrogen evolution reaction
HOMO	highest occupied molecular orbital
HREELS	high-resolution electron energy loss spectroscopy
ITO	indium tin oxide
LCAO	linear combination of atomic orbitals
LED	light emitting diode
LEED	low-energy electron diffraction
LUMO	lowest unoccupied molecular orbital
MIGS	metal induced gap states
MOCVD	metalorganic chemical vapor deposition
MOVPE	metal organic vapor phase epitaxy
NAP-XPS	near-ambient pressure XPS
NEXAFS	near edge X-ray absorption fine structure
OCP	open circuit potential
OER	oxygen evolution reaction
PCTFE	polychlorotrifluoroethylen
PEC	photoelectrochemical cell
PES	photoemission spectroscopy
PVD	physical vapour deposition

Acronym	Description
QCM	quartz crystal microbalance
RAS	reflection anisotropy spectroscopy
RE	reference electrode
RF	radio frequency
RHE	reversible hydrogen electrode
RT	room temperature
SCR	space charge region
SDR	spin-dependent recombination
SEE	secondary electron edge
SEM	secondary electron microscopy
SGS	shallow gap state
SHE	standard hydrogen electrode
SPV	surface photovoltage
SS	surface states
STH	solar to hydrogen efficiency
STM	scanning tunneling microscopy
TBP	<i>tert.</i> -butylphospine
TMIn	trimethylindium
TTIP	titan(IV)isopropoxid
UHV	ultra-high vacuum
UPS	ultraviolet photoemission spectroscopy
UV-Vis-NIR	Ultraviolet-visible-near-infrared spectroscopy
VB	valence band
VBM	valence band maximum
WE	working electrode
WF	work function
XPS	X-ray photoemission spectroscopy
XRD	X-ray diffraction

List of symbols

Symbol	Description	Unit
a	lattice parameter	\AA
A_H	Hall constant	$\text{m}^3 \text{C}^{-1}$
α	absorption coefficient	cm^{-1}
B	magnetic field	T
c_X	rel. concentration of element X	
$\chi_{\text{el.}}$	electron affinity	eV
d	film thickness	nm
δ	dipole moment offset	eV
E_{ads}	adsorption enthalpy	eV
E_{b}	binding energy	eV
E_{CB}	conduction band minimum	eV
edc	escape depth correction	
E_{kin}	electron kinetic energy	eV
μ_0^{redox}	standard redox potential	V vs. RHE
E_A	ionization energy of acceptor	eV
E_D	ionization energy of donor	eV
$E_{\text{el.}}(x)$	electric field	V m^{-1}
ε	static dielectric constant	
μ^{redox}	redox potential	V vs. RHE
η	overpotential	V
E_{vac}	vacuum level	eV
E_{F}	Fermi level	eV
E_{g}	bandgap	eV
E_{VB}	valence band maximum	eV
F_L	Lorentz force	N
F	Faraday constant	C mol^{-1}
FF	fill factor	%
ΔG	Gibbs free energy	kJ mol^{-1}
$h\nu$	energy of electromagnetic radiation	eV
I	electric current	A
I_{R}	reflected light intensity	photons/s
I_{T}	transmitted light intensity	photons/s
$I_{h\nu}$	light intensity	photons/ cm^2
I_X	integrated intensity of emission line X	cps eV
I_{P}	ionization potential	eV
I_{SC}	short circuit current	A
j	current density	mA cm^{-2}
j_{qn}	total angular momentum quantum number	

Symbol	Description	Unit
\vec{k}	wave vector	nm^{-1}
$k_{\text{B}}T$	thermal energy	eV
l	azimuthal quantum number	
λ	wave length	nm
λ_e	De Broglie wave length of electrons	Å
λ_{EAL}	effective attenuation length	Å
λ_{IMFP}	inelastic mean free path	Å
μ_{el}	electric mobility	$\text{cm}^2 \text{V}^{-1} \text{s}^{-1}$
n	principal quantum number	
N_{CB}	effective conduction band density of states	cm^{-3}
n_{el}	charge carrier density	cm^{-3}
N_{VB}	effective valence band density of states	cm^{-3}
N_X	atomic density of element X	cm^{-3}
N_{ac}	acceptor concentration	cm^{-3}
N_{don}	donor concentration	cm^{-3}
N_{SS}	surface defect concentration	cm^{-2}
φ	detector angle	°
Φ_{spec}	work function of spectrometer	eV
Φ_{B}	Schottky barrier	eV
ϕ_{BB}	band bending	eV
Φ	work function of sample	eV
P_{MPP}	maximum power point	W cm^{-2}
q	electric charge	C
Q_{SS}	total surface charge	C cm^{-2}
R	electrical resistance	Ω
$\rho(x)$	charge density	C m^{-3}
$\sigma_{\text{n,p}}$	capture cross section	cm^2
ASF	atomic sensitivity factor of emission line X	
σ	specific conductivity	S cm^{-1}
T	temperature	°C
θ	diffraction angle	°
Θ_e	emission angle	°
T_{spec}	transmission function of spectrometer	
U	electric voltage	V
eU_{Ph}	photovoltage	eV
V_{OC}	open circuit voltage	V
W_{SCR}	width of space charge region	nm
Z	atomic number	

1 Introduction

The need for sustainable and clean energy sources has never been more urgent. According to the most recent 2022 IPCC report,¹ technologically and ecologically it is still possible to limit global warming until 2100 to 1.5 °C compared to the preindustrial age. However, this requires a prompt expansion in renewable energy sources such as wind and solar energies.

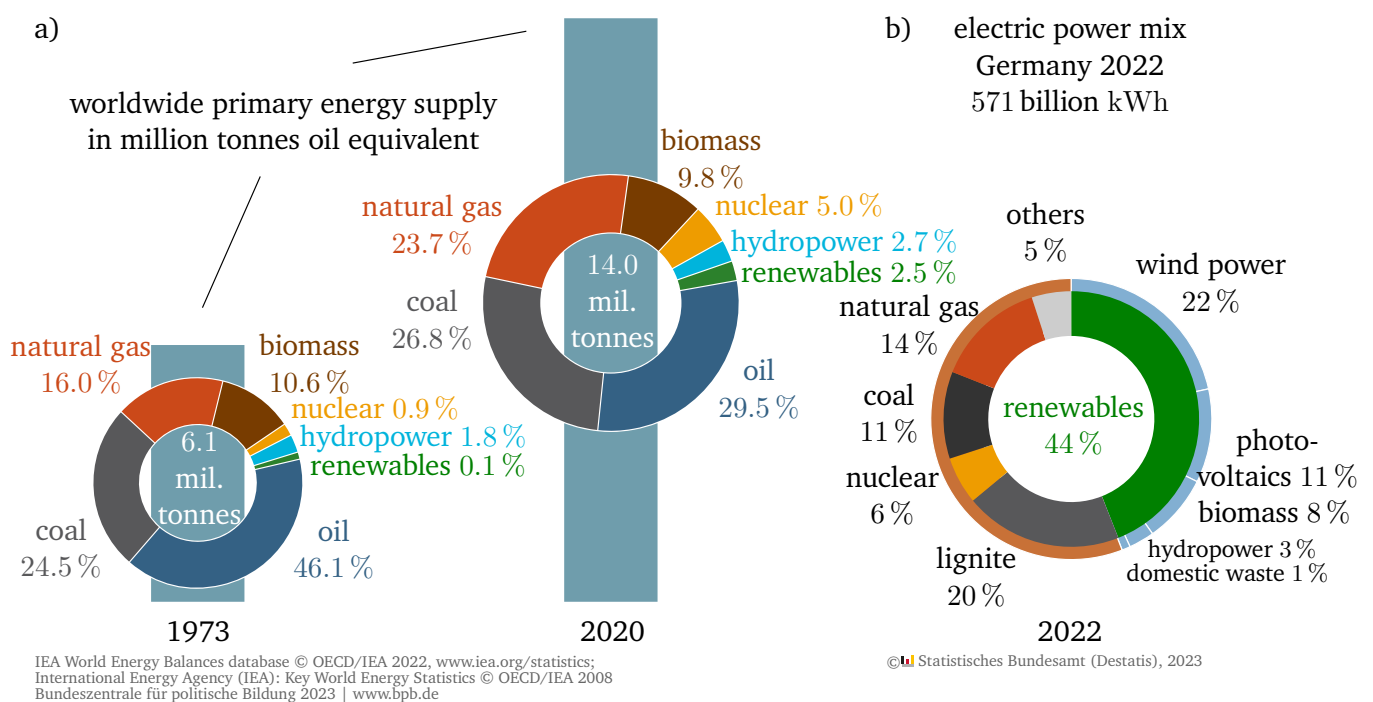


Figure 1.1: a) Worldwide primary energy consumption with contribution of different energy sources in 1973 and 2020.² b) Electric power mix for Germany in 2022 at a total electric consumption of 571 billion kWh.³

The worldwide energy demand doubled within the last 50 years, which was mostly satisfied by fossil fuels (Figure 1.1a)), leading to an ongoing increase in annual CO₂-emissions.¹ In 2020, around ≈90 % of worldwide energy consumption are still related to fossil fuels, therefore increasing the anthropogenic carbon footprint.² The rising demand in energy will become even more critical in the future, at least because of the continuous increase of human population. One strategy to mitigate climate change is the transformation from burning fossils to the use of electric power from renewable energy sources. Another aspect that forces mankind into this energy transformation is the depletion of exhaustible resources such as gas and oil by the end of the century.^{4,5}

In Germany, around 44 % of the electric power was supplied by renewable sources in 2022 (Figure 1.1b)).³ From all the renewable energies listed in Figure 1.1b), solely solar energy has the potential to meet all human energy needs.⁶ To further increase its contribution, one main challenge is its storage when it is

abundant, so it can be released on demand when it is needed.

There are different storing technologies available depending on the timescale of storage and demand when needed, i.e. supercapacitors, batteries, pumped-storage power plants etc.⁷ A very promising approach is to directly store the solar-converted energy in the form of chemical bonds by the synthesis of a synthetic fuel like hydrogen or hydrocarbons with in a photoelectrochemical cell (PEC).⁸ Inspired by the photosynthesis process in plants, these PEC devices are also denoted as “artificial leaves”. The simplest fuel is molecular hydrogen, which is the smallest molecule. It contains only two protons and two electrons and thus reveals the highest gravimetric energy density (143 MJ kg^{-1}) of all fuels.⁶ The production of hydrogen by the photoelectrochemical water splitting process is an uphill reaction, which requires energy in the form of (sun)light:



In contrast to organic fuels formed by CO_2 reduction, the electrocatalytic hydrogen half cell reaction only requires a two-electron transfer and resigns complex carbon capture technologies, which is thus less challenging. Furthermore, the stored energy can be readily converted into electricity again using the reverse reaction in fuel cells or by combustion without any CO_2 emission.^{6,9}

However, it should be noted that storing hydrogen is rather challenging and requires additional energy when compressing or cooling in liquid cryo-storages. Technological solutions are provided either in the form of high surface area physisorption or by forming chemical bonds in metal hydrides or organic fuels as well-established with the Fischer-Tropsch technology.⁹

The promising PEC approach is based on the spatial separation of photoexcited electron-hole pairs provided by a solid-state assembly based on semiconductor junctions.⁸ The excited charge carriers are then consumed at the electrodes to run the cathodic and anodic half cell reactions in order to produce the “solar fuel”.

The water splitting reaction thermodynamically requires 1.23 V, which is close to the bandgap optimum of single-bandgap absorbers revealing a maximum solar conversion efficiency of $\approx 32\%$.¹⁰ However, in order to run the catalysis at both electrodes, additional overpotentials are needed, which requires a photocell with a minimum photovoltage of $\geq 1.6 \text{ eV}$, at which it still provides reasonable photocurrents in the range of 10 to 20 mA cm^{-2} .^{11–13} It turned out that single absorber layers, i.e. metal oxide photoanodes, with reasonable bandgaps E_g could not provide these ambitious requirements in order to achieve considerable photo conversion efficiencies $\geq 10\%$.^{14,15}

Buried multi-junction device structures facilitate the use of the larger part of the solar spectrum, while the photovoltages of the single absorber systems sum up providing solar conversion efficiencies of more than 10% .^{14,16}

A schematic tandem absorber configuration is depicted in Figure 1.2. Two solid-state photoabsorber absorb light from two different wavelength. The top absorber absorbs photons of higher energy $E_{g,I}$ while the bottom absorber absorbs photons of lower energy $E_{g,II} < E_{g,I}$. The thermodynamic efficiency limit of such a tandem device would be at about 42% .¹¹ However, charge transport restrictions will limit the solar to hydrogen efficiency (STH) to about 25 to 30% .^{14,16} The number of photoabsorbers can even be increased to triple or quadruple junctions which will further increase the photovoltage of the PEC device. But, the photocurrents will be limited by the poorer transfer properties of the wide bandgap bottom absorber.¹⁸

Record efficiencies on different benchmark systems such as microcrystalline and amorphous Si triple-junction arrangements (9.5%),¹⁹ a-Si tandem cells in combination with metal oxide photoanodes

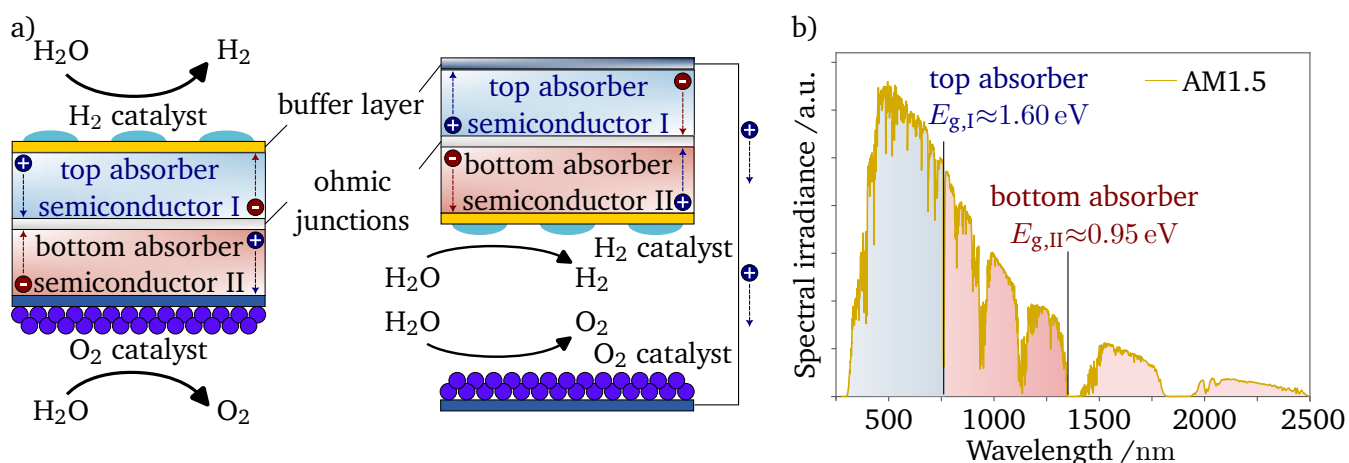


Figure 1.2: a) Tandem PEC structures, adapted from ¹⁷. In the left configuration both junctions are in contact to the electrolyte, whereas in the right configuration a photocathodic junction is separated from the metal anode. Both configurations are illuminated from the top. b) Bottom and top absorber will absorb the marked irradiance of the Solar AM1.5 spectrum, respectively. Optimal bandgaps are depicted according to Hu et al. ¹⁶.

(4.9 %),²⁰ and ternary III-V tandem arrangements (19.3 %)²¹ have been achieved recently, but are still below their physical limits.

High-performant solar cell systems based on Si or III-V elements are not stable in the presences of a hazardous electrolyte. Furthermore, buried PEC devices need active co-catalysts for the efficient half-cell reactions at the electrodes. Accordingly, an efficient PEC contains 3 functional device parts:

- i) The buried multi-junction photoabsorber:
The solar cell system has to be designed in a way that the photovoltage at the maximum power point is high enough to run the water splitting reaction at reasonable photocurrents.
- ii) The electrochemical buffer layer:
The electrochemical buffer or window layer has to protect the buried photoabsorber from corrosion in the liquid electrolyte. Furthermore, it should be transparent for a wide range of the solar spectrum, while providing an efficient and fast transfer of excess charge carriers from the photoabsorber to the catalyst.
- iii) The co-catalyst:
The co-catalysts for both half cell reactions have to be stable under operating conditions and catalyze the half cell reactions without considerable overpotentials.

The separated optimization of the single components will not be sufficient to optimize device efficiencies, since the electronic coupling at the functional device interfaces will be of high relevance when trying to impede charge transfer losses from one layer into the other.^{22,23} Furthermore, the contact of the photoabsorber to the liquid electrolyte will provide an additional contact formation, which leads to a charge redistribution at the semiconductor/electrolyte interface.

It has been shown that these contacts do not simply follow ideal semiconductor contact behavior, as classical models do not sufficiently consider the role of surface or interface states and reaction intermediates.^{13,23} The chemical arrangement as well as the final energy band diagrams at the functional device

interfaces in equilibrium as well as under operation have not been studied systematically yet, impeding the comprehension of efficiency-limiting factors of the overall device.

The present thesis aims to address this gap in knowledge and gain insights in the electronic properties of such buried interfaces through model experiments using surface science approaches.

Motivation of thesis

In detail, this thesis will address the comprehension of the band energy diagrams of photoelectrochemical devices with respect to the potential distribution as well as the formation of electronic surface and interface states mainly using photoemission spectroscopy. The origin of surface states on Si and InP model surfaces and their physical properties are investigated with regards to different surface treatments. The role of these surface defects has to be investigated with respect to surface stability and further defect evolution in the vicinity of the electrolyte to identify i.e. corrosion-induced potential offsets, which limit the effective photovoltage of the PEC device.

The main challenging aspect in this regard is to elucidate the electronic structure of these semiconductor/electrolyte interfaces by electron spectroscopies, since the very short electron inelastic mean free path impede an analysis directly through the liquid electrolyte. In addition, the electron detection classically requires ultra-high vacuum (UHV) conditions, at which the electrolyte typically evaporates. To overcome this limitation, model experiments have to be carried out by gas-phase adsorption in UHV under ambient but also cryogenic temperatures in order to investigate the water adsorption behavior with respect to chemical composition, surface reconstruction and structural defects.

These surface science methods have been developed and deployed already since the 1980's.^{24,25} These studies, however mainly focus on surface reactions of adsorbates on ideal surfaces. Specifically, the role of surface defects regarding surface reactivity and charge transfer mechanisms has not been studied systematically from a PEC device related point of view.

Furthermore, the electronic coupling of the photoabsorbers to a chemical and electronic passivation layer as well as to the co-catalyst have to be studied in more detail in special regards to chemical composition changes at the interfaces and defect formation, which may additionally act as potential loss and/or recombination center for photo-excited charge carriers.

The goal is to identify routes for optimizing the electronic coupling at the electrochemical hetero-interfaces, which will later bring multi-junction PEC devices to their physical limits. The studies in this thesis will not cover experiments on real microcrystalline or amorphous tandem devices, but cover specifically designed model interfaces, which reduce the complexity of such a device to a minimum through thin film approaches in UHV.

To adress these points, this thesis will begin with a brief introduction into the theoretical principles and used analysis techniques. Afterwards, surface defects on Si and InP model systems are investigated and characterized with respect to charge transfer and Fermi level pinning. In a next step, the reactivity of surface defects in contact to molecular water is explored. Furthermore, the intrinsic properties of TiO₂ are investigated using different deposition techniques and the contact formation to the photoabsorber is examined. In the last chapter, the contact formation of photoactive model absorbers to functional layers are studied, and the final device structures are tested and characterized with photoelectrochemical measurements.

2 Theoretical background

This chapter will cover the most important aspects of solid state physics, the working principle of photoelectrochemical devices and the material properties considered in this thesis. Fundamental concepts of solid state physics and semiconductor electrochemistry are based on the textbooks of Mönch²⁶, Memming²⁷, and Van de Krol and Grätzel⁶. Electrochemical concepts are mainly based on the book of Hamann and Vielstich²⁸.

2.1 Fundamental properties of semiconductors

The model experiments developed in the framework of this thesis are based on a solid state approach, which requires the combination of different material classes. The photoabsorber, where light is converted into electric power, is based on a semiconductor system. Stable passivation layers are systems of ionic bonds which are typically characterizing insulators. The co-catalysts for the chemical reaction are mostly based on noble metal systems. Accordingly, typical photoelectrochemical water splitting devices cover all three material classes, whose fundamental electronic properties are presented here.

2.1.1 Solid state material classes: Metals / semiconductors / insulators

Different from isolated atoms or molecules, the valence electrons in solids will interact with the surrounding atoms in all three dimensions and the periodic potentials within the crystal lattice will give rise to an energy dispersion $E(\vec{k})$ in dependence on the wave vector \vec{k} in reciprocal space.²⁷ From the energy

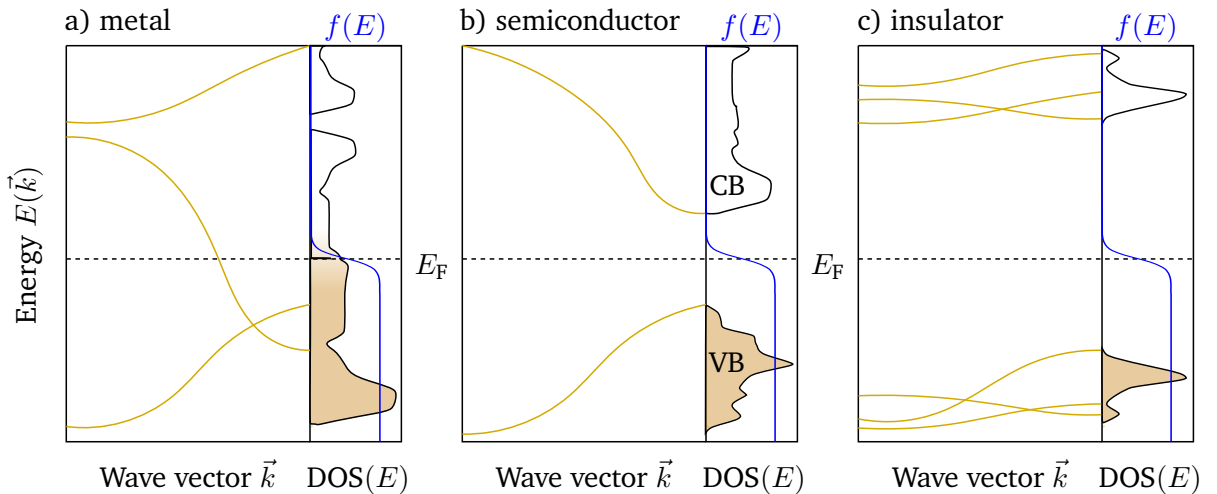


Figure 2.1: Schematic band structure diagrams for a) metals, b) semiconductors, and c) insulators. The electronic DOS represents typical electronic state distribution of solid states considering different states and directions.

dispersion, one can derive the density of states (DOS) representing the electronic states over the whole \vec{k} space, while the electronic occupation of the states is derived from the Fermi-Dirac distribution

$$f(E) = \frac{1}{1 + \exp((E - E_F)/k_B T)}, \quad (2.1)$$

with $k_B T$ as the Boltzmann term and E_F as the Fermi energy, at which the occupation probability is 1/2. In solid state physics, materials are categorized according to their electronic properties (Figure 2.1). In metals, the Fermi energy E_F is located within an energy band and electrons energetically located around E_F behave almost like a free electron gas as there are enough states around E_F which could be temporarily occupied by these free electrons and thus contribute to the good electric conductivity of this material class. In semiconductors and insulators, E_F is located within a forbidden band gap at which no electronic states exist. The highest occupied band is the so-called valence band (VB), while the lowest unoccupied band is the conduction band (CB). In the case of a semiconductor, the forbidden band gap E_g is narrow enough ($E_g < 3$ eV) that electrons e from the valence band maximum (VBM) can be excited by the thermal energy $k_B T$ to the conduction band minimum (CBM), leaving holes h in the VB. Due to the high DOS of free electron states in the CBM and hole states in the VBM, both free charge carrier with concentrations n and p are mobile with a certain mobility μ_{el} , and contribute to a moderate electric conductivity σ with

$$\sigma = ne\mu_{el,e} + pe\mu_{el,h}. \quad (2.2)$$

For insulators, E_g is typically too large to excite intrinsic charge carriers thermally ($E_g > 3$ eV). Furthermore, the charge carriers are rather localized within the crystal structure leading to no electronic conductivity. However, electronic charge carrier transport can still occur due to the existence of defect states within the bandgap referred to as *doping*.

2.1.2 Semiconductor doping

The electronic properties of semiconductors can strongly vary with temperature or by introducing dopants, which contribute additional free charge carriers to the CB (electrons, n-dopants) or VB (holes, p-dopants). As a consequence, E_F will move with respect to the valence and conduction band edges, and thus change the electronic occupation in CB and VB, respectively. Doping effects can arise from intentionally or unintentionally introduced "defects" in the crystal lattice such as impurity atoms on lattice or interstitial sites, vacancies, or other point-defects. In Si, n-type doping can easily be achieved by replacing a Si lattice site with a group V element such as P or As. In the four-fold coordinated Si matrix, these atoms exhibit an additional electron which can easily be delocalized, contributing to the "free electrons" in the CB. By introducing group III elements, p-type doping can be achieved similarly.

In an energy band diagram as shown in Figure 2.2, the dopants will introduce electronic states within the band gap, which are located slightly below the CBM for electron donors and above the VBM for electron acceptors. The respective ionization energy of the dopants within the corresponding crystal matrix E_D and E_A , has to be in a range of $k_B T$. Typical ionization energies in Si for donors are 45 meV (P) and 54 meV (As), while they are 45 meV (B) and 72 meV (Al) for acceptors.²⁹

The surface potentials I_p and χ_{el} are independent of doping and describe the distance from the respective

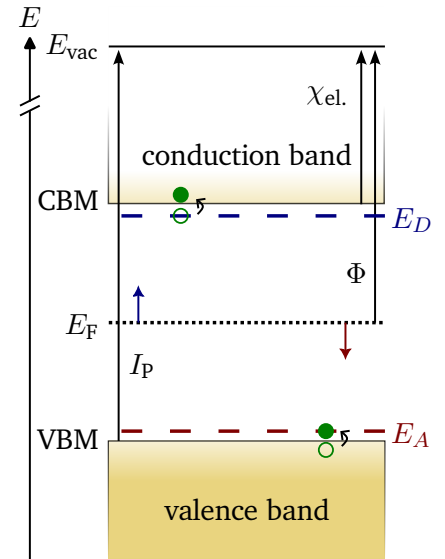


Figure 2.2: Semiconductor band energy diagram. Doping raises / lowers E_F .

band edges to the vacuum level E_{vac} , at which an electron is considered to be free of bulk potential interactions (Figure 2.2). The work function Φ describes the difference of E_F to E_{vac} and is consequently a parameter which depends on doping.

2.1.3 Contact formation at semiconductor interfaces and potential distribution

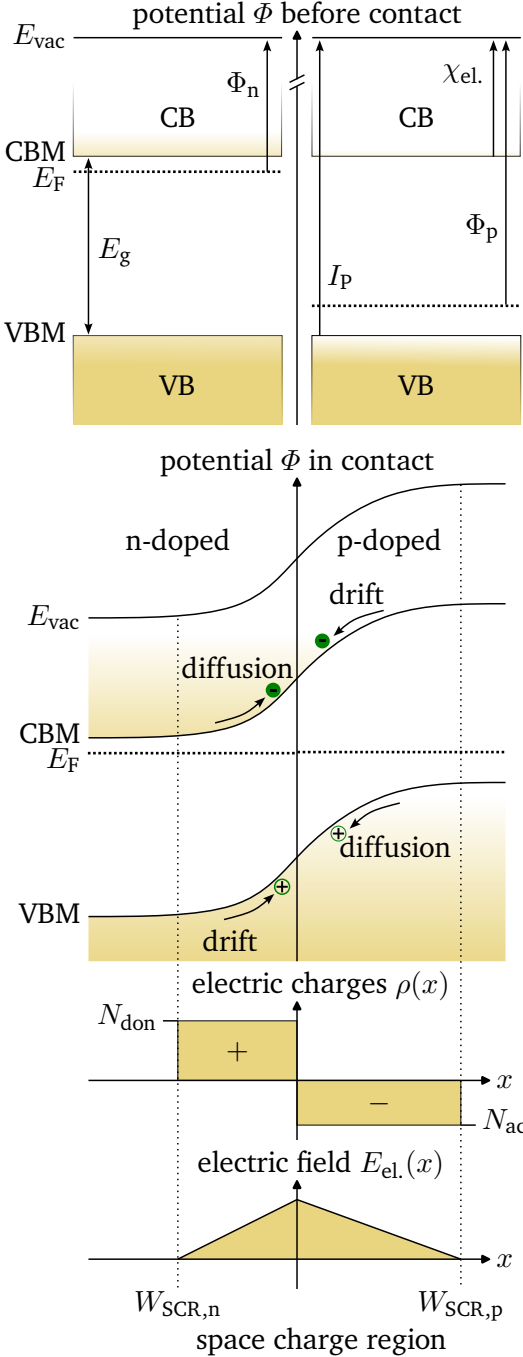


Figure 2.3: Band energy diagram of a homo-junction before and after contact formation with electric charge density and electric field distribution according to the *depletion approximation*.

When contacting two materials, the Fermi levels of both materials have to align in order to reach thermodynamic electronic equilibrium. In a simple case, the same semiconducting material but different doping will lead to a homo junction formation with a charge transfer of electrons from the low work function (WF) side with Φ_n into the high WF side with $\Phi_p > \Phi_n$, while holes move vice versa. The diffusion of free charges leaves the non-mobile dopant ions N_{don}^+ and N_{ac}^- behind, inducing an electric field $E_{\text{el}}(x)$. Accordingly, the interface layer is called space charge region (SCR). The electric field causes a drift current, which is contrary to the diffusion current, resulting in an equilibrium state. Figure 2.3 illustrates the schematic band diagrams before and after contact formation.

Potential and charge distribution: Poisson equation

The potential and charge distribution $\Phi(\vec{r})$, $\rho(\vec{r})$ at the space coordinate \vec{r} within the SCR are related by the Poisson equation²⁶

$$\Delta\Phi(\vec{r}) = \nabla^2\Phi(\vec{r}) = -\nabla\vec{E}_{\text{el}}(\vec{r}) = -\frac{\rho(\vec{r})}{\epsilon\epsilon_0}, \quad (2.3)$$

which is simplified in 1D to

$$\frac{d^2\Phi}{dx^2} = -\frac{dE_{\text{el}}(x)}{dx} = -\frac{\rho(x)}{\epsilon\epsilon_0}. \quad (2.4)$$

with $\rho(x) = qN_{\text{don}}^+$. The amount of ionized donors N_{don}^+ depends on the energetic difference of the donor level to the Fermi level $E_D - E_F$ according to the Fermi-Dirac distribution from Equation 2.1, for which the solution of Equation 2.4 becomes rather complex. The so-called *depletion approximation* has been used to simplify $\rho(x) = qN_{\text{don}}$ to a fixed value, implying that all dopants are ionized $N_{\text{don}} = N_{\text{don}}^+$ and the neutral regions are field free.³⁰ As a result, the electric field within the space charge region becomes linear with x and the potential shows a parabolic behavior (see Figure 2.3):

$$\Phi(x) = \iint_{\text{SCR}} -\frac{\rho(x)}{\epsilon\epsilon_0} dx dx = -\frac{qN_{\text{don}}}{2\epsilon\epsilon_0} \cdot x^2 \quad (2.5)$$

A drop of potential ϕ_{BB} in a semiconductor SCR is accordingly denoted as *band bending*

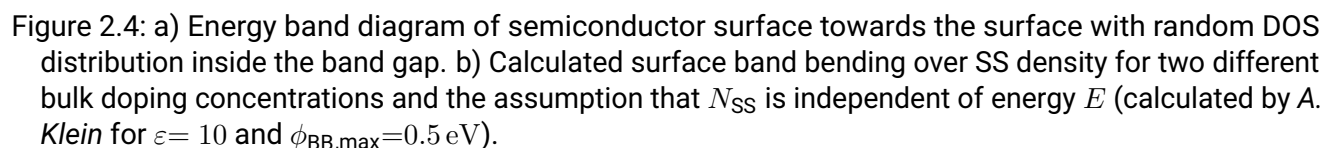
$$\phi_{\text{BB}} = -\frac{qN_{\text{don}}}{2\epsilon\epsilon_0} \cdot W_{\text{SCR}}^2, \quad (2.6)$$

By adapting $\rho(x)$, Equation 2.4 can also be solved for insulators, where $\rho(x)=0$ leads to linear potential curves or metals where $\rho(x)$ becomes a delta function with all charges constrained to the surface.

Homo-junctions as shown above are the centerpieces of diode devices, which are known to show rectifying resistance properties. Applying an external bias potential U to the junction will change the equilibrium state of diffusion and drift currents. According to Equation 2.4, the external bias will induce an electric field which is, depending on the sign of U , either amplifying or counteracting the inner field of the SCR. Consequently, the effective barrier height Φ_B for charge carriers to overcome the SCR changes with U and the current j can be described with the ideal diode law according to Shockley³⁰

with j_0 as reverse bias saturation current density. For $U > 0$ V, the external bias is counteracting the field of the SCR and the current increases rapidly when $qU \gg \Phi_B$. The current flows in *forward direction*. In case of $U < 0$ V, the external bias even increases the effective barrier and the current is approximating j_0 . The current flows in *reverse direction*.

In principle, the considerations from Section 2.1.3 are also valid, if the Fermi level alignment results from a charge transfer into another semiconductor (hetero-junction), a metal (Schottky contact) or an adsorbate. However, a charge exchange can even result from surface or interface states trapping the counter charges to the semiconductor surface. Surface states result from unsaturated bonds at the surface and are typically located within the band gap as pointed out by Bardeen³¹. In this case, since the surface



states can either act as donors or acceptors, the surface states are only partially occupied. In principle, there exists a concept of “surface Fermi level”, at which the surface is free of any isolated charge, even the surface itself cannot be separated from the bulk, as for example when contacting two bulk materials. This “surface Fermi level” is therefore referred to as the *charge neutrality level (CNL)*. From this level E_{CNL} , the surface can exchange charges with the bulk semiconductor in order to align the electrochemical potential of the surface with the bulk. In Figure 2.4 a), electrons from the n-doped semiconductor are getting trapped by the energetically favored surface state and induce surface band bending ϕ_{BB} in the substrate. In contrast to the classical Schottky model, the total amount of the surface states N_{SS} can vary and strongly depends on surface orientation and surface preparation.

In Figure 2.4b), the surface band bending over the total amount of surface states (SS) is depicted using the depletion approximation (compare Equation 2.6). It assumes that the maximum band bending $\phi_{\text{BB,max}}$ at which E_{F} and E_{CNL} coincide, is 0.5 eV and N_{SS} is independent on the energy E . Even though $N_{\text{SS}}(E)$ always shows a certain defect distribution with E , it is exemplary shown that the band bending due to SS, for which its CNL is located 0.5 eV below the bulk Fermi level E_{F} , strongly depends on the bulk doping concentration N_{don} as well as on the surface state density N_{SS} . For a defect concentration of $N_{\text{SS}}=10^{12} \text{ cm}^{-2}$, a band bending of 0.4 eV would be observed on an n-doped wafer with $N_{\text{don}}=10^{15} \text{ cm}^{-3}$, while on a higher doped wafer with $N_{\text{don}}=10^{17} \text{ cm}^{-3}$, only $\phi_{\text{BB}}=0.1 \text{ eV}$ could be observed. For $N_{\text{SS}} \geq 10^{13} \text{ cm}^{-2}$, E_{F} is approaching the CNL independently of bulk doping, which is referred to *Fermi level pinning* or *Bardeen limit*, since neither doping nor an external contact potential is able to shift E_{F} from the CNL.³¹

The presented model can be also applied to interface states, i.e. metal induced gap states (MIGS), as proposed by Cowley and Sze³².

2.1.5 Optical properties of semiconductor junctions

When illuminating a semiconductor with a bandgap E_{g} , electrons can be excited from the VB into the CB if the energy of the incident photon $h\nu$ exceeds the bandgap E_{g} . The transition can either occur at the same momentum vector \vec{k} (direct transition) or by changing \vec{k} due to photon-phonon interaction (indirect transition), which is less probable. Indirect semiconductors such as Si therefore typically reveal a lower absorption coefficient α than direct semiconductors such as InP.

For $h\nu \gg E_{\text{g}}$, photoelectrons are typically excited deep into the CB but relax quickly to the CBM due to the high DOS in the CB, converting the excess energy into heat. As the illumination deviates from thermodynamic electronic equilibrium, two different quasi-Fermi levels can be defined, where $E_{\text{F,p}}$ describes the electrochemical potential of the holes and $E_{\text{F,n}}$ that of the electrons as proposed by Würfel³³. Without an external field, the excess charge carrier can move freely in the crystal until they recombine after a certain lifetime τ . The recombination rate strongly depends on the purity of the crystal lattice, since the dominant recombination will occur over mid-gap states in the band gap as described by Shockley and Read³⁴. Accordingly, τ can be

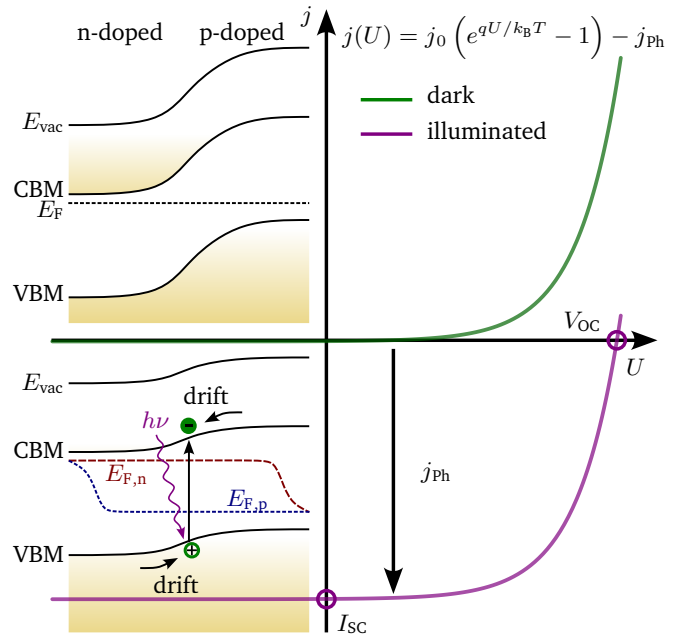


Figure 2.5: Current voltage curve of a photodiode under dark and illuminated condition.

Accordingly, τ can be

heavily reduced by surface or interface induced gap-states.

When exciting an electron-hole pair in the SCR of a semiconductor junction, the excess charge carrier will be separated by the impact of the present electric field and carrier distribution inside the SCR. By the choice of appropriate contacts, the excess charge carriers can be extracted, leading to a photocurrent j_{ph} . The photocurrent will consequently flow in reverse direction of the diode and shift the current voltage curve (Equation 2.7) to negative values (Figure 2.5). The intercepts with the coordinate axis' give on the one hand the maximum photovoltage V_{OC} (*open circuit voltage*), and on the other hand the maximum photocurrent I_{SC} (*short circuit current*), which can be achieved with the photodiode, even though at these conditions, no solar power $P_{ph} = U_{ph} \times j_{ph}$ can be supplied. The maximum conversion efficiency is reached when the solar cell is operated at the maximum power point P_{MPP} , where P_{ph} reaches its maximum.

2.2 Working principle of photoelectrochemical cells

The working principle of photoelectrochemical cells (PECs) is based on the combination of the photovoltaic effect, where the energy of light (solar power) is converted into electric power as described above, and electrolysis, which finally uses the electric power to run an endothermic reaction to split molecules, i.e. H_2O .

2.2.1 Fundamentals of electrolysis

Electrochemical reactions describe the relation between chemical redox reactions and electricity. In these reactions, electrons are transferred from an oxidized species Ox to a reduced species Red.



Ox and Red are labeled as the so-called *redox couple* (Red/Ox) with a standard redox potential of μ_{redox}^0 . μ_{redox} is a measure of how much Reaction 2.8 prefers to run in the one or the other direction and it is related to the thermal energy $k_B T$ and the activity a of Ox and Red by the Nernst equation:²⁸

$$\mu_{redox} = \mu_{redox}^0 + \frac{k_B T}{ne} \ln \frac{a(Ox)}{a(Red)} \quad (2.9)$$

In most cases, it is sufficient to use the concentration c instead of the activity.

Every reduction/oxidation reaction requires the counter reaction in order to release or consume the required electrons. The counter reaction can occur at another redox couple as exemplary depicted for the acidic water splitting reaction:



The reduction process is the hydrogen evolution reaction (HER) with $\mu_{redox}^0(H^+/H_2) = 0.0 \text{ V vs. RHE}$ giving the ultimate reference named as reversible hydrogen electrode (RHE), while the oxidation is the oxygen evolution reaction (OER) with $\mu_{redox}^0(H_2O/O_2) = -1.229 \text{ V vs. RHE}$.

The Gibbs free energy ΔG is then derived with the Faraday constant F and the number of transferred electrons n as

$$\Delta G = -nF \Delta \mu_{redox}. \quad (2.12)$$

Since μ_{redox} of both HER and OER depends equally on the proton activity $a(H_{aq}^+)$ and temperature T , $\Delta \mu_{redox}$ is a constant for the water splitting reaction, requiring $\Delta G = +237 \text{ kJ mol}^{-1}$.⁶

2.2.2 Butler-Volmer equation and charge transfer kinetics

In order to describe the kinetics for a one-electron transfer reaction, the “activated complex” is frequently used as model description.²⁸ According to this model, there is an activation barrier ΔG^* due to the formation of the “activated complex” which needs to be overcome to run the reaction (Equation 2.8) in either forward or backward direction which is described by a Boltzmann term $j \propto \exp(-\frac{\Delta G^*}{RT})$. In equilibrium, the oxidation and reduction currents j^+ and j^- extinguish each other. Applying an external potential η , the so-called *overpotential*, will affect the effective barrier height ΔG^* of the activated complex by $\alpha nF\eta$ with α as *charge transfer coefficient*, a symmetry factor of the barrier ranging from 0 to 1.

$$j(\eta) = j^+ + j^- = j_0 \left(\exp \left(\frac{\alpha nF}{RT} \eta \right) - \exp \left(- \frac{(1 - \alpha)nF}{RT} \eta \right) \right) \quad (2.13)$$

The sum of anodic and cathodic current then leads to the famous Butler-Volmer equation in 2.13, with j_0 as *exchange current density*.²⁸ The Butler-Volmer equation is displayed in Figure 2.6. At sufficiently high overpotentials, the backwards reaction can be neglected and 2.13 can be simplified to a single exponential term.

However, the Butler-Volmer equation is only valid to describe a one-electron transfer and does not consider tunneling through the barrier ΔG^* or intermediate states induced by adsorbates. Apart from the activation overpotential described here, also additional charge transfer limitations need to be considered for real systems. This could include diffusion limitations, other reaction overpotentials or ohmic losses.^{27,28}

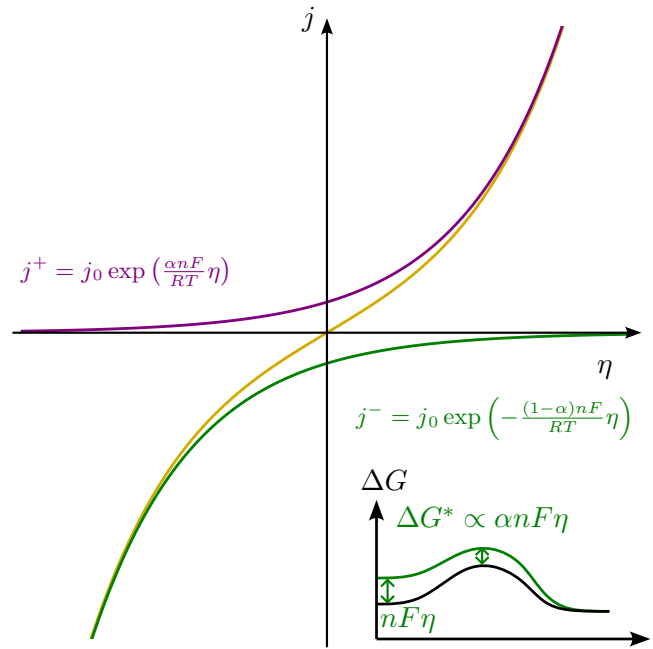


Figure 2.6: Butler-Volmer equation with anodic j^+ and cathodic j^- currents for $\alpha = 0.5$. Scheme of ΔG^* represents the activation barrier of the activated complex.

2.2.3 The semiconductor / electrolyte interface

Band bending as a result from contact formation as explained in Section 2.1.3, does not strictly require a solid state contact, but can also form at the semiconductor electrolyte interface.⁶ The driving force for the charge transfer at these electrochemical interfaces is the alignment of the electrochemical potential of the semiconductor E_F and the redox potential of the reactive redox couple in the electrolyte μ_{redox} .²⁷ As a consequence, most of the contact potential will drop in the semiconductor's SCR. The counter charges of the SCR are provided by the accumulation of oppositely charged ions in the solution leading to the so-called *Helmholtz double layer* at which additional potential can drop at a width of 2 to 5 Å.⁶

Ideally, the semiconductor electrolyte contact can be described by the Schottky model derived for semiconductor/metal contacts. However, the state distribution within the electrolyte is rather different from those of metals, where a quasi-continuous DOS of occupied electronic states is expected, that is occupied up to the Fermi level E_F .

In the 1950's Marcus³⁵ developed a detailed theory of electron transfer in polarized media such as electrolytes, which Gerischer³⁶ applied to the semiconductor electrolyte contact. He postulated a Gaussian

distribution for the reduced species in the solution, while the oxidized species is shifted towards the vacuum level.³⁷ The reason for the splitting of both levels is the reorganization of surrounding molecules in dependence of the redox couple charge. Accordingly, the energy levels E_{ox} and E_{red} are separated from μ_{redox} by the *reorganization energy*. In Figure 2.7a), the band alignment of a semiconductor electrolyte interface are depicted after contact formation. The distribution of E_{red} and E_{ox} has to be considered as probability distribution rather than an electronic DOS. This means that only one level exists at a time for each ion and an optical transition is not possible.⁶ For the electronic DOS of the electrolyte, the concentrations of oxidized c_{ox} and reduced c_{red} species have to be considered as well.²⁷ At this point, it should be noted that the charge exchange can either result from VB or CB edges or even directly from SS, depending on its concentration. Additionally, for multi-electron transfer reactions and for the often occurring cases that surface chemical bond formation and related electron states are involved, the *Marcus-Gerischer* concept is not valid any longer. In these cases buried PEC interface considerations must be developed, which requires detailed knowledge on the interfacial DOS.

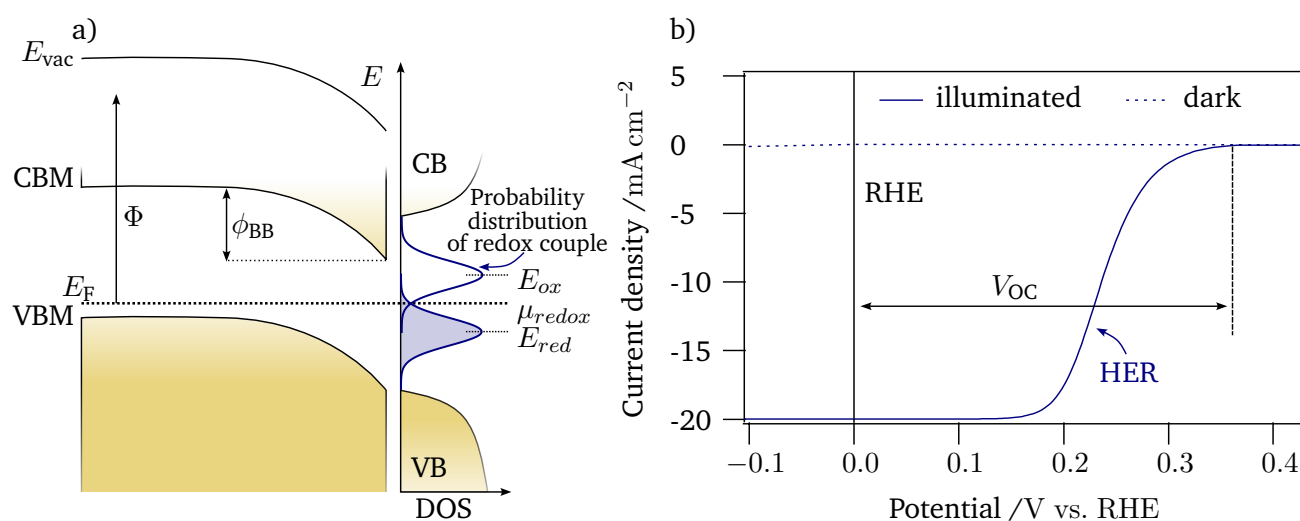


Figure 2.7: a) Energy band diagram of a semiconductor electrolyte interface with a reversible one-electron transfer redox couple after the alignment of E_F and μ_{redox} . b) Current-voltage curve of a photocathode for HER under dark and illuminated conditions. Illumination leads to a convolution photodiode behavior and charge transfer kinetics. Illumination induces a photovoltage, shifting the onset of the HER versus the RHE into anodic direction.

In Figure 2.7b), the schematic current-voltage characteristics of a photocathode for photoelectrochemical HER are shown. The SCR within the semiconductor in contact to the electrolyte leads to a separation of excess charge carriers during illumination (for $h\nu \geq E_g$). In case of a depleted p-type photocathode, illumination will accumulate photoelectrons at the electrochemical interface, promoting the cathodic HER. As a result, the photovoltage V_{OC} shifts the reaction onset into the anodic region. The inverse considerations can be made for depleted photoanodes, where the accumulation of holes shifts the onset of the oxidation reaction into cathodic potentials.

If V_{OC} is large enough (≥ 1.6 V), the complete water splitting reaction, i.e. HER at the photocathode and OER at the counter electrode, can run by the solar power without additional bias. However, the photocurrents are limited due to the charge transfer properties of the photodiode.

For these considerations, it does not matter if the photovoltage results from an illuminated SCR directly induced by the contact to the liquid electrolyte as utilized in photocatalysis, or if the photovoltage results

from a buried junction PEC device as considered in this thesis.

However, even for buried junctions, the interaction of the photodiode with the electrolyte can still induce band bending by charge transfers and therefore affect the PEC device properties.

2.3 Investigated materials

Buried PEC devices require a complex combination of different material classes. In this section, the electronic properties of the different materials relevant for this thesis are presented.

2.3.1 Photoabsorber: Si and InP

Silicon (Si) is an important elemental indirect semiconductor with a large variety in modern electronic applications such as transistors, integrated circuits, light emitting diode (LED) and solar cells. Especially as photoabsorber, Si attracted a lot of attention due to its bandgap of 1.12 eV²⁹ located close to the middle of the efficiency maximum for solar cell applications and its advantage in terms of abundance and nontoxicity over many other photoabsorbers.

Indium phosphide (InP) belongs to the group of III-V compound semiconductor and has a direct bandgap of 1.34 eV,³⁸ which is in the optimum of the *Shockley-Queisser* efficiency limit.¹⁰ Despite the fact that III-V semiconductors tend to show better photovoltaic performances, binary and ternary compound semiconductors are much more critical in terms of abundance and costs than Si, reducing their application potential in wide-spread applications.³⁹

Electronic structures

In silicon, the outer 3s and 3p orbitals combine to form hybrid sp³ orbitals, splitting in the 3D crystal into bonding and antibonding combinations that form VB and CB, respectively. InP is of more polar character, since the five-valent P atoms bond to the trivalent In. Accordingly, the bonding and antibonding combinations from the outer P 3s & 3p and In 5s & 5p states form VB and CB.

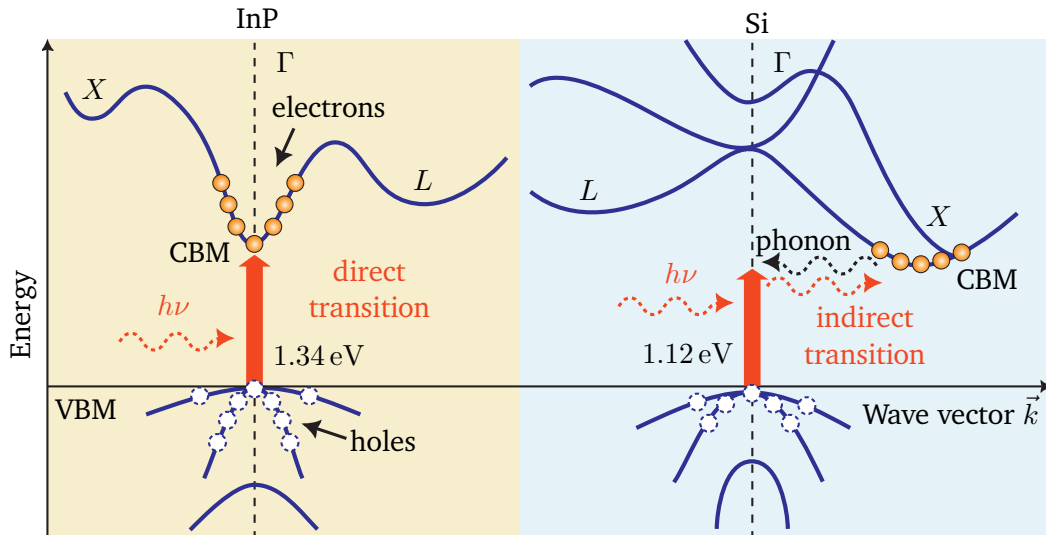


Figure 2.8: Band structure and optical transition scheme of InP (left) and Si crystals (right), adapted from ⁴⁰. InP reveals a direct band transition after optical excitation, while an indirect transition in Si requires an electron-phonon interaction.

The resulting electronic band structure calculations are shown in Figure 2.8. A direct inter band transition is observed in InP, while the indirect transition in Si requires an electron-phonon interaction, leading to lower absorption coefficients in comparison to InP. On the other hand, indirect semiconductors typically reveal longer charge carrier life times.⁴¹

Crystal structure and surfaces

In its pure form, Si reveals a diamond like crystal structure with a lattice constant a of 5.431 Å, while InP crystallizes in the similar face-centered cubic “zinc blende” structure with $a=5.869$ Å as many other III-V compounds (Figure 2.9). Furthermore, the relevant surface planes are depicted, at which single crystals

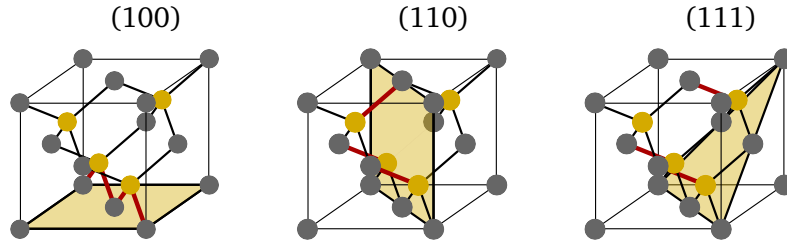


Figure 2.9: Surface planes of Si (diamond structure). For InP, grey and yellow atoms represent In and P atoms, respectively (“zinc blende” structure). Non-saturated bonds at specific surfaces are highlighted in red.

are cleaved. At the surface, the regularly fourfold coordinated atoms become unsaturated due to the lack of bonding partners. The non-saturated bonds at the respective surface of both semiconductors are highlighted in red. The (100) surface reveals 2 so-called *dangling bonds* per surface atom, while the (110) and (111) surface, only reveal one dangling bond per surface atom. The surface atom density slightly varies for each surface, but is in the range of $1 \times 10^{-15} \text{ cm}^{-2}$. In order to saturate the dangling bonds,

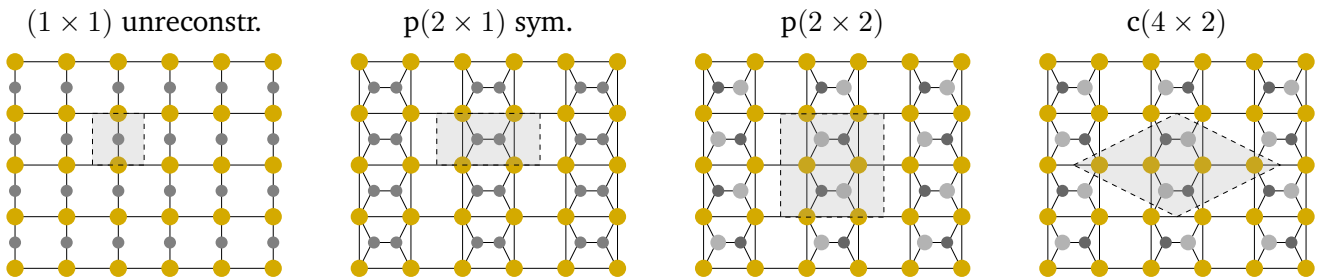


Figure 2.10: Surface superlattice of (100) surface reconstructions according to Zandvliet⁴². The different colors represent atoms of different level.

the surface atoms will relax and form surface reconstructions.⁴² In Figure 2.10, the relevant surface reconstructions for the Si (100) surfaces are shown. The unsaturated surface atoms form dimers leading to a symmetric $p(2 \times 1)$ structure. Chadi proposed that the out of plane buckling of the surface dimers forms higher order reconstructions and opens a gap between occupied and unoccupied surface states lowering the total energy of the dimer. The buckling can either appear *in-phase* or *out-of-phase* when neighboring dimer rows buckle in equal $p(2 \times 2)$ or opposite $c(4 \times 2)$ directions (Figure 2.10).⁴³

In principle, these structures are also valid for InP. However, the two different atomic species lead to even more complex superstructures with either In or P terminated surfaces.

Stability in aqueous solutions

Neither Si nor InP show relevant Pourbaix stabilities in aqueous solutions under realistic working conditions above -1.0 V vs. RHE.^{44,45} However, in acidic solutions ($pH \leq 7$), Si forms stable oxide passivation layers such as SiO_2 , H_2SiO_3 , H_4SiO_4 for potentials above -0.8 V vs. RHE.

For InP, there exists no stable phosphate passivation phase, while for a pH window of $5 \leq pH \leq 11$ In_2O_3 becomes passivating for potentials ≥ -0.5 V vs. RHE.^{46,47}

2.3.2 Electrochemical buffer layer: TiO_2

Titanium dioxide (TiO_2) is a versatile semiconductor material, belonging to the group of transition metal oxides, that finds applications in various fields, including electronics and energy conversion. It attracted a lot of attention in photocatalysis, when Fujishima and Honda⁴⁸ proved the photocatalytic activity of TiO_2 , which could catalyze the water splitting reaction solely by the power of UV-light.

Apart from that, TiO_2 is often employed as an electrochemical buffer layer in the context of photoelectrochemical multi-layer devices, playing a crucial role in improving device performance and stability.^{21,49} An electrochemical buffer layer requires specific electronic properties in terms of facilitating charge transfer, mitigating electron recombination, and providing a stable interface between different materials within the device. In this regard, TiO_2 combines good optical properties with a bandgap of ≥ 3.0 eV with still good electric conductivity and relatively high electron mobilities.⁵⁰ In addition, it can be deposited by a wide range of deposition methods, ranging from various ultra-high vacuum (UHV) thin film techniques to wet-chemical sol-gel procedures.⁵¹ In conclusion, TiO_2 has a good chemical stability and corrosion resistance, preventing the photoabsorber from degradation.

The anatase and rutile phase

The technologically most important polytypes of TiO_2 are the *rutile* and the *anatase* phase. Both polymorphs show tetragonal symmetry, which differ in distortion and linkage of TiO_6 octahedra (Figure 2.11).

In the anatase phase, TiO_2 tends to form oxygen vacancies, which can be controlled by adjusting film growth and annealing conditions.⁵¹ Even though anatase reveals a direct bandgap E_g of 3.2 eV, oxygen vacancies can lead to charge carrier concentrations of up to 10^{20} cm^{-3} , giving rise to a conductivity of up to $\approx 10 \text{ S cm}^{-1}$.⁵⁰

In contrast to anatase, rutile reveals a slightly narrower indirect bandgap of $E_g = 3.0$ eV and shows donor concentrations in the range of 10^{19} cm^{-3} in its reduced form. However, the anatase modification provides much higher electron mobilities μ_{el} than rutile due to the by a factor of 20 reduced effective electron mass leading to typically lower conductivities in the rutile phase of $\approx 0.1 \text{ S cm}^{-1}$.⁵⁰

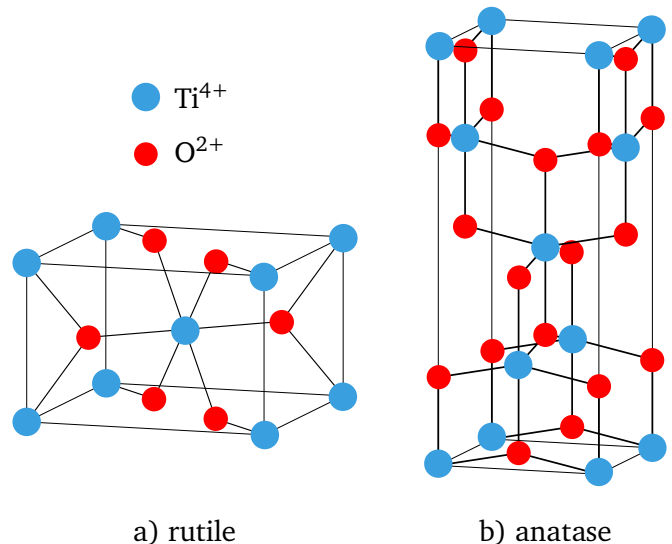


Figure 2.11: Crystal structures of a) rutile and b) anatase TiO_2 modifications.

The bonds in TiO_2 are highly polar or even of ionic character. The VB in TiO_2 is mainly composed of O 2p states, whereas the CB is primarily of Ti 3d character.⁶ Even though the rutile phase is thermodynamically

more stable than the anatase phase, the lower surface energy of anatase is favored when considering nanostructures with grain sizes below 20 nm.⁵²

TiO₂ stability in aqueous solutions

TiO₂ is stable for a broad potential window under alkaline conditions. For acidic solutions, the TiO₂ Pourbaix diagram shows Ti corrosion under HER working conditions ≤ 0.0 V vs. RHE.⁴⁷ However, there are several studies reporting that TiO₂ also forms a stable passivation layer under strong acidic conditions,⁵³ providing a protecting electrochemical buffer layer for photoabsorbers underneath.^{54,55}

2.3.3 Electrocatalyst: Pt

Platinum (Pt) is a widely recognized and extensively studied electrocatalyst for the HER at the cathode. It reveals remarkable electrocatalytic properties, including a high activity, conductivity, and selectivity, which makes it a preferred choice in electrocatalytic applications such as fuel cells and electrolyzers.^{56,57} Pt provides the best HER activity in acidic media, since Pt is located on the top of the *volcano plot*, showing the highest exchange current density due to a moderate binding energy of hydrogen adsorption (*Sabatier's principle*).⁵⁸

As very costly noble metal, the utilization of Pt for electrocatalysis can be optimized by nanostructuring and clustering, which maximizes the active surface sites at a minimum of loading.⁵⁹ For instance, a cluster size of 46 atoms Pt₄₆ has been found to maximize the photoelectrochemical hydrogen evolution rate on illuminated CdS nanorods.⁶⁰

According to the Pourbaix diagram, Pt is immune in all media under HER conditions.⁴⁷ However, nanostructuring and the contact to the catalyst support might limit the Pt stability under very corrosive conditions.

3 Analytical methods

In this chapter, the physical principles of the relevant analytical methods used in this thesis are presented. Fundamental principles of spectroscopy is based on the books of Hüfner⁶¹, and de Groot and Kotani⁶².

3.1 Photoemission spectroscopy (PES)

Photoemission spectroscopy (PES) belongs to the most crucial and extensively employed analysis techniques to investigate electronic structures of solid state surfaces and interfaces.^{61,63} The method is based on the photoelectric effect, which has been first analyzed in ultra-high vacuum (UHV) by Philipp Lenard in 1900.⁶⁴ Albert Einstein could provide a quantum mechanical explanation of the effect in 1905, for which he was awarded with the physic's Nobel Prize in 1921.⁶⁵ Accordingly, electrons can be released from a surface by the impact of electromagnetic radiation. The kinetic energy of the photoreleased electrons E_{kin} depends on the quantum energy of incoming photons $h\nu$, but is independent of the light intensity. As a consequence, the analysis of released photoelectrons gives information about their binding energy E_b within the material. E_b is element and orbital specific, since it depends on the atomic number Z and the first quantum number n , according to Bohr's theory.⁶⁶

$$E_b = -\frac{Z^2}{n^2} \cdot 13.6 \text{ eV} \quad (3.1)$$

A schematic scheme of the emission and detection process in PES is depicted for a semiconductor in Figure 3.1a). If the energy of incident photons $h\nu$ is large enough to overcome the electrons binding energy E_b and the samples work function Φ , the electron can be released and leaves the sample surface.

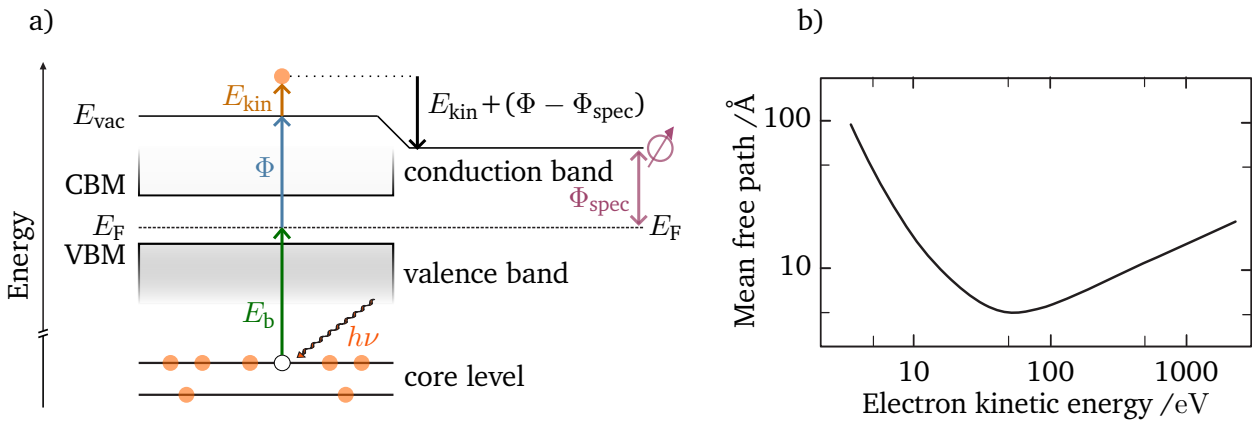


Figure 3.1: Schematic drawing of a) emission and detection process of photoelectrons from a semiconductor and b) mean free path of electrons in solids with respect to their kinetic energy adapted from⁶⁷.

The remaining energy of the photoelectron E_{kin} is

$$E_{\text{kin}} = h\nu - E_{\text{b}} - \Phi. \quad (3.2)$$

When analyzing and detecting the free photoelectron using a spectrometer, the sample and the spectrometer are in electric contact, increasing E_{kin} by the contact potential of both $(\Phi - \Phi_{\text{spec}})$ and E_{kin} becomes

$$E_{\text{kin}} = h\nu - E_{\text{b}} - \Phi + (\Phi - \Phi_{\text{spec}}) = h\nu - E_{\text{b}} - \Phi_{\text{spec}}. \quad (3.3)$$

Consequently, the analyzed E_{kin} of photoelectrons is independent of Φ but solely depends on Φ_{spec} . Φ_{spec} is taken into account by shifting the Fermi edge of a clean metallic sample to $E_{\text{b}}=0.0$ eV. As a consequence, under electronic equilibrium, all binding energies measured in PES are referred to E_{F} which makes it a feasible tool to follow potential changes at the sample surface.

The high surface sensitivity of the technique originates from the low electronic mean free path λ_{IMFP} of electrons in solids, which typically follows the so-called “bathtub curve” (see Figure 3.1b)). λ_{IMFP} describes the traveling distance of undisturbed electrons within a solid until their number has been reduced by e^{-1} due to inelastic scattering processes, which lead to losses of the electron’s kinetic energies. According to Figure 3.1b), λ_{IMFP} strongly depends on the electron E_{kin} , but is also slightly material dependent, which is typically neglected in PES. In PES only non or elastic scattered electrons contain relevant material specific information. Therefore, the information depth is related to λ_{IMFP} and ranges from 1 to 10 nm, depending on the excitation energy.⁶⁷ However, to consider the reduction of the effective attenuation, due to elastic scattering effects, the effective attenuation length λ_{EAL} is typically used nowadays.⁶⁸

Apart from the energetic reference to the electrochemical potential E_{F} , PES also provides chemical information about the sample surface. In chemical compounds, atoms are typically bound by their valence electrons which form quasi-continuous energy bands (see Section 2.1). The deeply located core levels barely contribute to the chemical bonding. However, the analysis of the core levels may provide information about the chemical environment of the atoms like the oxidation state with a high sensitivity for surface impurities.

In order to excite such deeply located core levels, high energetic photons are required. With the lab based X-ray photoemission spectroscopy (XPS) used in this thesis, monochromatic Al $K_{\alpha'}$ is used with a photon energy of about 1486.74 eV. For the analysis of the valence states, ultraviolet photoemission spectroscopy (UPS) is a suitable method, since the He I and II excitation of a He lamp are of higher intensity and higher energy resolutions.

3.1.1 XP-spectra

The spectrum gained by PES shows the total density of states (DOS) within the excited energy range. The binding energy E_{b} is calculated according to Equation 3.3.

A characteristic XP-survey spectrum of a sputter-cleaned Pt foil is shown in Figure 3.2. For conventional reasons, the binding energies in PES are defined positive, even though the x-scale is typically reversed. According to Equation 3.1, the core level binding energy in the PES scale typically decreases with increasing first quantum number n . Thus, the Pt 4s ($n=4$) emission line is located at a higher binding energy than the Pt 5s ($n=5$) line. Due to spin-orbit interactions, orbitals with an azimuthal quantum number $l>0$ show a doublet splitting, as observed for p-, d-, and f-orbitals in Pt. Each state of the doublet is indexed with the total angular momentum quantum number $j_{\text{qn}} = |l \pm \frac{1}{2}|$.⁶³

The valence band (VB) states arise from Pt 5d states, which overlap with partially occupied 6 s states leading to half-filled energy band at the Fermi level. As a result, a Fermi edge is observed confirming the

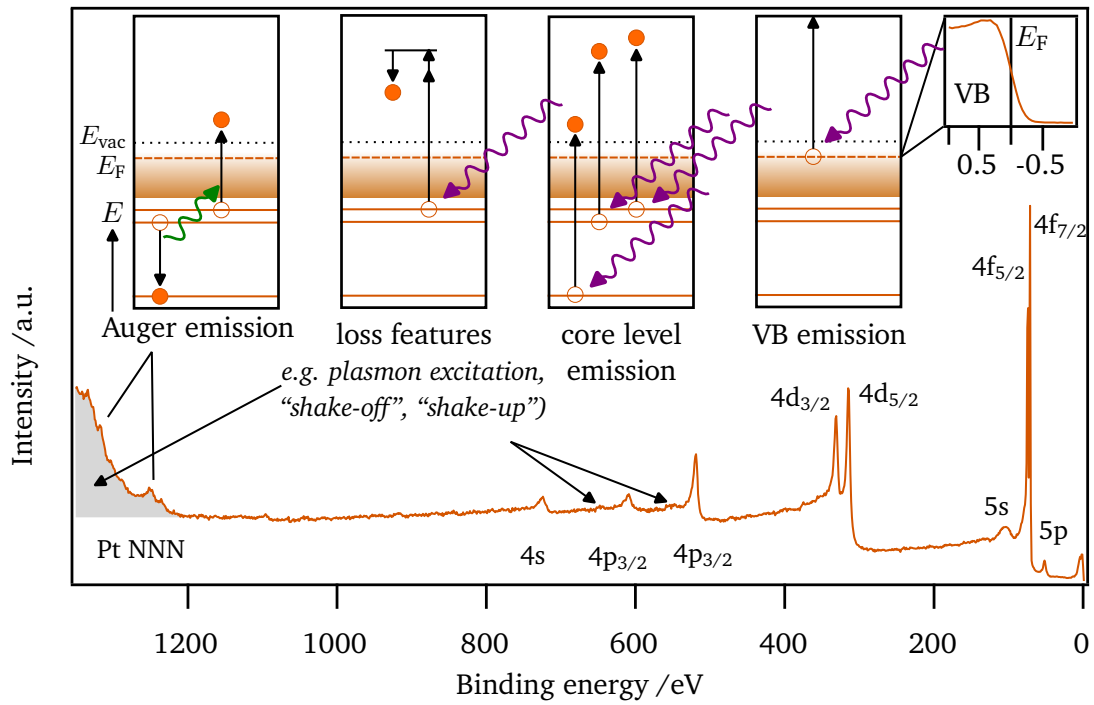


Figure 3.2: Exemplary XP-survey spectrum of a sputter-cleaned Pt foil. The 4 types of emission features are represented schematically in the boxes. The Fermi edge is extracted in higher resolution. Empty and filled spheres represent electrons before and after excitation.

metallicity of the Pt sample.⁶¹

Auger emissions typically are detected too, when measuring XPS. In this case, the emission of a photoelectron leaves an empty site at an inner core level. When this free site gets occupied by a core electron from an outer shell, the difference in energy is transferred to another core level electron. If the electron is excited above E_{vac} , it leaves the sample and can be detected by the spectrometer as an *Auger emission* line. In contrast to core level lines, Auger lines appear at constant kinetic energy and are independent of $h\nu$.⁶³ If the photoelectrons from these characteristic emissions experience inelastic scattering and partially transfer their kinetic energy to an electron transition nearby, satellite emissions can appear within the XP-spectrum. Depending on whether the other electron is excited above E_{vac} and thus leaves the sample or not, satellites are named as “shake-off” or “shake-up”.⁶² In addition, due to inelastic scattering, photoelectrons loose kinetic energy and satellites appear at higher binding energy, which result from excitations within the bulk of the material, e.g. often found for localized states due to different final states. In addition, multiple and inelastic scattering effects at electrons and nuclei over all energy states along the spectrum lead to a continuous background which correlates with the sum of DOS over the core levels and increases with higher binding energy.⁶¹ Furthermore, photoelectrons can excite surface and bulk plasmons, collective electron vibrations, which also reduces their kinetic energy. Plasmon excitation typically lead to a maximum in the background at the left edge of the spectrum.

Quantitative XPS analysis

The detected XP signal of a certain emission line I_X not only depends on the atomic density N_X of a certain element but on several parameters, which need to be considered when doing quantitative analysis with XPS. For the “magic angle” configuration, where X-ray source and electron detection are arranged in 54.7°

and angular distribution of photoelectrons can be neglected, I_X depend on the following parameters.⁶⁹

$$I_X = I_{hv} T_{spec}(E_{kin}) ASF(X, h\nu) edc(E_{kin}) \cos \Theta_e \cdot N_X \quad (3.4)$$

I_{hv} is the X-ray flux of the source, T_{spec} describes the spectrometer transmission and detector efficiency at a certain E_{kin} , ASF is the photoionization cross-section of a certain element X , and edc the escape depth correction of a certain emission line with Θ_e as angle between detection and surface normal.⁶³

When normalizing the integrated intensities I_X to these parameters, N_X or edc can be separated for stoichiometry or film thickness analysis. Further details are described in Section 4.1.1.

3.1.2 Ultraviolet photoemission spectroscopy (UPS)

The operation principle of UPS is rather similar to XPS.⁶³ In UPS, the photon excitation is produced from a gaseous discharge. The excitation from noble gases such as helium is in the hard UV range with very narrow line width of ≤ 30 meV. Consequently, binding energies in UPS do not refer to deep core levels but to VB levels. Due to the high surface sensitivity of excited photoelectrons, UPS also covers shallow states of adsorbates, which makes it a powerful tool to investigate interactions of adsorbates with surfaces.^{63,67} In addition, angular resolved measurements can be performed to investigate the band structure at the surface region and to explore the effect of adsorbates on the band structure.⁶¹

3.2 Near edge X-ray absorption fine structure (NEXAFS)

Near edge X-ray absorption fine structure (NEXAFS) is another powerful tool to analyze the electronic structure of a material. It is based on the absorption of X-rays by the excitation of a core level electron into the lowest unoccupied molecular orbital (LUMO). In contrast to PES, NEXAFS are sensitive to unoccupied electronic states within a material, providing additional information about electronic structures of the conduction band (CB) and chemical environment of certain atomic species.⁶²

NEXAFS requires a tunable X-ray source. This is why it is typically performed at synchrotron facilities. The absorption spectra are typically conducted by the analysis of photoelectrons. They can either be measured in total (TEY, all photoelectrons) or partial electronic yield (PEY, specific, e.g. Auger electrons), providing additionally surface sensitivity.

3.3 Low-energy electron diffraction (LEED)

Low-energy electron diffraction (LEED) is a UHV technique to investigate the atomic structure of the sample surface.^{70,71} The physical principle is based on electron diffraction at the periodic surface superlattice due to its wave character as postulated by De Broglie⁷² in 1923.

$$\lambda_e = \frac{h}{\sqrt{2m_e E_{kin}}} \quad (3.5)$$

According to him, the De Broglie electron wave length λ_e depends on the Planck constant h , the electron mass m_e , and its kinetic energy E_{kin} . For low electron energies in the range of 20 to 200 eV, the wave length is ranging from 0.8 to 2.7 Å. According to Figure 3.1b), the λ_{IMFP} of electrons is typically less than 10 Å, which is basically 2 to 3 surface layers and therefore ideal to investigate surface reconstructions.

When the low energy electrons hit the surface, they interfere with the electron density around the surface atoms. If the Bragg condition $a \sin \theta = 2n\lambda_e$ with n as integer diffraction order is fulfilled, constructive interference occurs. These interference spots image the reciprocal space of the surface, which can be

visualized using a LEED setup.⁷¹

The transition of the two translational vectors \vec{a}_1 and \vec{a}_2 into the reciprocal space are performed by the relations

$$\vec{a}_1^* = 2\pi \left(\frac{\vec{a}_2 \times \vec{n}}{\vec{a}_1 (\vec{a}_2 \times \vec{n})} \right) \text{ and } \vec{a}_2^* = 2\pi \left(\frac{\vec{n} \times \vec{a}_1}{\vec{a}_2 (\vec{n} \times \vec{a}_2)} \right) \quad (3.6)$$

with \vec{n} normal to the sample surface.⁷¹ The reciprocal space and with that the LEED image is then composed of the sum of both translation vectors $h\vec{a}_1^* + k\vec{a}_2^*$ with h, k as integer numbers.

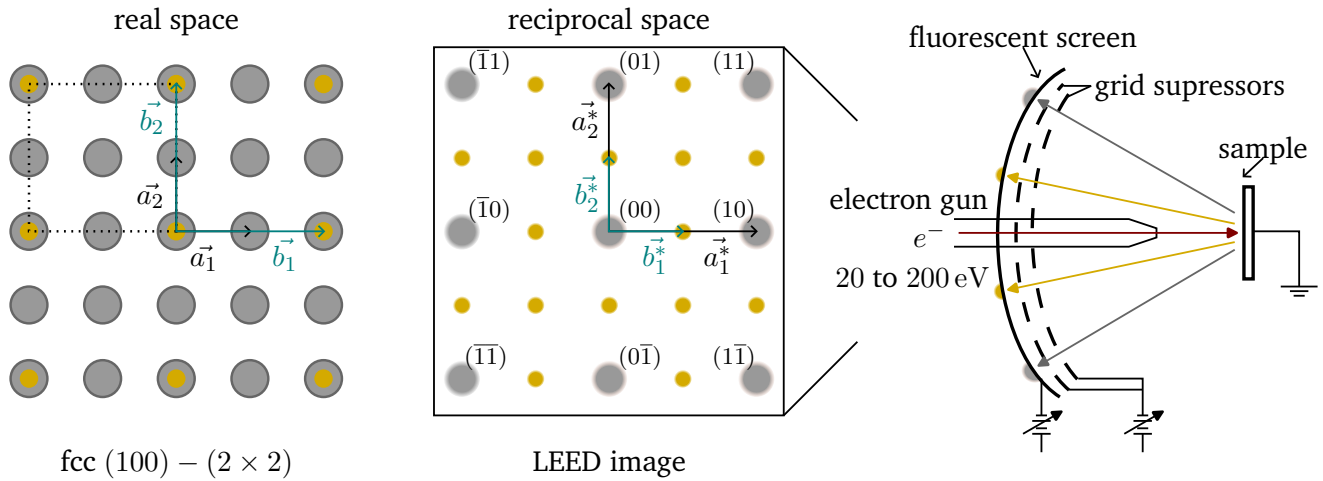


Figure 3.3: Exemplary surface structure of an fcc (100) - (2 x 2) surface in real and reciprocal space (left). Grey and yellow spheres could represent surface layer and ad-atoms, respectively. Scheme of LEED setup represents working principle (right). The LEED image on a fluorescent screen is equivalent to the reciprocal space.

In Figure 3.3, an unreconstructed fcc (100) surface with a periodic ad-atom coverage, e.g. adsorbates, are depicted. The (2×2) LEED image is composed of the superposition of crystal and ad-atom reflexes. On the right hand side of Figure 3.3, a scheme of the typical LEED setup is shown. An electron beam is diffracted at the sample surface, leading to bright spots on the fluorescent screen in case of constructive interference. The 2D image on the screen is recorded with a camera to visualize the 2D image of the reciprocal space. Dedicated voltages on screen and grids in front suppress background noise.

3.4 Electrochemical performance

Electrochemistry describes the chemical processes that cause an electron transfer between separated materials. There are various electrochemical methods to investigate the electrochemical properties of a certain sample surface.

In a 2-electrode configuration, where two electrodes are electrically connected but separated by an electrolyte, the performance of a full device setup can be tested, including the sum of single component performance and limitation, i.e. catalysis, charge transfer properties or ohmic losses, which occur on both cathode and anode simultaneously.

In order to investigate the half-cell performance of one electrode, a 3-electrode setup is to be chosen. With that, it is possible to investigate the current-voltage characteristics of the so-called working electrode (WE) independently of the counter electrode (CE). In this configuration, the potential of the WE, the electrode of interest, is measured against a reference electrode (RE) while the current flow is measured

between WE and CE. Due to the high ohmic contact between WE and RE, no currents flow between both electrodes and consequently no chemical reaction occurs at the RE.²⁸

3.4.1 Reference electrodes

In the 3-electrode setup, different reference electrodes are in use. For ideal measurement conditions, the reference electrode has to be stable within the used electrolyte media. For acidic solutions, the Ag/AgCl reference has been established, while for basic solutions the Hg/HgO reference has been proved. Both references are based on a redox couple with a fixed activity.⁷³

The most common reference scale which has been established today, is the reversible hydrogen electrode (RHE). It is a *pH* corrected standard hydrogen electrode (SHE) potential, which is defined as $E_{SHE}=0.0$ V for an H^+ activity of 1.

$$E_{SHE} = E_0 - 0.0591 \text{ V} \cdot pH \quad (3.7)$$

In order to compare measurements in different electrolytes, the RHE has been defined independently of *pH*:

$$E_{RHE} = E_{SHE} + 0.0591 \text{ V} \cdot pH \quad (3.8)$$

3.4.2 (Photo)current voltage curves

For a stable configuration, no current flows between the WE and CE under open circuit conditions and the electrochemical potential of the WE can be measured against the used RE. This potential difference is called open circuit potential (OCP). Under steady state conditions, the OCP is a fixed value.²⁸ When applying an additional potential between the WE and CE which is large enough to run a suitable redox reaction, a current flow can be measured in dependence on the electrochemical potential. Current voltage curves describe the current flow between WE and CE at a linearly changing potential, which is referred to the RE. The current density j , which is assigned to an oxidation or reduction reaction at the WE depending on the sign of current, is according to Faraday's law proportional to the reaction rate and with that to the amount of evolving product, which is in case of electrolysis either H_2 or O_2 evolution. For a simple one-electron transfer redox reactions, the current voltage characteristics are described by the Butler-Volmer equation (see Eq. 2.13). However, it should be noted that a current flow might be also related to side reactions, such as corrosion, or capacitive currents from electrochemical double layer charging.

Chopped light voltammetry

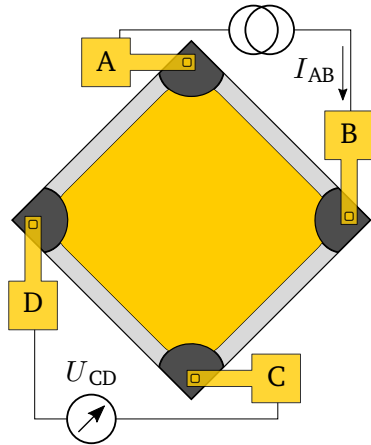
If the WE is photoactive, additional information can be drawn from current voltage curves using light illumination.⁶ Here, photo and dark currents as a function of applied potential can be analyzed by sweeping the potential with a constant scan rate and switching a light source at a fixed energy. As a result, one gets a dark current and a photocurrent curve from the same measurement. For proper photoelectrochemical cells (PECs), the photocurrent will be in principle larger than the dark current curves. Additional photogenerated charge carriers will contribute to the reaction and increase the applied potential bias. Since most single-junction photoelectrodes are not able to run the water splitting reaction without any additional bias, a half-cell solar to hydrogen efficiency (STH) or "applied bias photon-to-current efficiency"⁷⁴ is defined. Accordingly, the STH is

$$STH = |j_{ph}| \times \frac{V_{redox} - V_{bias}}{P_{illumination}}, \quad (3.9)$$

with j_{ph} as the photocurrent, $P_{illumination}$ as the light intensity and V_{bias} as the applied bias. V_{redox} is then 1.23 V vs. RHE for photoanodes and 0.0 V vs. RHE for photocathodes. For an additional bias $V_{bias} \neq 0$ V, the half-cell STH has to be interpreted as an “extrapolation towards a tandem cell device, in which the required bias voltage is generated by a photovoltaic cell that is placed behind the photoelectrode”.⁶ The photocurrent onset potential in reference to V_{redox} gives furthermore the information of photovoltage gain, which is produced by the illumination of the photoelectrode. In addition, this information can also be drawn from the OCP shift under illumination, which is related to the V_{OC} value of a solar cell device. Under dark conditions, the diodic character of the photoelectrode is in reverse direction, which limits the dark current drastically.¹²

3.5 4-point Hall measurements

The van der Pauw method is a feasible technique to measure the conductivity as well as the Hall coefficient of a thin film sample. As long as the film thickness is homogeneous, the measurement is independent of the film geometry.^{75,76}



Conductivity

By applying proper contacts, 4-point contact probes are attached on a thin film. When applying a current I_{AB} from contact A to B, a potential drop U_{DC} is measured between contact D and C. With these values a resistance $R_{AB,DC}$ is derived, with

$$R_{AB,DC} = \frac{U_{DC}}{I_{AB}}. \quad (3.10)$$

When deriving $R_{BC,AD}$ in the same way, the conductivity σ is calculated with the known film thickness d and a symmetry factor f , which is only a function of the ratio between $R_{AB,DC}$ and $R_{BC,AD}$

$$\sigma = \frac{\ln 2}{\pi d} \times \frac{2f}{R_{AB,DC} + R_{BC,AD}} \quad (3.11)$$

Figure 3.4: Scheme of van der Pauw method.

Hall mobility

When applying a magnetic field \vec{B} perpendicular to the thin film, the Lorentz force F_L will act on the free charge carriers of charge q moving between two contacts with the velocity \vec{v} :

$$\vec{F}_L = q \cdot \vec{v} \times \vec{B} \quad (3.12)$$

\vec{F}_L is acting perpendicular to the current flow and the magnetic field what will change the measured value of $R_{AB,DC}$.

The Hall coefficient A_H is then derived by the following relation

$$A_H = \frac{1}{qn_{el}} = \frac{d}{B} \times \Delta R_{AB,DC}. \quad (3.13)$$

From that, the free charge carrier concentration n_{el} can be determined. In addition, with the relation $\sigma = n_{el}q\mu_{el}$ the charge carrier mobility μ_{el} can be derived.

3.6 UV-Vis-NIR

With Ultraviolet-visible-near-infrared spectroscopy (UV-Vis-NIR), the optical properties in the region of visible light, i.e. sun-light, from near-infrared to ultraviolet light is investigated. In this energy (0.1 to 4 eV), electronic interband transitions can take place. It is therefore a feasible technique to investigate the forbidden optical band gap of semiconducting materials.⁷⁷ The attenuation of light of the intensity I_{hv}^0 is described by the Lambert-Beer law.

$$I_{hv} = I_{hv}^0 \cdot \exp^{-\alpha(h\nu)x} \quad (3.14)$$

In Equation 3.14, x describes the penetration depth of the light, while $\alpha(h\nu)$ is the absorption coefficient. In order to absorb a photon by exciting an electron from the VB into the CB, $h\nu$ has to be larger than the band gap E_g . Accordingly, α is strongly $h\nu$ -dependent.

In the used setup, the absorption spectrum is calculated from transmission and reflection spectra. For that purpose, the sample is usually tilted by an angle φ and the absorption coefficient $\alpha(h\nu)$ is calculated from Equation 3.14 if the sample thickness d is known with

$$\alpha(h\nu) = -\ln\left(\frac{I_T}{100 - I_R}\right) \times \frac{\cos \varphi}{d} \quad (3.15)$$

In order to identify the nature of the optical band transition and to derive the optical bandgap, the quantity $(\alpha \cdot h\nu)^{\frac{1}{r}}$ can be plotted over $h\nu$ which gives rise to the so-called “Tauc-plot” using the linear relation

$$h\nu - E_g = (\alpha \cdot h\nu)^{\frac{1}{r}}, \quad (3.16)$$

with r as characteristic exponent denoting the nature of the band transition.^{78,79} For an allowed direct band transition, r takes the value of 0.5, while r equals 2 for an allowed indirect band transition. With the right value for r , the linear region within the Tauc plot can be used to extrapolate the optical band gap E_g .

3.7 Thin film deposition techniques

In this Section, the deposition techniques used in this thesis are briefly introduced.

3.7.1 Magnetron sputtering

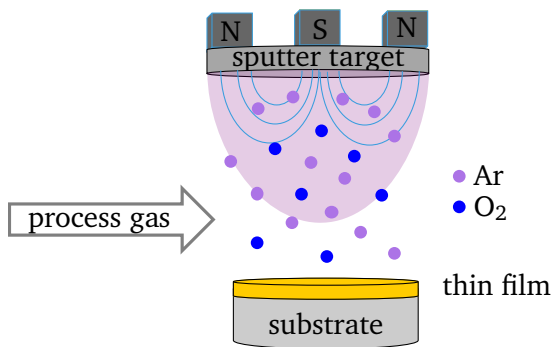


Figure 3.5: Scheme of used magnetron sputter process.

Magnetron sputtering belongs to the group of physical vapour deposition (PVD) techniques requiring vacuum conditions. The ignition of a plasma between a target and a surrounding anode ring by a high voltage source accelerates ions of an inert process gas onto the target material, where the impact of the high kinetic energy ions causes material ablation. The fine atomized sputter material disperses and passes the discharge zone and finally condenses on the substrate. Depending on the process parameter, a thin film will form according to the predominant growth mode and diffusion mechanisms.⁷⁷ The plasma is composed of an ionized process gas, commonly Argon and optionally a reactive gas. Pure metal thin films are deposited solely with Ar, leading

to pure, homogeneous and dense metal films. For the deposition of metal oxide films, typically reactive magnetron sputtering is used. Here, the oxide thin film forms from an elemental target, where the metal

atoms react with oxygen during the sputter process and form an oxide film on the substrate while the compound stoichiometry is controlled by the process parameters.^{80,81}

In case of magnetron sputtering, permanent magnets are placed behind the target and induce a circular magnetic field. When igniting the plasma due to an electric direct current (DC) voltage, Ar ions are forced to move along a circular path close to the target, increasing the ionization rate. This procedure allows to perform the sputter process even in the lower Pa-range, therefore promoting high deposition rates. The properties of the deposited film and the degree of crystallization depend on substrate temperature, discharge sputter power, substrate to target distance, ratio of reactive gases and working pressure.⁸²

3.7.2 Atomic layer deposition (ALD)

Atomic layer deposition (ALD) belongs to the group of chemical vapour deposition (CVD) techniques. It is based on the alternating purging of precursor gases.^{83,84} In contrast to other conventional CVD methods, the cyclic film growth process is self-terminating, leading to homogeneous films with strongly defined layer thicknesses on an atomic scale. The ALD process is also very suitable for 2D layers with high aspect ratio or complex 3D structures such as nanowires, and is consequently used a wide range of applications from catalysis to microelectronics.⁸⁵

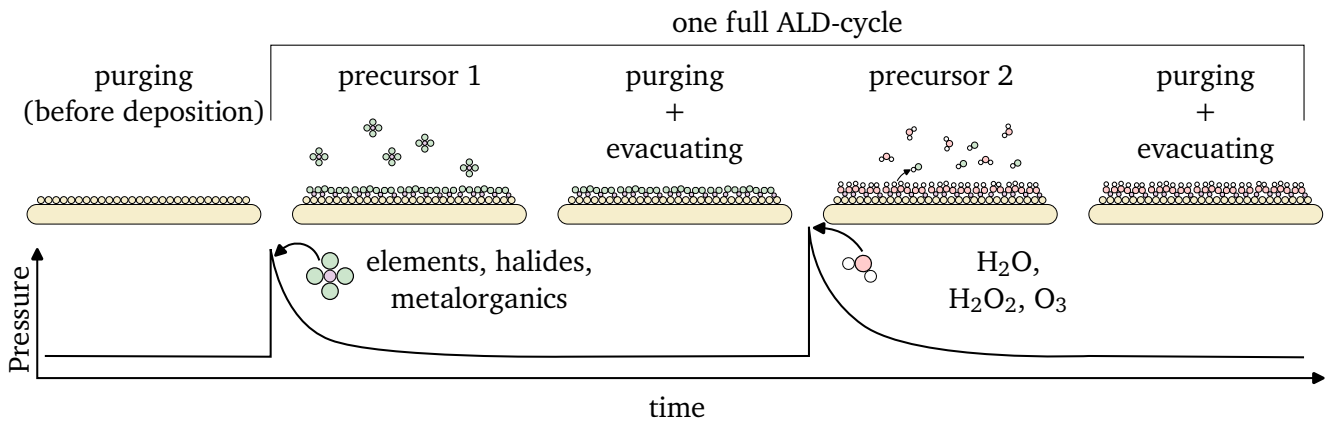


Figure 3.6: Atomic scheme of a full ALD-cycle assuming idealized deposition conditions.

In Figure 3.6 the working principle of the thermal ALD process is shown. Before starting the deposition process, a clean substrate is heated to a certain substrate temperature. The precursor pipes can be heated as well and the flow of an inert purging gas, typically Ar or N₂, is set confirming a constant base pressure, which is typically in the 10⁻¹ mbar range. Starting from a clean substrate, the layer growth during deposition consists of repeating four consecutive steps, which can be repeated any numbers of time:⁸⁵

- i) The sample is pulse-wise exposed to the first precursor terminating the substrate surface.
- ii) Purging and evacuating the process chamber removes the non-adsorbed reactants and gaseous by-products.
- iii) The sample is pulse-wise exposed to the second precursor terminating the sample surface. When adsorbing to the first reactant, both precursors react at the sample surface to form the ALD-layer. Formed by-products have to desorb from the sample surface to prevent contamination in the film.
- iv) Purging and evacuating the process chamber removes surplus precursors and the by-products from the ALD reaction.

The pulse-wise exposure of precursor gases is electronically controlled in the sub-second range by pneumatic valves. Purging can be established either pulse-wise or constantly. The used reactants have to be volatile. For the deposition of metal oxide layers, the precursors can be either inorganic, such as elements or halides, or metal-organic, such as alkyls, amides, or cyclopentadienyls. The second precursor is an oxidizing agent, typically H_2O , H_2O_2 or O_3 . Apart from metal oxides, pure metals, nitrides, and sulfides can be deposited by ALD.⁸⁵

Ideally, one covering monolayer forms within the first full cycle and the film grows by a layer-by-layer mode. In reality however, steric hindrance and incomplete chemical reactions will lead to a growth per cycle which is below the monolayer.⁸⁶ The different nature of the substrate surface can furthermore lead to an initial nucleation delay, depending on the reactant substrate interaction.⁸⁷ The substrate temperature has to be chosen high enough that the precursor can condensate and react with the substrate surface and low enough to prevent the reactants from desorbing or even decomposing.⁸⁴ In order to increase the reactivity of the process, an oxygen plasma can be used in the so-called plasma-enhanced-ALD process.^{83,84}

3.7.3 Electrodeposition

Electrodeposition has become a widely used rapid and low-cost deposition technique forming nanostructured coatings with low porosity.^{88,89} Furthermore, it gained attention for the synthesis of atomic-level metal catalyst.⁹⁰ The working principle is based on an electrochemical reduction reaction of metal ions Me^{n+} dissolved in an electrolyte:



The oxidation reaction takes place at the anode and might be either the oxidation of anions in the electrolyte or the dissolution of the electrode itself. To control and investigate the reduction process at the WE, electrodeposition is typically arranged in a 3-electrode setup. The thickness and morphology can vary and strongly depend on the deposition parameter such as electrode potential and current density, electrolyte concentration, substrate, and the deposition time.⁹⁰ Especially the potential can be applied potentiostatic (at constant potential vs. the reference) or galvanostatic (at constant current density). In addition, the potentials can be applied periodically by cyclic or pulsed voltammetry methods, leading to a huge amount of variable process parameters with strongly different coating properties.⁸⁸ Specially developed process techniques even allow strongly controlled or terminated film thicknesses such as “underpotential deposition”⁹⁰ or “self-terminated deposition”.⁹¹

4 Sample preparation and experimental setup

If not stated otherwise, sample preparation and photoemission spectroscopy (PES) analysis presented in this thesis was performed in the **Darmstadt Integrated System for Fundamental research (DAISY-FUN)** located at the material science department at TU Darmstadt.

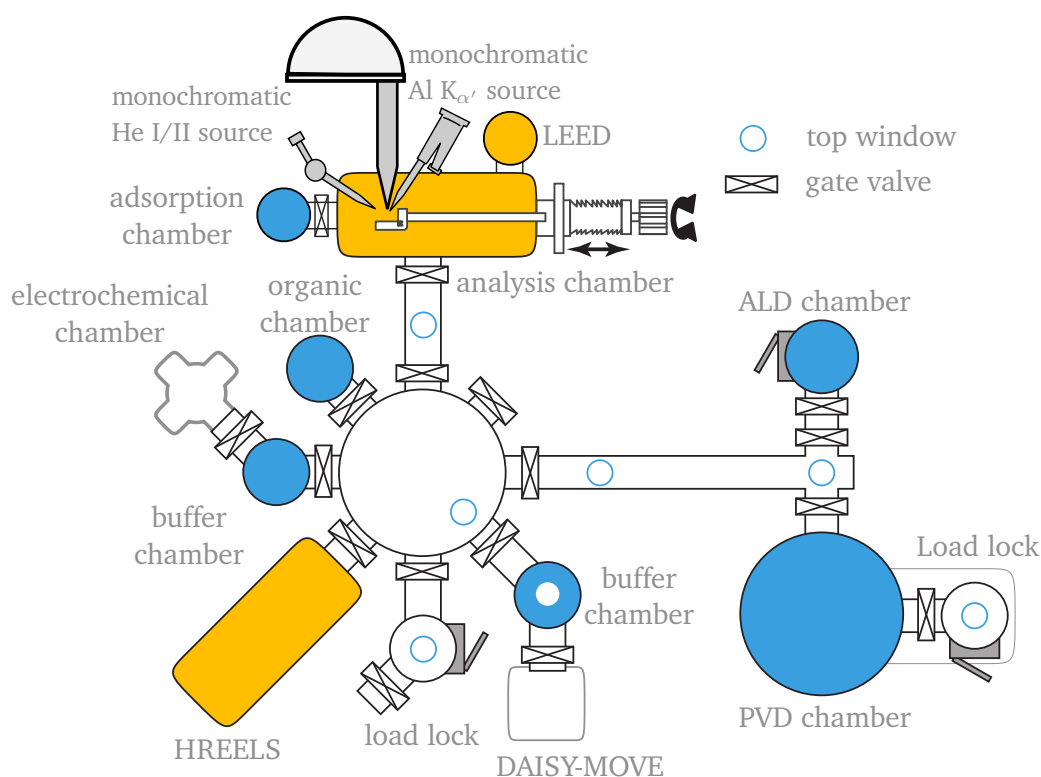


Figure 4.1: Scheme of DAISY-FUN with analysis chambers (yellow) and thin film preparation chamber (blue), adapted from⁹².

The system is an integrated ultra-high vacuum (UHV) system with base pressures from 10^{-7} to 10^{-10} mbar. All chambers are separated by gate valves and samples can be transferred from the preparation chambers into the analysis chamber without breaking the vacuum conditions, preventing sample contamination, such as hydrocarbons or water. The analysis chamber was used for PES and low-energy electron diffraction (LEED) experiments. Low temperature adsorption and water exposure were performed in the adsorption chamber. Atomic layer deposition (ALD) chamber was used for the deposition of TiO_2 , while surface preparation and sputter deposition (Pt and TiO_2) were conducted in the physical vapour deposition (PVD) chamber. The *DAISY-MOVE*⁹³ was used for the *in vacuo* sample transfer to *BESSY II* synchrotron, while the sample transfer from TU Ilmenau was conducted with another UHV shuttle.⁹⁴

4.1 PES analysis

PES measurements were conducted normal to the sample surface with a *PHOIBOS 150* spectrometer from *SPECS Surface Nano Analysis GmbH, Berlin*. For X-ray photoemission spectroscopy (XPS), a monochromatic Al K_{α} X-ray source (*SPECS Focus 500* with *XR50 M*) with a defined photon energy of $h\nu=1486.74$ eV was used. Survey and detail spectra were measured in fixed analyzer transmission mode if not otherwise stated with a pass energy of 20 eV (step size of 0.5 eV) and 10 eV (step size of 0.05 eV), respectively. The spectrometer was regularly calibrated by yielding the Fermi level edge of Au, Ag, and Cu to $E_F=0.0$ eV binding energy as well as Au $4f_{7/2}$ at 83.98 eV, Ag $3d_{5/2}$ at 368.26 eV, and Cu $2p_{3/2}$ at 932.67 eV binding energy with deviations ≤ 50 meV. For ultraviolet photoemission spectroscopy (UPS), a *HIS 13 Mono* (*Focus GmbH, Hünstetten*) was used as monochromatic He I ($h\nu=21.21$ eV) and He II ($h\nu=40.81$ eV) source on the same spectrometer with a pass energy of 5 eV (step size of 0.05 eV).

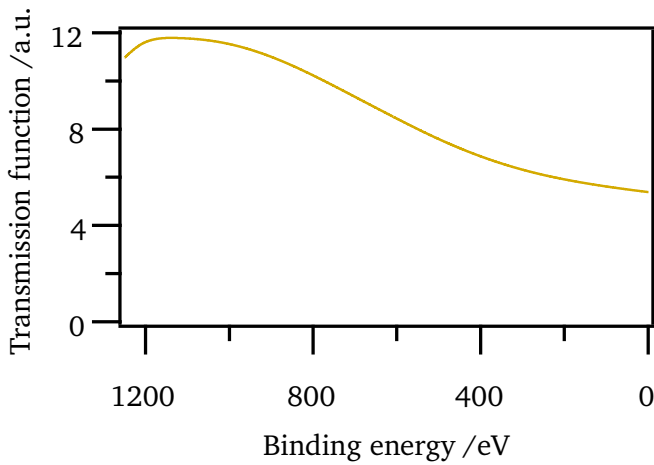


Figure 4.2: Evaluated transmission function for survey measurement at 20 eV pass energy.

The maximum XPS energy resolution was limited by the X-ray monochromator and a minimum full width at half maximum (FWHM) of the Ag $3d_{5/2}$ line of about 0.50 eV and 0.45 eV could be achieved for 10 and 5 eV pass energy, respectively. For the monochromatic UPS, the Ag Fermi edge revealed a very high resolution with a FWHM of ≤ 0.15 eV. For element quantification, the spectrometer transmission including the transmission of the detector as well as of the lens system was evaluated with a sputter cleaned Ag foil measuring the 4d, 3d, and 3p core levels as well as the MNN Auger line at different pass energies. The transmission function T_{spec} for a survey measurement at 20 eV is depicted in Figure 4.2. The effective attenuation length λ_{EAL} empirically evolved by Seah⁹⁵ has been used to consider the electron escape depth correction *edc*. For matrix related electron escape depth

corrections, the inelastic mean free path λ_{IMFP} was used.

Casa XPS was used for Shirley background subtracted peak areas and stoichiometry calculations. *SpecsLab Prodigy* was used for chemical component fitting.

4.1.1 Surface oxide thickness and stoichiometry

Due to its high surface sensitivity, XPS can be used to determine the thickness of very thin surface oxide layers. For electron detection normal to the surface plane, the oxide to substrate intensity ratio I_{ox}/I_{subs} can be calculated by the infinite bulk intensity ratio $I_{ox}^{\infty}/I_{subs}^{\infty}$, the oxide thickness d_{ox} and the inelastic mean free path in the oxide matrix for the specific core level kinetic energy $\lambda_{IMFP}(E_{kin, ox})$ and $\lambda_{IMFP}(E_{kin, subs})$ according to Equation 4.1.

$$\frac{I_{ox}}{I_{subs}} = \frac{I_{ox}^{\infty}}{I_{subs}^{\infty}} \times \frac{1 - \exp[-d_{ox}/\lambda_{IMFP}(E_{kin, ox})]}{\exp[-d_{ox}/\lambda_{IMFP}(E_{kin, subs})]} \quad (4.1)$$

When the oxide related component can easily be separated from the same core level, as is the case for SiO_2 on top of c-Si in the Si 2p emission, Equation 4.1 simplifies and the oxide thicknesses d_{SiO_2} is obtained from XPS intensities of bulk I_{Si} and oxide I_{SiO_2} taking raw areas of Shirley background-

subtracted Si 2p spectra according to Equation 4.2 using the inelastic mean free path $\lambda_{\text{IMFP}}(E_{\text{kin}}=1400 \text{ eV in SiO}_2)=3.8 \text{ nm}$ ⁹⁶ and the ratio of bulk intensities $R_0 = 0.88$.⁹⁷

$$d_{\text{SiO}_2} = \lambda_{\text{IMFP}} \cdot \ln \left(1 + \frac{I_{\text{SiO}_2}/I_{\text{Si}}}{R_0} \right) \quad (4.2)$$

It should be noted here that R_0 strongly depends on surface contamination.

The relative stoichiometry of the native SiO_2 layer ($c_{\text{O}}/c_{\text{Si}}$) is given by

$$\frac{c_{\text{O}}}{c_{\text{Si}}} = \frac{I_{\text{O}1s, \text{ox.}}}{ASF_{\text{O}1s} T_{\text{spec}}(\text{O}1s) edc_{\text{SiO}_2}(\text{O}1s)} \times \frac{ASF_{\text{Si}2p} T_{\text{spec}}(\text{Si}2p) edc_{\text{SiO}_2}(\text{Si}2p)}{I_{\text{Si}2p, \text{ox}}}, \quad (4.3)$$

with the raw area of O 1s $I_{\text{O}1s}$ and oxide-related Si 2p $I_{\text{Si}2p, \text{ox.}}$, Scofield atomic sensitivity factor ASF ,⁹⁸ spectrometer transmission function T_{spec} , and the escape depth correction edc . The native SiO_2 layer ($c_{\text{O}}/c_{\text{Si}}$) has a finite thickness, which has to be considered in the escape depth correction according to Equation 4.4.

$$edc = \int_0^{d_{\text{SiO}_2}} \exp^{-x/\lambda_{\text{IMFP}}(E_{\text{kin}})} dx = \lambda_{\text{IMFP}}(E_{\text{kin}}) \times (1 - \exp^{-d_{\text{SiO}_2}/\lambda_{\text{IMFP}}(E_{\text{kin}})}) \quad (4.4)$$

Reasonable oxide stoichiometry values can therefore only be achieved with d_{SiO_2} from Equation 4.2 and λ_{IMFP} in the SiO_2 matrix with $\lambda_{\text{IMFP}}(E_{\text{kin}}, \text{O}1s(900 \text{ eV}))=2.7 \text{ nm}$ and $\lambda_{\text{IMFP}}(E_{\text{kin}}, \text{Si}2p(1400 \text{ eV}))=3.8 \text{ nm}$ according to Tanuma et al.⁹⁶.

4.1.2 Potential corrected line shapes

Potential corrected line shapes have been used in literature to describe the potential distribution over Schottky contacts^{99,100} or insulator interfaces.^{101–103}

The potential distributions inside the space charge region (SCR) of Si surfaces and interfaces presented in this thesis were modeled by calculating the total photoemission line shape $I(E_b)$ as the sum of emissions shifted by the local potential U_{SCR} over the XPS information depth, for which λ_{IMFP} was assumed. Accordingly, the total line shape is defined as

$$I(E_b) = \int_0^\infty I_0(E_0 + U_{\text{SCR}}(x)) \times \exp^{-x/\lambda_{\text{IMFP}}} dx, \quad (4.5)$$

with $I_0(E_0)$ as flat-band line shape. The total line shape $I(E_b)$ is convoluted with shifted flat-band line shapes using $\exp^{-x/\lambda_{\text{IMFP}}}$ as attenuation term according to the Lambert-Beer law. The most unknown factor is the potential distribution $U_{\text{SCR}}(x)$, which can become a very complex model when solving numerically the 1D Poisson's equation as presented in Equation 2.4.²⁶

In order to minimize complexity of the used model, two approximations were considered:

- i) No free charge carriers: This is considered for the SiO_2 surface layer due to its dielectric properties. The total potential δ is considered to drop linear over the SiO_2 thickness d_{SiO_2} :

$$E_0 + U_{\text{SCR}}(x) = E_0 - x \frac{\delta}{d_{\text{SiO}_2}} \quad (4.6)$$

For a finite oxide thickness, the integration limits in Equation 4.5 should be limited to d_{SiO_2} .

- ii) Constant charge carrier concentration within a SCR: This is known as the so-called *depletion approximation* and is valid for moderately doped semiconductors.³⁰ The band bending ϕ_{BB} is considered to drop parabolically over the Si SCR as derived in Section 2.1.3:

$$E_0 + U_{SCR}(x) = E_0 - \phi_{BB} \left(1 - \left(\frac{W_{SCR} - x}{W_{SCR}} \right)^2 \right) \quad (4.7)$$

with W_{SCR} as the width of the SCR:

$$W_{SCR} = \sqrt{\frac{2\epsilon\epsilon_0}{qN_{don}} \phi_{BB}} \quad (4.8)$$

Accordingly, the final line shape depends mainly on two parameters: the doping concentration N_{don} and the total band bending ϕ_{BB} .

In Figure 4.3, the deconvolution of a semiconductor line shape with a narrow SCR is depicted schematically for the example of a Si 2p line. At the bottom, the calculated line shapes of a single crystalline Si

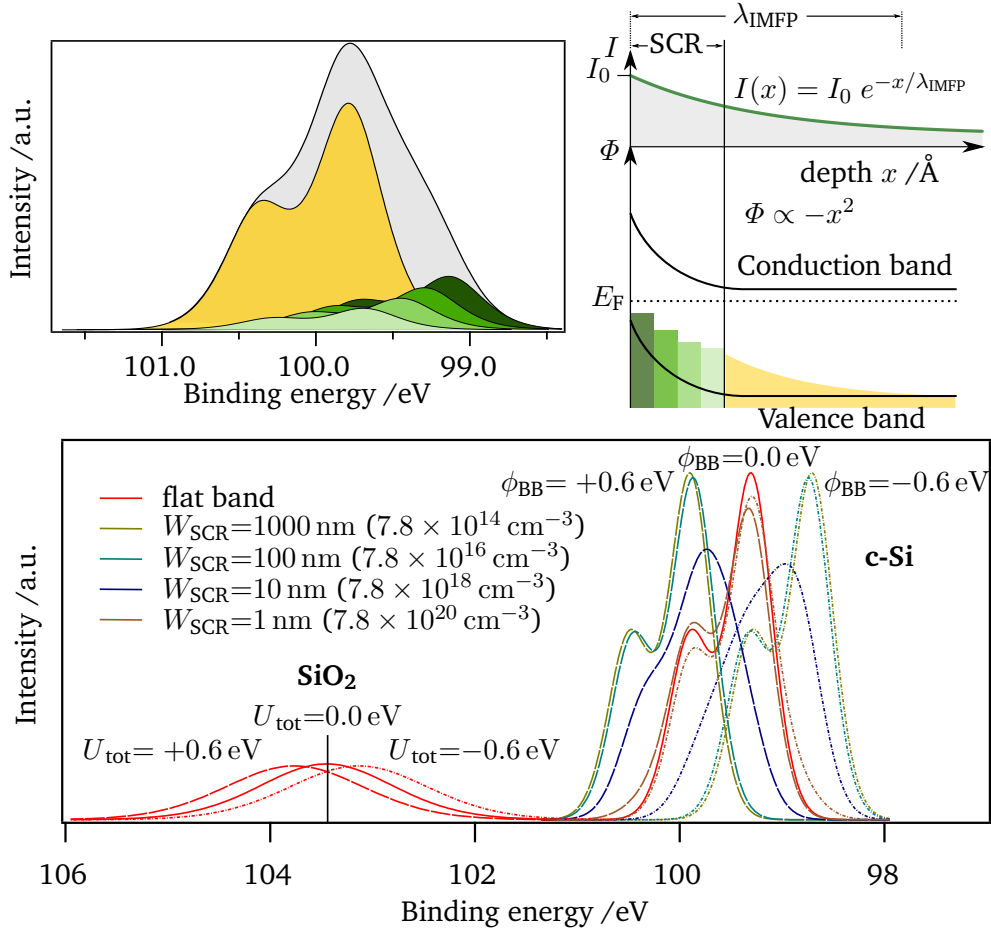


Figure 4.3: Deconvolution of potential distribution over the measurement depth schematically shown (top) and simulated line shapes for oxide covered Si (bottom). The influence of potential distribution of ± 0.6 eV on the Si 2p line shape are depicted in dependence on the doping concentration. The bulk position of all samples has been aligned to the flat band energy position (red curve).

wafer covered by about 1 nm SiO₂ without any potential drop is presented (solid curve). Furthermore, a potential drop of ± 0.6 eV is simulated according to the presented model (dashed curves). For the SiO₂ related component at higher binding energy, where a linear potential distribution is expected, the main line will mainly shift due to the potential drop. As the initial line is rather broad, the line shape will not be significantly affected by the potential drop. However, in this example, the maxima of the potential corrected line shape only differ by about 0.3 eV, even though the total potential drop is about 0.6 eV. Furthermore, it should be noted that E_0 of the oxide will be affected from band bending in the semiconducting c-Si substrate.

According to Equation 4.8, the line shape of the semiconducting c-Si contribution strongly depends on W_{SCR} and with that on the doping concentration N_{don} . In Figure 4.3, the line shapes for a constant band bending of 0.6 eV dropping over different W_{SCR} are shown. In the bulk, beyond the SCR, the energy of all samples is aligned to the red curve. For W_{SCR} ranging from 100 to 1000 nm, no significant changes are observed in the Si 2p line. Only the kink between the doublet is slightly less pronounced compared to the flat band condition. The peak maxima only differ by about 30 meV, indicating that the effect of band bending on the shape itself does not play a crucial role for doping concentrations below 10^{17} cm^{-3} and the peak maximum will correlate with the total band bending. This changes for doping concentrations in the range of 10^{18} cm^{-3} (blue curve), where the whole SCR is contributing to the overall line shape. The line shape also depends slightly on the direction of band bending, due to the asymmetric doublet shape. For even thinner SCR, the line shapes almost resemble the bulk line shape. Only the broader shoulders at lower or higher binding energy indicate upward and downward band bending, respectively, while the peak maxima differ by ≤ 20 meV.

Igor Pro 6 has been used for the potential correct line shape fitting procedure.

4.1.3 Synchrotron XPS and NEXAFS

Synchrotron XPS measurements were performed on *SoLIAS* endstation at the undulator beamline *U49-2/PGM-1* of the *BESSY II*, Berlin storage ring with excitation energies ranging from 80 to 2000 eV. Near edge X-ray absorption fine structure (NEXAFS) measurements of Si surfaces were performed at the undulator beamline *UE56-2/PGM-2*, *BESSY II*. Absorption spectra were obtained in partial Auger yield using a *SPECS PHOIBOS 150* spectrometer in constant-final-state mode. Si L_{2,3} and the O K-edges were measured at kinetic energies of 93.9 and 474.9 eV, using step sizes of 0.1 eV.

4.2 Semiconductor surface preparations

4.2.1 Si surface preparation

Unless otherwise stated, samples were prepared and analyzed in DAISY-FUN. The silicon single crystals were supplied as $10 \times 10 \text{ mm}^2$ cut wafers by *Silchem Handelgesellschaft mbH*, *CrysTec GmbH*, and *Si-Mat -Silicon Materials e.K.*. Wafers that were not wet-chemically treated, were rinsed with acetone and isopropyl alcohol subsequently for 10 min in an ultrasonic bath before being loaded to the UHV system. A complete list of prepared Si surface are listed in Table A1 of the Appendix.

Flash annealing treatment

The flashed samples were obtained from (100)-oriented wafers, which were flash annealed by a direct electron beam impact (1 kV acceleration voltage) onto the sample back side for about 3 s to up to 1400 °C

(sample name: *flash*). The 2×1 reconstruction monitored by LEED was achieved by subsequent UHV annealing at 300 °C for 3 h (*flash-2×1*) under base pressures at room temperature of $\leq 10^{-9}$ mbar.

Oxygen termination

The native oxide (*nat. ox*) was analyzed as received from the supplier. Prior to preparation of a thermal oxide (*therm. ox*) layer, the wafer was softly radio frequency (RF)-sputtered for 5 min (5 W at 0.5 Pa partial Ar pressure). Subsequently, it was annealed for 5 h in 0.5 Pa O₂-atmosphere at 275 °C. Oxide thicknesses d_{SiO_2} were obtained from XPS intensities of bulk I_{Si} and oxide I_{SiO_2} taking raw areas of Shirley background-subtracted Si 2p spectra according to Equation 4.2.

Hydrogen termination

The dry H-terminated samples (*dry-H*) were prepared by Mohammad Amin Zare Pour, TU Ilmenau. The wafer were annealed in H₂-atmosphere in a commercial metalorganic chemical vapor deposition (MOCVD) reactor (Aixtron, AIX200). p- and n-Si (100) substrates with 2° offcut towards [110] direction were used. A wet-chemical pretreatment was applied to the Si (100) substrates before processing in the MOCVD reactor. The pretreatment consisted of: (i) boiling the substrates in a 1:1:6 mixture of ammonium hydroxide (NH₄OH, 25 %), hydrogen peroxide (H₂O₂, 30 %) and deionized water (DI water) to remove organic contamination and metals (RCA1); (ii) dipping Si (100) for 10 s in HF (10 %) diluted in water (1:4); and (iii) thin oxide layer formation (RCA2). The Si(100) substrates were annealed at 1000 °C for 30 min at 950 mbar H₂ pressure in order to remove the oxide layer.¹⁰⁴ Subsequently, the Si (100) substrates were cooled to 740 °C to prepare a H-terminated, double-layer stepped surface with prevalence of (2×1) domains.^{105,106} This step was controlled by *in situ* reflection anisotropy spectroscopy (RAS) (shown in Figure A1 in the Appendix).¹⁰⁷ Samples were contamination-free transferred from the MOCVD reactor at TU Ilmenau via a dedicated UHV transfer shuttle⁹⁴ with base pressures $< 5 \times 10^{-10}$ mbar to TU Darmstadt and finally loaded to DAISY-FUN without breaking vacuum.

The wet-chemical hydrogen termination was prepared according to Angermann et al.¹⁰⁸ by etching the oxide of the (100) (*100-H*) and (111) (*111-H*) wafers for 10 min at 80 °C in piranha solution (1 H₂SO₄ (96 %):1 H₂O₂) and 6.5 min at room temperature in buffered 5 % hydrofluoric acid (HF (40 %):7 NH₄F (40 %)). Subsequently, the etching step in piranha solution was repeated and finally the samples were etched in ammonium fluoride (NH₄F, 40 %) for 10 min. The samples were rinsed after every etching step with DI water. After preparation, the samples were loaded within 10 min to the UHV system. The so-called “defective H-termination” (*111-H def.*) was achieved by storing the wet-chemically prepared H-terminated sample for 4 weeks at $< 10^{-9}$ mbar in UHV.

4.2.2 InP surface preparation

The homoepitaxial InP (100) was grown by Mohammad Amin Zare Pour, TU Ilmenau on a commercial p-type InP (100) wafer (Zn-doped, $2.3 \times 10^{-18} \text{ cm}^{-3}$ with 2° miscut toward the [111] direction) in a horizontal-flow metal organic vapor phase epitaxy (MOVPE) reactor (Aixtron, AIX-200) modified to enable a contamination-free transfer to UHV using H₂ as carrier gas. *Tert.*-butylphospine (TBP) and trimethylindium (TMIn) were used as precursors for the InP (100) epilayer while diethylzinc (DEZn) was used as a p-dopant source. The molar flow of DEZn was adjusted to ensure a carrier concentration of $2 \times 10^{-18} \text{ cm}^{-3}$ in the InP (100) epilayer, which was finally confirmed by electrochemical capacitance–voltage profiling (CV profiling). The growth was monitored by RAS, which allows the preparation of the specific surface (see Hannappel et al.¹⁰⁹ and Letzig et al.¹¹⁰ for further information).

After growing the InP layer, the well-ordered P-rich and In-rich InP (100) surfaces were prepared according

to Hannappel et al.¹¹¹. The P-rich surface was achieved by cooling the sample down from the growth temperature 873 to 575 K in the presence of precursor TBP and subsequent heating to 673 K in the absence of TBP. The In-rich InP (100) surface has been prepared by cooling down from 840 to 725 K in the presence of TBP and from 725 to 630 K in the absence of TBP. Afterwards, the samples were transferred to UHV, moved via an UHV transfer shuttle with a base pressure of $\leq 5 \times 10^{-10}$ mbar⁹⁴ to TU Darmstadt and finally loaded to the DAISY-FUN cluster tool.

4.3 Water adsorption

Low-temperature water adsorption was performed in the adsorption chamber by cooling the sample substrate with liquid nitrogen. For that purpose, nitrogen gas with 2 bar over pressure flowed through cooling lines, which were immersed in a filled liquid nitrogen dewar. The condensed nitrogen passed the sample stage afterwards, where it cooled the sample substrate to -176°C . This temperature was directly measured on the sample substrate via a K-type thermocouple. Then, ultrapure water from the gas phase was exposed to the chamber. The water dose was controlled by the exposure time and partial water pressure, which was measured by a full range pirani/cold cathode gauge (PKR 251, Pfeiffer Vacuum GmbH, Aßlar). A dose of 100 s at 1×10^{-8} mbar corresponds to 1 L (Langmuir). Finally, the cooling process was stopped, and the sample returned to room temperature. After each treatment step, including cooling and desorption, XPS and UPS measurements were carried out.

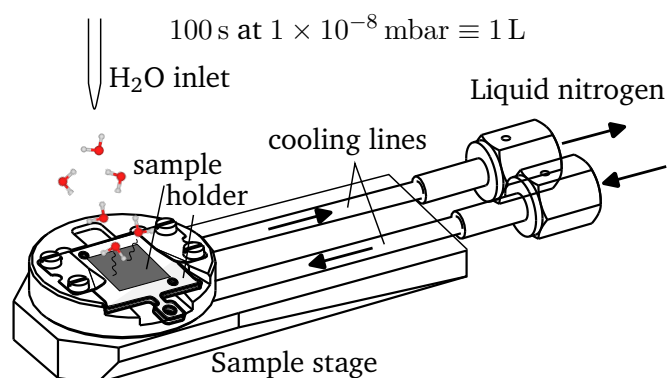


Figure 4.4: Sample stage with liquid nitrogen cooling lines, H₂O inlet and sample holder with sample.

4.4 Thin film deposition

Thin films of TiO₂ and Pt were deposited by direct current (DC)-magnetron sputtering. In addition, TiO₂ was also deposited by ALD.

4.4.1 Magnetron sputtering

DC-magnetron sputtering was performed inside the PVD chamber at regular base pressures of 1×10^{-8} mbar. It is equipped with a central rotatable sample holder capable of holding 4 sample holders with samples of $10 \times 10 \text{ mm}^2$. Substrates can be heated by a 700 W SiC heater. Heating calibration curves were conducted by a thermocouple glued on a fluorine doped tin oxide (FTO)-substrate. The deposition was carried out using two 2-inch MS/63C12 magnetron sputter sources and DC-power supplies from PREVAC. The process pressure and gas composition during sputter deposition were controlled using gas flow controllers from MKS and an automatic regulating valve from VAT. The process gases of 99.999 % purity were supplied by AirLiquide.

TiO₂ was deposited at 20 W from a metallic Ti target with a purity of 99.995 % from Kurt J. Lesker Company, Jefferson Hills, USA. The metallic Pt target of 99.99 % purity was supplied by Scottech Ltd, Port Glasgow, UK. Pt was deposited at 10 W. For all samples the total gas flow was set to 20 sscm at a fixed process pressure of 0.5 Pa. The substrate-to-sputter source distance during deposition was set to 20 cm. In order to remove

adsorbates from the target surface and to establish an equilibrium state, the targets were pre-sputtered 5 min under closed shutter.

4.4.2 Atomic layer deposition of TiO₂

In-house ALD processing

Internal ALD-TiO₂ films were prepared by a thermal ALD-process in the ALD chamber with a base pressure of 10^{-8} mbar. During the deposition process, the turbo pump was separated with a gate valve, and the chamber was pumped through a bypass using a rotary vane pump. Additionally, a cold trap was installed in front of the rotary vane pump to condensate any surplus reactants and side products in order to protect the pump. During the deposition process, the pressure reached approximately 10^{-3} mbar between precursor purging. To control the pumping power, a butterfly valve was used and set to 5 % opening position. As precursors, only H₂O and TiCl₄ were used for the TiO₂ deposition. The deposition process was developed and optimized by Thorsten Cottre¹¹² (see chapter 3.1 for a detailed description of the used components). The relevant process parameters are listed in Table 4.1.

Table 4.1: Parameters of in-house ALD-TiO₂ deposition.

Ti precursor	substrate temperature	precursor/inlet temperature	H ₂ O pump/purge sequence	TiCl ₄ pump/purge sequence	constant N ₂ purge
TiCl ₄	160 °C	40 °C/30 °C	300 ms/180 s	250 ms/180 s	20 sscm

After accomplishing deposition, the heating was shut off and the chamber was evacuated via the turbo pump again. After reaching a base pressure of 9×10^{-8} mbar, the samples were transferred to the XPS for analysis.

External ALD processing on Si photocathodes

External ALD-TiO₂ layers were deposited by *Jennifer Velázquez Rojas, Helmholtz-Zentrum Berlin* using two different Ti precursors (TiCl₄ and titan(IV)isopropoxid (TTIP)) and H₂O. Process parameters are listed in Table 4.2. Before each precursor exposure, Ar was purged pulse-wise into the system. The base pressure after each purging step was 4×10^{-6} mbar. Three different sample thicknesses were prepared within the same process, while one sample was separated after 50 (1.5 nm), 100 (3.0 nm), and 200 (6.0 nm) cycles. A total growth per cycle rate of 0.3 Å/cycle was determined using *in situ* ellipsometry. All samples revealed a little nucleation delay.

Table 4.2: Parameters of external ALD-TiO₂ deposition.

Ti precursor	substrate temperature	precursor temperature	H ₂ O pump/purge sequence	precursor pump/purge sequence	Ar pump/purge sequence
TiCl ₄	200 °C	RT	1.5 s/30 s	0.1 s/30 s	0.1 s/30 s
TTIP	200 °C	54 °C	1.5 s/30 s	0.75 s/30 s	0.1 s/30 s

After deposition, samples were shipped to Darmstadt under ambient atmosphere.

4.4.3 Thermal evaporation of Pt

The thermal evaporation of Pt thin films were conducted by *Jennifer Velázquez Rojas, Helmholtz-Zentrum Berlin*. The Pt was evaporated at 1.28 kW while the deposition rate was 10.8 Å min^{-1} as controlled by a quartz crystal microbalance (QCM). The base pressure of the deposition chamber during evaporation was 3×10^{-7} mbar. After deposition, samples were shipped to Darmstadt under ambient atmosphere.

4.4.4 Interface experiments

In order to analyze the interfacial band alignment, interface experiments were conducted by the stepwise deposition of TiO_2 and Pt. After every step, the total deposition time was doubled leading to a thickness doubling. XPS and UPS was carried out after each deposition step. The film thickness was calculated by assuming constant deposition rates, which were determined by profilometry. The contact potential was deduced from XPS secondary electron edge (SEE) cut-offs of the clean substrate and the thick added layer.

4.5 Electrochemical characterization

Electrochemical measurements were conducted in a photoelectrochemical cell (PEC), which consists of a polychlorotrifluoroethylen (PCTFE) housing (PECC-2, Zahner-Elektrik GmbH & Co. KG, Kronach) as schematically depicted in Figure 4.5. This cell allows the electrochemical characterization of a sample in 3-electrode configuration where currents are measured between the sample as working electrode (WE) and the counter electrode (CE). The CE consists of a metallic Pt coil in order to pass the incident light and to achieve a homogeneous electric field distribution between WE and CE. The potential is measured between the sample as WE and the reference electrode (RE). As reference, a silver chloride electrode (Ag/AgCl) was used. Before assembling the cell, the RE was measured in the used electrolyte versus a reversible hydrogen electrode (RHE). This value reference $E_{\text{Ag/AgCl}}$ was then used to convert all measured potentials to E_{RHE} in V vs. RHE using the following relation:

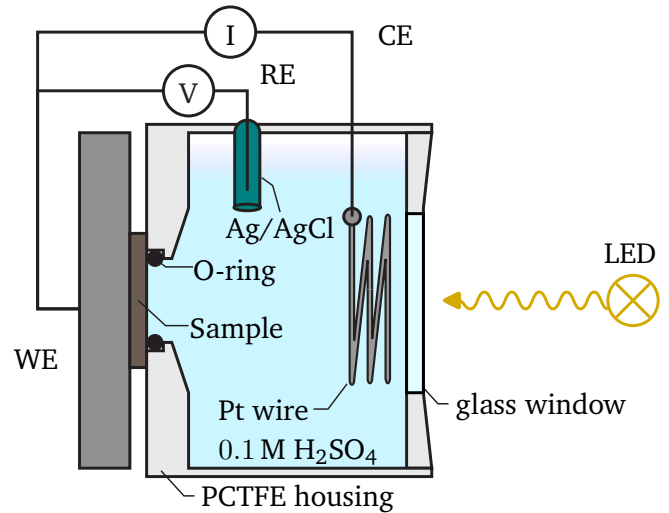


Figure 4.5: Scheme of used PEC, adapted from ⁹².

$$E_{\text{RHE}} = E_{\text{Ag/AgCl}} + 0.197 \text{ V} + 0.0591 \text{ V} \times \text{pH} \quad (4.9)$$

The electric back contact of the sample was realized by pressing a gold covered metal plate onto the samples' back side by using screws for the assembly. To improve the back contact for bare Si wafers, a GaIn eutectic from *Alfa Aesar, Karlsruhe* was put on the backside of the wafer, which was additionally scratched in order to partially remove the native oxide. Between the eutectic and the metal plate, a copper foil was placed in between, which was previously rinsed in 6 M HCl for 2 min.

The measurements have been performed using *Zahners ZENNIUM PRO* potentiostat and the *Zahner PP212* LED control with an active feedback loop to ensure constant light intensity during the measurement.

4.5.1 Chopped light open circuit potential (OCP)

In order to measure the open circuit photovoltage of the buried model device, chopped OCP measurements were conducted measuring the electrochemical potential versus the reference without any current flowing from the sample to CE. If not otherwise stated, the OCP was measured for 5 min while every 15 s the white light light emitting diode (LED) (2285lsw-2, Zahner) with a mean wave length of 536 ± 60 nm was switched on for 15 s and illuminated the sample with 1000 W m^{-2} intensity, imitating AM1.5 sunlight.

4.5.2 Chopped light voltammetry

For the chopped voltammetry sweeps, typical scan rates of 10 mV s^{-1} were used. The same white light LED as mentioned above was used for sample illumination with 1000 W m^{-2} with light periods of 0.5 s if not otherwise specified.

4.5.3 Galvanostatic Pt deposition

For the deposition of Pt particles as hydrogen evolution reaction (HER) catalyst, Pt was electrochemically reduced from a Pt salt solution (2 mM K_2PtCl_4 (99 %, Carbolution Chemicals GmbH) in 0.1 M H_2SO_4 (Carl Roth GmbH)). The galvanic Pt particles presented in this thesis were deposited galvanostatically enforcing a constant current density at the WE of -0.5 mA cm^{-2} for 120 s using the 3-electrode configuration in the PEC cell as presented above. These parameters led to a theoretical (for 100 % Faraday efficiency) loading of $1.9 \times 10^{17} \text{ atoms/cm}^2$.

4.6 Other techniques

4.6.1 LEED setup

LEED measurements were performed using the BDL800IR-LMX LEED optics from OCI Vacuum Microengineering Inc., London, Canada. A retarding and focus voltage was adjusted in order to sharpen the LEED pattern and to increase the image contrast.

4.6.2 Hall measurements

To determine the charge carrier concentration of the investigated Si wafers and the sputter deposited TiO_2 films, Hall and conductivity measurements were carried out in a van-der-Pauw geometry. Four-point Pt-contacts were sputtered on top of the $10 \times 10 \text{ cm}^2$ samples. For Hall measurements, a magnetic field of 1.3 T was applied. Currents were chosen according to the conductivity of the sample ($\approx 1 \text{ mA}$ for Si wafers).

4.6.3 UV/vis spectroscopy

Ultraviolet-visible-near-infrared spectroscopy (UV-Vis-NIR) measurements on sputtered TiO_2 thin films were performed on a Cary 7000 Universal Measurement Spectrophotometer (UMS) purchased from Agilent Technologies, Santa Clara, USA. After the baseline correction by the machine, the sample was inserted with a tilt of 6° and a reflectance and transmission spectrum from 250 to 2500 nm was recorded under 12° and 180° , respectively.

4.6.4 Profilometry

Film thickness measurements were carried out on a *DektakXT* profilometer from *Bruker Corp., Billerica, USA*. Two line scans were conducted perpendicular to the edges at each of the four sample edges. The mean thickness was determined based on the height difference between the film and the substrate. Assuming uniform and linear film growth, a constant deposition rate was determined by dividing the film thickness by the deposition time.

4.6.5 External measurements

The following measurements were kindly performed by my colleagues.

SEM

Secondary electron microscopy (SEM) images were conducted on a *Philips XL30 FEG* with a lateral resolution of about 2 nm at 30 kV. Used SEM images of this thesis have been conducted together with *Kerstin Lakus-Wollny* and *Sumanth Pulluru*.

AFM

Atomic force microscopy (AFM) imaging was conducted by *Chuanmu Tian* with a *Bruker Icon Dimension AFM* in amplitude modulation mode using *PPP-Zeihl* cantilevers (*NanoAndMore GmbH, Wetzlar*). The scanning area of the sample surface was $1 \times 1 \mu\text{m}^2$ with a tip velocity of $2 \mu\text{m/s}$. *Gwyddion* was used for roughness analysis and visual illustration.

XRD

Grating incidence X-ray diffraction (XRD) on TiO_2 thin films were performed by *Chuanmu Tian* at 5° on a *SmartLab* diffractometer from *Rigaku (Tokyo, Japan)* equipped with $\text{Cu-K}\alpha$ radiation and a parallel beam geometry.

5 Silicon surfaces

Parts of this chapter have been published in Encyclopedia of Solid-Liquid Interfaces.¹⁷

Photoelectrodes based on silicon offer significant advantages as reference systems due to the extensive number of research in both fundamental and application-oriented studies documented in the literature. The combination of crystalline and amorphous silicon photoelectrodes offers efficient and intriguing device architectures, particularly when integrated into multi-junction cells^{19,113} and nanorod structures.¹¹⁴ In this chapter, a detailed surface science study on the electronic properties of Si surfaces is presented. In model experiments, the effect of surface states found on differently doped Si (111) and (100) surfaces is investigated in relation to the resulting surface electronic structure after applying different surface preparation and processing procedures. As an elemental semiconductor, silicon provides the ideal model system to analyze semiconductor surfaces and their interfaces to a liquid electrolyte. The reactivity and changes in electronic structure are studied following a “frozen electrolyte” approach, which is based on low temperature water adsorption.

5.1 Dangling bond defects on Si surfaces

The results and content of this study have been published in Solar RRL.¹¹⁵

Before analyzing the contact formation of a semiconductor with an electrolyte, it is essential to understand the electronic structure of the surfaces including a detailed description of surface states and electronic defect distribution, which might be involved when interacting with adsorbates and intermediates at the contact to an electrolyte.

Although surface preparation of Si has been investigated for many decades and wet chemical surface preparation for native oxide etching as well as electronic surface passivation became a widely and common method in Si wafer processing,^{108,116,117} the role of surface defects with respect to photoelectrochemical applications is not fully understood yet.^{118,119} The chemically harsh conditions at photoelectrochemical interfaces require a deeper understanding of the energetic role of surface defects, with respect to chemical environment and electronic distribution of the defect centers in order to identify Fermi level pinning mechanisms leading to barrier formation and trapping of excess charge carriers.^{119,120}

Due to the lack of bonding partners in one dimension, non-saturated bonding states caused by dangling bonds, appear at the Si surface and thus form the dominating surface defect. The paramagnetic and diamagnetic character of such trivalent $\text{Si}_3 \equiv \text{Si} \cdot$ dangling bonds, depending on the electronic occupation of the defect, have been identified as so-called P_b -centers at the interface to a native oxide layer and are well studied with electron spin resonance spectroscopy (ESR) as well as spin-dependent recombination (SDR).^{121,122} The formation of Si-O, Si-H or Si-R terminated surfaces lead in case of perfect adsorbate covered dangling bond states to an electronic and chemical passivation of the Si surfaces. The quality of these passivation layers corresponds to the number of remaining dangling bonds and depends on surface orientation and quality of the surface passivation treatment.^{120,123}

To understand the impact of surface preparation on defect distribution and surface band bending,

different surface preparation procedures are provided and described in detail in Section 4.2.1. A complete list of prepared Si surface with regarding Si 2p_{3/2} binding energy position can be found in Table A1 of the Appendix.

5.1.1 Surface band bending and surface defects

In order to determine surface band bending the main discussion is based on the energetic position of the spectra in dependence of the applied surface preparation. In Figure 5.1, the survey spectra of p-Si surfaces after the different pre-treatments are shown, with detail spectra of the Si 2p and O 1s emission inserted.

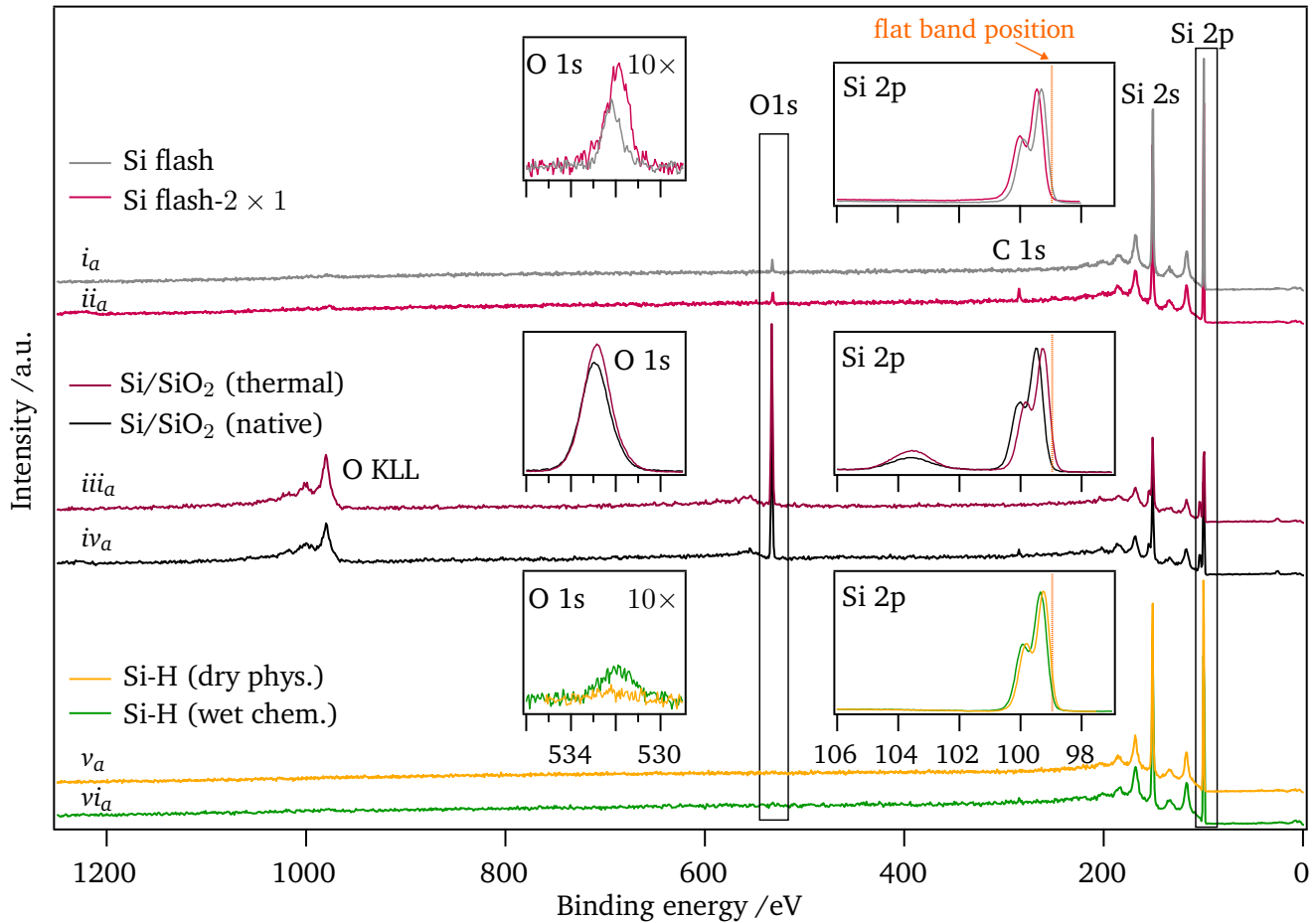


Figure 5.1: XPS spectra of prepared flash-annealed (top), oxide-terminated (middle), and hydrogen-terminated p-Si surfaces (bottom) with normalized detail spectra of Si 2p and O 1s. The calculated flat band position for the Si 2p_{3/2} is marked as a dashed orange line. Sample indices ($i_a - vi_a$) are noted according to Table A1.

Besides the expected elemental Si emissions, traces of O emissions appear to a certain extent as contaminant on the sample. Furthermore, the flash-annealed as well as the air exposed samples reveal traces of carbon contamination, which is according to the binding energy of C 1s at ≈ 285.0 eV assigned to adventitious carbon not affecting surface band bending. For that reason, the following discussion focuses on surface states on pure silicon and oxidized surfaces.

The energetic position of the Si 2p line depends on the charge carrier concentration in the bulk as well

as on the defect concentration at the silicon surface. With its band gap $E_g=1.12$ eV,²⁹ crystalline Si has an intrinsic charge carrier concentration of $<1 \times 10^{-10} \text{ cm}^{-3}$ in the bulk.¹²⁴ For that reason, the doping concentration is the dominating contribution to the charge carrier concentration and can therefore be derived from Hall measurements. The majority charge carrier concentration for each Si wafer was derived from Hall measurements as given in Table 5.1.

Table 5.1: Fundamental bulk properties of Si wafers used in this work with sheet conductivity, charge carrier mobility, and charge carrier concentration as derived from Hall measurements (in van der Pauw measurement geometry with a magnetic field of $B=1.3$ T). Flat band onset $E_F - E_{VB}$ calculated according to Eq. 5.1 and 5.2.

Si wafer/ orientation	Dopant	Sheet conductivity in S cm^{-1}	Mobility in $\text{cm}^2 \text{V}^{-1} \text{s}^{-1}$	Charge carrier concentration in cm^{-3}	Calculated flat band $E_F - E_{VB}$
p-Si (100)	Boron	0.15	290	3.2×10^{15}	0.22 eV
p-Si (111)	Boron	0.11	270	2.5×10^{15}	0.22 eV
p-Si (100)*	Boron	0.67	111	3.8×10^{16}	0.16 eV
n-Si (100)	Phosphorous	0.19	1270	9.3×10^{14}	0.86 eV
n-Si (111)	Phosphorous	0.10	1330	4.6×10^{14}	0.84 eV
n-Si (100)*	Phosphorous	110	102	1.9×10^{18}	1.02 eV

* Wafer with different doping concentration used for dry-physical H-termination.

With an ionization energy of 45 meV for both B and P,²⁹ the dopants are almost completely ionized at room temperature (shallow dopants). Furthermore, the charge carrier concentration is low enough to approximate the Fermi-Dirac distribution with a Boltzmann term. Accordingly, with the measured acceptor concentration N_{ac} for p- and donor concentration N_{don} for n-type doping, the bulk Fermi level position E_F with respect to the valence band edge E_{VB} and conduction band edge E_{CB} can be determined by Equations 5.1 and 5.2

$$E_{VB} - E_F = k_B T \cdot \ln \left(\frac{N_{ac}}{N_{VB}} \right), \quad (5.1)$$

$$E_F - E_{CB} = k_B T \cdot \ln \left(\frac{N_{don}}{N_{CB}} \right), \quad (5.2)$$

using the Boltzmann term for the thermal energy $k_B T$ and the effective valence and conduction band density of states $N_{VB}=1.8 \times 10^{19} \text{ cm}^{-3}$ and $N_{CB}=3.2 \times 10^{19} \text{ cm}^{-3}$.²⁹ With $E_{CB} = E_{VB} + E_g$, the valence band onset in the bulk of the Si crystal can be calculated for all wafers (Table 5.1) in order to compare these theoretical bulk values with the surface measured by photoemission spectroscopy (PES).

Both, the valence and conduction band in Si are formed by sp^3 related bonding σ and anti-bonding σ^* combinations. Due to missing bonding partners at the surface, dangling bonds form a characteristic surface state distribution N_{SS} inside the band gap. Depending on the surface state distribution and the surface' charge neutrality level (CNL) with respect to the bulk Fermi level, charge transfer from the

surface into the bulk occurs and induces band bending towards the surface (see Section 2.1.4 for more details). Using the invariant energetic difference of the Si 2p core level line to the valence band maximum (VBM) $E_{VS} = E_{Si2p_{3/2}} - E_{VB}$, the valence band (VB) onset $E_{VB} - E_F$ at the surface can be precisely determined by the position of the Si 2p_{3/2} line. In case of crystalline silicon, E_{VS} is equal to 98.74 eV and is independent of doping and surface band bending.¹²⁵ With that, the Fermi level position at single crystalline Si surfaces is calculated as $E_{VB} - E_F = E_{Si2p_{3/2}} - 98.74$ eV. In principle, these values can be determined by the HeII VB edge as well. However, for comparing these values a precise evaluation of the valence band onset, contributions of surface states and modified source-induced photovoltages must be considered. The calculated flat band position of Si 2p_{3/2} has been marked in orange into the Si 2p spectra of Figure 5.1. According to that, all the depicted p-type Si surfaces reveal a higher Si 2p binding energy at the surface than expected from the bulk doping indicating an electron accumulation at the hole depleted surfaces. In order to understand the charge depletion at the surface, a detailed understanding of present surface defects in Si is required.

5.1.2 The intrinsic dangling bond states at Si surfaces

Threefold-coordinated Si surface atoms, which localize a nonbonding sp orbital are described by $Si_3 \equiv Si \cdot$ dangling bonds. These trivalent $Si_3 \equiv Si \cdot$ dangling bonds are known to form two corresponding states inside the band gap of Si with one donor state (bonding state) at around 0.25 eV and one acceptor state (anti-bonding state) at about 0.85 eV above the VBM.^{126,127} The amphoteric character of this dangling bond surface states (SS) leads to an U-shape like density of states (DOS) distribution with the CNL located at about 40 meV below mid-gap position.¹²⁸ The reason for the splitting of the defect level is the effective correlation energy of 0.6 eV.¹²⁹ It is defined by the energy difference which is required to add an electron to an unoccupied and to an already singly occupied dangling bond orbital and is composed by the Coulombic repulsion and compensating lattice relaxation energy.^{129,130} According to that, the $Si_3 \equiv Si \cdot$ dangling bonds can exist in three different charge states (see Figure 5.2b)): The neutral dangling bond SS^0 exhibits one singly occupied sp³ orbital. the positive SS^+ is characterized by a sp² hybrid with an empty p_z orbital, and the negative SS^- exhibits an s²p³ hybridization forming a doubly occupied Si lone pair.¹³⁰

The detailed Si 2p spectra of flashed n- and p-doped Si (100) surfaces are depicted in Figure 5.2a), without any visible oxide or suboxide species that should be located at higher binding energies of 101.1 to 103.2 eV.¹³² The Si 2p_{3/2} emission of the p-doped sample is located at 99.34 eV, which correlates to a mid-gap Fermi level position of 0.60 eV above the VBM what is in good agreement to pinning levels previously found on Si (111) surfaces.^{125,129} In contrast, the n-doped surface reveals a 0.2 eV higher Fermi level position. But after reduction of the X-ray intensity a downward shift of the Fermi level also nearly to mid-gap is observed on the n-doped sample indicating a source-induced SPV reducing the initial band bending at the n-doped surface. This is most probably related to different capture cross sections of minority charge carriers ($\sigma_n(p-Si) \gg \sigma_p(n-Si)$) at the surface, which has been found to decrease the recombination velocity at the n-Si/SiO₂ interface in comparison to p-type Si.^{133,134} Accordingly, the binding energy of the p-doped sample is independent of the variation of the X-ray intensity which indicates a fixed Fermi level position, confirming the higher recombination rate of photoelectrons as minority charge carrier at the p-Si surface. The identical energy position at low X-ray intensities for both, the n- and p-type sample, respectively indicates a strong Fermi level pinning which is independent of the bulk doping N_{Dopant} concentration. Fermi level pinning is expected for ionized surface state concentrations $N_{SS} \geq \sqrt{2\epsilon\epsilon_0 E_g N_{Dopant}}$, as this corresponds to the maximum charge stored in the semiconducting space charge region with a band gap of E_g (Bardeen limit, see Section 2.1.4). In this case, the Fermi level position coincides with the CNL of the Si dangling bond states, indicating $N_{SS} \gg 10^{11} \text{ cm}^{-2}$ as most of the

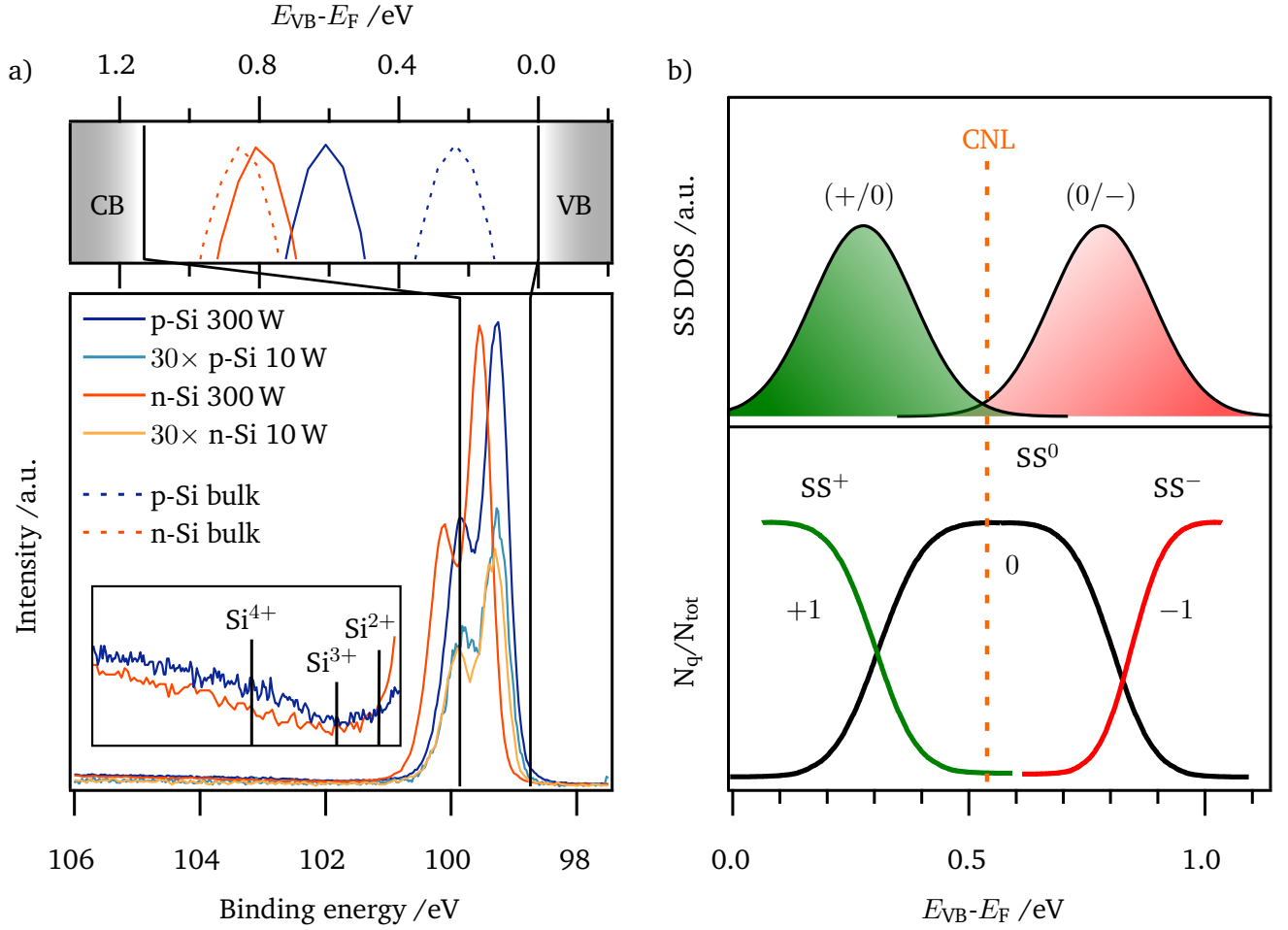


Figure 5.2: a) Si 2p spectra of flashed n- and p-doped Si(100) surfaces with different X-ray source intensities. Intensity dependence on binding energy indicates surface photovoltage (SPV). Fermi level positions are derived from Si 2p core level by $E_{Si2p_{3/2}} - 98.74 \text{ eV}$ and seem to be independent of bulk doping. b) Schematic surface states distribution SS DOS of Si dangling bonds with charge occupation N_q/N_{tot} in dependence on surface Fermi level position and marked CNL according to Broqvist et al.¹³¹.

surface states remain uncharged close to the CNL (Figure 5.2b)). Due to the pinning level at 0.6 eV above the VBM, the surface band bending ϕ_{BB} is about 0.38 eV. Considering a parabolic potential drop inside the Si space charge region (SCR) (*depletion approximation*, see Section 2.1.3), the amount of total surface charges Q_{SS} can be calculated with the acceptor concentration of $N_{ac}=3.2 \times 10^{15} \text{ cm}^{-3}$ (Table 5.1) and $\epsilon_{Si} = 11.7$ ²⁹ using Equation 5.3.

$$-Q_{SS} = \sqrt{\epsilon \epsilon_0 \phi_{BB} N_{ac}} = 1.44 \times 10^{11} \text{ cm}^{-2} \quad (5.3)$$

Accordingly, less than 0.1 % of the surface atoms contribute to a positively charged defect by releasing an electron into the Si SCR ($SS^0 \rightarrow SS^+ + e^-$). If one assumes that the defect SS is very narrowly distributed around the defect level $\Delta E_D \pm < 0.1 \text{ eV}$, the ionized surface defect density N_{SS}^+ can be calculated with the total defect density N_{SS} :

$$N_{SS}^+ = N_{SS}(1 - f(E_D)) = N_{SS} \left(1 - \frac{1}{1 + \frac{1}{2} \exp \frac{E_D - E_F}{k_B T}} \right) \quad (5.4)$$

By taking N_{SS}^+ as the total surface charge Q_{SS} derived from Equation 5.3, the literature value for $E_D=0.26$ eV,¹²⁶ and the pinning level $E_F=0.6$ eV, one can calculate for N_{SS} a value of $2.2 \times 10^{17} \text{ cm}^{-2}$. This value exceeds the density of surface atoms by a factor of 100 and is therefore an unrealistic defect concentration. Consequently, the “narrow defect distribution” cannot describe the real defect distribution on Si surfaces, indicating a more complex defect distribution spread over the band gap region with donor states reaching up to the Fermi level. In any case, it can be concluded that after flashing of the Si surface, the defect density is rather high and the number of dangling bond states is approaching the number of Si surface atoms ($\approx 10^{15} \text{ cm}^{-2}$), since the unreconstructed Si (100) surface reveals two dangling bonds per surface atom.

In order to characterize the different surface preparation in more detail, electronic and structural analysis have been performed using ultraviolet photoemission spectroscopy (UPS) and low-energy electron diffraction (LEED). Figure 5.3 shows the UP valence band spectra after surface preparation and LEED pattern for those samples, which revealed LEED reflexes. The expected surface structures are depicted in Figure 5.4. The high amount of Si dangling bonds straight after flashing leads to a high surface reactivity

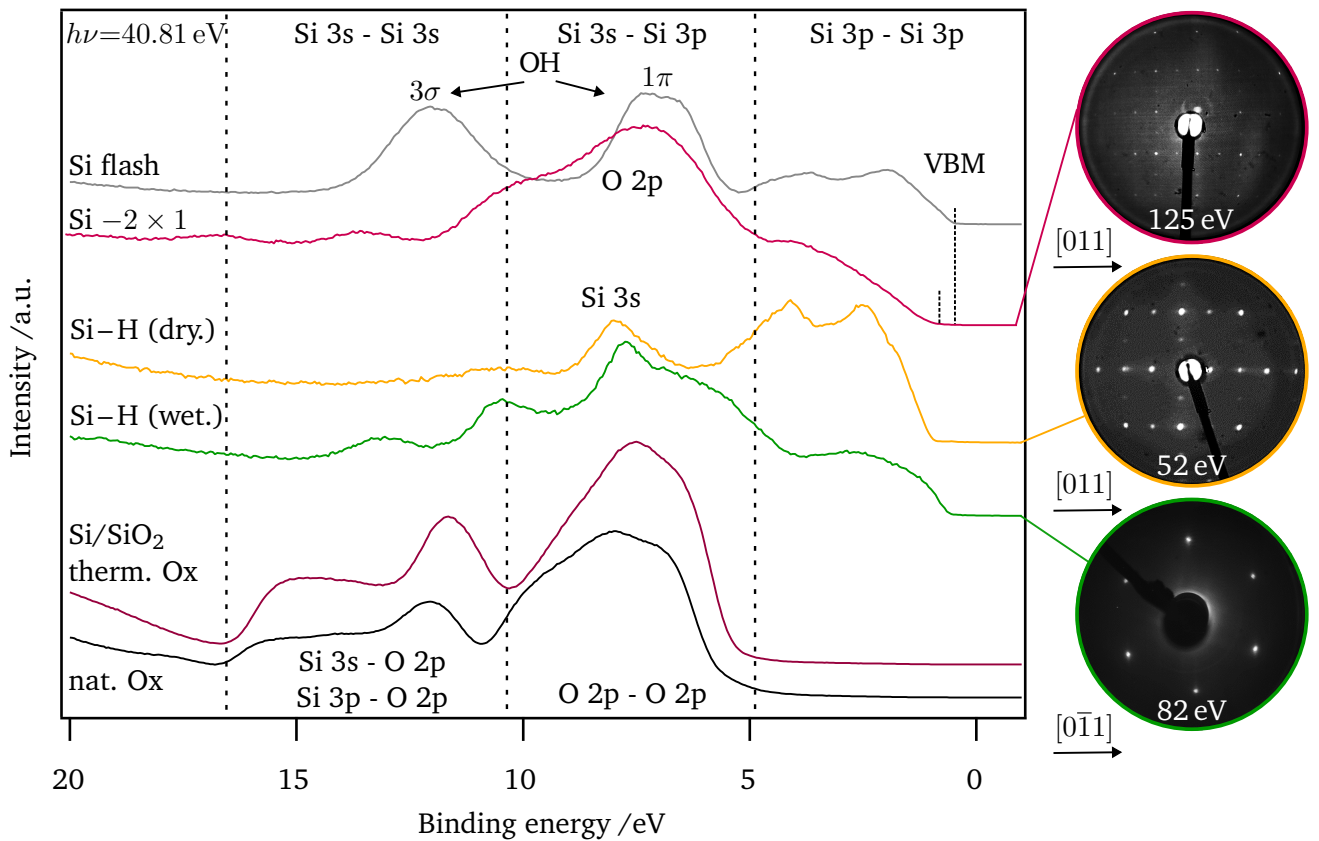


Figure 5.3: Hell ($h\nu=40.81$ eV) spectra of prepared p-Si surfaces with depicted valence state regions (represented by the broken lines). LEED images with denoted beam energies shown on the right for the samples, which revealed LEED reflexes.

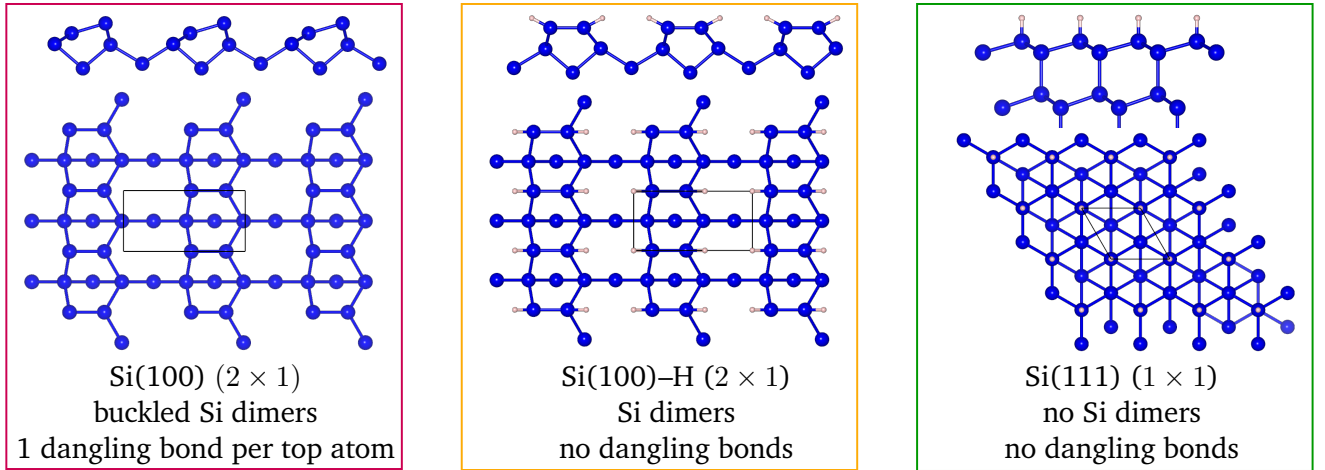


Figure 5.4: Si surface structures as expected from UP-spectra and LEED pattern. Blue and white balls indicate Si and H atoms visualized with VESTA.

of the surface as observed in the HeII spectra (grey) revealing a progressing, rapid hydroxylation of the surface even at a base pressure below 8×10^{-10} mbar. Two rising features at 7 and 12 eV which correspond to the 1π and 3σ antibonding and bonding orbitals of OH^{135} appear after a short time and increase in intensity (see Section 5.2 for more details).

Only after subsequent annealing of the surface in ultra-high vacuum (UHV), a two-domain 2×1 LEED pattern with domains orientated perpendicular to each other indicates a stable Si dimer formation. Nevertheless, the reconstructed Si(100) (2×1) surface, still reveals one dangling bond per top Si surface atom (Figure 5.4, left). However, specific emissions appear in the HeII spectra from 7 to 11 eV which are related to the O 2p σ - and π -bonding states. Moreover, the XPS O 1s emission shows a chemical shift from the hydroxide species at 532.2 eV to a more oxidic species at 531.8 eV (Figure 5.1). As a result, the VBM shifts to higher binding energies in the same manner as the Si 2p line, indicating an upward Fermi level shift to 0.7 eV above the VBM resulting from oxygen-induced donor states localized above mid-gap.

Conclusively, the flashed surfaces show a high amount of reactive surface defects, leading to a pinned surface. Furthermore, it is observed, that oxygen contamination lead to an energetic shift. In order to further discuss, the influence of defects on the electronic structure, the impact of hydrogen and oxygen termination on Si surfaces on the observed spectra will be analyzed in more detail in the following two sections.

5.1.3 Oxide specification and oxygen-related dangling bond defects

The σ and π interaction of oxygen with silicon atoms is capable to passivate surface defects as bonding and antibonding states formed by Si sp^3 hybrid orbitals interacting with O sp hybrids, and O 2s as well as O 2p contributions appear below the band edges.^{136,137} HeII spectra of oxidized silicon surfaces show broad O 2p emissions at around 7 eV (Figure 5.3). In addition, the Si 3s, 3p and O 2p related states reveal a characteristic valence band feature at 12 eV and around 14 eV.¹³⁸ The sputter annealing procedure of the bare wafer leads to pronounced valence band features indicating a well-defined oxide layer, which seems to be homogeneous and stoichiometric. In the Si 2p core level region, broadened SiO_2 -related contributions appear between 103.5 and 103.8 eV dependent on substrate doping with a full width at half maximum (FWHM) of about 1.5 eV (Figure 5.1). From the SiO_2 to Si ratio of the

Si 2p region, an oxide layer thickness of around 8.1 Å with an oxygen to Si ratio of 2 : 1 (67 atm.% O and 33 atm.% Si) results for the untreated wafer (see Table A2 in the Appendix). After the sputter annealing step, the thickness increased to 10.5 Å with no significant change in the oxide stoichiometry.

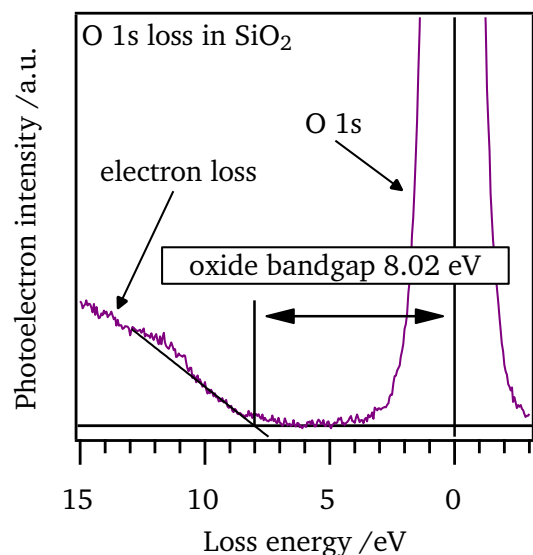


Figure 5.5: Electronic bandgap determination of native SiO₂ layer.

As expected, for none of the oxide terminated wafers a LEED pattern can be observed, indicating an amorphous SiO₂ layer for both native and thermal oxides. For a sufficient amount of XPS scans, the loss feature of the O 1s signal provides information about the electronic band gap of the native oxide layer on top of the Si wafer (Figure 5.5).^{139,140} The electron loss is caused by the direct interband transition from the SiO₂ VBM into the conduction band minimum (CBM). By doing so, a value of 8.02 eV is evaluated for the native oxide, which is lower than the literature value of 9.0 eV found by the same method of thermally grown 2.3 nm thick SiO₂ layer¹³⁹ or by photoconductivity on thicker (500 nm) SiO₂ films.¹⁴¹

The VB onset from the HeII spectra (Figure 5.3) is found to be at about 5 eV. This is 0.5 to 1.0 eV above the SiO₂ mid-gap position which might be caused by charging effects. However, as the Fermi level in SiO₂ is far from the band edges, the dielectric character of the SiO₂ termination layer is confirmed and no free charges nor a charge transport over the valence and conduction bands are expected.

For entropy reasons, even a fully oxidized Si surface possesses dangling bond defects. In this case, the surface state distribution in the bandgap strongly depends on the oxidation state of the defect centers induced by dangling bonds. These partially oxidized P_b centers can be assigned to either Si₂O₁≡Si· or Si₁O₂≡Si· structures. They are known to show only donor-like states within the Si bandgap at around 0.4 and 0.7 eV above the VBM, revealing a narrower distribution than the symmetrical mid-gap states.¹⁴² The donor state of the O₃≡Si· center is expected to be even above the CBM, thus related to a fixed positive oxide charge.¹²⁸ For the native oxide termination, both p- and n-type Si show donor-like doping at the surface. This results in an inversion layer at the surface of the p-Si as the Fermi level is located 0.74 eV above the VBM which is slightly above mid-gap position. For the n-Si, an electron accumulation at the surface is observed as well, since donor states are shifting the Fermi level to 1.00 eV above the VBM which is located 0.13 eV above the flat band position in the bulk. Due to the temperature treatment, excess dangling bonds are consumed by the reaction with oxygen and to some extent by the reaction with silicon, leading to a more pronounced flat band like situation than the initial native oxide termination does. The p-Si reduces the initial surface band bending to 0.29 eV. On n-Si, the Fermi level equals the flat band position. In contrast to bare Si, the Fermi level position for the oxide terminated Si seems to be independent of the source intensity. The reason for the more pronounced flat-band situation on n-Si/SiO₂ compared to p-Si/SiO₂ is attributed to the amphoteric interaction of the P_b acceptor states above mid-gap and partially oxidized P_b centers acting as donors accordingly.

In conclusion, oxidized defect center lead to donor-like states inside the Si band gap. But, proper oxidation treatments can minimize the total amount of defect states by the passivation of dangling bonds.

5.1.4 Dangling bond passivation by hydrogen termination

Saturating Si dangling bonds with atomic hydrogen is a well-known surface treatment in order to passivate the dangling bond states at Si surfaces. In this study, a wet chemical treatment according to Angermann et al.¹⁰⁸ is compared to a dry physical treatment under 950 mbar H₂ ambient right away transferred to UHV according to Brückner et al.¹⁰⁵. It turns out that the H₂-prepared Si-H samples are spotless and show neither carbon nor oxygen contamination (Figure 5.1, yellow spectrum). By applying dedicated fitting routines, the Si 2p emission can be deconvoluted, resulting in separated single Si 2p components with different 2p doublet structure pointing to different back-bonding centers as depicted in Figure 5.6a). A surface related component of about 10 % relative intensity is found with a chemical shift of about 0.25 eV compared to the bulk-related Si₃–Si₃ center that can be assigned to Si₃≡Si–H. The same chemical shift was found by Lewerenz et al.¹⁴³, which they also assigned to Si–H species according to their density functional theory (DFT) calculations. In addition, reflection anisotropy spectroscopy (RAS) (Figure A1 in the Appendix) and LEED (Figure 5.3) pattern reveal a 2 × 2 reconstructed surface indicating a monohydride surface phase with two 2 × 1 domains rotated by 90°^{105,144} (see Figure 5.4 for the surface structure).

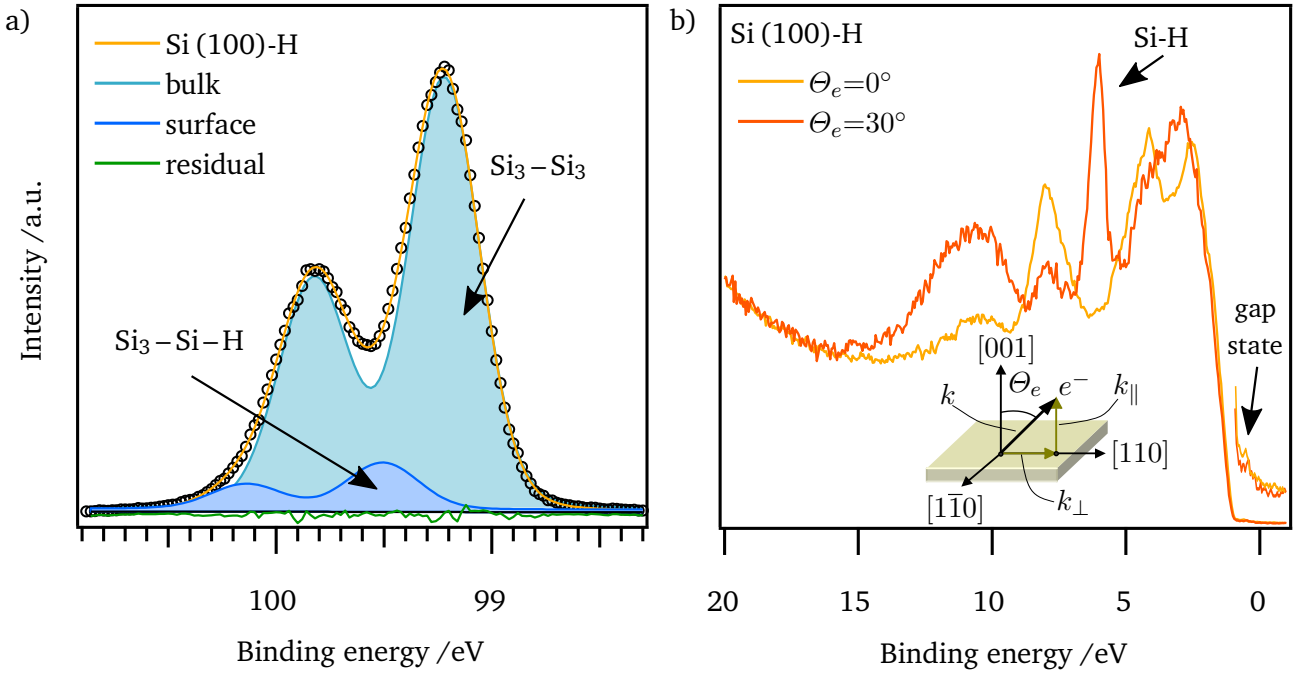


Figure 5.6: Photoemission spectra of dry physical prepared monohydride Si(100) surface according to Brückner et al.¹⁰⁵. a) Si 2p deconvolution of bulk and surface component. b) Angular resolved Hell ($h\nu=40.81$ eV) spectra revealing the Si–H bonding orbital at 6.0 eV.

Due to the sample transfer from Ilmenau to Darmstadt, first PES measurements have been conducted 24 h after preparation. The n-Si:H sample exhibits a binding energy position of the core level of $E_b(\text{Si } 2p_{3/2})=99.85$ eV and a Fermi level position of 1.01 eV above the VBM. According to the higher doping concentration of the wafer which was used for this sample, the measured value is only 30 meV below the calculated bulk position, indicating flat-band situation at the surface. For p-Si:H, the Si 2p appears at $E_b(\text{Si } 2p_{3/2})=99.23$ eV, which can be assigned to a Fermi level located 0.49 eV above the VBM in contrast to the calculated bulk position of 0.16 eV. Nevertheless, source-induced SPV plays a role for both samples since reduced light intensity moves the Fermi level 100 meV towards mid-gap in both cases,

n- and p-type Si, respectively. In order to obtain these energy shifts in n-Si, the source intensity needed to be decreased from 300 W to 1 W. In contrast to that, it was sufficient to decrease the source-intensity for the p-Si to 10 W, showing again that the depleted n-Si layer is more susceptible to SPV than p-Si.

The HeII line of the Si (100):H prepared samples show two degenerated Si 3p features at around 2.5 and 4.1 eV, which are clearly associated with the reconstructed surface (Figure 5.6b)). At 8 eV a strong Si 3s-3p peak arises whereas the broad feature at around 10.5 eV is more of a 3s character. By changing the photoelectron emission angle Θ_e from 0° to 30° in azimuthal [110] direction shown in Figure 5.6,¹⁴⁴ one can probe the surface Brillouin-zone from the Γ to the J -point showing a very sharp peak at 6.0 eV, which can be associated to a Si–H surface bonding and is in good agreement with previous findings and tight binding calculations at the J -point.^{145,146} Furthermore, the 3s feature at 10.5 eV is enhanced due to the hybridization of the H 1s and Si 3s orbitals at the K-point of the surface Brillouin zone as predicted by Pandey¹⁴⁶ and has been also found on fully hydrated Si(111):H-(1×1) surfaces.^{147,148} To my knowledge, this prominent H-resonance has not been observed on Si (100) yet, confirming the high surface order of the present monohydride surface.

Despite the well-defined surface with almost flat-band condition, the HeII line reveals a small amount of states showing up above the valence band edge up to the Fermi level with a small peak structure 290 meV above the VBM, which is attributed to the occupied Si dangling bond state (see magnified VBM region in Figure 5.6b)). Repeating the measurements 48 h after preparation (not shown here), the Si 2p line of the n-doped Si shifts about 200 meV to $E_b(\text{Si } 2p_{3/2})=99.63$ eV which seems to be source intensity independent. This indicates a strong Fermi level pinning 0.89 eV above the VBM due to partially H-desorption, increasing the amount of Si dangling bond states in UHV.

During the wet-chemical H-termination, the native oxide is etched and remaining dangling Si-bonds are terminated in NH_4F solution with atomic hydrogen. The H-terminated samples were loaded within 10 min after preparation into the XPS analysis chamber. The prepared H-terminated surfaces reveal low oxygen contents of less than 1.5 atm.% with XPS. However, the HeII spectra reveal clear indications of surface oxidation as shown in a broad O 2p feature at around 5 to 10 eV. At the same time, the VBM from Si 3p states and the Si 3s-3p feature at 8 eV are clearly visible, while the oxidized contributions appear as two features at 11 and 13 eV. Both preparations led to 1×1 LEED pattern (compare Figure A2), indicating a fully hydrided surface with no surface reconstruction due to dimer formation on both (111) and (100) surfaces¹¹⁷ (see Figure 5.4 for the surface structure). Energetically, H-terminated n-Si (100) and (111) show a Fermi level position very close to the conduction band $E_b(\text{Si } 2p_{n-111})=99.88$ eV and $E_b(\text{Si } 2p_{n-100})=99.94$ eV, indicating an accumulation surface layer due to oxygen related donor states similar to the oxygen terminated surfaces as discussed before. The H-terminated p-doped surfaces show for both orientations a mid-gap Fermi level position at $E_b(\text{Si } 2p_{3/2})=99.35$ eV. In case of p-Si, donors and acceptors of partially oxidized and non-oxidized P_b centers pin the Fermi level 0.6 eV above the VBM. On n-Si, the acceptor states are fully occupied due to the higher bulk Fermi level. In combination with the oxygen related donor states, this results in an electron accumulation at the surface. This is in good agreement with Schlaf et al.¹²⁰ who found a strong donor level pinning the Fermi level at 0.2 eV below the CBM for HF-etched p- and n-Si surfaces. Storing the p-Si (111):H sample for 4 weeks at $<10^{-9}$ mbar led to further surface oxidation and a Fermi level shift of 50 meV towards the conduction band indicating further oxygen-induced electron accumulation.

For the very defined dry-physical H-terminated Si surface, the PES analysis allowed the investigation of occupied donor states. To investigate non-occupied acceptor states close to the Si bandgap region near edge X-ray absorption fine structure (NEXAFS) spectroscopy of wet chemically H-terminated Si surfaces were measured in the surface sensitive partial Auger yield at the BESSY II synchrotron storage ring. In

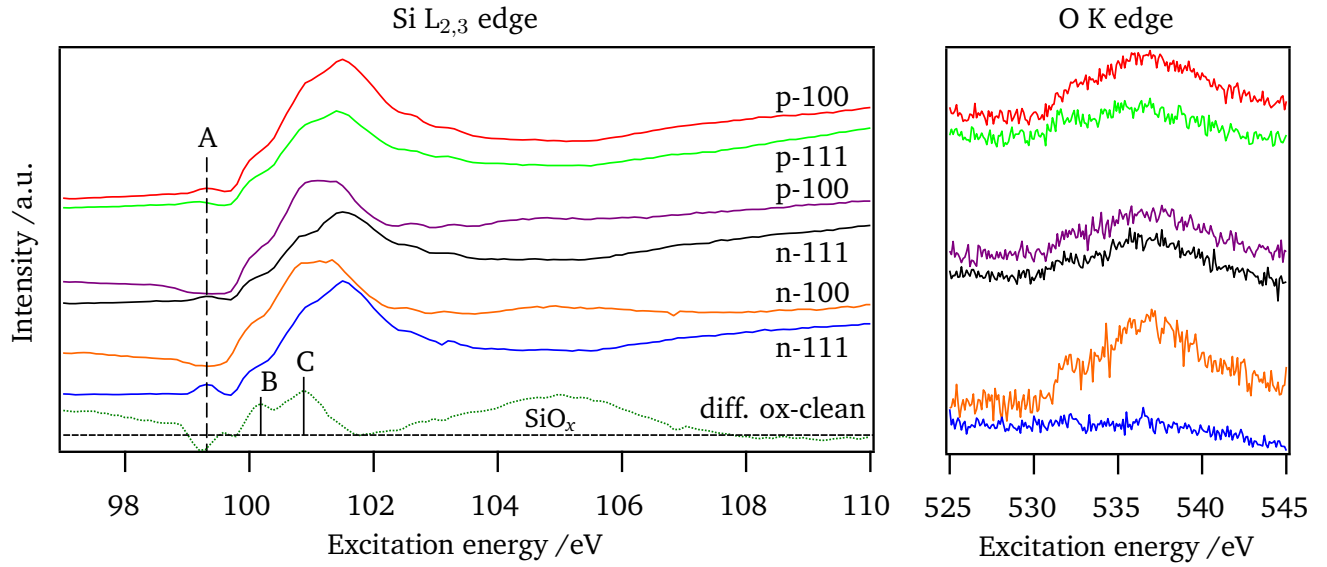


Figure 5.7: NEXAFS spectra of wet-chemically prepared H-termination of Si with Si $L_{2,3}$ and O K-edges. Dotted green spectra depicts difference of clean (orange) and oxidized (blue) spectra revealing two additional adsorption features close to the main adsorption edge after partial oxidation.

Figure 5.7 the Si $L_{2,3}$ and the O K-edges are shown. The n-(111) surface shows almost no absorption in the O K-edge region (blue spectra), indicating the lowest amount of surface oxidation. At the same time, the n-111 Si samples reveals the most prominent pre-edge feature, labeled with A, 0.4 eV below the main Si absorption L-edge starting at $h\nu=99.75$ eV, indicating the CBM. This pre-edge structure can be assigned to the Si dangling bond acceptor states which was reported to appear ≈ 0.3 eV below the CBM.¹²⁹ Furthermore, the observed acceptor state on the wet-chemical (111) surface coincides with the pinning level of the 48 h altered UHV H-terminated (100) surface indicating that Si dangling bonds are the dominating defects on both surfaces. Samples, which do not show that prominent pre-edge feature in the NEXAFS spectra, reveal significant amounts of oxygen confirming that the acceptor states of the oxidized P_b centers are located far above the CBM leading to only donor states within the Si bandgap as previously described.¹²⁸ By comparing the NEXAFS of clean and oxidized samples (green spectra), two additional features B and C appear 0.53 and 1.23 eV above the CBM, which may be assigned to the acceptor states of the $Si_2O \equiv Si \cdot$ and $SiO_2 \equiv Si \cdot$ defect centers. The ionized donor state of the $O_3 \equiv Si \cdot$ defect, is also expected to contribute in this region.¹²⁸ The main absorption of the native SiO_x oxide layer, is known to appear far beyond the conduction band edge at about $h\nu=105$ eV.^{149,150} However, the broad distribution of the oxide species in this region indicates the presence of Si^{2+} , Si^{3+} , and Si^{4+} species, which would support the assumption of present oxidized P_b centers.¹⁵¹

To summarize the investigated defect distribution of Si dangling bonds, Figure 5.8 represents the whole surface state distribution of non-oxidized Si dangling bond centers within the bandgap according to the measurement results. The obtained pinning levels from X-ray photoemission spectroscopy (XPS) and UPS are related to the donor and acceptor states, which are found 0.29 and 0.89 eV above the VBM. With that, the effective correlation energy of 0.6 eV is confirmed with photoemission spectra as previously derived from ESR^{126,129} and DFT¹³¹ studies. As soon as the surface starts to oxidize, the acceptor states are shifted apart from the conduction band (CB) edge and therefore play no role for surface band bending and excess charge carrier recombination at the surface. However, their donor states remain in the Si bandgap

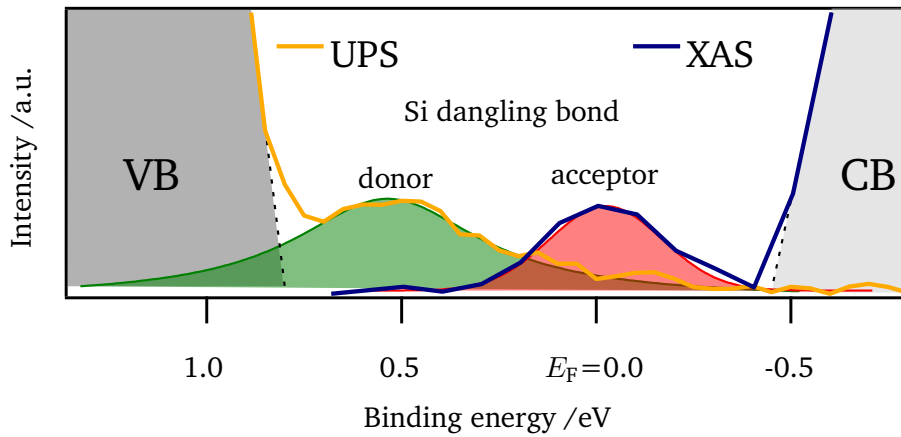


Figure 5.8: In-gap states of Si dangling bonds at H-terminated Si surfaces. UP- and XA-spectra reveal occupied and unoccupied dangling bond states, respectively. UP-spectrum is conducted from a dry physical prepared n-Si(100)-H and XA-spectra from a wet chemical prepared n-Si(111)-H surface. VB cut-off and XA onset were normalized to mid-gap states and separated by the optical bandgap of around 1.2 eV.

and may cause electron injection into the Si surface. With that assignment, the effective correlation energy of the $\text{Si}_2\text{O} \equiv \text{Si} \cdot$ defect would be around 0.9 eV and is increasing with further oxidation to 1.7 eV for the $\text{SiO}_2 \equiv \text{Si} \cdot$ defect.

5.1.5 Source-induced photovoltages at cryogenic temperatures

Band bending due to surface states results in a SCR which acts as a charge separator for excess charge carriers and with that is able to induce a SPV while illumination. Even under fully dark conditions, the X-ray source itself can induce SPV as already observed on the flashed Si surfaces (Figure 5.2a)). The extent of SPV measured at a depleted SCR due to surface states depends on several substrate properties. Besides the absorption properties, the diffusion length of the minority and majority charge carrier, which is a bulk property, and the lifetime of excess charge carriers in the bulk compared to the surface (surface recombination) is of importance. For Si with high carrier mobilities ($\geq 10^3 \text{ cm}^2 \text{ V}^{-1} \text{ s}^{-1}$, compare Table 5.1) and bulk carrier life times from 10^{-6} to 10^{-3} s ,^{29,152} most of the non-equilibrium charge carriers will be separated and recombine at the surface by Shockley-Read-Hall recombination³⁴ involving surface states. As a result, the mobility of charge carriers at surfaces is considerably lower than in the bulk, since Coulomb scattering occurs at charge carriers which are trapped at surface states.¹⁵³ The measurement of SPVs depending on light intensity is thus an easy experimental tool to characterize the quality of surface preparation, as the surface recombination will strongly be affected by the number of surface states.^{21,154}

Figure 5.9 depicts the surface band bending of a clean p-Si surface in the dark and under illumination. Required that under illumination the total surface charge Q_{ss} will not change, the source-induced excess charge carriers will screen the fixed surface charge and thereby reduce the initial surface band bending.¹⁵⁵ Consequently, the SPV shifts the Si 2p to lower binding energies by eU_{ph} . Source-induced SPVs always lead to a decrease of apparent band bending. In order to pronounce this effect, cryo-XPS measurements can be performed to probe the SCR at the prepared Si surfaces.^{156,157} By cooling with liquid nitrogen, a measured substrate temperature of -176°C is achieved. As the thermally induced transitions of holes as majority carriers are exponentially reduced with that temperature, the recombination of excess charge carriers with intrinsic counter charges is suppressed which also leads to strong temperature dependence

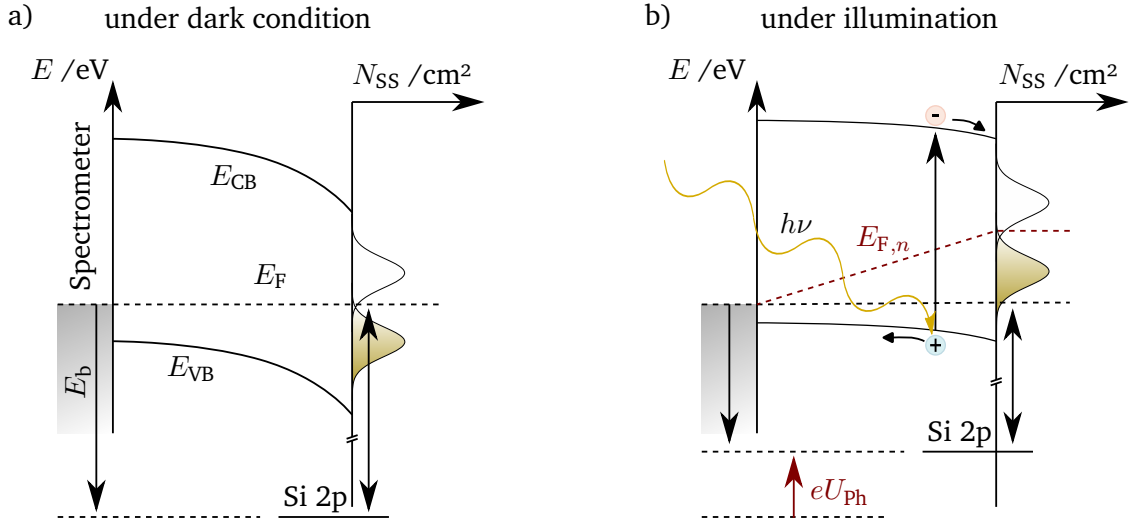


Figure 5.9: Scheme of a depleted p-Si surface with dangling bond states a) in the dark and b) under illumination where SPV lead to more flatband conditions, due to a higher concentration of electrons in the SCR indicated by their quasi-Fermi-level $E_{F,n}$.

of the reverse saturation current density of the rectifying SCR.⁶⁷ It is evident that with decreasing thermal carrier velocity also the surface recombination velocity drops at low temperatures according to Stevenson and Keyes¹⁵⁸ with $\propto T^{-1} e^{-\frac{\Delta E}{k_B T}}$. However, apart from the pronounced SPV, resulting in binding energy shifts when approaching flat-band condition, there are other energetic effects which need to be considered when analyzing surface band bending at liquid nitrogen temperature. One is the “freeze-out” of doping levels, since the thermal energy is too low to ionize all dopants and leads to a flatband Fermi level position of $E_{VB} - E_F(-176^\circ\text{C}) = 0.08\text{ eV}$ and $E_F - E_{CB}(-176^\circ\text{C}) = 0.09\text{ eV}$ for the p-Si and n-Si wafers, respectively. Another fact is the band gap spreading by $\Delta E_g(-176^\circ\text{C}) = +40\text{ meV}$.²⁹

By considering all these effects, the Fermi level positions within the Si bandgap for all p- (bottom row) and n-Si surfaces (top row) as evaluated from the Si $2p_{3/2}$ position according to Table A1 are depicted in Figure 5.10 in comparison to the expected flatband potential from Table 5.1. The difference between the measured surface Fermi level position and the calculated bulk (or flatband) Fermi level position (dashed lines) at room (green) and liquid nitrogen (red) temperature is representing the total surface band bending ϕ_{BB} by the size of the bars. The shift of the flatband energy due to cooling is related to the freeze-out effect of dopants as explained above. The bandgap of the Si-H (dry) was reduced due to the bandgap narrowing of the n-type wafer because of the high doping concentration of $N_{\text{don}} = 1.9 \times 10^{18}\text{ cm}^{-3}$.¹⁵⁹ The reduction of the bar size after cooling (green vs. red bars) can be considered as source-induced SPV at low temperature. The extent of SPV gives conclusions about the total amount of surface defects and to what extent they can act as recombination centers for excess charge carriers. It should be mentioned that additional bias light could even enhance SPV.¹⁶⁰ However, at low temperature no significant shifts toward the flatband position could be observed by additional white light illumination, indicating that the X-ray source itself almost brings the SPV to its physical limits.

All p-Si samples show a depletion region due to the previously discussed donor states inside the Si bandgap at the surface. In contrast to that, only oxygen-free samples (*flashed* and *dry-H-terminated* Si) reveal a slight electron depletion in n-Si surfaces due to unoccupied acceptor levels below the bulk Fermi level. All other n-Si surfaces show either flat band (*therm. Ox*) or electron accumulation at the surface due to oxygen-related donors close to the CBM.

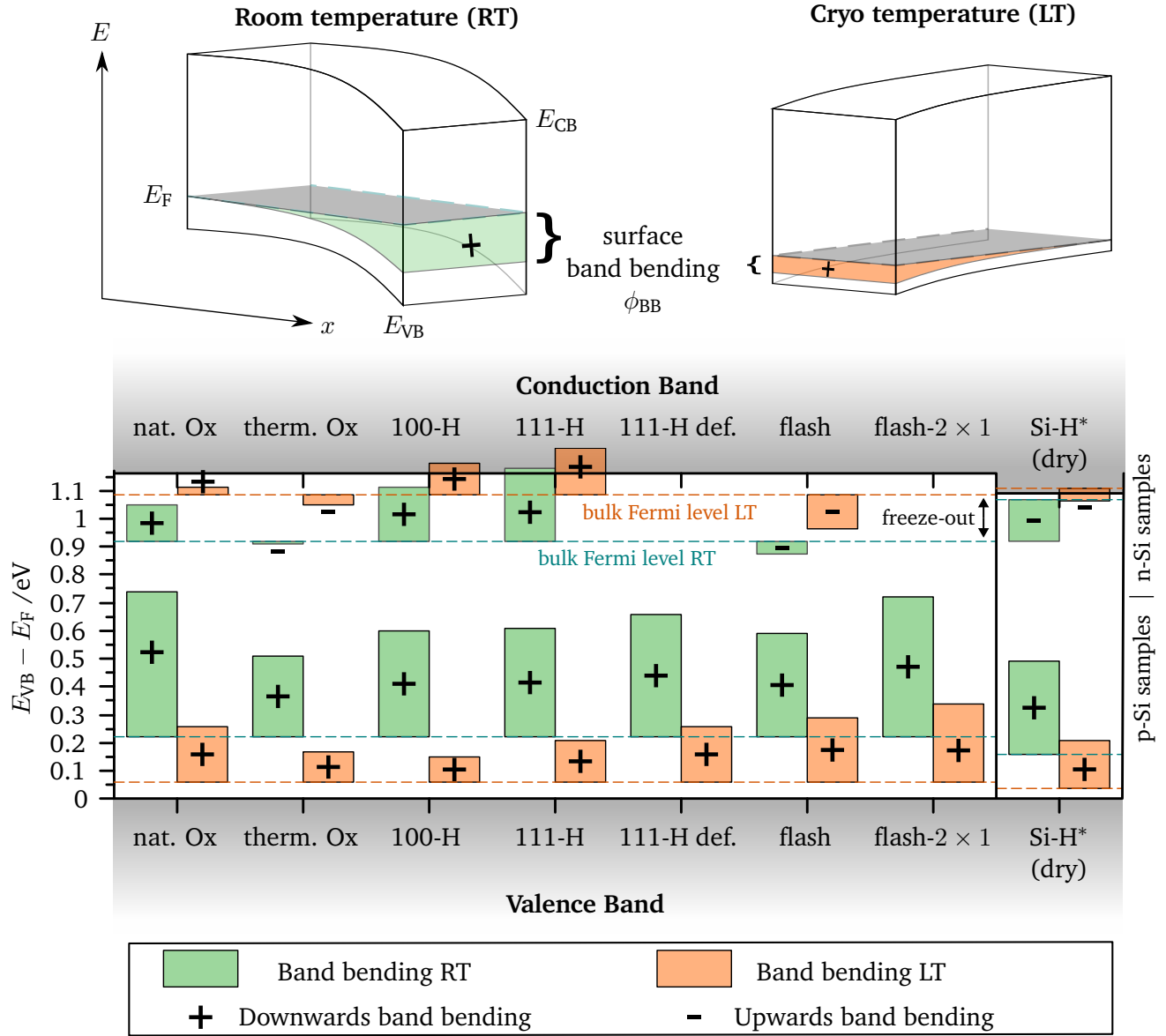


Figure 5.10: 2D projection of SCR inside the Si bandgap of all samples due to surface band bending at room temperature (green) and liquid nitrogen temperature (red). Bottom and top row represent p-Si and n-Si samples, respectively. Bar edges indicate VBM to Fermi level energy difference in the bulk and at the surface. Reduction of band bending at liquid nitrogen temperature indicates a source-induced SPV. *Bandgap narrowing and different bulk Fermi-level positions due to higher doping concentration of used wafer for sample Si-H (dry).

From the shown set of samples, the following conclusions might be drawn:

- At low temperature, oxygen-free surfaces show lower source-induced SPV indicating that the recombination activity of the Si dangling bonds gets reduced by the oxidation of P_b centers. This is in good agreement with Flietner¹⁴², who attributed the main recombination activity to the non-oxidized dangling bond states, as the amphoteric character of this defect enhances the Shockley-

Read-Hall process when the splitting of Quasi-Fermi level at mid-gap ionizes donors and acceptors simultaneously.

- ii) All p-Si surfaces show more band bending than equivalent n-Si surfaces as already observed elsewhere.^{120,161} This behavior might be attributed to the following observations: Clean n-Si surfaces are more susceptible to SPV even at room temperature as discussed above, which renders the evaluation of total band bending by photoemission spectroscopy nearly impossible. Furthermore, the oxidation of dangling bond centers shifts acceptor levels above the conduction band and prevents upward band bending.
- iii) The sputter annealed sample (*therm. Ox*) shows for n- and p-type, the lowest band bending at room and low temperature indicating that the total amount of surface states is the lowest in comparison to all other samples.

5.1.6 Conclusion on Si surface defects

In this Section the role of Fermi level pinning due to Si dangling bonds on different Si (100) and (111) surfaces has been investigated. The findings on flashed Si surfaces confirm the U-shape distribution of clean Si dangling bond centers, exhibiting amphoteric behavior. Both p- and n-type Si show Fermi level pinning in the middle of the bandgap, coinciding with the defect's CNL. Furthermore, on surfaces entirely devoid of oxygen, an occupied in-gap state 0.29 eV above VBM and an unoccupied in-gap state 0.40 eV below the CBM is found, which coincide with these dangling bond states. According to the present results, surfaces contaminated with oxygen tend to accumulate electrons since the unoccupied in-gap states vanish, resulting in only donor-like states within the bandgap. These oxygen-related donor states were attributed to partially oxidized Si dangling bond centers. Hence, none of the present p-type surfaces reveal flat-band conditions after preparation, whereas n-type surfaces reveal comparatively lower surface band bending. Nevertheless, it is inferred that flatband conditions alone not sufficiently describe the overall defect density of the analyzed surface, as only ionized surface states contribute to surface band bending. Moreover, Fermi level pinning requires the amphoteric character of a defect center at which several charge states coexist. For high defect concentrations, the pinning level will correspond to the CNL of the defect, provided that there are electronic states at this energy. In this case, the electronic distribution of the defect plays a minor role for the pinning itself. For lower defect concentrations, the amphoteric character is provided by the defect itself when neutral and ionized states coexist and lead to a half-filled defect band. Consequently, identical surface defects but with varying concentrations result in different pinning positions within the bandgap.

Furthermore, the cryo-XPS measurements suggest that donor-like oxidized P_b centers reveal lower recombination activities than the amphoteric non-oxidized dangling bond centers. According to the results, none of the investigated surfaces could be considered as defect-free. Nevertheless, sputter-annealed oxide layers provided the most effective surface passivation for photoelectrochemical applications, since for p- and n-Si the lowest surface band bending is observed at room temperature but also liquid nitrogen temperature, indicating the lowest recombination activity of excess charge carriers.

Even though the oxide layer is capable to passivate the majority of Si surface and interface states with low surface recombination velocities of $<1 \text{ cm s}^{-1}$,¹³³ the dielectric character of the oxide layer will act as tunnel barrier at the electrochemical interface and thus limits the charge transfer properties of the interface, thereby impeding the overall device efficiency.

5.2 Surface reactivity of Si dangling bonds

In the previous section, it was shown that the high amount of Si dangling bonds straight after flash-annealing leads to a high reactivity of the hot surface. To monitor the reactivity of excess dangling bonds, a time resolved measurement sequences and angular resolved UPS measurements were conducted on a flashed Si (100) and (111) surface.

5.2.1 Reactivity of Si (100)

The color maps in Figure 5.11 show the O 1s, Si 2p, and HeII VB spectra of a p-Si (100) wafer straight after flashing over consecutive scan numbers related to a certain time sequence. The time resolution for each scan is about 30, 25 and 90 s for O 1s, Si 2p, VB, respectively.

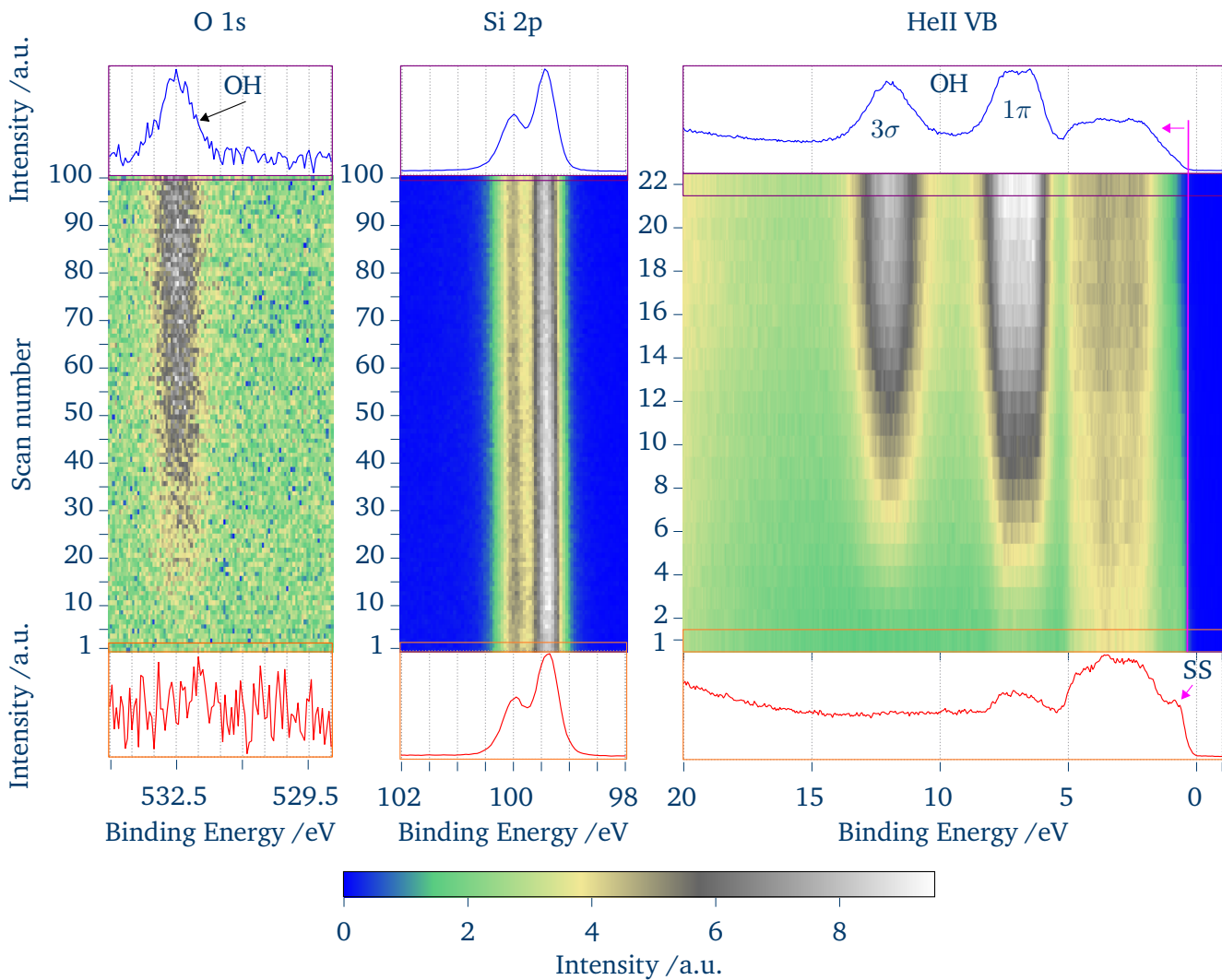


Figure 5.11: Hydroxilation process of an as-flashed p-Si (100) wafer. Rising O 1s and highest occupied molecular orbital (HOMO) OH features in the valence band indicate dissociative adsorption of water at a base pressure of $<10^{-9}$ mbar. SS disappear with hydroxilation while Si 2p remains unchanged.

With a base pressure of about 7×10^{-10} mbar at room temperature, which shortly raises during flashing

to 1×10^{-8} mbar, one can assume an average partial water pressure of about 1×10^{-9} mbar during the measurement time. This would lead to a final water dosage of <2 L after the last scan. After 10 min (20 scans) a signal starts to rise in the O 1s region at about 532.5 eV. At the same time, two features at 7 eV and 12 eV which correspond to the 1π and 3σ antibonding and bonding orbitals of OH,¹³⁵ appear in the HeII VB. In addition, clear gap states arise 0.2 eV below the Fermi level as marked in purple. It is yet not clear whether these gap states originate from isolated dangling bonds as discussed before¹⁶² or from the π -interaction of the dangling bonds of the Si dimers at the surface forming the 2×1 surface reconstruction.^{163–165} These gap states vanish with the ongoing hydroxylation, confirming that they result from SS. Interestingly, the Si 2p line does not change in binding energy, indicating a strong Fermi level pinning at mid-gap, which remains after hydroxylation. Accordingly, not all dangling bonds can be saturated by dissociated H₂O molecules. The Si 2p line gets slightly narrower with time, which might be mainly caused by a temperature effect when the sample slowly cools down after flashing. However, the unknown impact of remaining heat impedes a consistent fitting routine for the Si 2p during hydroxylation.

The observed evidence for adsorbed OH_{ads} at the surface, which is expected to be caused by the dissociation of H₂O, raises the question if H_{ads} could be also identified as the second product of water cleavage, or if even the evolution of H₂ desorbing from the surface has to be considered. In Figure 5.6b) it was shown that the Si–H bonding could be identified on the very well defined 2×1 Si (100):H surface by angular resolved VB spectra. By repeating these measurements on the hydroxylated Si (100) surface, a deconvolution of the upmost 1π state could be observed (Figure 5.12), where the upper contribution appears quite sharp at $E_b=6.75$ eV. Schmeisser et al.¹³⁵ assigned this feature to an oxygen lone pair revealing a chemical shift for H₂O on Si (100). However, as at the same time, the broad Si 3s contribution increases at about 11 eV and both features have been similarly observed at the H-terminated surface (orange spectra, Figure 5.12), where the spectral data suggest an Si–H assignment.

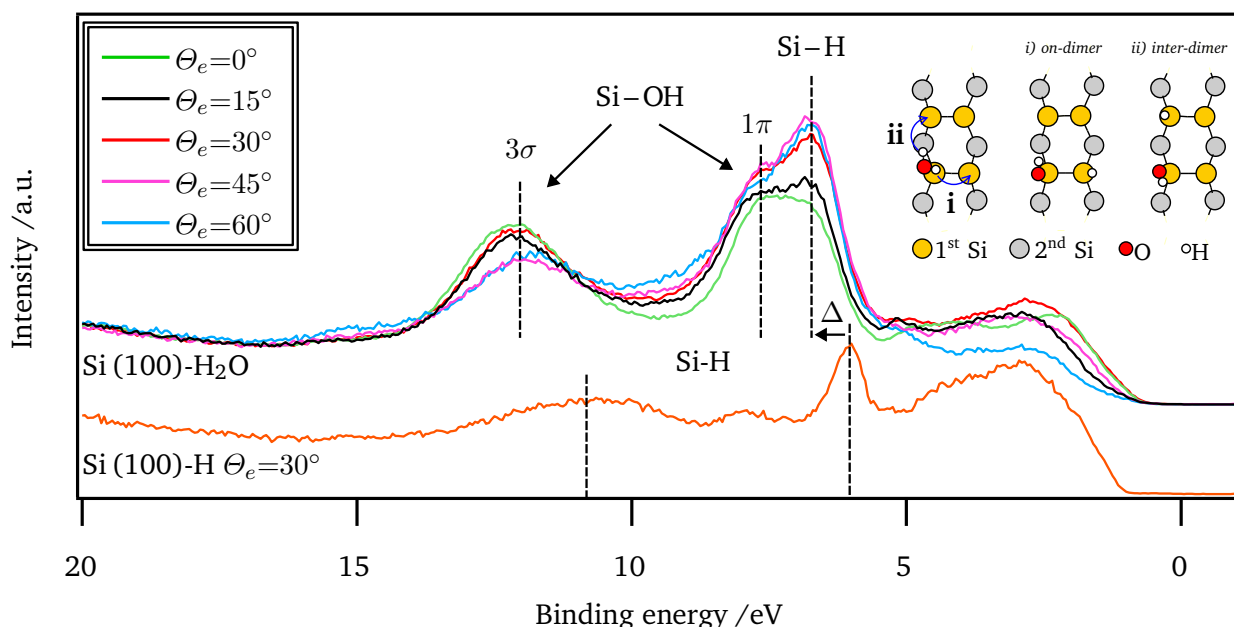


Figure 5.12: Angular resolved HeII ($h\nu=40.81$ eV) spectra of hydroxylated Si (100) in comparison to 2×1 Si (100) surface. *on-dimer* and *inter-dimer* configuration is inset as adapted from Yu et al.¹⁶⁶. Si-H bonds appear at $E_b=6.75$ eV, while features at 7.50 and 12 eV are assigned to hydroxyl orbitals.

However, both Si-H contributions at the hydroxylated surface reveal a chemical shift of $\Delta=0.75$ eV in

comparison to Si (100):H surface. This shift, might be explained by different back bonding contributions of the surface Si–H bonds. In the case of the monohydrided 2×1 Si (100) surface the Si–H is backbonded to a Si surface dimer.¹¹⁷ Apparently, this is no longer the case for the hydroxilated surface, which is also confirmed by the decrease of SS during hydroxylation (compare Figure 5.11).¹⁶³ DFT calculations of Lewerenz et al.¹⁴³ reveal a chemical shift for Si with OH_{ads} and H_{ads} bonded to the same Si atom in comparison to a Si₃≡Si–H bond of about 0.6 eV. This might suggest that one surface atom carries both products of H₂O dissociation. In principle, this is possible, since (100) surfaces reveal two dangling bonds per Si surface atom when breaking the Si dimers. However, DFT and scanning tunneling microscopy (STM) studies strongly suggest a dissociative H₂O adsorption where two configurations are energetically favorable compared to a molecular adsorption with $E_{\text{ads}}=0.74$ eV:

- i) the *on-dimer* configuration, where H and OH sits at the two Si atom of the same Si dimer (with $E_{\text{ads}}=2.38$ eV per H₂O), and
- ii) the *inter-dimer* configuration, where H and OH are located at Si atoms of neighboring dimers (with $E_{\text{ads}}=2.12$ eV per H₂O).^{166,167}

The mechanisms are schematically depicted in Figure 5.12 according to Yu et al.¹⁶⁶. Beyond the similar adsorption energies also the kinetics for both reaction pathways i) and ii) with calculated barriers of ≈ 0.25 eV¹⁶⁷ are almost the same, what suggest that both configurations coexist at the hydroxilated Si (100) surface as experimentally observed.¹⁶⁶ From the present spectroscopic data, it is not possible to distinguish between both configurations, even though the H-resonance appears to be slightly broader in comparison to the ordered 2×1 Si (100) surface. However, the polar back bonds of the Si–H features in *on-dimer* configuration is expected to cause a larger chemical shift than for the *inter-dimer* configuration. Final computational calculations are missing in order to identify the chemical shifts for both configurations and thus verify the reaction mechanism of H₂O dissociation on Si (100).

5.2.2 Reactivity of Si (111)

In comparison to the (100) surface, the flat Si (111) surface only reveals one dangling bond per surface atom. The electronic structure of this surface strongly depends on the surface reconstruction.¹⁶⁸ As already observed on the (100) surface, no LEED pattern could be observed on the as-flashed (111) surface indicating a low surface ordering with a high amount of excess dangling bonds.

Figure 5.13 reveals at the top the dangling bond energy dispersion of a Si (111) (1×1) surface without surface reconstruction according to tight binding calculations of Chadi¹⁶⁹. Accordingly, the unreconstructed Si (111) surface reveals a strong metallic character with three distinct surface states spread over the Fermi level region. The state at the Γ -point of the surface Brillouin zone is located above the surface E_F , which is the equivalent to the CNL of the surface. According to these calculations, the states below E_F at K and M reveal a very high localization of surface charge density, which is also demonstrated by the “flatness” of the bands at these points.¹⁶⁹ These calculations are fully consistent with the HeII spectrum of the Si (111) surface straight after flushing (bottom). It reveals two distinct SS features (a and b) at 0.43 eV (FWHM=0.34 eV) and 1.04 eV (FWHM=0.42 eV), and has been assigned to dangling bond states.^{125,168} The broad energy dispersion and the spectrometer acceptance angle of $\pm 8^\circ$ might be the reason why both features can be measured even under normal electron emission $\Theta_e=0^\circ$. These features have been found on Si (111) (1×1) as well as (7×7) surfaces.^{168,170,171} For comparison, the (2×1) surface only shows feature a, which disperses with a bandwidth of about 0.8 eV^{172,173} and is of s, p_z character confirming the dangling bond state.¹⁷⁴

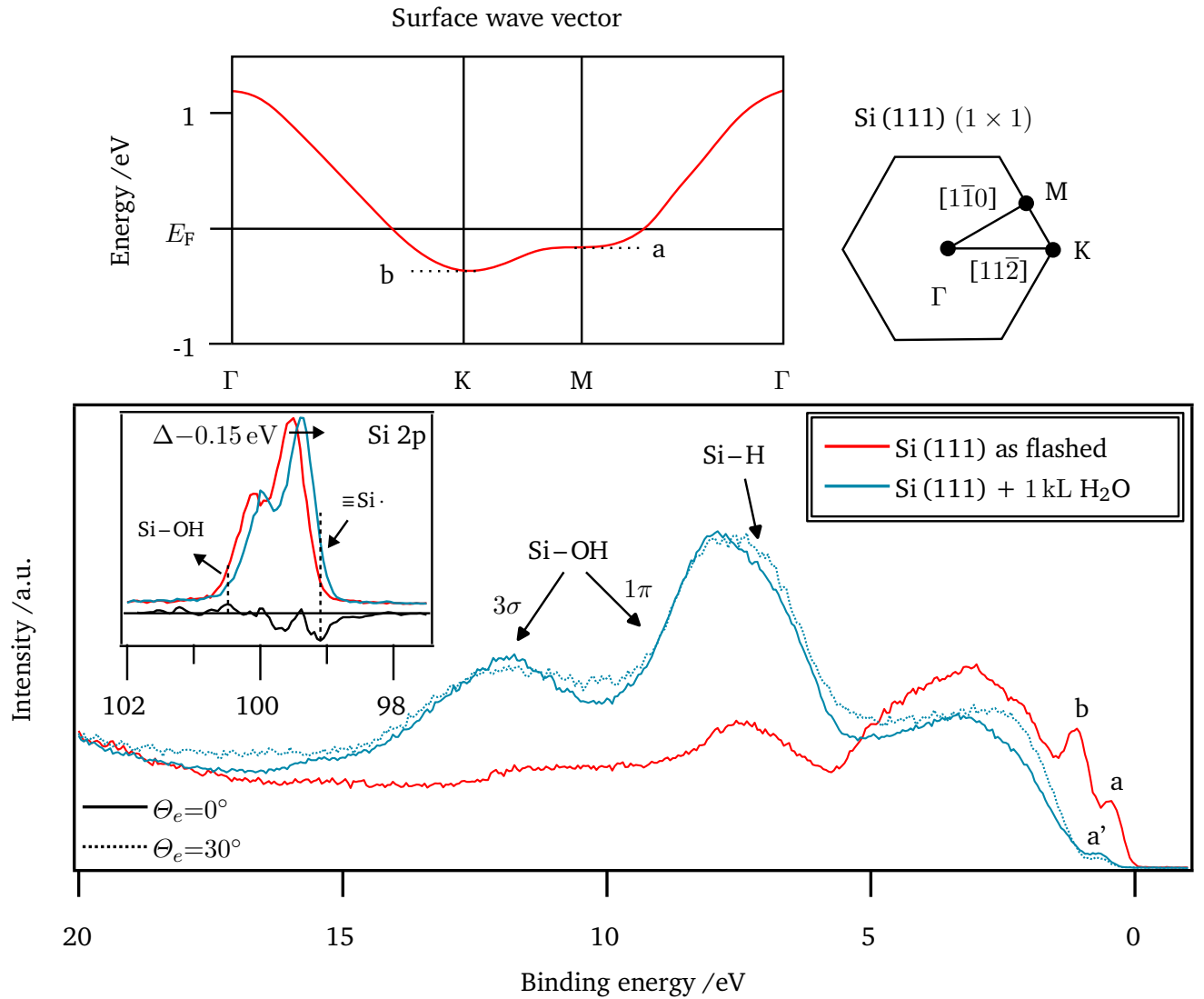


Figure 5.13: Dangling bond dispersion and surface Brillouin zone of not reconstructed Si(111) (1×1) surface according to Chadi¹⁶⁹ (top). HeII spectra of Si(111) surface straight after flushing and after exposed to 1 kL H₂O (bottom).

As similarly observed on the flashed Si(100) surface, the (111) surface seems to be highly reactive. The blue HeII spectra in Figure 5.13 show the characteristic hydroxilation feature at 7.9 and 11.9 eV. In comparison to the (100) surface, not only the intensity ratio of the 1π and the 3σ state differs, but also the energetic distance decreases by about 0.5 eV. The 1π orbital appears at a higher energy, what might indicate a stronger interaction of the oxygen lone pairs with the (111) surface. By changing the photoemission angle Θ_e to 30° in azimuthal $[11\bar{2}]$ direction, the surface Brillouin zone is probed from the Γ to the K-point. A rising feature at ≈ 6.8 eV can be observed, which is attributed to a H resonance at the K-point.¹⁴⁵ It should be noted that the H-resonance at the K-point of the hydroxilated (111) surface is clearly lower in intensity than observed at the M-point of the (100) surface. With the dissociative adsorption of H₂O, the surface states a and b get clearly damped and only one surface state a' at 0.66 eV (FWHM=0.5 eV) remains. The change in Θ_e does not show a clear energy dispersion and coincides with the dangling bond

state found by Chadi et al.¹⁷² on the Si (111) (2×1) and (7×7). As a consequence, neither on the (100) nor the (111) surface all dangling bonds are consumed upon the dissociative water adsorption.

The related Si 2p XP spectra are inset in Figure 5.13. In comparison to the spectra of the flashed Si (100) surface, the Si 2p is less distinct, indicating a more complex reconstruction configuration most probably due to the larger variety of back bonding geometries on the (7×7) surface. The Si 2p_{3/2} is located at 99.54 eV and shifts to 99.43 eV by reducing the X-ray power from 300 to 1 W, indicating an upward band bending at the n-Si (111) surface. When exposing the (111) surface to 1 kL H₂O, the Si 2p shifts further down in binding energy to 99.36 eV (see Figure 5.13). Interestingly, it is located at the same position as found on the flashed p- and n-Si (100) surfaces, which correlates again with the mid-gap pinning 0.6 eV above the VBM. Furthermore, no SPV are observed when reducing the X-ray power. The shape of the Si 2p gets slightly narrower after water exposure (most indicated by the more prominent kink between the dublett, Figure 5.13). However, the consumption of surface states which appear at the edge to lower binding energies of the Si 2p_{3/2}¹²⁵ can be barely resolved with Al K α radiation, just as little as the formation of Si¹⁺ at higher binding energies¹³² after hydroxilation. For that purpose, highly surface sensitive synchrotron radiation is needed,^{125,175} which could not be performed in the framework of this thesis. Assuming that both surfaces reveal a high enough surface state density of $N_{SS} \gg 10^{11} \text{ cm}^{-2}$, the observed energy shift could only be caused by two effects:

- i) The CNL of the surface, changes after hydroxilation, while the CNL of the unreconstructed (1×1) surface is located above the E_F of the bulk, therefore inducing electrons into the bulk.
- ii) Both surfaces, the clean and the hydroxylated, reveal mid-gap Fermi level pinning due to the dangling bond distribution around mid-gap but the clean n-Si surface shows a more flat-band like surface due to source-induced SPV as described in Section 5.1. This would imply that the surface hydroxilation of Si (111) induces fast recombination centers preventing SPVs, even though the total surface state density decreases.

As both conclusions are of high relevance for photoelectrochemical applications, further Kelvin probe or photoconductive decay measurements are necessary in order to clarify this observation.¹⁵⁵

In conclusion, it is shown that the surface reactivity of Si (100) and (111) surfaces is strongly related to dangling bond defects leading to water dissociation. However, even after high water exposures in the range of 1 kL, a considerable amount of defects remains and pin the Fermi level at the surface CNL. However, high fluctuation of the H₂O molecules absorbing from the gas phase, might not fully saturate the surface with water as it is expected in the liquid electrolyte.

5.3 Low-temperature water adsorption on Si surfaces

In Section 5.2, the chemical reactivity of Si dangling bonds has been discussed in detail for highly reactive surfaces. In these experiments, water has been adsorbed at room temperature from the gas phase leading to high desorption rates. In a next step, the focus is placed on the electronic interaction of reconstructed and partially passivated surfaces as prepared and characterized in Section 5.1, including charge transfer mechanisms when defects are created or passivated due to the chemical and electronic interaction with the electrolyte. This might be indicated by a change of the energy band diagrams of the Si/adsorbate (electrolyte) contact showing the change of band bending, surface positioning of the Fermi level vs the bulk, and possible changes of the band edge positions. To increase the amount of water at the surface preventing desorption, the electrochemical interface of the Si surfaces with molecular water is investigated by low-temperature adsorption experiments using the “frozen electrolyte” approach.¹⁷⁶

5.3.1 Model experiment at the example of H-terminated p-Si(100) / H₂O

The first objective is to provide a thorough presentation of the H₂O adsorption model experiment, which uses the previously described well-defined dry H-terminated p-Si(100) surface (see Section 5.1.4). Strength and weaknesses of conducting low-temperature adsorption experiments is extensively examined and the conclusions that can be derived from them are discussed.

To enhance the sticking coefficient of H₂O molecules, the sample substrate is cooled using liquid nitrogen, resulting in a constant substrate temperature of $-176\text{ }^{\circ}\text{C}$. Ultrapure water from the gas phase is then gradually adsorbed using controlled water partial pressure and exposure time. A dose of 100 s at 1×10^{-8} mbar is considered equivalent to 1 L (Langmuir). Finally, the cooling process is stopped, and the sample returns to room temperature. XP survey and detail spectra are obtained, as well as high surface sensitive UP valence band spectra using monochromatic HeII emission with $h\nu=40.81\text{ eV}$, after each step. The O 1s and Si 2p core level lines are shown in Figure 5.14 after each step of the adsorption experiment. The H-terminated Si surface exhibits no emissions from O or C as shown in Section 5.1. The O 1s signal rises at about 533 eV when exposing the H-terminated surface step-wise to molecular water, indicating a molecular adsorption on the surface. Simultaneously, the Si 2p signal gets slightly damped by the adsorbate. The evolution of binding energy position of O 1s, Si 2p_{3/2} and the work function (WF) are shown at the bottom of Figure 5.14. The adsorption experiment can be divided into four regions as depicted accordingly:

- i) **Cooling:** The first region of the experiment involves cooling the sample without any exposure to water, which induces a core level shift in the Si 2p line due to a source-induced surface photovoltage (SPV). The SPV flattens the initial surface band bending of the p-doped wafer as has been discussed in detail in Section 5.1. In contrast to room temperature measurements, the reduction of the X-ray intensity from 300 to 10 W does not lead to a reduction of the source-induced SPV at liquid nitrogen temperature. This indicates a saturation of SPV even at very low excitation intensities and a remaining surface band bending of 0.17 eV (compare Figure 5.10, Section 5.1). Accordingly, source-induced SPV become one of the main weaknesses of the model experiment as low temperature PES measurements do not represent the thermodynamic equilibrium of charge carriers.
- ii) **Sub-monolayer adsorption:** The second region represents the initial adsorption of water in the sub-monolayer range ($<1\text{ L}$). In case of surface reactions during the initial contact with water, significant spectral changes are expected. In case of the present H-terminated surface, no spectral changes can be observed in the Si 2p line, indicating a chemically immune surface during low-temperature water adsorption. Furthermore, no shifts in the Si 2p emission can be observed, showing that the initial

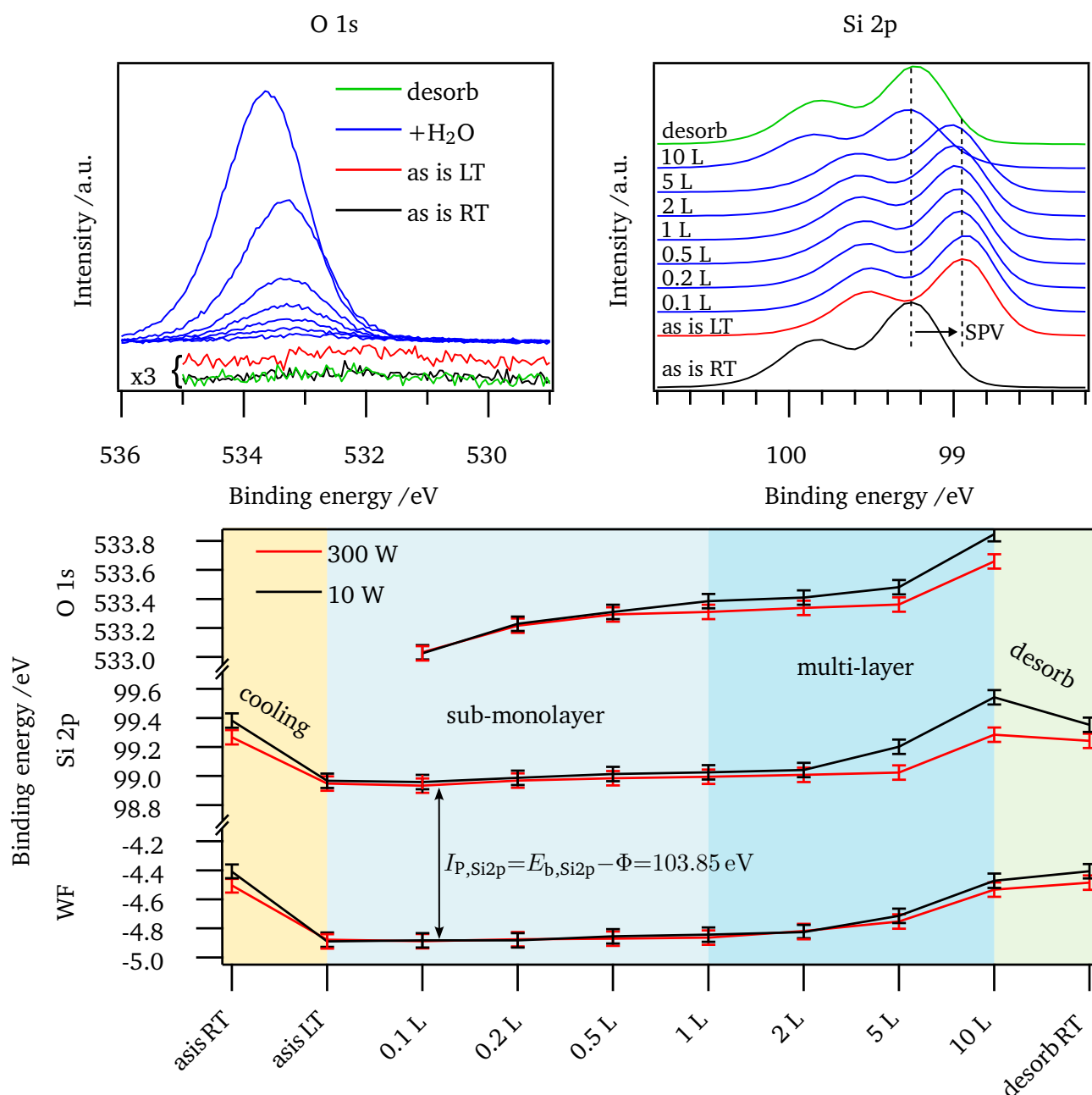


Figure 5.14: O 1s and Si 2p spectra at different exposures with water (top). Binding energy and work function according to secondary electron cutoff over water dosage are shown for using 300 W and 10 W X-ray source intensity (bottom).

surface band bending is not affected by adsorption of molecular water and the electronic interaction of the adsorbate with the Si substrate is rather low. In contrast, the O 1s line exhibits a slight shift of approximately 0.3 eV towards higher binding energies during monolayer formation, which could result from an electrochemical double layer formation or a charging effect of the adsorbing water molecules. The calculated WF, however, which was derived from the XPS secondary electron edge

(SEE) does not shift upon water adsorption and with that follows the Si 2p lines, meaning that the ionization potential of the Si 2p core level electrons $I_{P, Si2p}$ (given by the binding energy of the Si 2p_{3/2} line $E_{b, Si2p}$ and the ionization potential of the sample $I_P=5.11$ eV) is constant in contact with water. As a result, no surface dipole is detected confirming that there is no interaction of the Si substrate with the water molecules as a preferential water adsorption is expected to induce an overall surface dipole δ due to the electric dipole moment of the H₂O or adsorbed OH molecules. The shift in the O 1s line could therefore result from a charging effect of the water molecule or a forming ice multi-layer indicating an island growth mode of the adsorbate.¹⁷⁷

- iii) **Multi-layer adsorption:** In the multi-layer regime of the experiment, both the substrate-related Si 2p and the H₂O-related O 1s spectra exhibit clear shifts to higher binding energies, with the extent of the shift appearing to be dependent on the intensity of the probing X-rays. Here, a reduction of intensity leads to even higher shifts. Two contrary effects make the interpretation of these shifts not trivial. On the one hand, band flattening by SPV would lead to a downward shift in binding energy, while on the other hand potential charging of the water molecules could shift the O 1s line to higher binding energies. The shifts to higher binding energies by lowering the excitation intensity could consequently indicate an overall reduction of source-induced SPV. In contrast, the absence of any spectral changes in the Si 2p line does not support the hypothesis that there is a reduction in source-induced SPV resulting from interfacial defect formation. It is also unlikely that there is any loss in intensity due to additional X-ray absorption in the adsorbed water molecules, as X-rays can penetrate in the micrometer range and such thin ice layers do not cause significant X-ray absorption. It is more likely that the reduced source intensity might result in fewer secondary electrons that accumulate at the depleted p-type surface under illumination, which can finally compensate the emission of emitted photoelectrons in the ice layer. However, the exact origin of the substrate shifts in the multi-layer regime cannot finally be deduced by this experiments.
- iv) **Room temperature desorption:** In the final stage of the experiment, the cooling is stopped and the sample warms up to room temperature again. Analyzing the O1s line suggests that all water molecules desorb completely from the surface, with no remaining water, in either molecular or dissociative form. In addition, the Si2p line returns to its original binding energy position revealing a slightly broader appearance.

Based on the XPS data, the conclusion is that no electronic charge transfer occurred during the water adsorption experiment, indicating that no alteration in surface band bending was observed due to defect formation or passivation for this particular monohydrided Si(100):H surface.

To further study the effect of water adsorption, monochromatic UP valence band spectroscopy using the HeII ($h\nu=40.81$ eV) line is conducted as it is a useful technique for detecting adsorbate species and surface reactions because of its high surface sensitivity.¹⁷⁸ The valence band spectra of the low-temperature water adsorption experiment are depicted in Figure 5.15. As the water coverage increases, a distinct water feature emerges in the spectra, consisting of three features that can be assigned to the 1b₁ (6.5 eV), the 3a₁ (8.5 eV), and the 1b₂ (12.5 eV) highest occupied molecular orbitals of molecular water.^{24,179} Apart from the three water features, a surface feature emerges from 9.4 to 11.2 eV binding energy, which persists even after the total desorption of water. Even though, no O 1s signal is detected by XPS, this feature might be assigned to OH 1 π and 3 σ states, indicating partial OH adsorption.¹⁷⁹ Apparently, the 1 π feature appears with much lower intensity and at about 2 eV higher binding energy on the reconstructed Si surface than compared on the unreconstructed Si surface presented in Section 5.2. In contrast to the surface state feature due to the hybridization of H 1s and Si 3s orbitals at the K-point of the surface Brillouin zone appearing at similar energies,^{147,148} this feature is sharper and does not show a significant

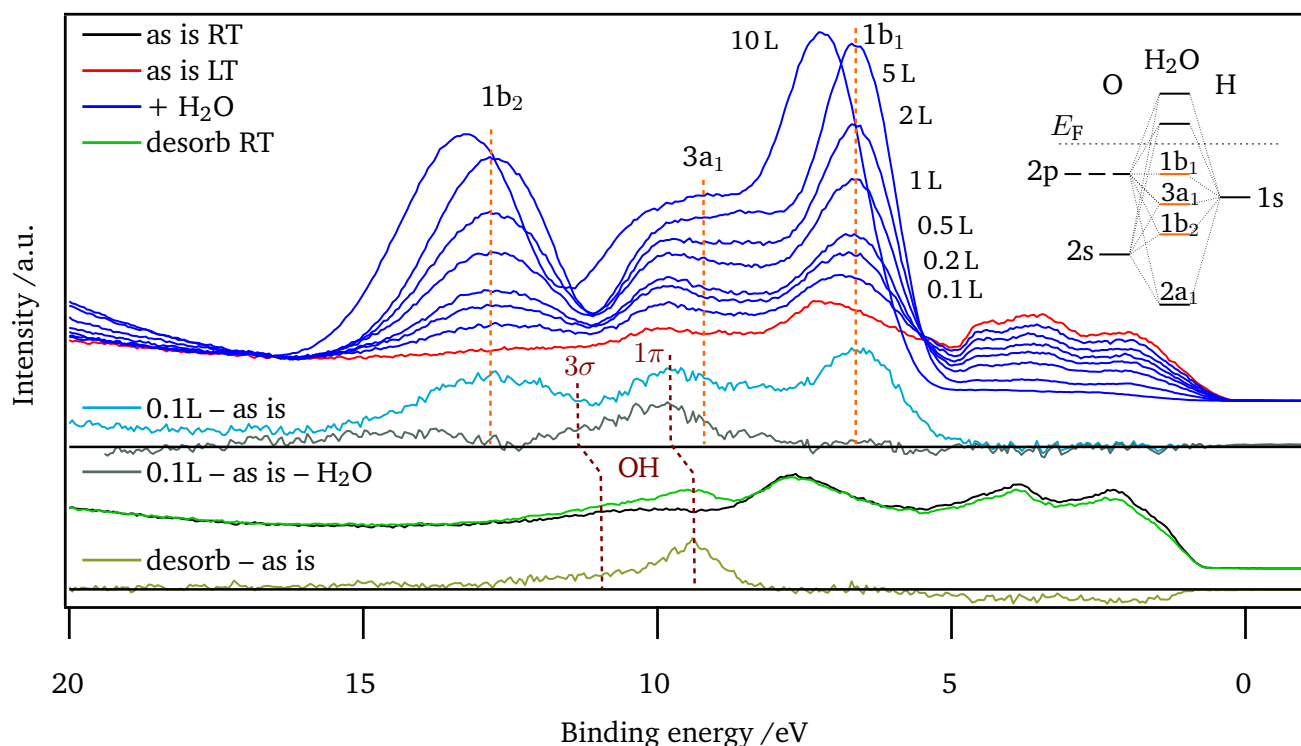


Figure 5.15: Monochromatic HeII UP spectra ($h\nu=40.81$ eV) of a low-temperature water adsorption experiment on Si(100):H. The three HOMO features of molecular water arise with increasing water coverage as depicted with the linear combination of atomic orbitals (LCAO) approach of the H₂O molecular states. Difference spectra show a surface state appearing at around 9.4 to 11.0 eV, which remains after the desorption of water. These states might be related to adsorbed OH species.

energy dispersion by conducting angular-resolved measurements. Furthermore, the intensity of the H resonance does not change (see Figure A3 in Appendix), which indicates no further hydration of the surface. However, the 2×2 LEED pattern forms into a 2×1 pattern after the desorption of water showing that the surface order decreases upon water adsorption (see Figure A3 in Appendix), which is also reinforced by the slightly broader Si 2p spectrum as observed by XPS. However, the initial surface band bending remains as the VB onset is not shifting and the Fermi level remains at the pinning position 0.6 eV above the VBM. Accordingly, no complete defect passivation is indicated by the adsorption of additional H or OH at unsaturated dangling bonds, even though partial OH absorption is observed. However, further dangling bond formation increasing the DOS at E_F even further cannot be ruled out since E_F coincides already with the CNL of dangling bonds as found in Section 5.1. In any case, it can be concluded from the adsorption experiment: Neither the Si dangling bond defects of this surface seem to be reactive upon water adsorption nor the water itself induces any additional electronic states within the Si bandgap since the initial surface band bending is not affected due to water adsorption. However, LEED images suggest that the structural ordering of the surface is reduced after the adsorption experiment which might increase the concentration of dangling bonds reinforcing the initial Fermi level pinning.

5.3.2 H₂O adsorption on treated Si surfaces

In the next step, the described model experiment is applied to oxidic, wet-chemically hydrogen terminated, and flash annealed Si surfaces as characterized in the previous section. In Figure 5.16 the O 1s and Si 2p

core level lines of the water adsorption experiments on the differently terminated Si surfaces are shown exemplarily for each termination type. The logarithmic dependence of the water adsorption on the VBM with respect to E_F is plotted as well.

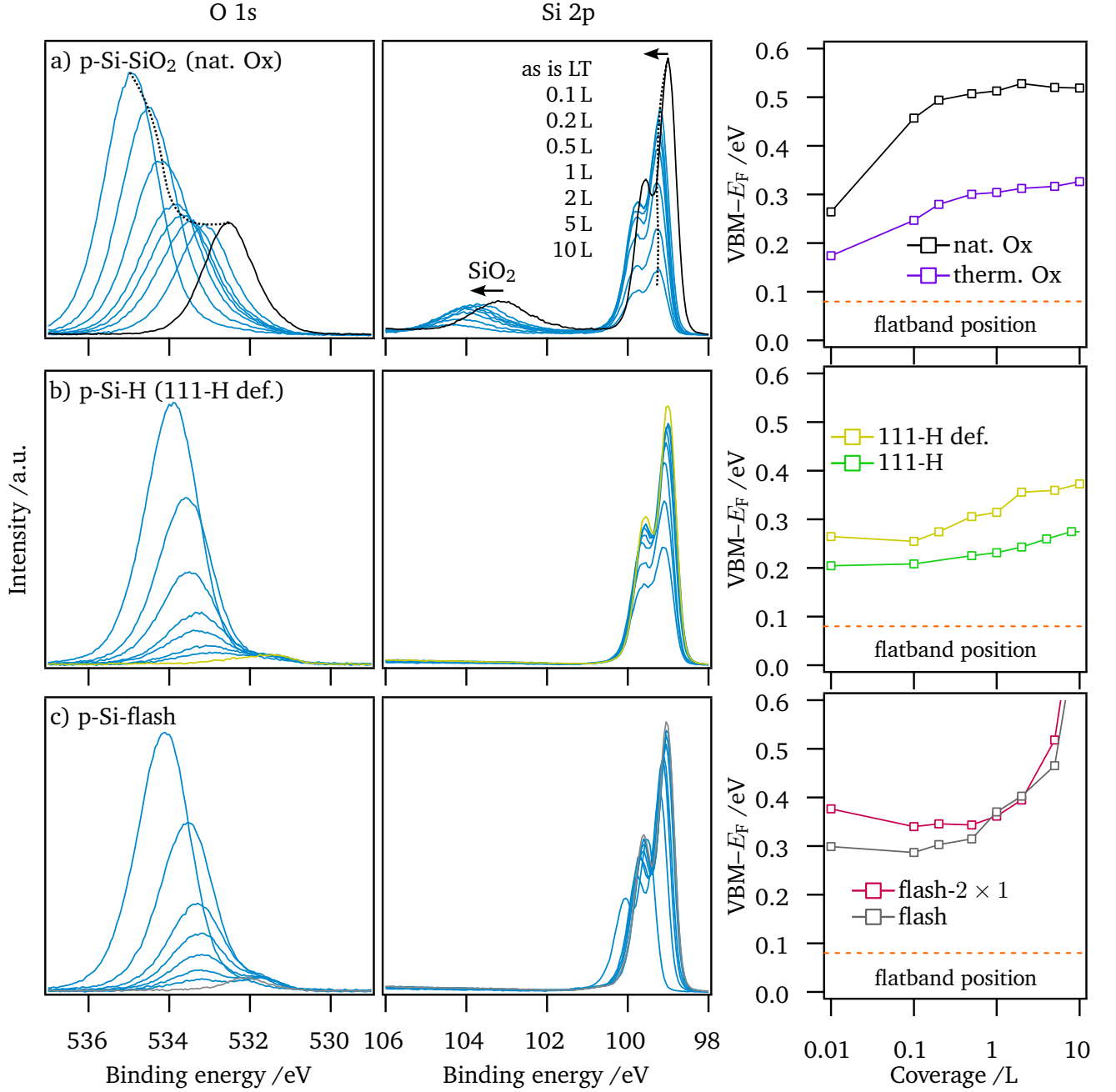


Figure 5.16: O 1s and Si 2p spectra of water adsorption experiments on prepared p-Si surfaces with one a) Si-O, b) Si-H, and c) Si-R termination each (left) with evolution of VBM over water coverage (right). Samples are prepared according to Section 5.1 with specifications given in Table A1.

The oxidic terminated surfaces in Figure 5.16a) clearly reveal a binding energy shift with the initial contact to water towards higher binding energies. The observed shift implies that the semiconductor/adsorbate interface experiences an increase in initial surface band bending when it comes into contact

with water, which results from an electron transfer from the interface into the Si SCR. Notably, the increase in band bending is more pronounced for the native oxide (with a shift of $\Delta E=0.25$ eV) than for the thermal oxide (with a shift of $\Delta E=0.15$ eV). In both cases, the largest shifts occur in the initial steps of adsorption, while it saturates in the multi-layer regime. In contrast to the clean 2×2 H-terminated surface, the energy shifts are therefore not related to a charging of the adsorbates, but indicate a real change in the electrochemical potential of the Si/SiO₂ surface. Additionally to the shift in the crystalline Si 2p contribution, the oxide related Si 2p component shows significantly larger shifts of up to 1 eV during the adsorption experiment, indicating the formation of a surface dipole. Furthermore, the O 1s line reveals a chemical shift of the oxide-related SiO₂ component at about 532 eV to the water-related multi-layer at about 534 eV. Nevertheless, the SiO₂ contribution of the O 1s line also shifts to higher binding energies at the presence of water as equally seen in the SiO₂ component of the Si 2p spectra. Following the line of argumentation, it cannot finally be deduced, if this shift is due to a dielectric potential drop results from a charging of the multi-ice layer or due to a charge transfer from adsorbates into the Si SCR. Additional bias light using the HeII excitation, reveals that the SiO₂ component is further shifting, while the metallic Si 2p component remains constant reinforcing that adsorbate charging plays a role, even though a double layer formation that is independent of the photo excitation might occur in addition (compare Figure A4, in the Appendix).

The wet-chemically terminated Si (111) surfaces in Figure 5.16b) also reveal energy shifts when coming into contact with water. In contrast to the oxide terminated surfaces, the shifts are clearly smaller ($\Delta E < 0.1$ eV). Especially the initial contact with water does not lead to appreciable energy shifts. As there is no saturation observed in the multi-layer regime, these shifts might be related to charging effects as already observed for the contaminant free monohydrided 2×2 Si surface shown in the previous section. Nevertheless, one might note that the “defective” surface (yellow) reveals slightly larger shifts than the “intact” surface (green) indicating a slightly higher interaction with the adsorbates.

Rather different is the situation on the flash-annealed surfaces in Figure 5.16c). Here, an extremely strong charging effect is observed in the multi-layer regime with shifts of up to 0.8 eV at 10 L. As these samples reveal the highest defect concentration with the highest recombination rate, the high initial band bending leads to very low conductivities in reverse direction of the depleted surface. The high surface recombination rates at these surfaces prevent the accumulation of excited secondary photoelectrons compensating the photoholes in the adsorbate during the measurement. Consequently, the highly defective surfaces are inappropriate to investigate charge transfers, as the Fermi level is pinned anyway.

The influence of bulk doping on charge transfer behavior

Since there is an evident electron transfer from the p-Si/SiO₂ terminated surface into the Si SCR, the question arises, whether this electron originates from an occupied state and where it is located. To address this query, the experiments shown above were repeated on n-type surfaces, which were equally prepared as the p-type surfaces before.

Figure 5.17 shows the low-temperature adsorption experiments on n-type wafers. The results are similar to the experiments performed on the p-type wafers. Again, the oxide terminated surfaces reveal an energy shift to higher binding energies at the initial contact to water. Here, both surfaces form an electron accumulation layer with no difference whether they initially start from a slight electron depletion (therm. Ox) or flat band conditions (nat. Ox). In both cases, the Fermi level shifts into the CB and finally pins at the CBM due to the high DOS at the band edge. Furthermore, the Si 2p_{3/2} shows no further shifts in the multi-layer regime reinforcing that no charging occurs in the Si SCR. The total energy shift of the thermal oxide terminated sample is with about $\Delta E=0.15$ eV the same as found on the p-type sample. Due to the higher initial Fermi level on the native oxide terminated surface, the total energy shift of

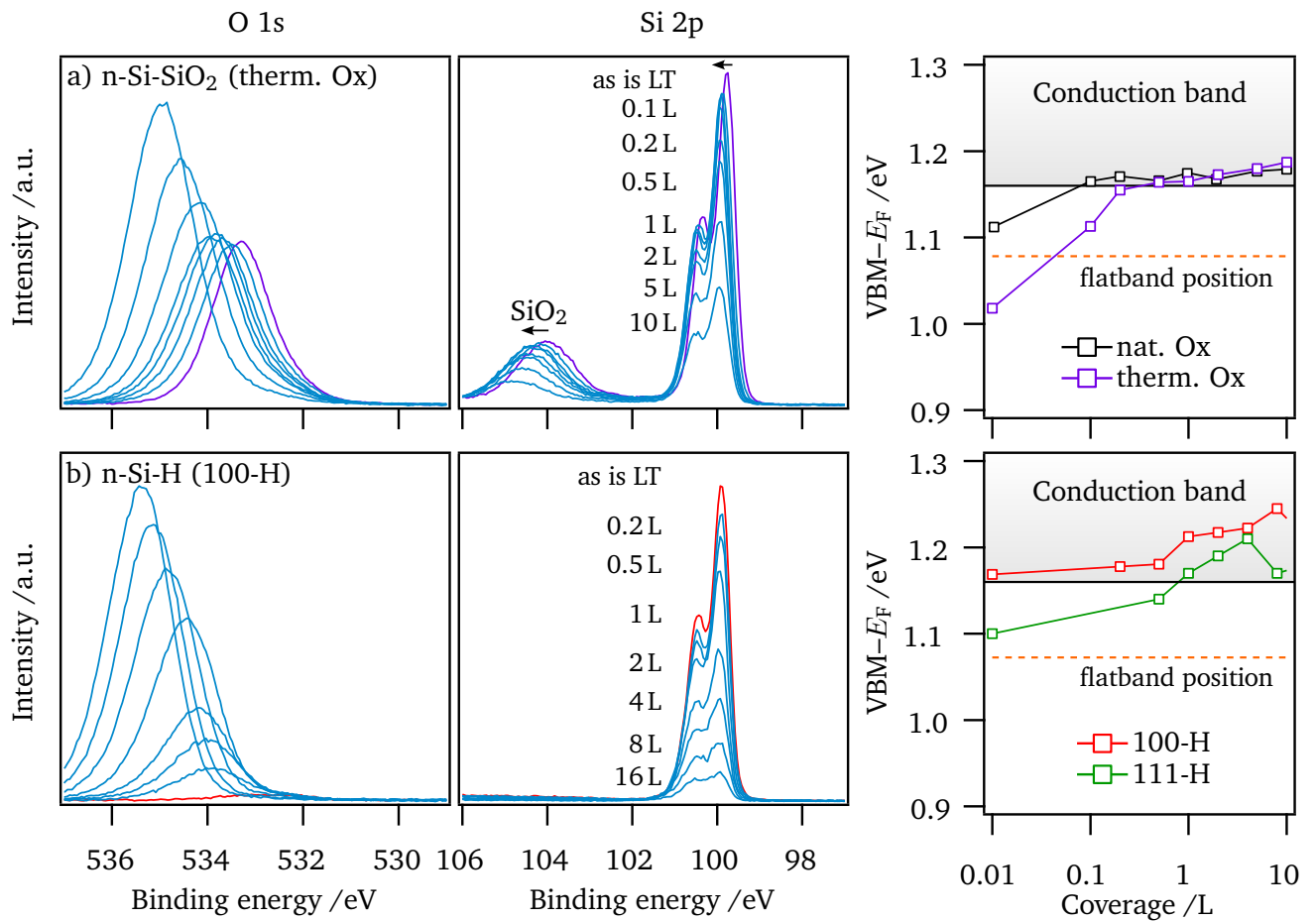


Figure 5.17: O 1s and Si 2p spectra of water adsorption experiments on prepared n-Si surfaces with a) Si-O and b) Si-H termination (left) with evolution of VBM over water coverage (right). Samples are prepared according to Section 5.1 with specifications given in Table A1.

$\Delta E=0.05$ eV is limited by the Fermi level pinning at the CBM. The potential drop in the oxide layer seems to be independent of the bulk doping and increases up to 1 eV. In any case it can be concluded that for both p- and n-type samples, electrons from the Si/SiO₂ interface are injected into the Si SCR, which requires that they have to come from an energy state, which is located above CBM.

Interestingly, the wet-chemically H-terminated surfaces reveal similar behaviors. In the sub-monolayer regime, the (111) surface experiences a slight upward shift in binding energy until the Fermi level gets pinned at the CBM as observed for the oxide terminated samples, indicating again an electron injection into the SCR upon the first contact to water. In contrast to that, the Fermi level of the (100) surface is initially pinned at CBM instead, which prevents further upward binding energy shifts. In the multi-layer regime (>1 L) however, both H-terminated samples again show further binding energy shifts, which again suggest a sample charging. This is surprising as the electron accumulation actually should lead to a metallic behavior of the Si-H/H₂O interface. The broadening of the Si 2p features seen in Figure 5.17b) for high coverages also reinforces the hypothesis of charging, as after desorption the Si 2p regains its initial shape.

5.3.3 Origin of electron injection into Si substrates

The XPS results above clearly reveal an indication for an electron injection at the interface of the Si surfaces in contact to the frozen electrolyte. This injection was found to be independent of bulk doping and more pronounced on oxidic terminated than on wet-chemically H-terminated surfaces. This raises the question of where these electrons come from and what reaction mechanisms are involved. In order to address this question, HeII valence band spectra are analyzed.

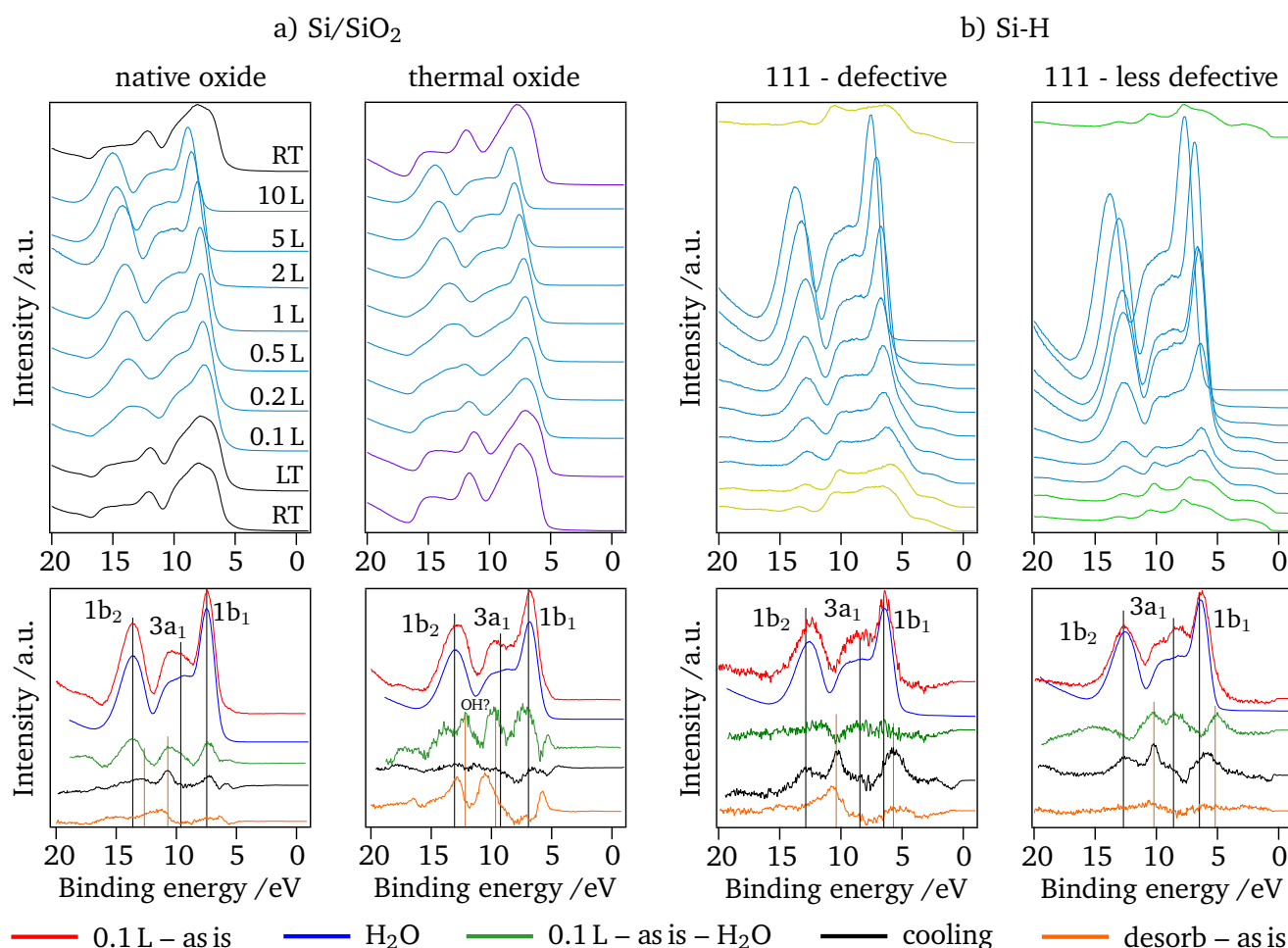


Figure 5.18: Monochromatic HeII ($h\nu=40.81$ eV) UP spectra of water adsorption on a) Si/SiO₂ and b) Si-H terminated Si surfaces. The bottom spectra show differences after first adsorption step (red), pure ice (blue), first adsorption step subtracted with molecular water spectrum (green), after cooling (black), and after desorption (orange).

Figure 5.18 displays the HeII valence band spectra of the electrochemical interfaces of a) Si/SiO₂ and b) Si-H with water. The adsorption experiment on the flashed surfaces c) Si-R is shown in Figure 5.19. The characteristic water signature already appears for all samples, after only the initial water coverage of about 0.1 L, suggesting primarily molecular adsorption of water. The spectral changes after certain adsorption steps are apparent in the difference spectra at the bottom. The green spectra represent the differences in the valence band spectra after the adsorption of 0.1 L H₂O, with the molecular water structure subtracted. Additionally, the spectra after cooling (black) and after desorption (orange) are

shown as spectral differences. The sample is cooled at base pressures of around 5×10^{-10} mbar, which leads to a small but observable amount of water adsorption. Taking into account a partial water background of approximately 1×10^{-10} mbar, a water dosage of 0.1 L can be achieved in about 15 min. Except for the three H₂O HOMO features labeled with black bars, hardly any other spectral changes can be seen. From Section 5.2 it is known that the 1π and 3σ features at about 6.50 and 11.25 eV below the VBM indicate present Si–OH species. On the thermal oxide terminated Si in a), two additional features appear in the difference spectra after the first adsorption step at binding energy of 9.8 and 12.2 eV (green) and is similar to the surface states observed on the reconstructed Si(100):H(2×1) surface. They remain after desorption (orange), which might be again attributed to Si–OH species chemically shifted by the oxygen backbond environment in SiO₂ compared to clean Si surfaces.^{24,180} However, it is reported that OH species on SiO₂ surfaces are hard to observe by UPS measurements,¹⁸¹ although dissociative water adsorption has been reported by Nishijima et al.¹⁸² based on high-resolution electron energy loss spectroscopy (HREELS) measurements. Furthermore, the 1π and 3σ separation is only 2.4 eV and with that lower than the typically observed range of 3.7 to 5.4 eV.¹⁸³ These features are less prominent in the difference spectra of the native oxide than for the *in situ* thermal oxide, as it was prepared *ex situ* and could already be hydroxylated by ambient air. In any case, if these features really indicate the hydroxylation of the oxidized surface, they do not correlate with the electron injection observed upon water adsorption.

The wet-chemically prepared H terminated Si-H surfaces also show two additional features apart from the molecular ice spectrum at 5.8 and 10.4 eV, which could also indicate traces of Si–OH backbonded to Si.^{24,184} As traces of water even adsorb during cooling, the difference spectra after cooling (black) reveals the most significant differences. However, the possible OH related features disappear again after desorption from the less defective sample, while the defective sample still reveals OH traces after desorption.

The observations on the flash-annealed Si-R samples upon water adsorption are rather similar to those on the Si-H samples (Figure 5.19). The as flashed sample on the left shows some indications of further hydroxylation, particularly after desorption (orange), while the spectral changes for the 2×1 surface are almost negligible.

All UP spectra mainly show molecular water adsorption. Minor spectral indications for traces of hydroxy formation due to dissociation can be found on almost all surfaces. However, the hydroxylation is far from a monolayer formation, reinforcing that structural defects such as vacancies or steps are necessary

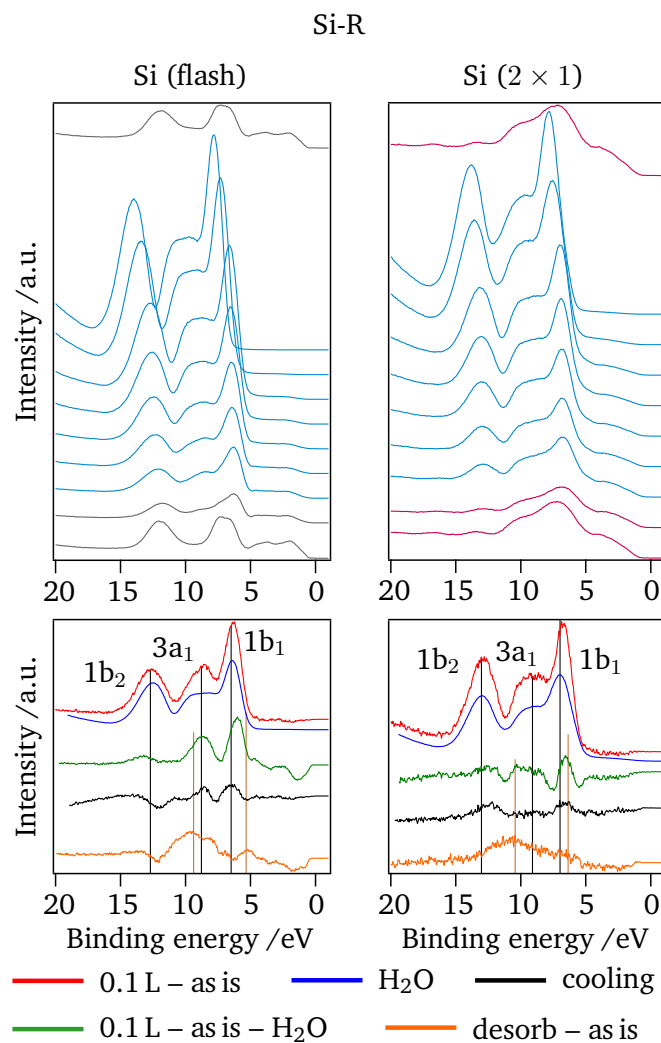
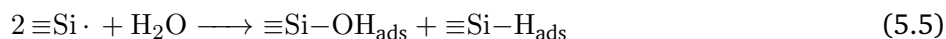


Figure 5.19: Hell UP spectra of water adsorption on Si-R terminated Si surfaces.

for water dissociation.^{24,185} The observation of increasing downward band bending on the oxidic and wet-chemically H-terminated surfaces upon water adsorption suggests that electrons are injected from the adsorbate interface into the Si substrate. The UP valence band spectra indicate that the HOMO of molecular water (1b₁) is about 7 eV below the substrate's Fermi level, making it unlikely to directly act as a donor by injecting an electron from its orbitals. The interaction between the surface and water is highly dependent on the quality of surface termination as quantified by the initial band bending, suggesting that the mechanism of electron injection upon molecular water adsorption is likely to be mediated by surface states or defects. However, the lack of electronic interaction on the dry-physical H₂-annealed H termination as well as the flash-annealed surfaces suggests that oxygen related defects such as vacancies are necessary for the electron transfer to occur. The wet-chemically prepared H termination, which showed a minor shift in binding energy, may have contained oxygen-related surface states as discussed in Section 5.1 that facilitated the electron injection. The large shifts observed on oxidic terminated surfaces further support this hypothesis. The largest shift is observed on the native oxide, as this surface fulfills the requirements of oxygen-related surface defects and a higher density of surface states compared to other terminations. In the previous section, it was demonstrated that the primary defect centers at Si surfaces are dangling bonds, known as P_b centers. It is therefore suggested that only polar backbonded dangling bonds will interact with water by inducing electrons, which necessitates a partial oxidation of the defect as explained in the Section 5.1. As less than 1 % of surface atoms are expected to contribute to surface defect states, it is difficult to directly observe spectral changes that indicate the origin of electron injection in the UP spectra shown above. Consequently, conclusions about surface defect chemistry can only be drawn from shifts in the Fermi level. Based on these observations, two reaction mechanisms are considered, which could occur when molecular water comes in contact with the dangling bond defect center ($\equiv\text{Si}\cdot$). First, the dissociation of H₂O, which requires two neighboring active sites to bind both dissociation fragments OH_{ads} and H_{ads} on the surface:



In case of reaction mechanism 5.5, the electronic activity of the dangling bond center would be passivated by the adsorbed hydrogen and hydroxyl groups forming bonding orbitals below the Si bandgap. As a consequence, the defect passivation would lead to a flattening of downward surface band bending on the p-Si, contradicting the observed increase of surface band bending upon water adsorption. In Section 5.2, it was shown that the energy levels of chemisorbed OH or H species is too low ($E_b > 6 \text{ eV}$) to ionize them for an electron transfer reaction. For that reason, the injection of electrons into the surface is proposed to be caused by the adsorption of the intact water molecule. In that case, an isolated dangling bond binds water molecularly tentatively by the oxygen lone pairs of H₂O as already proposed by Takagi et al.¹⁸⁵. The lone pair interaction with the dangling bond defect causes a splitting of bonding and anti-bonding orbitals. One electron from the dangling bond state and one electron from the H₂O lone pair occupy the common bonding orbital, while the second lone pair electron occupies the anti-bonding orbital located above the CBM. This electron is then lifted in energy above the CBM, which finally leads to a transfer into the Si conduction band and thus into the space charge region of the Si. This leaves the bonded water molecule as an ionized donor at the surface as similarly proposed by Mayer et al.¹⁸⁶:

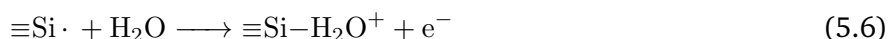


Figure 5.20 illustrates an LCAO approach for the proposed electron injection mechanism according to Equation 5.6. It is evident that this type of electron injection into the Si CB only occurs when no unoccupied states below the CBM remain at the surface. This is consistent with the findings from Section 5.1, which showed that this is only the case for partially oxidized P_b-centers. This might be another reason why the

charge transfer upon low-temperature water adsorption is predominantly observed on oxidized surfaces. The difference spectra showed on almost all surfaces the biggest differences at about ≈ 10 eV. It is therefore quite possible that this difference is partially contributed by an adsorbed water molecule in the vicinity of a dangling bond shifting the $1b_1$ orbital towards higher binding energies when forming bonds to the undersaturated Si site.

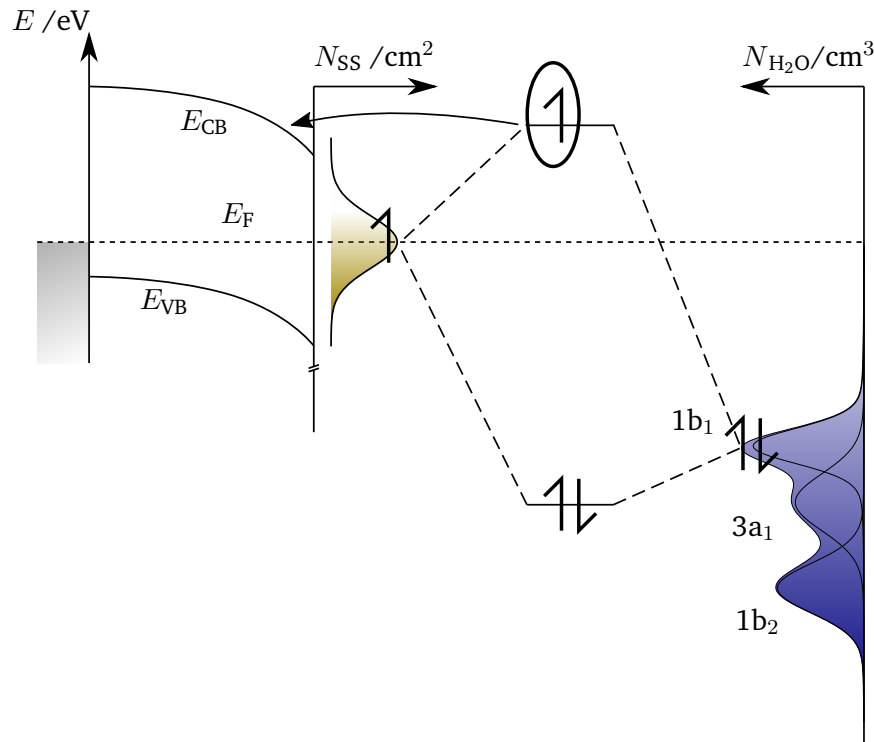


Figure 5.20: LCAO scheme of molecular water forming bonding and anti-bonding orbitals with the Si dangling bond surface defect. The additional electron from the anti-bonding orbital is injected in the Si space charge region leaving the ionized water molecule at the surface.

In addition, the shift of the SiO_2 -related component of the Si 2p spectra, which is equivalent to the shift of the SEE, is larger than the shifts observed in the crystalline component related to the SCR. This indicates a changing surface dipole moment and with that a change in ionization potential. The observed shift of $\Delta\delta \approx 0.1$ eV in the submonolayer region suggests the presence of ionized water molecules at the surface. The mechanism for the ionization, whether it is due to charge transfer upon bond formation or source-induced charging by the emission of photoelectrons, cannot be fully elucidated by these experiments. Despite not expecting charging in the monolayer range (Figure 5.14), the oxide layer may still impede charge compensation in the adsorbate even in the monolayer regime.

However, further experimental as well as theoretical studies are necessary to confirm this proposed model and to fully reveal the underlying mechanism of electron injection upon water adsorption on Si surfaces.

5.3.4 Conclusion and energy band diagrams

In this Section, the low-temperature model experiment of the semiconductor/electrolyte interface was presented. The results show that this type of model experiment reaches a qualitative problem when assuming thermodynamic equilibrium condition, which might lead to misinterpretation in similar studies.^{177,183,187} The model and methodology of low-temperature adsorption experiments induces further questions such

as the influence of temperature effects,¹⁸⁸ the effect of excited charge carriers^{155,160} or inhomogeneous field effects due to adsorbate charging,¹⁶¹ which have only been addressed by a few incoherent studies yet.

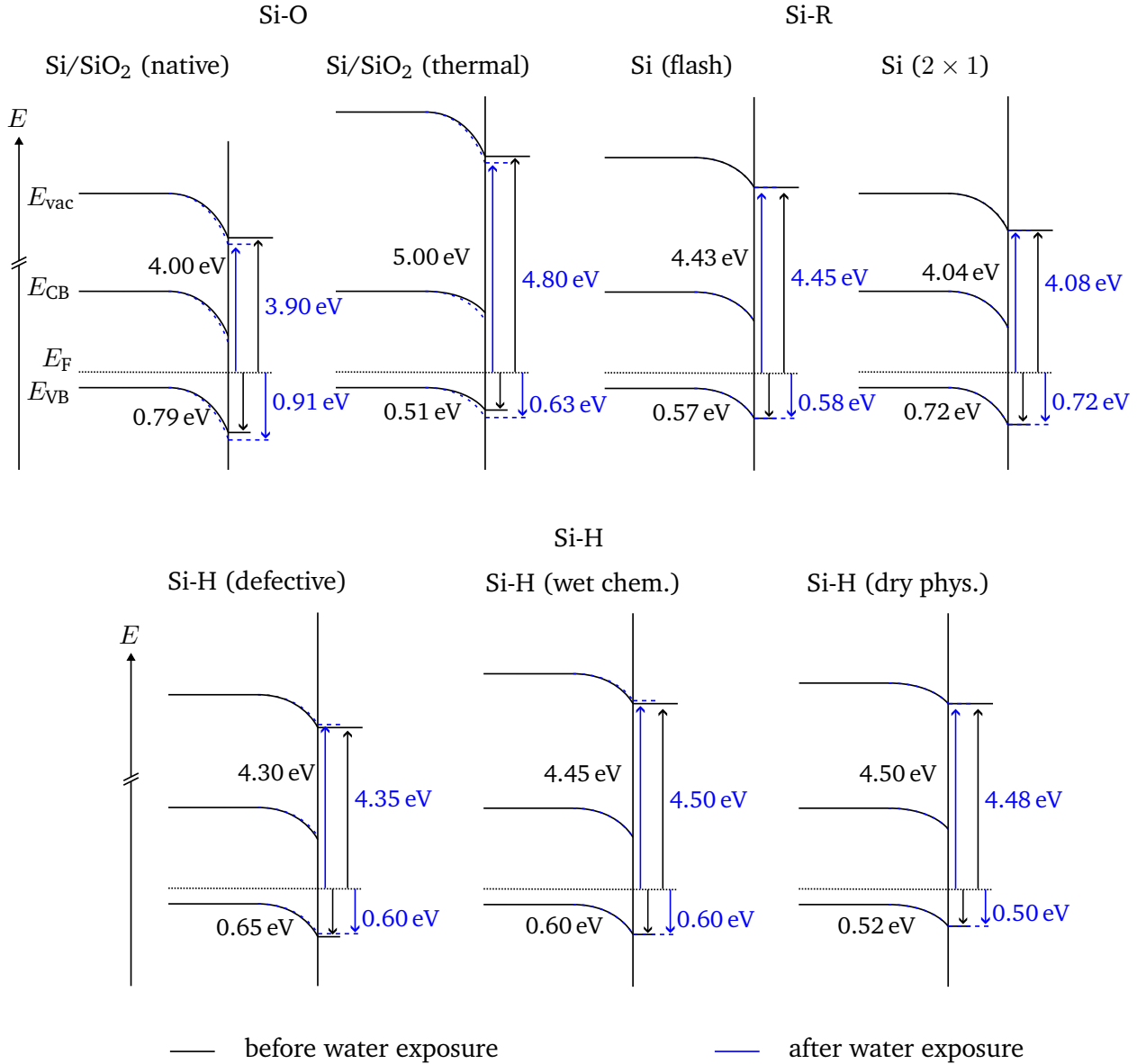


Figure 5.21: Band energy diagrams of p-doped Si with Si-O, Si-R, and Si-H terminated surfaces before (black) and after the water adsorption experiment (blue) with depicted measured values $VBM-E_F$ and WF with sample specifications given in Table A1. Only the oxidic terminated surfaces show an increase of band bending remaining after the desorption of molecular water.

To summarize the effects of molecular water adsorption on p-Si surfaces with different surface passivation, a comparison of band energy diagrams at room temperature before and after the adsorption experiments is presented in Figure 5.21. The observed change in surface band bending upon contact with water is only observed for the oxidic terminated surfaces indicating an electron transfer into the Si SCR showing that the charge transfer process during the adsorption experiment is not fully reversible after the

desorption. The WFs, determined from XPS SEEs closely follow the Fermi energy, revealing that there is no significant change in the surface dipoles (δ) upon water adsorption. As charge transfer mechanism, molecular water adsorption at isolated P_b centers via the oxygen lone pair of H_2O is proposed. The single occupied antibonding orbital combination is consequently lifted above the CBM and induces its electron into the CB. This mechanism requires on the one hand a positive adsorption enthalpy when the molecular orbitals overlap. On the other hand, the dangling bond should only be singly occupied with no acceptor states inside the bandgap, since the acceptor state would aspirate the excess electron preventing the charge transfer into the Si CB. These requirements are only fulfilled for fully or partially oxidized P_b centers.

5.4 Contact formation of Si with Pt catalyst

So far, surface states of Si and their interaction and reactivity with molecular water were discussed. However, the real photoelectrochemical device structure requires an adequate catalyst for an efficient cell reaction process. For the device performance with low overpotentials, the electric coupling of the catalyst is essential in order to maintain the loss minimized charge transfer from excited charge carriers in the photoabsorber into the catalyst phase. Pt is an expensive but well known catalyst for the cathodic hydrogen evolution reaction (HER). As free H^+ protons in an acidic electrolyte are reduced to H_2 gas, light-induced electrons need be transferred to the catalyst in order to run the reaction.

To investigate the electronic coupling, the formation of the Si/Pt interface is examined first. Next, the water adsorption behavior of the heterojunction is investigated, followed by testing the photoelectrochemical performance in a three-electrode setup.

5.4.1 The Si/Pt interface energetics

In order to investigate the Si/Pt interface formation, Pt is step-wise deposited onto a native oxide terminated p-Si (100) wafer using a direct current (DC)-magnetron sputter process (see Section 4.4.1 for details). According to profilometry step edge line scans, the deposition rate is determined with a value of 2.3 nm min^{-1} . It should be noted that in this experiment five different but equal substrates have been deposited within the same process.

Figure 5.22 shows the core level shifts of the crystalline (c-Si) and SiO_2 related Si 2p, the SiO_2 related O 1s, and the Pt related Pt 4f core levels for the initial Pt deposition steps. From the peak maxima, the core level shifts were derived after each deposition step shown at the bottom.

All spectra clearly reveal shifts towards lower binding energies after the contact formation. Initially, the Si $2p_{3/2}$ is found at 99.51 eV, which is equivalent to a Fermi level position of 0.77 eV above the VBM indicating an initial surface band bending of 0.51 eV due to oxide-related donor states as extensively discussed in Section 5.1.3.

After the Pt deposition, the Si $2p_{3/2}$ shifts to $E_b(\text{Si } 2p_{3/2})=99.11 \text{ eV}$, resulting in a slightly remaining band bending of 0.11 eV. However, it is clearly observed that the SiO_2 related core levels shift by about $\approx -1.0 \text{ eV}$, while the Pt $4f_{7/2}$ shifts by -0.6 eV with increasing film thickness to its well known metallic value of $E_b(\text{Pt } 4f_{7/2})=71.1 \text{ eV}$.^{189,190} For the initial deposition steps, an additional Pt species arises at $E_b(\text{Pt } 4f_{7/2})=72.2 \text{ eV}$, which could either indicate Pt–Si^{189,191} or Pt–O^{192–194} bond formation. According to the SEE, the WF of the clean p-Si (100) surface is found to be $WF_{\text{Si/SiO}_2}=4.1 \text{ eV}$. For the thick Pt layer, a value of $WF_{\text{Pt}}=5.3 \text{ eV}$ was found (while E_F was found to be at $E_b=0.0 \text{ eV}$), which is slightly below the values reported in literature ranging from 5.4 to 6.4 eV.^{195,196} However, the contact potential, which is given by the difference in workfunction of both surfaces, is therefore at least $\Delta WF=1.2 \text{ eV}$. As described

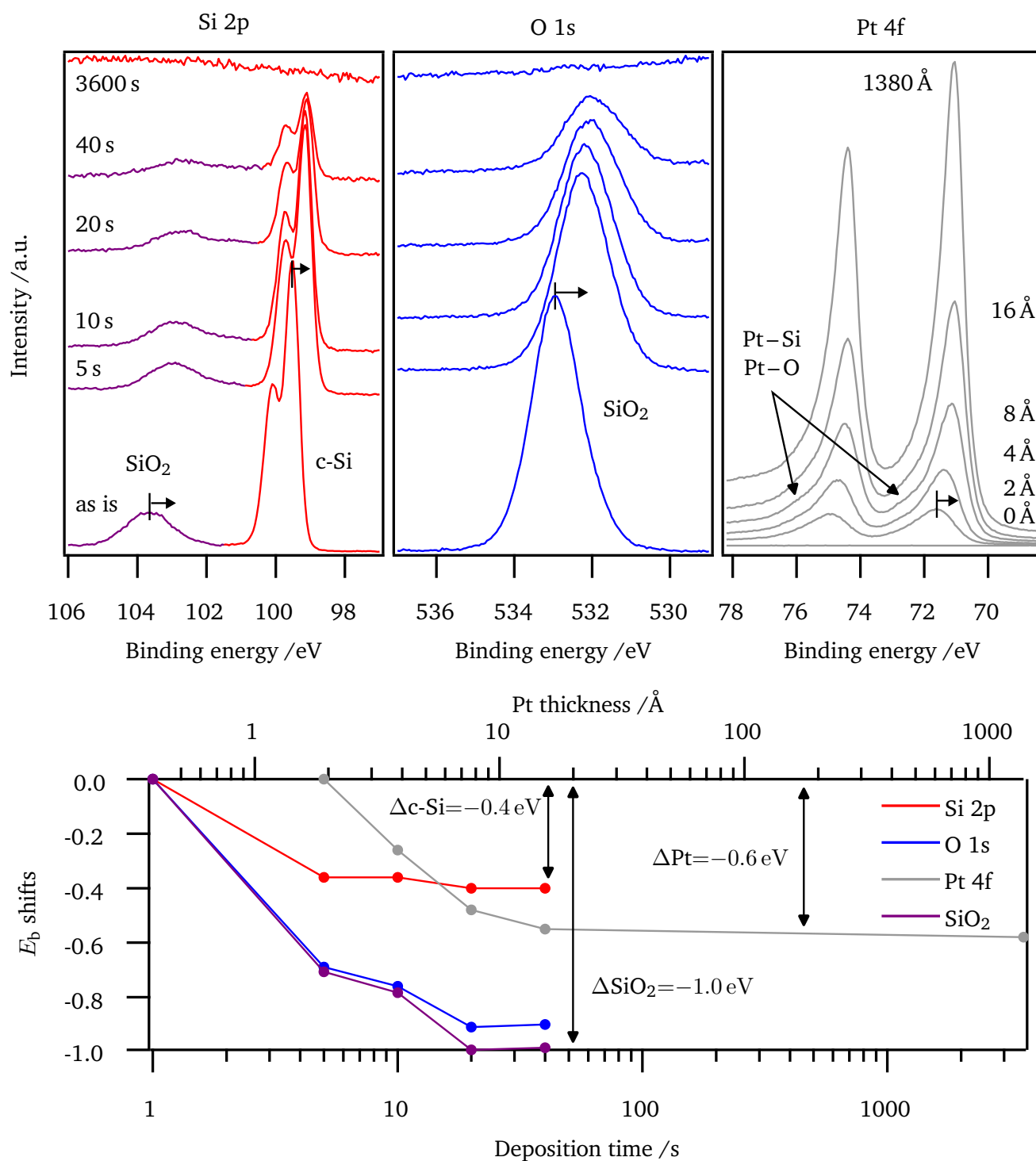


Figure 5.22: XP core level spectra of Si 2p, O 1s, and Pt 4f at the p-Si/Pt interface experiment after each sputter deposition step (top). The shifts in binding energy E_b represent the potential drop in the Si SCR and the SiO₂ interlayer.

above, 0.4 eV of the contact potential drops in the Si SCR. An additional potential of about 0.6 eV (1.0 eV total SiO₂ shift subtracted by 0.4 eV substrate shift) is dropping in the interfacial SiO₂ layer. For these low coverages of metallic Pt, the Pt components are referred to the substrate E_F of the p-Si. The potential drop in the SiO₂ interlayer is therefore shifting the Pt 4f by the same value (0.6 eV). It should be noted that for the initial Pt deposition steps, size effects of the Pt might also affect the binding energies in Pt clusters. However, binding energies in metallic Pt clusters are expected to be smaller than in bulk Pt while here, the binding energy increases with decreasing layer thicknesses.¹⁹⁰ Secondary electron microscopy (SEM) analysis could not resolve the initial deposition steps indicating a flat and homogeneous covering of the multi-crystalline Pt layer.^{197,198}

For an ideally passivated, defect-free interface, the contact potential of the Si/Pt interface is large enough to fully accumulate holes at the p-type Si substrate, therefore shifting E_F into the VBM as the ionization potential of the Si wafer $I_P(\text{c-Si})=5.2 \text{ eV}$ ²⁹ is lower than the Pt work function. This is not the case though, as E_F remains 0.37 eV above the VBM, indicating Fermi level pinning due to defect formation.

Potential corrected line shapes

In order to verify the potential distribution and to deconvolute electronic and chemical shifts, the line shapes of the SiO₂ related contributions can be analyzed assuming that the potential across the SiO₂ layer drops linearly as expected according to its dielectric properties. The used model has been presented in Section 4.1.2. The O 1s line was used as line shape for the potential correction at the Pt/Si interface. The thickness of the native oxide layer of the bare wafer d was determined according to Equation 4.2 as 8 Å. The fitting routine reveals an potential drop δ of -1.0 eV when using the O 1s line shape of the native wafer, the substrate shift of -0.4 eV due to a change in band bending, and the $\lambda_{\text{IMFP}}(\text{O } 1s) \approx 29 \text{ Å}$

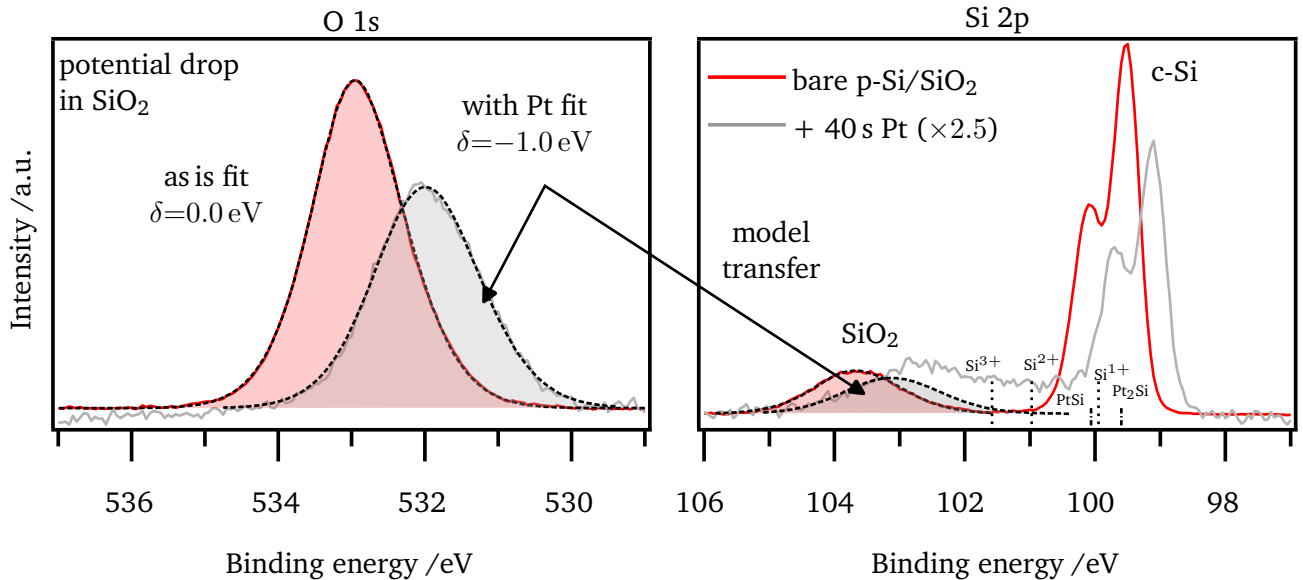


Figure 5.23: Fit of contact potential drop at Si/Pt interface along the SiO₂ interface layer according to the model presented in Section 4.1.2. Fitting the Shirley background subtracted O 1s of bare SiO₂ line shape (red) into interfacial SiO₂ core level (grey) reveals a potential drop δ of 1.0 eV. Applying the same model to the SiO₂ related Si 2p spectrum indicates additional suboxidized Si species.

in the SiO₂ matrix⁹⁶ (Figure 5.23). It should be mentioned that λ_{IMFP} might get reduced when adding Pt as top layer. However, the differences of considering $\lambda_{\text{IMFP}}(\text{O } 1s) \approx 13 \text{ \AA}$ in a Pt matrix are negligibly low ($< 0.1 \text{ eV}$). Consequently, the total contact potential of this specific p-Si/Pt interface is 1.4 eV, where about 0.4 eV is dropping in the Si SCR and about 1.0 eV is dropping in a dipolar layer over the interfacial oxide layer. Considering a simple plate capacitor model, the total charge per area $\frac{Q}{A}$ accumulating at each side of the SiO₂ interlayer is given by Equation 5.7 with $\epsilon_{\text{SiO}_2} = 3.9$:¹⁹⁹

$$\frac{Q}{A} = \frac{1}{2} \epsilon \epsilon_0 \frac{\delta}{d} = 1.3 \times 10^{-13} \text{ cm}^{-2} \quad (5.7)$$

The high interface charge concentration compared to the bare surface state charges Q_{SS} observed on bare Si/SiO₂ wafer,^{200,201} indicates additional defect formation when the Si/SiO₂ substrate comes into contact with metallic Pt.

Transferring the same model, including the potential drop of -1.0 eV to the SiO₂-related Si 2p line shape shows that the fit suits well at the high binding energy flank, but fails for the lower binding energy region. The constant signal between the SiO₂ and c-Si components hints at sub-oxidized Si species with oxidation states below +4 indicating additional defect formation at the interface.

The interdiffusion of Pt into Si is a well-known phenomenon observed at Si/Pt interfaces²⁰² and even occurs at room temperature.²⁰³ The more pronounced Si 2p_{1/2} peak at the Si/Pt interface is therefore superimposed by Pt₂Si and PtSi contributions. However, the constant signal at even higher binding energies indicate further sub-oxidized Si species, suggesting a chemical reduction of the SiO₂ interlayer during the interface formation. The raw area relation of O 1s to Si 2p shows a reduction by absolutely 5 %, which might indicate a removal of oxygen by the sputter deposition process. Oxygen is known to be preferentially sputtered on SiO₂ surfaces.^{204,205} However, as the working distance from the sputter target is rather high (20 cm), ion bombardment on the Si substrate is an unlikely process. According to the stoichiometry considerations presented in Section 4.1.1 it is assumed that the changing damping factor due to the added Pt with $\lambda_{\text{IMFP}}(\text{Pt}) < 0.5 \lambda_{\text{IMFP}}(\text{SiO}_2)$ leads to an underestimation of oxygen content when getting covered by metallic Pt.

From PtSi synthesis it is known that oxygen is detrimental and binds preferentially to the Pt side.^{203,206} Furthermore, Pt needs to diffuse through the SiO₂ passivation layer, which might lead to a formation of a mixed Pt_xSiO_y reaction compound, e.g. containing Pt_xSi and PtO_y phases. This would be in good agreement to the additional Pt species found in the Pt 4f core level as shown in Figure A5 in the Appendix.^{192–194}

All in all, the interface formation to Pt leads to an interdiffusion of Pt atoms which might induce additional defect states, which is indicated by Fermi level pinning in the lower half of the Si band gap.

Electronic defect distribution at Si/SiO₂/Pt interface

To understand the defect distribution at the Si/SiO₂/Pt interface, surface defects and Pt interface defects need to be considered and compared to the present data. From Section 5.1, it is known that a reduced SiO₂ layer is not capable to passivate the crystalline Si surface, thus indicating oxidized Si dangling bonds. Oxidized P_b centers form only donor-like states at the Si/SiO₂ interface. The pinned Fermi level 0.37 eV above the VBM coincides therefore with the donor level of an Si₂O≡Si· defect, which is expected 0.4 eV above the VBM.¹⁴² As there is an equally high indication for Si²⁺ and Si³⁺ showing their defect levels above mid-gap (see Section 5.1), these defects might be depleted by the higher WF of the Pt contact layer and the p-Si substrate bulk.

In addition, the interdiffusion of Pt into the Si wafer is a frequently observed phenomena and is related to “deep level” impurities.²⁰⁷ Deep impurity defects of Pt in Si, also reveal an amphoteric character with two

dominant defect levels at $E_{VB} + 0.32$ eV, acting as donor and at $E_{CB} - 0.25$ eV, which is known as acceptor level.²⁰⁸ This was similarly observed for the clean P_b center on clean Si surfaces. It is frequently reported that the origin of the acceptor results from a single substitutional Pt site.^{208–210} The origin of the donor state is discussed to be related with a lattice reconstruction about the substitutional defect center²¹⁰ or a defect pair of neighboring sites.²⁰⁹ Additional reported defect levels such as a donor at $E_{VB} + 0.36$ eV seem to originate from process-dependent metallurgical defects.²⁰⁸

When repeating the Pt interface experiment on n-type Si, shown in Figure A5 of the Appendix, the Fermi level shifts from 1.10 eV to 0.45 eV above the VBM indicating an electron depleted SCR. The Fermi level at the n-Si/Pt interface is therefore located only 70 meV above the Fermi level observed at the p-Si/Pt interface, confirming Fermi level pinning. The slightly higher Fermi level in the n-type Si might additionally indicate the amphoteric character of the Si/Pt defect formation since the lower Si WF is not fully depleting the unoccupied acceptor state above midgap as expected for p-type Si.

With the similar pinning level, the linear potential drop at the SiO_2 layer, is expected to be in the same range for both, p- and n-type interfaces. Applying the line shape model to the n-Si/Pt interface (shown in Figure A5), gives a potential drop of 1.2 eV in the oxide layer. Taking into account the 70 meV higher Fermi level observed in the n-type Si, the potential models predict similar potentials with a difference of only 130 meV, verifying the model itself with a good reproducibility of the fitting routine. The WF=4.1 eV on native oxide terminated Si is independent on bulk doping and equals the commonly reported value for the Si electron affinity.²⁹ Interestingly, the WF of the equally deposited 138 nm thick Pt film on the n-type Si differs from the value of 5.3 eV derived on p-Si and is equal to the literature reported value of $WF_{Pt}=5.6$ eV.^{195,196} In fact, it seems that the contact potential of both substrates depends indeed on the Si doping, since the potential drop in SiO_2 is more or less the same regarding the pinning level at $E_{VB} + 0.32$ eV. The additional contact potential in n-Si is therefore dropping in the SCR. The acceptor level at $E_{CB} - 0.25$ eV is not affecting the band alignment, since it gets depleted by the high Pt WF. However, it will still affect the charge transfer properties, since it is known as recombination center for photocarriers with capture cross sections of $\sigma_{n,p} \approx 10^{-15} \text{ cm}^2$.^{211,212} Furthermore, the reduction of the SiO_2 layer will further enhance the recombination activity of electrons for which the capture cross section is found to be in the range of $\sigma_n \approx 10^{-17} \text{ cm}^2$.¹³³

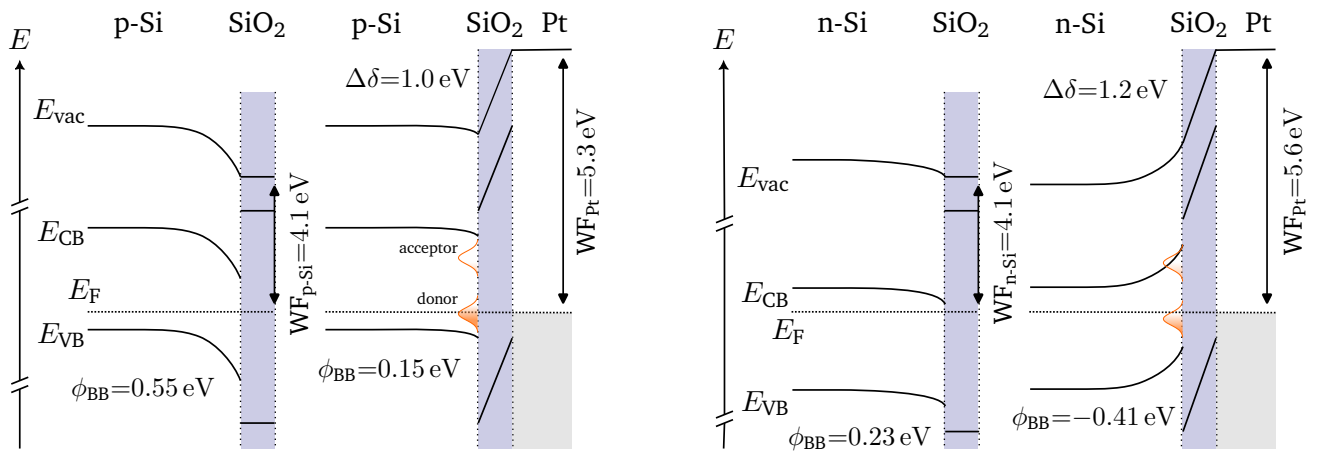


Figure 5.24: Interface formation of Si/ SiO_2 /Pt Schottky contact on p (left) and n-type substrate (right). Defect levels from substitutional Pt_{Si} are taken from Mantovani et al.²⁰⁸. Oxygen related defect levels are not depicted. WF are deduced from XPS SEE.

The summary of all obtained values for the Si/SiO₂/Pt interface for p- and n-doped Si substrates is depicted as final band diagrams in Figure 5.24. Both substrates show Fermi level pinning in contact to sputter deposited Pt due to substitutional Pt defects. The VB and CB-offsets at the Si/SiO₂-interface are expected to remain unchanged after Pt deposition.

It is reported that a substrate bias of -90 V during the Pt sputter deposition changes the grain morphology of the Pt and with that influences the interdiffusion of Pt into Si.^{198,202} Unfortunately, there is no study yet that investigates if substrate bias might be able to prevent Fermi level pinning at the Si/Pt interface.

The meaning of the presented band diagram will be presented later in Section 5.4.3, when the charge transfer over the interface is investigated in a photoelectrochemical setup.

5.4.2 Water adsorption on Pt covered Si

In a next step, the adsorption behavior of water is investigated for Pt covered Si (100) in comparison to the bare Si surfaces presented in Section 5.3. Before investigating the H₂O adsorption behavior on Pt covered Si, the adsorption experiment was conducted on sputter-cleaned Pt and Pd foil (Figure A6 of the Appendix). Due to their good known HER activity, both metals clearly show dissociative adsorption of H₂O at RT. However, the position of the OH related 1π and 3σ features differ with 9.05 and 11.6 eV for Pt and with 7.95 and 10.85 eV for Pd and are narrower than observed on flashed Si (7.56 and 12.08 eV). Both spectra reveal additional O 2p lone pair features between 2.0 to 3.5 eV. As expected from the high charge carrier concentration, the core level lines of the metallic surfaces remain at the same binding energy during water adsorption.

With these references, the interaction of partially Pt covered p-Si/SiO₂/Pt surfaces with water were investigated.

Room temperature water exposure on Si/SiO₂/Pt

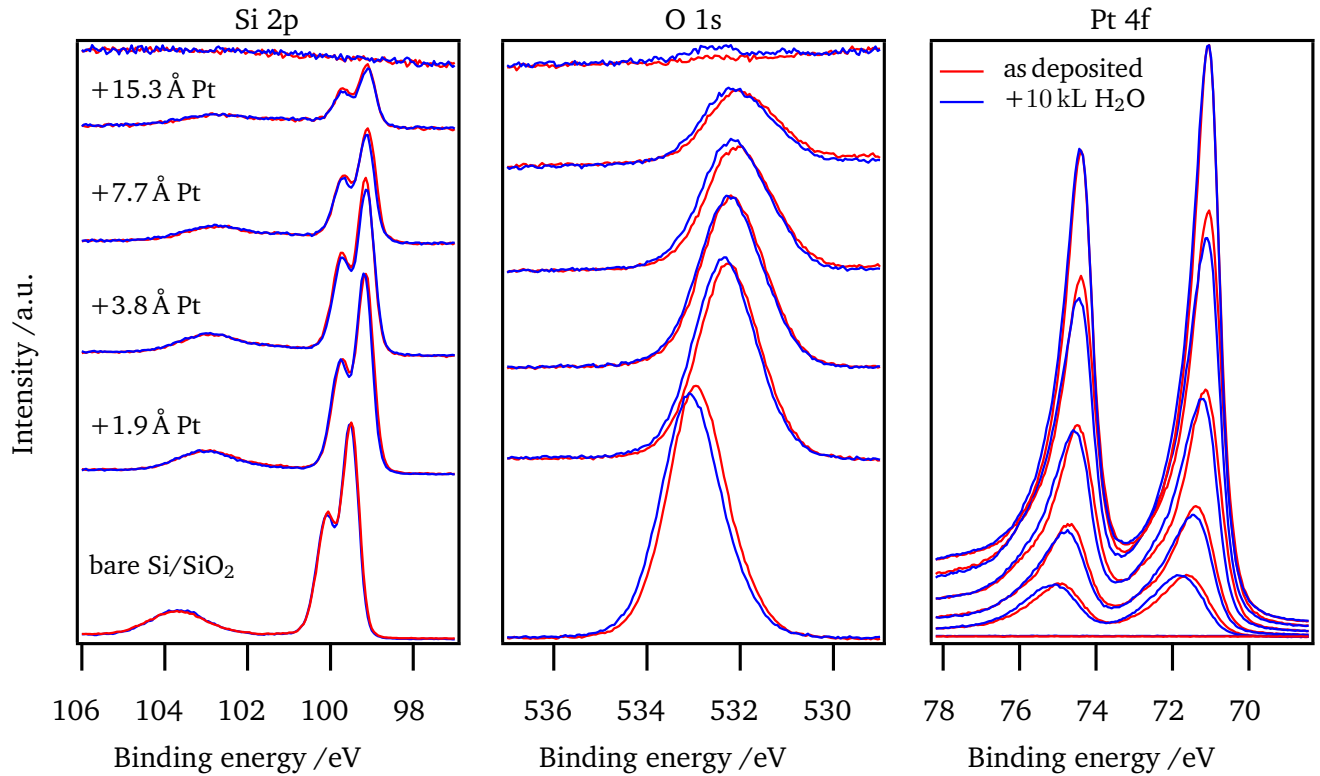


Figure 5.25: XP core level spectra of Pt covered p-Si/SiO₂ interfaces before (red) and after 10 kL water exposure (blue) at RT.

First, the surfaces of the interface experiment above were exposed at room temperature (RT) to 10 kL H₂O with the respective core level lines of the p-Si/SiO₂/Pt interfaces shown in Figure 5.25. The crystalline Si 2p contribution does not show significant shifts ≥ 50 meV, indicating that the interfacial band alignment in the Si SCR does not change after the exposure to water. However, the SiO₂ related Si 2p and O 1s contribution shows a shift in energy of about 0.1 eV to higher binding energies for the bare Si/SiO₂ as well as the Pt covered substrates. The SEE shift by about the same amount, indicating a reduction in

WF due to a change in surface dipoles. This effect might be induced by a partial hydroxylation of the surface, decreasing the WF. On the 138 nm thick Pt film, the WF on the n-Si substrate is reduced from $\Phi=5.6$ eV to 5.3 eV, while on the p-Si substrate the initial WF of $\Phi=5.3$ eV remains unaffected after the exposure to water. This shows how sensitive to adsorbates the photoemission SEEs are, even though no O 1s signal is found (compare O 1s signal for the as deposited pure Pt film at the top of Figure 5.25).^{213,214}

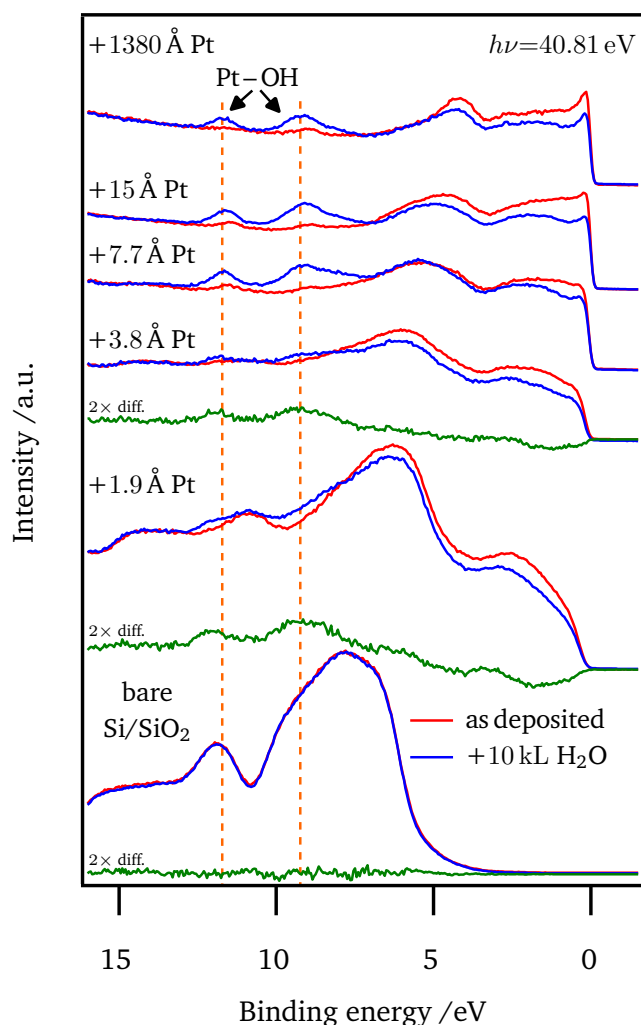


Figure 5.26: HeII UP spectra of partially Pt covered Si/SiO₂/Pt interfaces before (red) and after room temperature exposure to water (blue).

multi-layer stack, especially for nanosized clusters on surfaces. Such effects have been suggested to occur at interfaces between semiconductor substrates and nanosized co-catalyst metal layers at electrochemical junctions (*pinch-off effect*).^{215,216}

Low-temperature water adsorption on p-Si/SiO₂/Pt

In a next step, low temperature water adsorption experiments were conducted on Pt covered p-Si/SiO₂/Pt interfaces. For this purpose, two different deposition techniques have been compared:

Interestingly, the biggest changes are observed on the metallic Pt top layer. After the first deposition of a sub-monolayer Pt, a shift of up to 0.2 eV is observed after the exposure to water. It decreases with higher coverages and vanishes for the thick Pt layer. In the previous section it was shown that the potential distribution within the SiO₂ phase also affects the Pt related binding energies. This might suggest, that the interface dipole, which might be induced by the adsorbates, lead to a potential drop in the SiO₂ layer.

In Figure 5.26, the HeII spectra of the partially Pt-covered surfaces are shown. The He II spectra of the bare Si/SiO₂ surface do not reveal any changes after the exposure to water. With Pt on top, the 1 π and 3 σ related P–OH features appear at 9.1 and 11.6 eV as observed on the sputter cleaned Pt foil. Accordingly, it is assumed that water preferentially dissociates at Pt atoms, changing the overall surface dipole due to adsorbed Pt–H_{ads} and Pt–OH_{ads} species. For these low coverages, the charge carrier concentration in the Pt layer is far below the expected bulk value of typically 10²² cm^{−3}. Consequently, the change in surface dipole cannot be shielded completely by Pt and affects therefore the potential distribution in the SiO₂ layer. With higher Pt coverages, the charge carrier concentration reaches its bulk value and the surface dipole is shielded completely by Pt.

As a conclusion of this experiment, the potential drop of electrochemical double layers also depends on the surface charge carrier concentration of the apparent co-catalyst, which might also affect the potential distribution for the underlying layer of a

- i) One sample was prepared by an electrodeposition process where Pt was reduced from a 2 mM K_2PtCl_4 solution with a galvanostatic current density of -0.5 mA cm^{-2} .
- ii) Another sample was prepared by a 2.5 s sputter deposition process as described above. The layer thickness is calculated by about 1 \AA which is expected to be around 25 % of a Pt monolayer ($\approx 10^{14} \text{ atoms/cm}^2$). Consequently, the depletion of the p-Si SCR is not fully developed and the Fermi level is found to be 0.50 eV above the p-Si VBM.

In Figure 5.27, the particle distribution of a galvanostatic deposited Pt on top of a Si/SiO₂ substrate is shown as measured by SEM. Internal studies on Ti and p-InP could show that these type of electrodeposited Pt leads to $230 \pm 90 \text{ nm}$ particles and a surface coverage of about 10 %.¹¹² The main difference between the two deposition techniques is the potential distribution of the Si/SiO₂ surface in contact with Pt. When Pt is sputter-deposited, it is expected to form fine and dispersed Pt clusters, resulting in an equipotential surface with electronic potentials varying only over the thickness of the functional layers (thin film approach). On the other hand, galvanostatic deposition of Pt leads to the formation of bulk-like Pt particles on the Si/SiO₂ surface, resulting in a lateral 2D potential distribution in the vicinity of these particles as schematically shown in Figure 5.28. Consequently, lateral SCR will form while most of the p-Si surface is depleted due to oxygen related surface states, while close to the Pt particles the p-Si surface reaches flatband conditions as depicted in the previous band diagram (Figure 5.24).

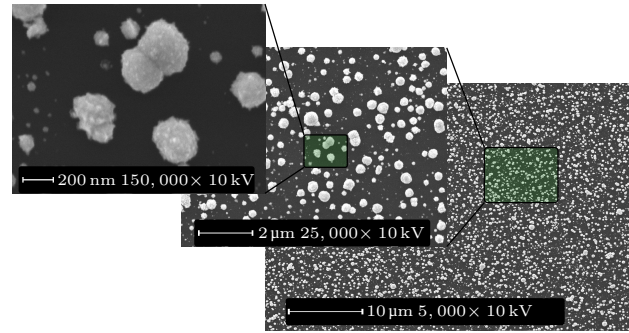


Figure 5.27: SEM images of galvanostatic deposited Pt particles.

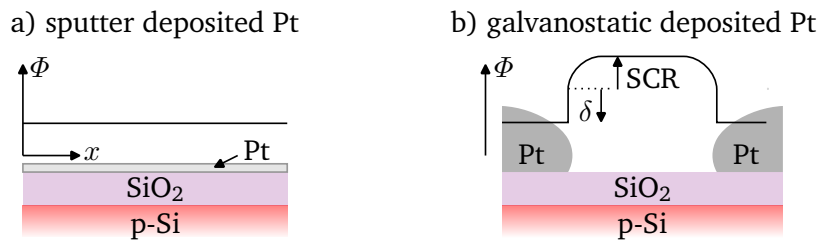


Figure 5.28: Lateral potential distribution of a) sputter deposited Pt and b) galvanostatic deposited Pt.

Because of the structural differences of the surfaces, the spectroscopic characteristics displayed in Figure 5.29 differ for the two surfaces upon low temperature water adsorption. Sputter deposition of Pt results in a broad Pt 4f distribution due to the low Pt concentration, which means there is no clear Fermi edge observed in the HeII spectra. Si 2p indicates a downward band bending of 0.28 eV which reduces to 0.15 eV upon cooling. On the other hand, the electrochemically Pt-covered surface shows a slightly broader Si 2p contribution due to the lateral potential gradient. However, the main Si 2p line indicates a downward band bending of 0.57 eV which reduces to 0.32 eV upon cooling. The bulk-like Pt particles lead to sharp Pt 4f contributions and a distinct Fermi edge in XP and HeII valence spectra. Accordingly, the Fermi edge in XPS is observed at -0.11 eV binding energy, indicating a source-induced SPV even at room temperature, while the HeII spectra reveal the Fermi edge at almost zero with $E_b = -0.02 \text{ eV}$. After cooling, the Fermi edges for XPS and UPS are found at $E_b = -0.60$ and -0.66 eV , respectively, confirming the enhanced SPV at low temperatures as described in Section 5.1.5. Furthermore, the peaks attributed to

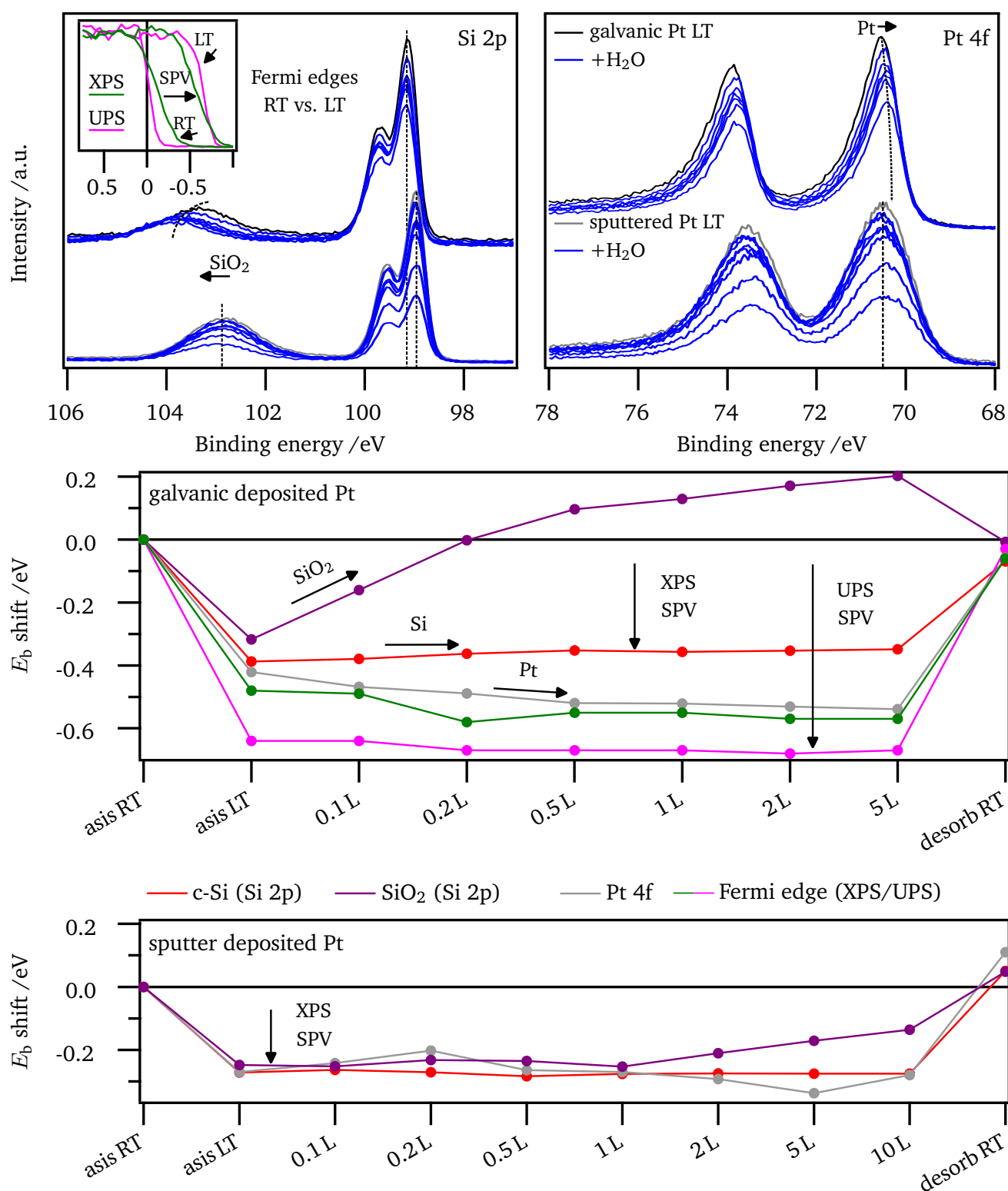


Figure 5.29: Low temperature water adsorption experiment of Pt covered Si/SiO₂ surfaces. Si 2p and Pt 4f spectra of electrodeposited Pt are compared to sputter deposited Pt. Binding energy E_b shifts are depicted for both galvanic (middle) and sputter deposited Pt (bottom). The main difference is observed in source-induced SPV and the SiO₂ component, only shifting on the galvanic deposited Pt sample.

c-Si and Pt show different shifts while cooling, which confirms an inhomogeneous potential distribution and, consequently, lateral variations in SPV.

Upon exposure to molecular water, the Si 2p line associated with SCR does not exhibit any significant changes, suggesting a constant surface band bending. However, the Si 2p component associated with SiO₂ shifts to higher binding energies, which has been observed previously on bare Si/SiO₂ surfaces and is attributed to an adsorbate-induced change in potential. Interestingly, when water comes in contact with the surface, the Pt related Pt 4f line, as well as the Fermi edge, shift to slightly lower binding energies by about -0.10 eV (Δ_{Pt4f}) and -0.07 eV ($\Delta_{\text{Fermi edge}}$). This indicates, that the photovoltage in the vicinity of the Pt particle increases in contact to water. This tendency is also observed on the HeII Fermi edges coinciding with the XP Fermi edge at $E_b = -0.69$ eV, which is the maximum observed photovoltage at the p-Si/SiO₂/Pt surface. This requires an initial surface band bending by at least the same amount. The rising photovoltage can result from an increased surface band bending in lateral regions inducing the photovoltage to the Pt particles or to a reduced recombination activity due to defect passivation. The high photovoltage contradicts the observed Fermi level pinning at the Si/Pt interface, which might indicate that the galvanostatic deposition does not form substitutional Pt_{Si} which leads to deep impurity defects as discussed above. Another explanation for the increasing photovoltage in the vicinity of the Pt particles could be that mobile OH and H groups lead to a partial passivation of P_b dangling bond defects. The sputter deposited Si/SiO₂/Pt surface does not show any significant changes upon water adsorption. As expected, due to the depleted surface states, the source-induced SPV is rather small ($eU_{\text{ph}} = 0.13$ eV). Furthermore, the water adsorption does not show any impact on the photovoltage. After the desorption, all core level show slightly higher binding energy, as already observed on the H₂O exposed interfaces above.

The HeII spectra show no significant spectral differences between the surfaces except for the molecular water feature. On the sputter deposited surface, the 1b₁ feature is observed at $E_b = 6.00$ eV with OH features at 9.0 and 12.2 eV, while on the galvanostatic deposited Pt surface, the 1b₁ orbital of molecular water is found at 6.5 eV with OH features at 9.8 and 13.0 eV. The same features have been found on the metallic Pt foil at 5.5 eV (1b₁ of molecular water) and 9.0 and 11.6 eV (1 π and 3 σ of OH) and thus are expected to be located only at Pt sites. However, the slightly broader splitting of OH features on the prepared surfaces in comparison to Pt foil, could indicate that the H₂O dissociation products might also interact with Si surface sites.

5.4.3 Electrochemical performance of the n-Si/Pt hetero contact

Photoelectrochemical performance measurements were used to connect the electronic interface alignment at the n-Si/SiO₂/Pt interfaces (Figure 5.24) with the interfacial charge transfer properties. This interface might be of interest as model experiment, when considering the charge transfer properties of an n⁺-emitter layer to the HER catalyst in case of a buried photoelectrochemical cell (PEC)-device.

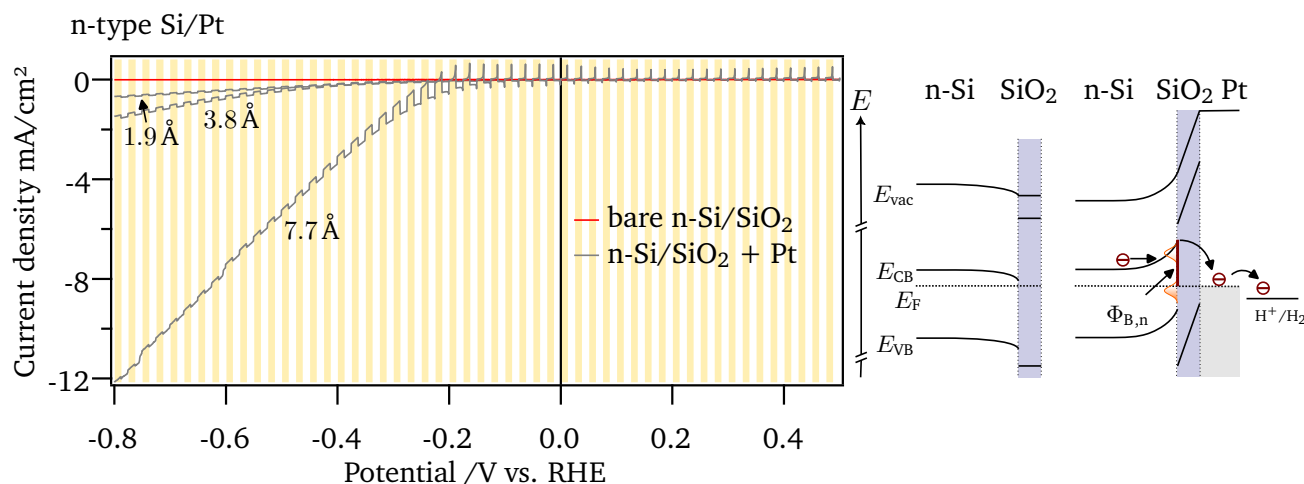


Figure 5.30: Linear chopped light sweeps in 0.1 M H₂SO₄ for bare (red) and Pt covered n-Si/SiO₂ surfaces (5 mV s⁻¹). Pt was deposited by DC-sputtering with thicknesses as given in the graph. Yellow and light bars, represent dark and white light illumination (1000 W m⁻²), respectively. Energy band diagram for bare and covered n-Si/SiO₂ are shown on the right as deduced from the interface experiment.

In Figure 5.30, chopped light sweeps for differently Pt covered n-Si/SiO₂ are shown. At this interface, electrons need to be transferred from the n-Si substrate into the Pt catalyst by overcoming the Schottky barrier for electrons $\Phi_{B,n}$. This can be calculated by $\Phi_{B,n} = E_g - \Phi_{B,h}$, with $\Phi_{B,h}$ as Schottky barrier for holes, which is given by the VB-onset and is determined for the n-Si/SiO₂/Pt interface with $\Phi_{B,n} = 0.68$ eV. Even though the transfer direction for the cathodic HER is in forward bias, overcoming this barrier will require additional overpotentials, resulting in charge transfer losses along this interface, that are notable by the shifted onset potentials for the HER of at least 0.2 V.

For the n-type substrate, the illumination of this junction leads to a photocurrent response, since the deposition of Pt will induce a SCR into the n-Si interface, which is able to separate excess charge carriers when illuminated. But, the depleted n-Si will accumulate holes at the interface to metallic Pt and thus hinder the cathodic HER which requires free electrons. Consequently, the overpotentials for the HER reaction are even higher under illuminated condition than under dark conditions since the induced photocurrents are pointing in reverse direction. Current-voltage curves on similarly Pt-covered p-Si/SiO₂ are shown in Figure A8 in the Appendix. In this case, the Fermi level is pinned close to the VBM and almost no photoresponse is observed in the cathodic regime, since the inversion layer at the interface becomes very narrow and impedes the charge separation of excess charge carriers.

In conclusion, when considering a buried junction device where photoelectrons are generated in the photoabsorber and must be transferred to the catalyst without loss, it is demonstrated that a depleted emitter layer will inevitably restrict charge transfer properties due to the formation of a barrier Φ_B . When light is absorbed within this depleted layer, a photovoltage is generated that counteracts the photovoltage of the inner buried junction. Therefore, it is essential for the overall efficiency of the device to avoid depleting the emitter layers on both electrodes.

Electrodeposited Pt however, changes this depiction. As already observed in the low-temperature water adsorption experiments, a gain in photovoltage is observed for galvanostatic deposited Pt particles on top of a p-Si/SiO₂ substrate (Figure 5.31). Consequently, the depleted p-Si layer accumulates light-induced electrons at the surface during illumination inducing a photovoltage U_{Ph} at the surface, which shifts the onset of the HER to positive values by about 0.25 V. This value coincides with similarly prepared photocathodes under 1000 W m⁻² white light illumination in literature^{217,218} but is significantly lower (<50 %) than the values achieved by HeII illumination under liquid nitrogen temperature. Furthermore, the light-induced currents are significantly lower for the electrodeposited Pt than observed for the sputter deposited Pt suggesting that the lateral inhomogeneous potential distribution impedes the lateral charge transfer from the excited photoabsorber to the active Pt sites limiting the total photoconversion efficiency.

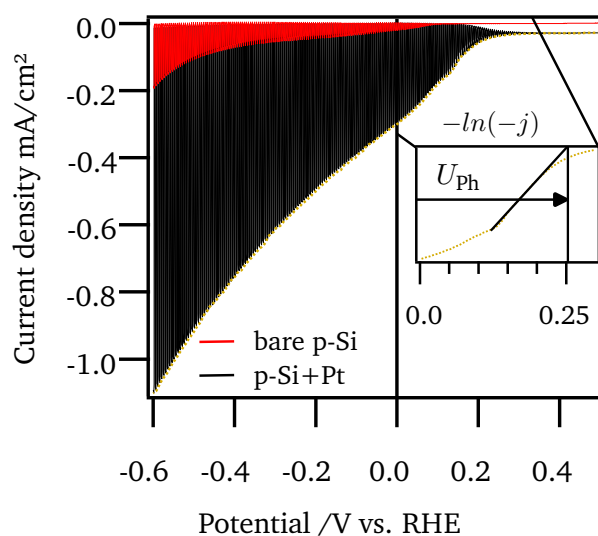


Figure 5.31: Chopped light sweep in 0.1 M H₂SO₄ for bare (red) and galvanostatic deposited Pt covered p-Si/SiO₂ (black). 200 W m⁻² illumination with a red light LED ($h\nu=635$ nm) increases photocurrents and induces a photovoltage U_{Ph} .

6 InP surfaces

Due to their promising photovoltaic performance, III–V photoabsorbers have gained significant attention for potential applications in photoelectrochemical water splitting.^{21,55} In the realm of binary III–V semiconductors, InP (100), as a benchmark system, can be terminated either In-rich or P-rich using metal organic vapor phase epitaxy (MOVPE). Extensive experimental and theoretical investigations have been conducted in the past to understand its preparation and surface reconstructions.^{219,220} Notably, experiments on InP have demonstrated that distinct atomic surface reconstructions significantly influence stability and reaction pathways upon contact with water.²²¹ Nevertheless, the exact role of surface defects, as characterized by Fermi level pinning, particularly at the interface with the liquid electrolyte, remains not completely understood hampering further enhancements in photoelectrochemical efficiency. Consequently, research efforts have recently shifted towards exploring the electrochemical interface between the semiconducting photoabsorber and the liquid electrolyte.^{184,221,222} Additionally, the interaction of InP as a photoabsorber with water gains prominence when depositing conductive oxides as electrochemical buffer layers using atomic layer deposition (ALD), where water often serves as the oxide precursor.^{177,223}

6.1 P-rich p-InP (100)

The results and content of this study have been published in ACS Applied Materials & Interfaces.¹⁷⁸ DFT calculations were performed by Isaac Azahel Ruiz Alvarado under supervision of W.G. Schmidt, University of Paderborn.

6.1.1 Electronic structure and surface states of P-rich p-InP (100)

P-rich InP (100) are known to form stable $(2 \times 1)/(2 \times 2)$ surface reconstruction characterized by P-dimers which can additionally bond to hydrogen atoms.^{110,219,220} The well-ordered P-rich p-InP (100) surface has been prepared at *TU Ilmenau* with a p-doping concentration of $2 \times 10^{18} \text{ cm}^{-3}$ according to Section 4.2.2. One day after preparation, the sample has been transferred and analyzed at **Darmstadt Integrated System for Fundamental research (DAISY-FUN)**.

The XP survey scan of the as received P-rich InP (100) surface reveals a very clean surface only showing emissions from In and P (Figure 6.1). In particular, no traces of oxygen or carbon can be found at binding energy $E_b(\text{O } 1s) \approx 530 \text{ eV}$ and $E_b(\text{C } 1s) \approx 285 \text{ eV}$. The In $3d_{5/2}$ emission is located at 444.25 eV and can be fitted with a single Voigt line with a total full width at half maximum (FWHM) of 0.68 eV , indicating a homogeneous compound surface with no oxidized or segregated subspecies. The associated P $2p$ emission clearly contains a surface component, which appears about 0.51 eV toward higher binding energies than the bulk-related emission at 128.45 eV with a relative intensity of about 9 %. With an inelastic mean free path $\lambda_{\text{IMFP}}(E_{\text{kin}}=1300 \text{ eV})$ in InP of 22.8 \AA ,⁹⁶ 9 % results according to Beer-Lambert law from the first 2.15 \AA of the sample surface, which is a bit less than half the lattice constant of $a(\text{InP})=5.87 \text{ \AA}$. This surface component can therefore be attributed to P dimers at the reconstructed P-rich InP (100) surface.²²⁰ With a FWHM of 0.55 eV , the component resolution is close to the spectrometer resolution (FWHM of Ag $3d_{5/2} = 0.50 \text{ eV}$). According to the secondary electron edge (SEE), the work function (WF) of the P-rich InP (100)

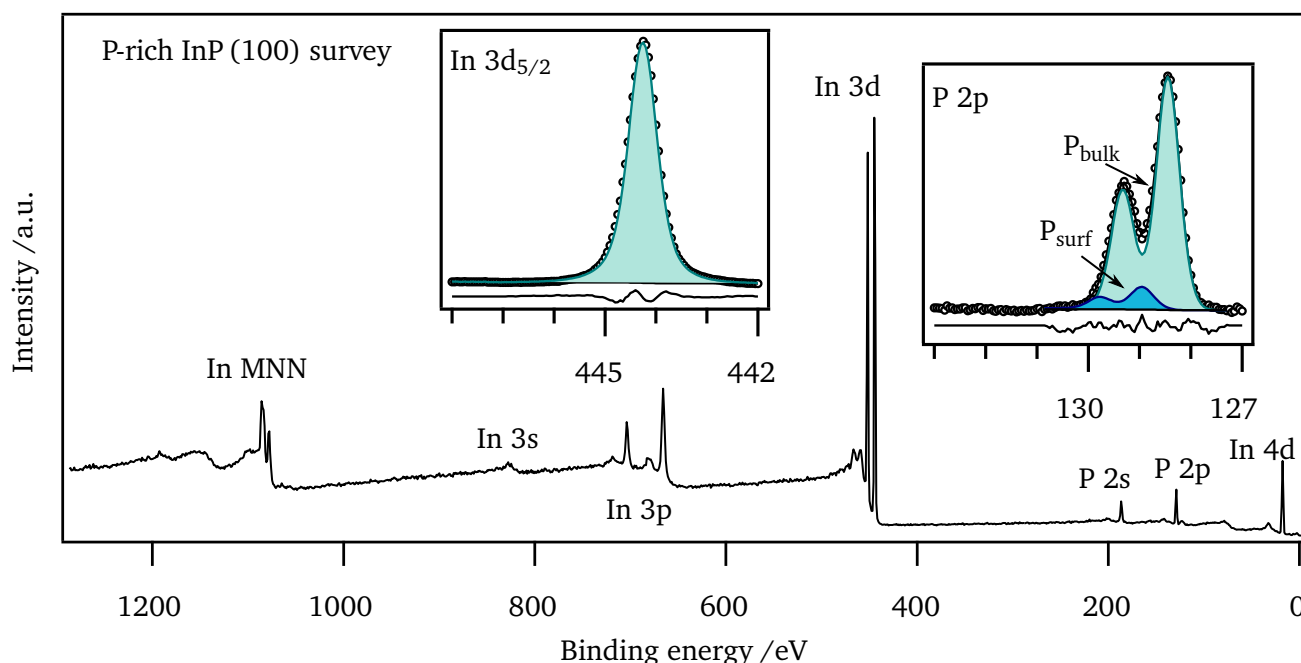


Figure 6.1: Survey XP spectra of P-rich p-InP(100) with detailed spectra of In $3d_{5/2}$ and P 2p core levels. The In $3d_{5/2}$ can be fitted with a single Voigt line, while the P 2p core level reveal a surface component shifted by 0.51 eV to higher binding energy.

is found to be at 4.35 eV. Stoichiometry analysis results in almost 1 : 1 In (52.4 atm.%) to P (47.6 atm.%) composition.

In a next step, the surface structure has been investigated by low-energy electron diffraction (LEED). The LEED patterns clearly reveal a 2×1 surface reconstruction as depicted in Figure 6.2a). The first-order spots (yellow circles) are separated by diffuse streaks (dashed lines) along the $[110]$ direction. During the MOVPE process, where H_2 is used as carrier gas, the buckled P dimers are stabilized with atomic hydrogen. The stabilization can be arranged in-phase resulting in a $p(2 \times 2)$ unit cell, or out-of-phase corresponding to a $c(4 \times 2)$ unit cell (compare Figure 2.10 in Section 2.3.1).^{224,225} The superposition of both unit cells leads to the 2×1 -like LEED pattern with the characteristic streaks in the $\times 2$ half-order, indicating a $2 \times 2 - 2D-2H$ surface reconstruction with two buckled P dimers with two atomic hydrogen. The $2 \times 2 - 2D-2H$ structure is depicted in Figure 6.2b) and predicted as the most stable P-rich InP(100) surface from *ab initio* calculations.²¹⁹

In Figure 6.2c) the normalized UP valence band spectra with two different excitation energies are shown. The valence band features have been studied in detail by Hannappel et al.¹¹¹. The valence feature S_1 is attributed to a superposition of bulk and surface states.²²⁶ The surface state contribution can be attributed to the phosphorous dangling bonds at the phosphorous dimers. Hydrogen saturation leads to a damping of S_1 , indicating the presence of atomic hydrogen.¹¹¹ Hydrogen could be also confirmed by the S_3 feature, which is assigned to a hydrogen surface resonance. S_4 is associated accordingly to a phosphorous state. Surface state S_2 results from a resonance with the bulk and is characteristic for the P-rich 2×2 surface of InP(100).

With that, the structural and chemical analysis of the surface confirms a clean and homogenous surface with the overall $2 \times 2 - 2D-2H$ surface configuration. XP and UP valence-spectra reveal the valence band maximum (VBM) at 0.60 eV below the Fermi level as shown in Figure 6.3a). With an InP bandgap of 1.34 eV,⁴¹ the Fermi level at the surface is located slightly below midgap. However, according to the

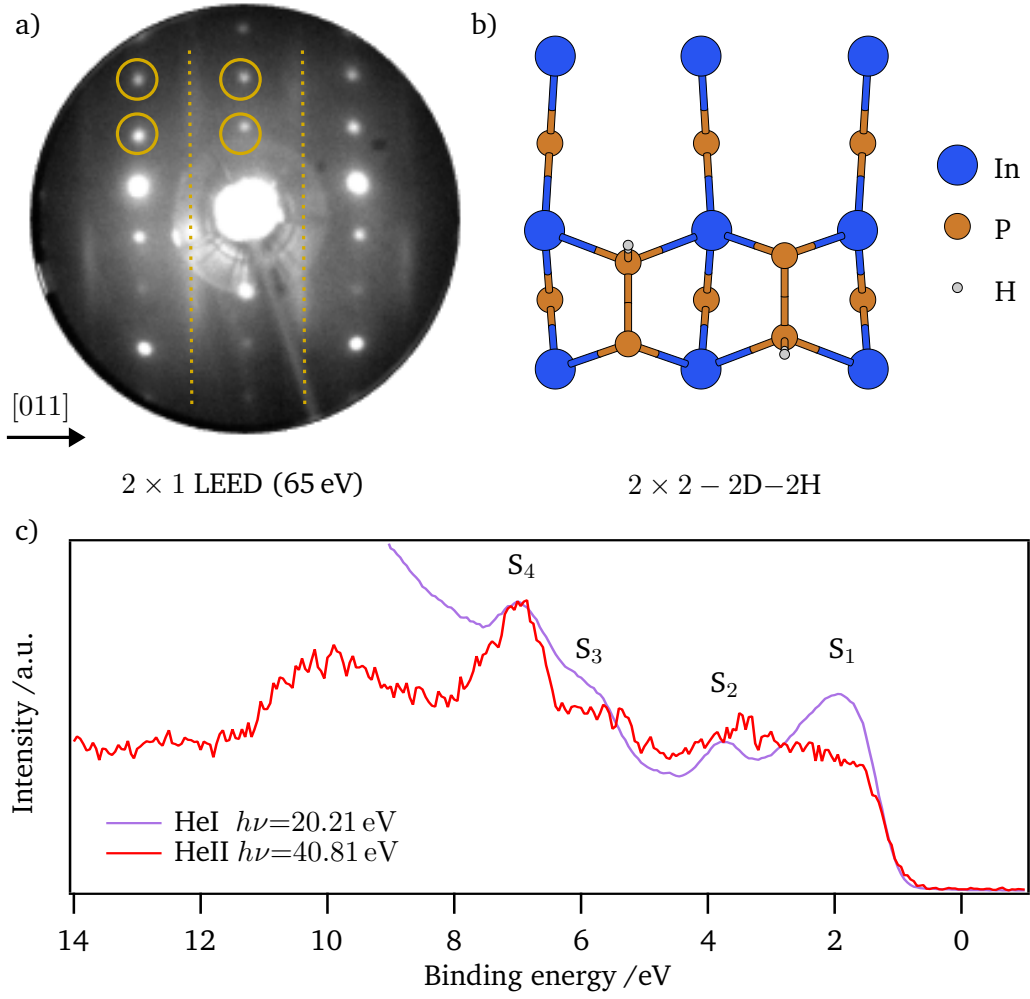


Figure 6.2: LEED pattern of P-rich InP (100) surface at 65 eV beam energy (a). 2×1 spots and diffuse streaks along the $[110]$ direction result from superposition of in-phase $p(2 \times 2)$ and out-of-phase $c(4 \times 2)$ unit cells indicating the $2 \times 2 - 2D-2H$ surface structure depicted in (b). UP valence band spectra with HeI and HeII excitation are shown with labeled features (S_1-S_4) as explained in the main text (c).

p-doping concentration of the grown InP with zinc as a shallow acceptor of about $N_{ac} = 2 \times 10^{18} \text{ cm}^{-3}$, the Boltzmann term $k_B T$, and the effective valence band density of states N_{VB} of about $1.1 \times 10^{19} \text{ cm}^{-3}$ ⁴¹ the Fermi level in the bulk is expected to be ≈ 40 meV above the VBM.

$$E_F - E_{VB} = k_B T \ln \left(\frac{N_{ac}}{N_{VB}} \right) = 43 \text{ meV} \quad (6.1)$$

This discrepancy between the measured and calculated Fermi level position relative to the valence band indicates a strong surface band bending of $\phi_{BB} = 0.56$ eV due to apparent surface states inducing electrons into the surface, which pin the Fermi level (see Section 2.1.4). Considering a parabolic potential drop inside the InP space charge region (SCR), the amount of total surface charges Q_{SS} can be calculated with Equation 6.2 as done for the Si surfaces (see Section 5.1), meaning that $< 1\%$ of the surface atoms contribute to a charged defect.

$$-Q_{SS} = \sqrt{\epsilon\epsilon_0\phi_{BB}N_{ac}} = 3.9 \times 10^{12} \text{ cm}^{-2} \quad (6.2)$$

The band structure of the $2 \times 2 - 2D-2H$ surface has been studied in detail by Hahn and Schmidt²²⁷. According to them, the highest occupied surface band results from an out-of-plane unsaturated dangling bond on the phosphorus atom of the P dimers. The lowest unoccupied surface band is attributed to antibonding combinations of p orbitals, which are localized in-plane at the P-dimers. However, in both cases these surface bands appear very close to the bulk valence and conduction band edges. For that reason, the identified $2 \times 2 - 2D-2H$ surface cannot cause the observed surface band bending.

As possible defect mechanisms, hydrogen-related defects, namely desorption and adsorption of one or two H atoms, were considered using *ab initio* thermodynamics and band structure calculations performed by Isaac Azahel Ruiz Alvarado (see¹⁷⁸ for computational details).

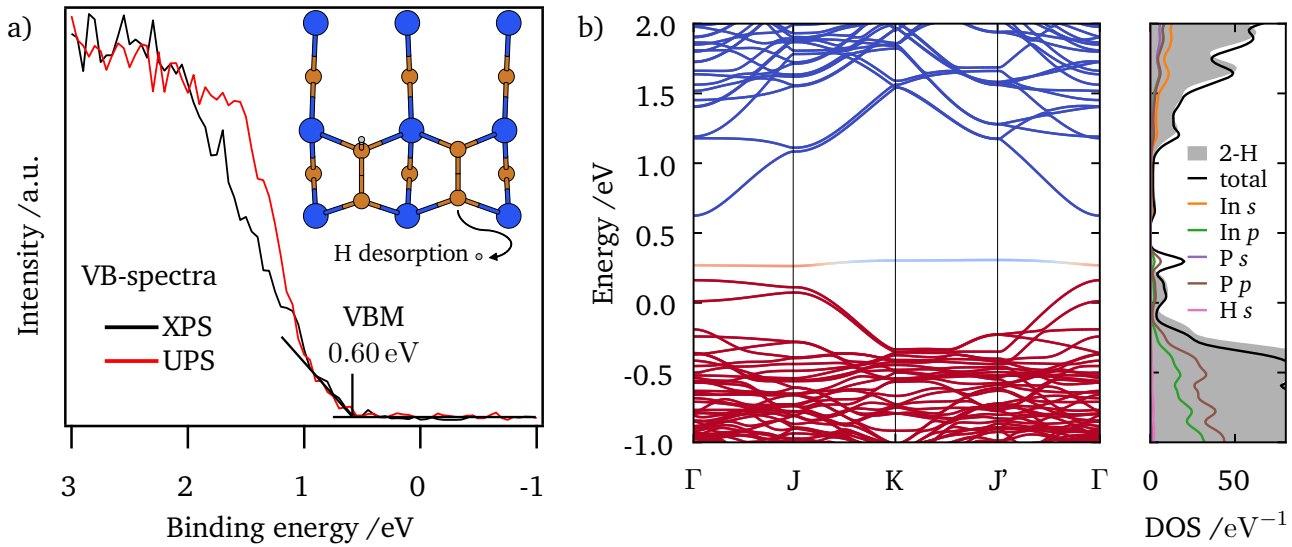


Figure 6.3: Partial hydrogen desorption from p-InP (100) surface leads to in-gap states. a) VB-spectra reveal Fermi level pinning at 0.60 eV above the VBM while VB cut-off under flat-band conditions would be expected to be located at 0.04 eV. b) Band structure and atomic as well as orbital resolved electronic density of states of the InP $2 \times 2 - 2D-1H$ surface. The red/blue lines correspond to occupied/unoccupied bands. The energy of zero corresponds to the InP bulk valence band maximum. The shaded area represents the DOS for the ideal $2D-2H$ InP surface, without any defects calculated by I.A. Ruiz Alvarado.

The desorption of one hydrogen atom from the $2D-2H$ surface is the by far predominant defect type under MOVPE and analysis conditions, leaving an additional phosphorus dangling bond at the surface. It corresponds to the formation of the InP (100) $2 \times 2 - 2D-1H$ surface. The band structure and density of states (DOS) calculations are shown in Figure 6.3b). The additional phosphorous dangling bond due to the hydrogen vacancy gives rise to a half-filled surface band located slightly below the calculated midgap position. This is in good agreement with the photoemission valence band (VB)-spectra, indicating that the surface P dangling bond is the dominating defect causing the Fermi level pinning at the present P-rich p-InP (100) surface.

The consideration of spin-polarized calculations leads to a splitting of the dangling bond state into an occupied spin-up state at the VBM and an unoccupied spin-down state in the bandgap similar to states observed spectroscopically on Si surfaces (see Section 5.1). However, the charge neutrality level (CNL) of the

defect does not change and the Fermi level will be pinned between these two states in the lower half of the bandgap.

The defect concentration of a hydrogen vacancy at the P-rich InP surface is given in Figure 6.4 as a function of partial H_2 pressure and temperature. At room temperature (RT) (black dashed line) and for typical ultra-high vacuum (UHV) conditions with a hydrogen partial pressure in the range of 10^{-10} to 10^{-7} Pa (red dashed lines), a surface defect density in the order of 10^{10} to 10^{12} cm^{-2} can be expected. This is sufficient to lead to surface band bending but is slightly lower than the calculated surface charges experimentally evaluated from Equation 6.2. However, the strong temperature dependency might also lead to a higher defect concentration, as the prepared surface was transferred to UHV while cooling after the preparation procedure at 300°C .

All other defects are very unlikely to be observed at the conditions modeled here. The adsorption of one additional H atom is the second most likely defect with a calculated density of $<10^3 \text{ cm}^{-2}$ and thus does not affect the surface band bending.

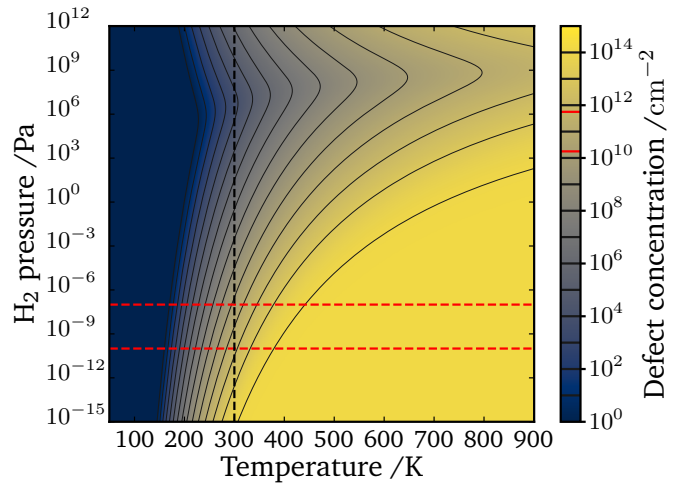


Figure 6.4: Hydrogen vacancy concentration on a $\text{InP } 2 \times 2 - 2\text{D} - 2\text{H}$ surface as a function of pressure and temperature.

It should be mentioned that there are other point defects such as anti-sites or vacancies which are known to form defect states in bulk InP,²²⁸ which might also play a role at InP surfaces.

6.1.2 Reactivity of P-rich p-InP (100) with water

In a next step, the surface reactivity of the observed surface states under water adsorption was investigated experimentally using the “frozen electrolyte” approach as presented in Section 5.3.

The XP spectra of the In $3d_{5/2}$, O 1s and the P 2p core level are shown in Figure 6.5 for each step of the adsorption experiment.

After cooling the surface, the In $3d_{5/2}$ and P 2p core levels shift towards lower binding energies by about 0.27 eV due to a source-induced surface photovoltage (SPV) as observed similarly on the Si surfaces (see Chapter 5). The SPV leads to a reduction of the initial surface band bending from 0.56 eV to 0.25 eV. After the stepwise adsorption of water, both core levels reveal a shift toward higher binding energies and get damped by the growing water layer, rising the O 1s signal at $\approx 533 \text{ eV}$. As the shift shows a linear dependence on the water coverage even in the multilayer regime ($>1 \text{ L}$), it can be attributed to a charging effect of the surface when the insulating ice layer charges due to the emission of photoelectrons. However, the water adsorption itself does not lead to any spectral changes in the core level lines, indicating a chemically immune surface upon water adsorption. After warming up the surface back to room temperature, the water fully desorbs from the surface, and no O 1s emission remains. At the same time, the In and P core levels shift back to their initial energy positions, and no spectral changes are visible.

With the He II UP spectra, a very surface sensitive In 4d emission spectrum can be measured as shown in Figure 6.6. After cooling, the 4d core level shifts about $\Delta E_b = 0.33 \text{ eV}$ towards the Fermi level, similar to the observation from the XP core levels. The same effect is also observed for the SEE with HeII emission, where the WF shifts about 0.35 eV to a value of 4.70 eV. With higher water coverage, a characteristic

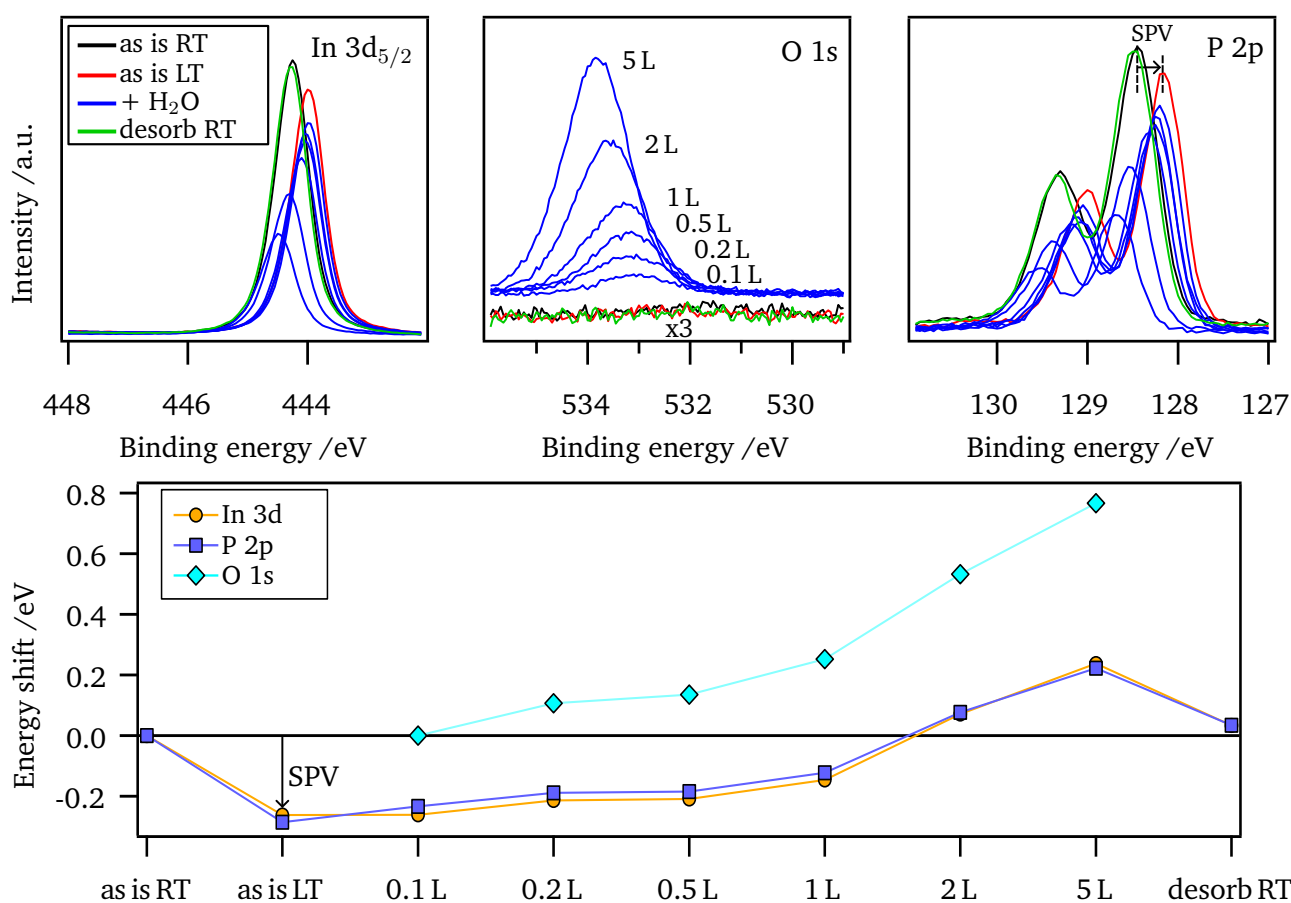


Figure 6.5: XP core level spectra of of low-temperature water adsorption on P-rich p-InP (100) (top) with core level shift after each adsorption step (bottom).

water spectrum arises in the valence band with three features, which can be attributed to the $1b_1$ (6.5 eV), $3a_1$ (8.5 eV), and $1b_2$ (12.5 eV) highest occupied molecular orbitals of molecular water.¹⁷⁹ The water features shift to higher binding energies with increasing coverage, indicating charging of the water layer as similarly observed by X-ray photoemission spectroscopy (XPS). In contrast to the XP spectra, the In 4d line and the SEE seem to be unaffected by the water layer. Only water coverages of >1 L shift the In 4d line slightly to higher binding energies, confirming that all core level shifts observed with XPS and UPS are source dependent and can be related to the charging of the topmost ice layer. The SEE follows the In 4d shifts. For moderate coverage by the ice layer, the InP core levels are not shifted as the substrate photoelectrons are equally retarded and accelerated when passing the charged layer. This apparently changes when the charging of the ice layer increases due to its increased thickness. In this case, the substrate core levels reveal shifts to higher binding energies, too. Even though the photon flux of the monochromatized HeII source ($\approx 10^{11}$ photons/s/mm²) is in the range of the XPS source, the HeII measurement is less susceptible to charging as the lower photon energy leads to less photoionization. After the desorption of the ice layers, the UP spectra reveal only slight spectral changes. However, at 8.0 and 9.9 eV, two features appear in the difference spectra, which might be assigned to 1π and 3σ bonds of adsorbed OH groups,^{179,229} indicating a dissociation of adsorbed H₂O. Dissociative water adsorption has been reported on the InP (110)²³⁰ as well as on the In-rich InP (001) surface.^{221,231} However, the weak signal in UPS and no signal in the XPS O 1s line indicate that OH is only present on a few surface sites far

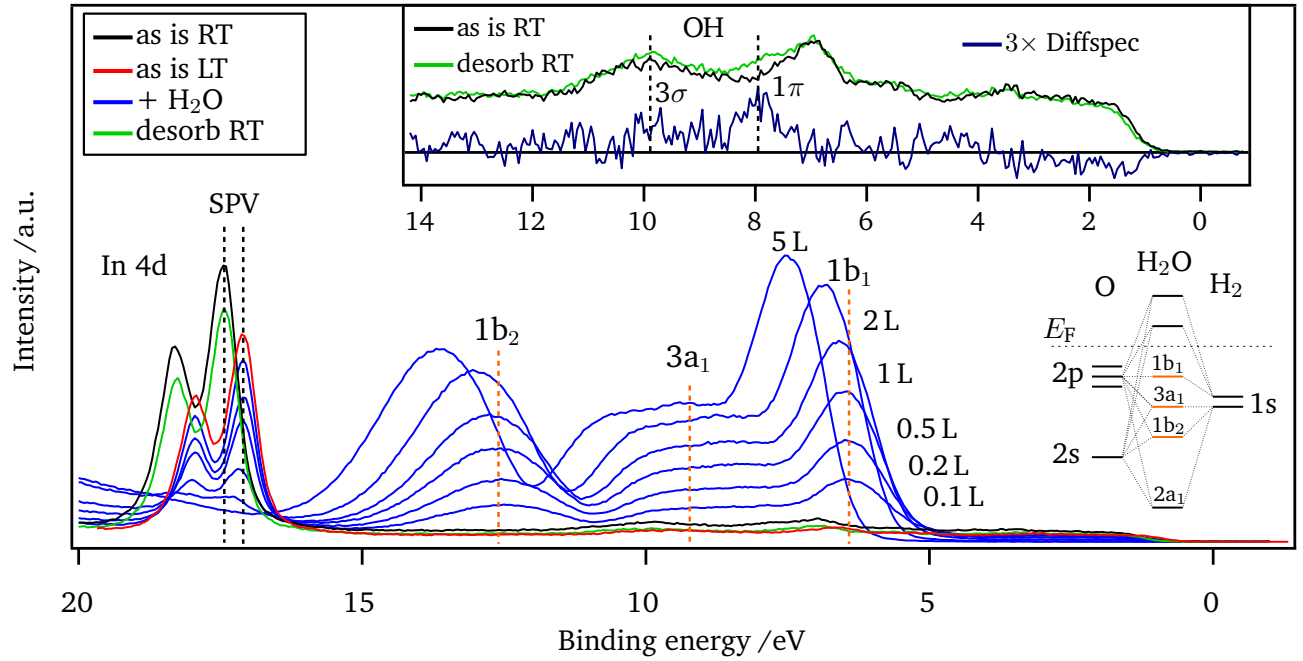


Figure 6.6: Monochromatic Hell spectra ($h\nu=40.81$ eV) of low-temperature water adsorption on P-rich p-InP(100). The difference spectrum of the valence band before and after water adsorption as well as the LCAO approach of molecular water are inset.

below a monolayer coverage. Furthermore, the LEED pattern still exhibits the 2×1 surface reconstruction, indicating that there are no structural changes after the desorption of water.

As a conclusion from the experimental data, it can be stated that, starting from a defective P-rich InP(100) surface, almost no electronic interaction with chemical bond formation to water is observed.

To verify these experimental findings, the water adsorption configuration for the ideal $2 \times 2 - 2D - 2H$ and the hydrogen-deficient $2 \times 2 - 2D - 1H$ surfaces are determined computationally. The potential energy surface for a single H_2O molecule adsorbed on the ideal P-rich InP(100) surface is shown at the top of Figure 6.7. Interestingly, the P dimer does not provide a favorable bonding site for water, which agrees well with earlier findings on In-rich InP surfaces,^{231,232} where water prefers adsorption on In sites rather than P sites. Nevertheless, the water molecule tends to adsorb in the trench between the P dimer rows on the P-rich surface. Examining the calculated charge redistribution under the equilibrium bonding geometry of a surface-adsorbed water molecule, a subtle charge accumulation is observed between the water proton and the P dimer up-atom along with an even weaker charge accumulation between the water oxygen and the second-layer In atom.¹⁷⁸ However, the adsorption enthalpies are rather low (<1 eV) and therefore in the range of weak physisorption.²³³ The band structure calculations with H_2O as an adsorbed add-atom reveal that water adsorption does not give rise to additional gap states.

Interestingly, the potential energy surface of H_2O on the hydrogen-deficient surfaces are rather similar as shown exemplarily for $2 \times 2 - 2D - 1H$ surface on the right of Figure 6.7. In this case, the absolute adsorption energies are slightly higher (by ≈ 0.03 eV) than on the ideal $2D - 2H$ surface, indicating a slightly higher surface reactivity towards water. The preferential adsorption site, however, remains in the trench between the P dimer rows and the H_2O molecule bonds weakly to the P dimer, which is partially H saturated and thus far from the hydrogen vacancy defect. For that reason, the electronic midgap state resulting from H desorption is not affected by water adsorption, confirming the experimental

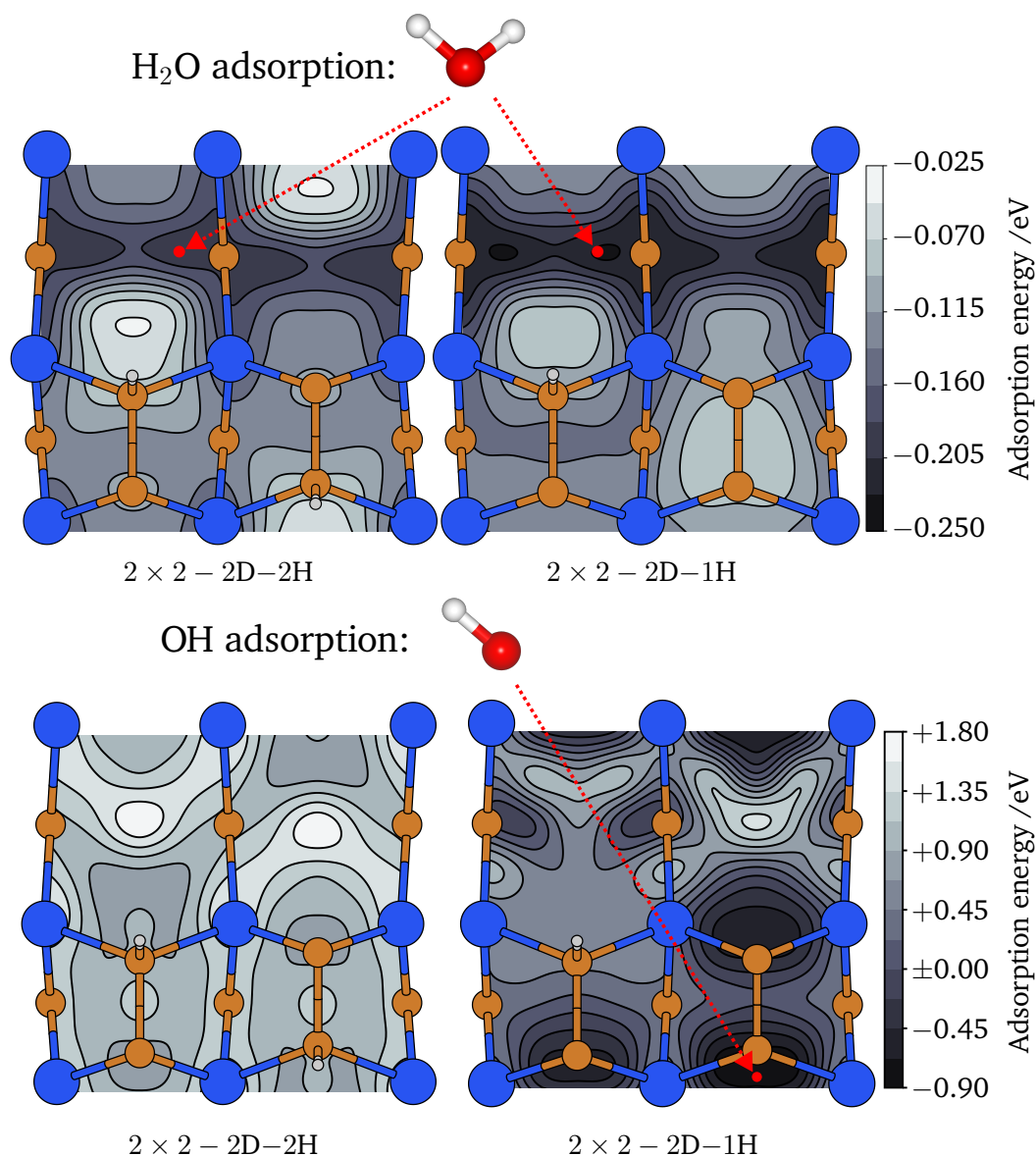


Figure 6.7: Potential energy surfaces for a single water molecule (top) and a hydroxyl group (bottom) on InP (100) $2 \times 2 - 2D-2H$ (left) and $2 \times 2 - 2D-1H$ (right) surfaces calculated by *I.A. Ruiz Alvarado*. The red marks correspond to the most favorable adsorption sites. Blue and orange spheres indicate In and P, respectively.

results, according to which no electronic nor chemical reactions could be identified upon the adsorption of molecular water.

As the UP spectra could reveal traces of remaining OH after the desorption of molecular water, the calculations were repeated with OH as potential adsorbate. At the bottom of Figure 6.7 potential energy surfaces are shown for OH adsorbed on the ideal 2D–2H surface (left) and the H deficient 2D–1H surface (right). The calculations indicate that OH adsorption is strongly favorable on the H deficient 2D–1H surface, but not at all on the intact 2D–2H surface where all adsorption sites are energetically unfavored. In case of the H deficient surface, the P dangling bond changes the adsorption energy not only

at the dangling bond site itself but also on all P atoms of the $2 \times 2 - 2D-1H$ surface lattice. The most favorable adsorption site, however, is at the P dimer dangling bond with an adsorption energy of almost -1 eV. With that the observed OH groups in the UP spectra could further indicate apparent P dangling bonds at the prepared P-rich InP (100) surface. The chemisorbed OH leads to a saturation of the half-filled dangling P orbital which results from H desorption. Band structure calculations reveal the midgap surface state is removed and the band structure of the $2D-1H-1OH$ resembles that of the $2D-2H$ without any defect. Even though the UP spectra reveal adsorbed OH groups at the surface preferentially adsorbing on the H vacancy site, the Fermi level position within the bandgap, and with that the surface band bending, remain unaffected after the adsorption of water, indicating that not all dangling bond defects could be passivated by the OH groups. This also confirms that the P dangling bond center itself is not the active site for water dissociation on the P-rich InP surface, because beyond the H vacancy as a stable OH site, a neighboring active site for the remaining H adsorption as a further product of H_2O dissociation is missing. The positive adsorption energy map for the intact $2D-2H$ surface (Figure 6.7 bottom left) confirms that the stabilization of an H and an OH adsorbed species at the two P dimer atoms is energetically unfavored. This is in good agreement with recent studies on In-rich InP (100), suggesting that free In sites are required for the dissociation of molecular water on InP surfaces.²³¹

From the findings on the P-rich InP (100) surface, it can be concluded that the electronic interaction with water is rather low. However, water dissociation may still occur at step edges rather than on terraces of this surface. As a future perspective, it would be interesting to expose this surface to acidic and basic aqueous solutions offering solvated H^+ or OH^- ions, which may strongly interact chemically to separated defect sites and may lead to a complete electronic surface passivation.

6.2 In-rich p-InP (100)

6.2.1 Electronic structure and surface states of In-rich p-InP (100)

The In-rich InP (100) surface has already been investigated theoretically by Schmidt et al.²³⁴. The surface reveals a (2×4) surface reconstruction which is stable for a wide range of preparation conditions. One day after the preparation of the p-doped In-rich InP (100) surface according to Section 4.2.2, the sample was transferred and analyzed at DAISY-FUN.

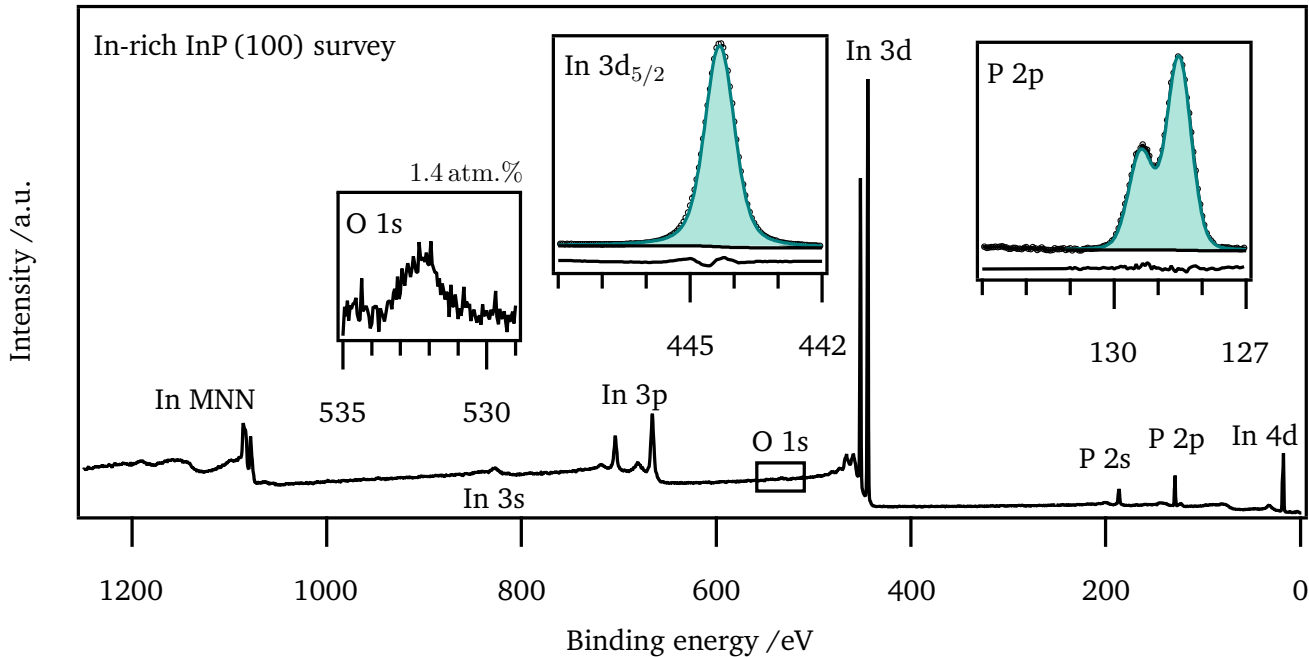


Figure 6.8: Survey XP spectra of In-rich p-InP (100) with detailed spectra of In $3d_{5/2}$ and P 2p core levels. The In $3d_{5/2}$ and P 2p core level can be fitted with a single component. Oxygen contamination after UHV transport to Darmstadt is visible in the O 1s signal.

Figure 6.8 shows the survey spectra of the as received In-rich p-InP (100) surface. Similar to the observation on the P-rich surface, the In $3d_{5/2}$ is located at $E_b=444.33$ eV and can be fitted with a single Voigt line showing a similar residual spectrum. However, with a FWHM of 0.80 eV the In $3d_{5/2}$ line is about 0.12 eV broader than observed on the P-rich surface. The P 2p line is found to be at $E_b=128.53$ eV and consists of only a single component. In contrast to the P-rich surface, no surface component can be detected. The FWHM is increased by the same value to 0.66 eV. The In $3d_{5/2}$ to P $2p_{3/2}$ energy difference is constant and seems to be independent of both surfaces, confirming that the bulk InP matrix is equivalent. Furthermore, the In-rich surface reveals slight traces of oxygen as surface contamination with a concentration of around 1.4 atm.%. With $E_b=532.1$ eV, the O 1s is attributed to OH species.^{235,236} However, oxidized indium or phosphates as surface species cannot be ruled out at these binding energy.^{222,237} From these results, it is not clear if the peak broadening in the core level lines finally results from the oxygen contamination or from the more complex surface reconstruction. In addition, the oxygen surface contamination leads to slight divergence of the 1:1 stoichiometry at the expense of In (42.3 atm.%) in comparison to P (56.3 atm.%). However, this could confirm that the O 1s signal results from an adsorbed oxygen species, as the more surface sensitive In 3d line is more damped by adsorbates than the P 2p signal.

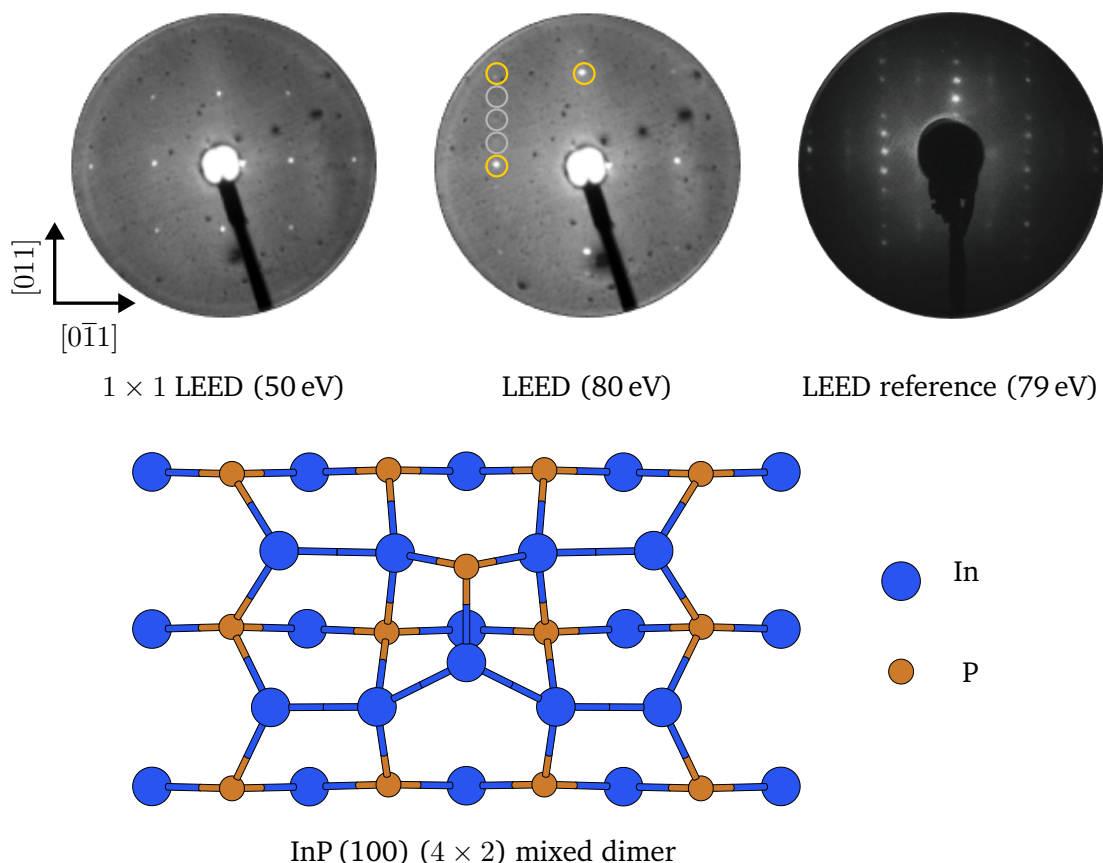


Figure 6.9: LEED images of as received In-rich InP (100) at 50 and 80 eV beam energies in comparison to an ideal LEED pattern from TU Ilmenau as published by Hannappel et al.¹¹¹. On the as received sample only a 1×1 surface reconstruction can be observed. Most stable InP (100) (2×4) mixed dimer surface reconstruction as shown below is indicated by reference LEED pattern.

Figure 6.9 shows the LEED pattern of the as received In-rich surface compared to the ideal oxygen free In-rich one as prepared at TU Ilmenau. The described mixed dimer 4×2 surface structure is shown below as previously described.^{234,238,239} In contrast to the P-rich surface, the ordered In-rich mixed dimer 4×2 surface is not stabilized by additional hydrogen.²¹⁹ However, the LEED pattern of the as received sample clearly shows a 1×1 pattern which differs from the typical 4×1 pattern with weak streaks in the twofold periodicity. This indicates the coexistence of 2×4 and $c(2 \times 8)$ domains^{234,240} as depicted in the reference pattern. 1×1 pattern (yellow circles) also have been reported for etched InP (100) surfaces.^{241,242} Nevertheless, the as received sample shows very weak reflexes in the $[011]$ direction (grey circles), which might still be assigned to remaining mixed dimer 2×4 domains.

The HeII VB spectra of the as received In-rich InP (100) surface is shown in Figure 6.10. Reference spectra of a clean mixed dimer 2×4 surface as well as an oxygen saturated surface are added according to the study of May et al.²²¹. The clean In-rich surface reveals four characteristic surface features.²⁴³ The highest occupied features have been investigated in detail by Frisch et al.²²⁶. The surface state S_1 results from a superposition of the σ bonds of the topmost In atom with the two cations below and a dangling bond of the top surface P atom forming the surface highest occupied molecular orbital (HOMO). S_2 is related to the In and P mixed dimers. These valence features can also be identified on the as received surface confirming intact 2×4 domains as assumed from the weak LEED pattern. For the mixed-dimer

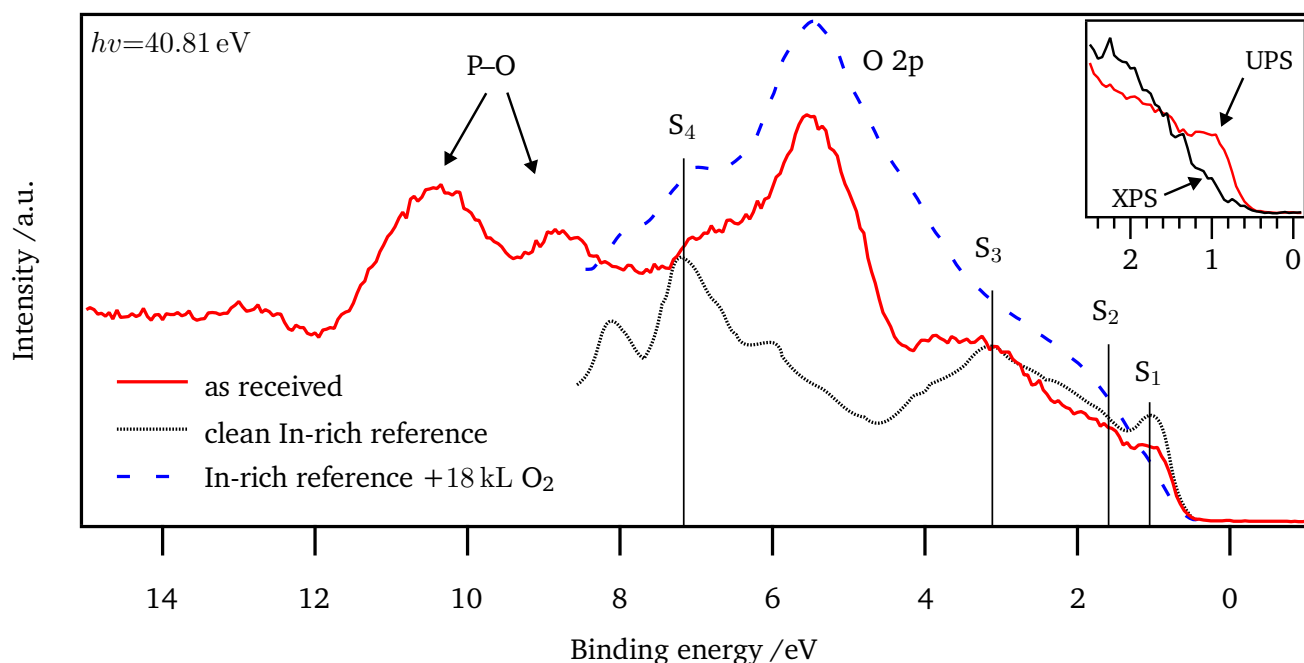


Figure 6.10: Hell spectra of received In-rich p-InP (100) with clean (black) and oxygen exposed (blue) In-rich reference spectra adapted from May et al.²²¹.

surface, the surface lowest unoccupied molecular orbital (LUMO) mainly consisting of In dangling bonds extend into the upper half of the bulk bandgap.^{244,245}

However, at binding energy regions of 5 to 7 eV, a clear O 2p-induced signal arises, which are most likely related to InO_x formation. Furthermore, two features at 8.7 and 10.5 eV show up and can most probably be assigned to P–O species,^{246,247} which have been identified as most favorable adsorption site for a single oxygen atom at the mixed-dimer In-rich surface.²⁴⁸ In addition, the 1π and 3σ bonds of OH might also appear at these energies.^{178,179}

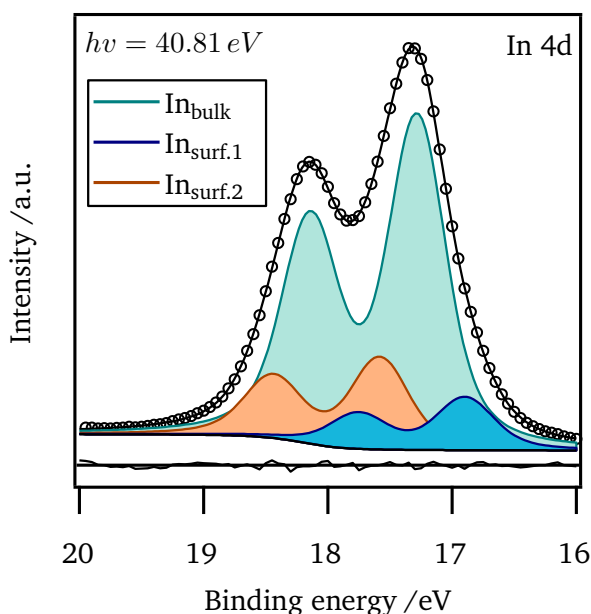


Figure 6.11: Deconvolution of surface sensitive In 4d line measured with Hell excitation.

Besides the valence band features, the UP spectra reveal a very surface sensitive In 4d line as shown in Figure 6.11. Apart from the main component related to the bulk In_{bulk} , two surface core level components can be deconvoluted with $\text{In}_{\text{surf.1}}$ shifted -0.39 eV to lower and $\text{In}_{\text{surf.2}}$ shifted $+0.47$ eV to higher binding energies. These surface core level shifts have already been observed on 2×4 GaAs²⁴⁹ as well as on $\text{InP}^{234,250}$ surfaces. Schmidt et al.²³⁴ suggest that $\text{In}_{\text{surf.2}}$ is attributed to an electron transfer from surface In to P, resulting in an empty dangling bond at the In site and a double occupied P dangling bond as postulated by the electron counting rule.²⁵¹ $\text{In}_{\text{surf.1}}$ is attributed to a relative electron accumulation compared to the phosphorous coordinated bulk In. $\text{In}_{\text{surf.1}}$ could therefore represent the In dimers at the mixed-dimer 2×4 surface. Consequently, the spectrum suggests an In-rich surface structure. The role of surface oxidation

is not clear in this specific case. May et al.²²¹ found that $\text{In}_{\text{surf.2}}$ increases after oxygen exposure while $\text{In}_{\text{surf.1}}$ disappears. However, for clean In-rich surfaces, $\text{In}_{\text{surf.1}}$ is reported to be slightly more intense than $\text{In}_{\text{surf.2}}$ which might indicate partial In oxidation.^{221,234} In conclusion, the overall valence spectra suggest that oxygen attacks both surface indium and phosphorous on the present InP surface indicating In–O and P–O surface species.

In conclusion, the as received In-rich InP (100) surface reveals oxygen contamination due to adsorbed oxygen. Nevertheless, the LEED pattern and valence band features show that there are still intact 2×4 domains of the clean surface. This is also confirmed by the SEE, which corresponds to a WF of 4.05 eV and is identical to the reported value for the clean surface.¹¹¹ The oxygen related adsorbates are therefore not completely covering the sample surface.

Surface band bending at the p-doped In-rich surface

The experimental XP VB spectra of the as received p-doped In-rich sample reveals the VBM at 0.74 eV below the Fermi level, which corresponds to a downward surface band bending of about 0.70 eV at the In-rich surface when considering a Zn doping concentration of $2.5 \times 10^{18} \text{ cm}^{-3}$. When analyzing the surface sensitive UP VB spectra, the surface state S_1 (Figure 6.10) reaches up to 0.45 eV below the Fermi level. With Zn as shallow acceptor dopant with an ionization energy of $\approx 35 \text{ meV}$,³⁸ the Zn dopants might get fully occupied by electrons from the occupied surface states S_1 , leading to a hole depletion at the In-rich surface since the DOS of the surface states is several times larger than the p doping concentration at the surface. Similar VB onsets have been found for intrinsic²²¹ as well as p- and n-doped^{111,243} In-rich surfaces. This affirms the observation that surface band bending is only observed on p-type samples due to Fermi level pinning at the upper half of the bandgap.

Density functional theory (DFT) band structure calculations of the In-rich mixed dimer 2×4 InP (100) and the impact of single oxygen atom adsorption have been investigated by Schmidt and Bechstedt²⁴⁴. Apart from the occupied surface states S_1 (Figure 6.10) appearing close to the VBM, no states appear inside the surface bandgap, suggesting an ideal electronic surface passivation on this specific surface domain. According to these first-principle DFT calculations, the highest occupied surface bands of the mixed-dimer 2×4 surface should appear below the bulk valence band edge.²⁴⁴ However, since the surface states S_1 are clearly observed above the VB edge, the experimental data indicate the presence of defective domains deviating from the intact In-rich mixed dimer surface structure. In this regard, it has to be noted that there also exists stable In-rich 2×4 surface reconstructions where the highest surface band appears above the bulk VBM (i.e. the top-P-dimer model or the $\alpha(2 \times 4)$ InP surface). In these cases the highest occupied surface band results from P dangling bonds at P dimers.²⁴⁴ For the P-rich surface, it was shown that there exists a certain probability of stable surfaces to form side domains in a concentration that these domains will determine the electronic properties of the overall surface. Therefore, the top-P-dimer and $\alpha(2 \times 4)$ configuration need to be considered as well when discussing the overall surface band bending of the In-rich p-InP (100) surface.

Apart from the clean In-rich surfaces, potential energy calculations show that the adsorption of a single oxygen atom on the In-rich surface is strongly favored on almost all surface atoms with adsorption energies down to -2 eV .²⁴⁸ The HeII spectra (Figure 6.10) clearly reveal oxygen contamination on the as received In-rich surface. O_2 has been reported to adsorb dissociatively on the surface breaking In–In and In–P bonds in order to form In–O–In and In–O–P bonds.^{221,252} First principle calculations show that adsorption of single oxygen atoms does not lead to surface states inside the InP bulk bandgap since surface dangling bonds are saturated.²⁵² The situation changes, however when partial surface oxidation is considered and oxygen substitutes surface atoms. Those defects lead to oxygen-induced gap-states

which appear in a broad distribution over the InP bandgap correlated with an oxygen coordinated P dangling bond.^{248,252} It is therefore not finally deduced if the observed surface band bending results from the clean In-rich surface or is due to partial oxygen adsorption as it has been observed for clean and oxygen saturated surfaces.^{111,221}

6.2.2 Reactivity of In-rich InP with water

From the analysis of the as received In-rich InP surface above, the conclusion can be drawn that the In-rich surface is far less stable than the P-rich surface, as it clearly revealed oxygen and hydroxy contamination even though transported from TU Ilmenau to TU Darmstadt under the same vacuum conditions as the P-rich surface. This gives a clear indication that the In terminated InP shows a strong interaction with residual water. To further investigate this interaction, a low-temperature water adsorption experiment was performed.

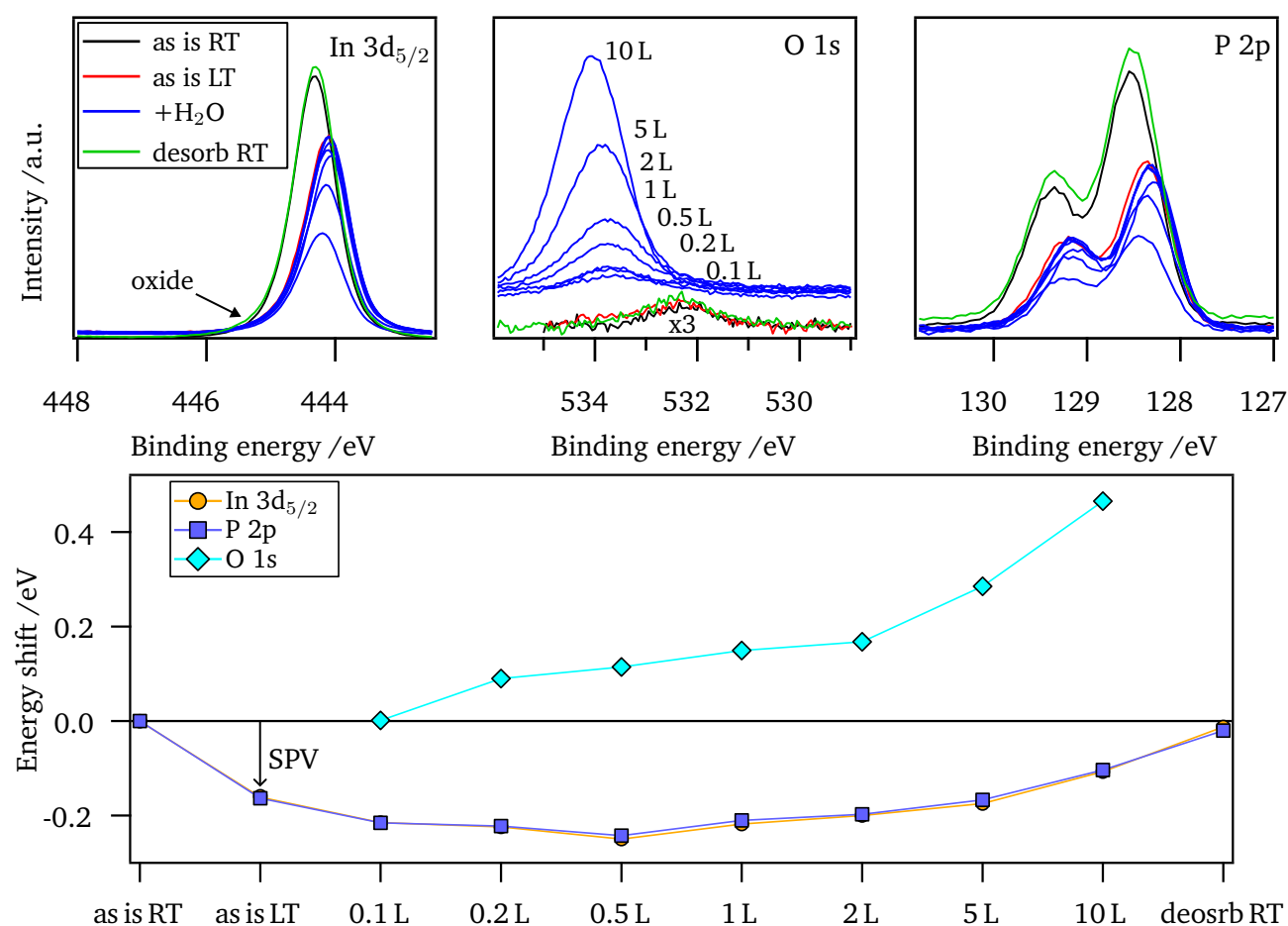


Figure 6.12: XP core level spectra of low-temperature water adsorption on as received p-doped In-rich InP(100) (top) with core level shifts after each adsorption step (bottom).

Figure 6.12 shows the XP core level spectra upon each adsorption step. After cooling, a source-induced SPV can be observed, that confirms a hole depleted space charge region at the In-rich InP surface. However, with an In 3d shift of 0.16 eV, the SPV is ≈ 110 meV lower than found on the P-rich InP surface, indicating a higher recombination rate of excess charge carriers. From the XPS data, it cannot be concluded if the

higher recombination rate results from the clean In-rich domains or the partial surface oxidation. In the submonolayer range of water adsorption, In 3d and P 2p show an energy shift of up to -90 meV towards lower binding energies. The SEE follows the core level shifts equally. This indicates either a reduction of surface band bending or an increase of SPV. Both is strongly related with a change of DOS distribution at the InP surface. In the multilayer (>1 L) regime, the In 3d and P 2p core levels follow the shifts of the O 1s line of the adsorbed water, which might be related mostly to a charging of the water adlayer as already observed on the P-rich InP surface. Interestingly, there are some fundamental differences when considering the charging of the adsorbates. First, the O 1s signal after the first adsorption step appears at $E_b=533.6$ eV, while on the P-rich surface the adsorbate starts to appear at 533.0 eV. Second, the charging in the multi-layer regime is far less pronounced on the In-rich surface (O 1s shift after 5 L: 0.3 eV) than on the P-rich surface (O 1s shift after 5 L: 0.8 eV). Both effects indicate that the interaction of the adsorbate with the substrate is significantly stronger on the In-rich surface, since the higher binding energies indicate a stronger bonding strength. Furthermore, the charge compensation by the emission of photoelectrons from the surface into the adsorbate is enhanced, indicating a better charge transfer. After the desorption of water, the In 3d and P 2p core level shift back to their initial position. However, the oxygen content seems to increase after the desorption of water to 2.1 atm.%. In addition, the In $3d_{5/2}$ line shows a shoulder at about 445.2 eV, indicating an oxidized indium species, while the P 2p spectrum does not show significant spectral changes.

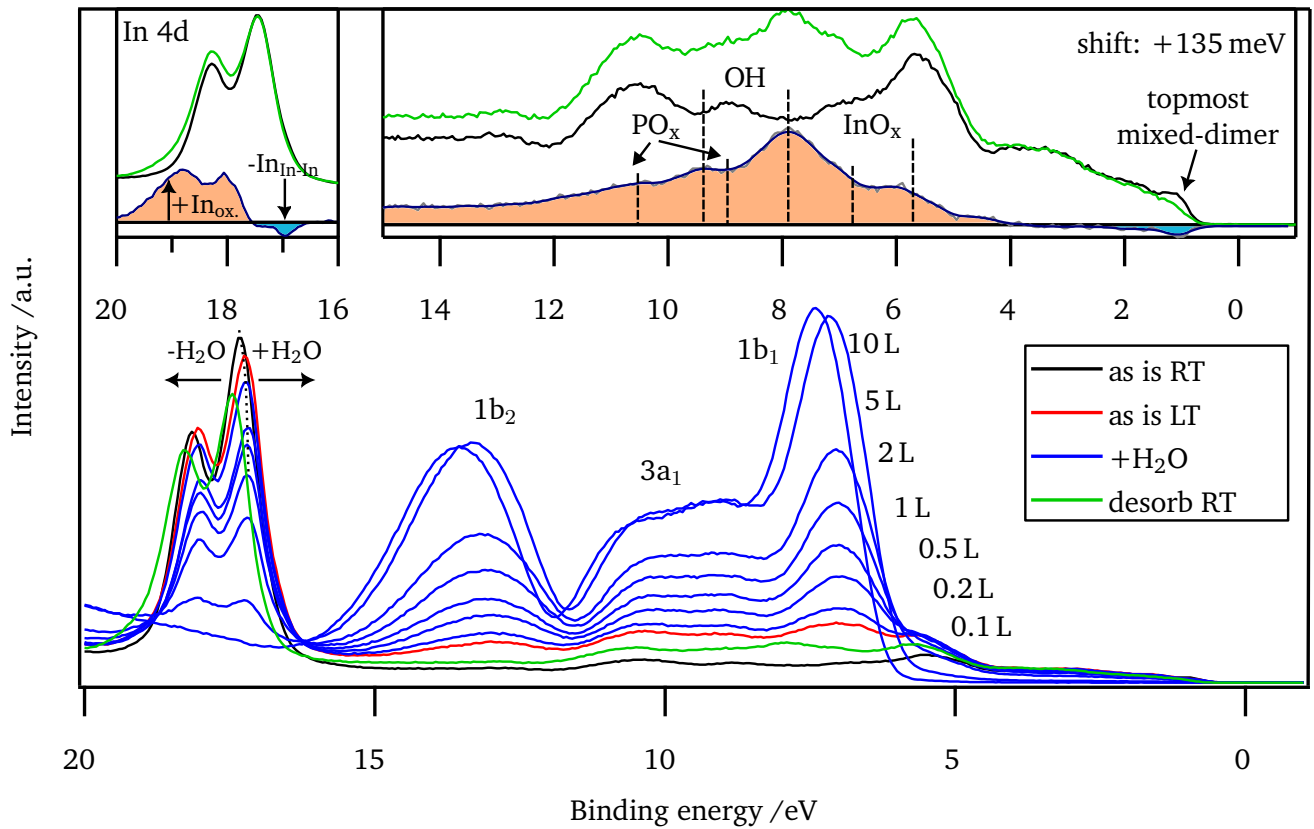


Figure 6.13: Monochromatic HeII spectra ($h\nu=40.81$ eV) of low-temperature water adsorption on In-rich InP (100). The difference spectrum of the In 4d line and the valence band before and after water adsorption are presented in the inset.

Figure 6.13 shows the HeII spectra of the In-rich InP surface after each adsorption step. Already

after the cooling of the sample, the three HOMO features of molecular water appear at $E_b(1b_1)=7.0$ eV, $E_b(3a_1)=9.0$ eV, and $E_b(1b_2)=13.1$ eV and with that at about 0.5 eV higher binding energies than at the P-rich InP surface. Accordingly, the UP valence features of the molecular water follow the trend of the higher binding energy in O 1s as observed in XPS. With the He lamp as excitation source, the core level shift of the In 4d line of about 80 meV due to the source-induced SPV is far lower than observed in XPS, confirming the assumption that the recombination rate of photogenerated charge carriers is remarkably higher on the In-rich surface in comparison to the P-rich surface, where no difference in SPV shift between XPS and ultraviolet photoemission spectroscopy (UPS) could be observed. Furthermore, the In 4d shows a slight shift of 40 meV towards lower binding energies as observed with XPS, indicating a reduction of surface band bending upon water adsorption. This is in contrast to the as received low temperature spectrum, where no spectral changes in the valence states apart from the three rising HOMO features of molecular water can be observed. Neither the highest occupied surface band S_1 nor the In 4d level reveal spectral changes. This changes however, when comparing the spectrum at room temperature with the low temperature spectrum and is even enhanced in the spectrum after desorption. These changes are indicated by the inset in Figure 6.13. It can be concluded that low temperature adsorption kinetically hinders chemical surface reaction. This is in good agreement with first principle calculations, according to which the dissociation of the H_2O molecule on the mixed-dimer surface is favored but reveals an energy barrier of about 0.87 eV.^{231,232} The observed reduction of surface band bending due to an electron depletion at the surface is therefore related to a weak electronic bonding interaction of surface atoms with the intact H_2O molecule. The most favorable H_2O adsorption site on the mixed-dimer surface has been found on the dangling In bonds forming weak In–O bonds when the water donates electrons from its $1b_1$ orbital into the unoccupied In dangling bond.^{231,244} However, according to this interaction an electron injection rather than an electron depletion would be expected to be observed upon water adsorption. From another perspective, this effect shifts the anti bonding surface states of the dangling In bonds beyond the InP band edges, which could also lead to an elimination of recombination centers at the InP surface. Accordingly, the shift of core levels to lower binding energies could be interpreted as an increase of source-induced SPV. This consideration is supported by the fact that the observed core level shifts in XPS are larger than observed with UPS, where also a small SPV has been observed.

However, the initial surface oxidation might play a role when the surface interacts with the molecular water, too. In another study it was found, that partial surface oxidation leads to oxygen coordinated P, leading to “O-modified P dangling bonds”,²⁴⁸ which appear as a half-filled defect band inside the InP bandgap as observed similarly on the P-rich surface. In this case, the saturation of these P dangling bonds by molecular water could passivate some surface states causing the slight Fermi-level shift towards the VBM. In summary, it cannot be concluded from the present data which effect causes the core level shifts. Not even local temperature fluctuations can be ruled out causing the small core level shifts in this case.

As mentioned above, spectral changes before and after the water adsorption experiment that indicate surface reactions are only observed at finite temperatures. The UP spectra clearly shift to higher binding energies by about 135 meV, indicating an increased surface band bending to ≈ 0.84 eV after the exposure to water. The fact that this shift was not observed with XPS is assigned to a not fully warmed-up surface during the XPS measurement, leading to an enhanced SPV. The In 4d core level shift corresponds to a quenching of the surface state S_1 , indicating that water attacks the top In-P mixed-dimer. Wood et al.²³² suggest that the mixed dimer is the active site for H_2O dissociation. Alvarado Ruiz and Schmidt²³¹ calculated that the favorite dissociation ends up with an hydroxyl group bonding to In-In dimers forming In–O–In bonds whereas the remaining hydrogen atom is bound to the top P atom at the mixed-dimer, which is also in good agreement to experimental data.²²¹ However, as S_1 also consists of interactions of the topmost In mixed-dimer and the second-layer In, the present UP spectra suggest that the mixed-dimer

surface is destroyed. Furthermore, no LEED pattern can be observed after water exposure on the In-rich InP surface, confirming a loss of surface order. The In 4d line shows a reduction of the surface component $\text{In}_{\text{surf},1}$ of the initial spectra (Figure 6.11) which is assigned to a breaking of In dimers, while the oxidized surface component increases and therefore suggests that oxygen or hydroxyl is inserted to form In–O–In bonds. However, the VB spectra reveal clear indications of surface hydroxylation with the distinct 1π and 3σ features at 7.9 and 9.4 eV.¹⁷⁹ However, the O 2p features at 5.9 eV and 6.9 eV are most probably related to In–O formation,^{230,253,254} while the two components at 8.9 and 10.9 eV might be assigned to P–O.^{246,247} Interestingly, the WF simply follows the core level shifts with a final value of about 3.95 eV, indicating no significant change of the surface dipole due to the surface oxidation.

As final conclusion, the exposure of the partially oxidized In-rich InP surface leads to further surface oxidation with clear indications for In–O–P and In–O–In formation, indicating substitutional adsorption of oxygen on the surface. The chemical interactions are limited to the top surface layer, as no spectral changes in XPS could be identified. The Fermi level shift after water exposure, identified by a rising downward surface band bending, might be assigned therefore to oxidized P dangling bond centers, that lead to an electron accumulation at the surface as observed for oxidized P_b centers in Si. Neither molecular nor dissociative adsorption of water on the mixed-dimer InP (100) surface give rise to midgap states in the InP bandgap.²³¹

6.3 O-rich InP

6.3.1 Surface composition of native oxide terminated InP (100)

For reference reasons, the interaction of an oxidized p-InP (100) wafer, as supplied by *Wafer Technology Ltd.* with water was investigated as well. The wafer was specified with a Zn doping concentration N_{ac} of 6.2×10^{16} to $1.0 \times 10^{17} \text{ cm}^{-3}$. Thermally grown as well as native oxide formation on InP has been extensively investigated in literature.^{255–257} As there exists an comprehensive internal study on etched III-V surfaces by Hajduk et al.²⁵⁸, this chapter will not cover the exact determination of chemical surface species and composition in detail.

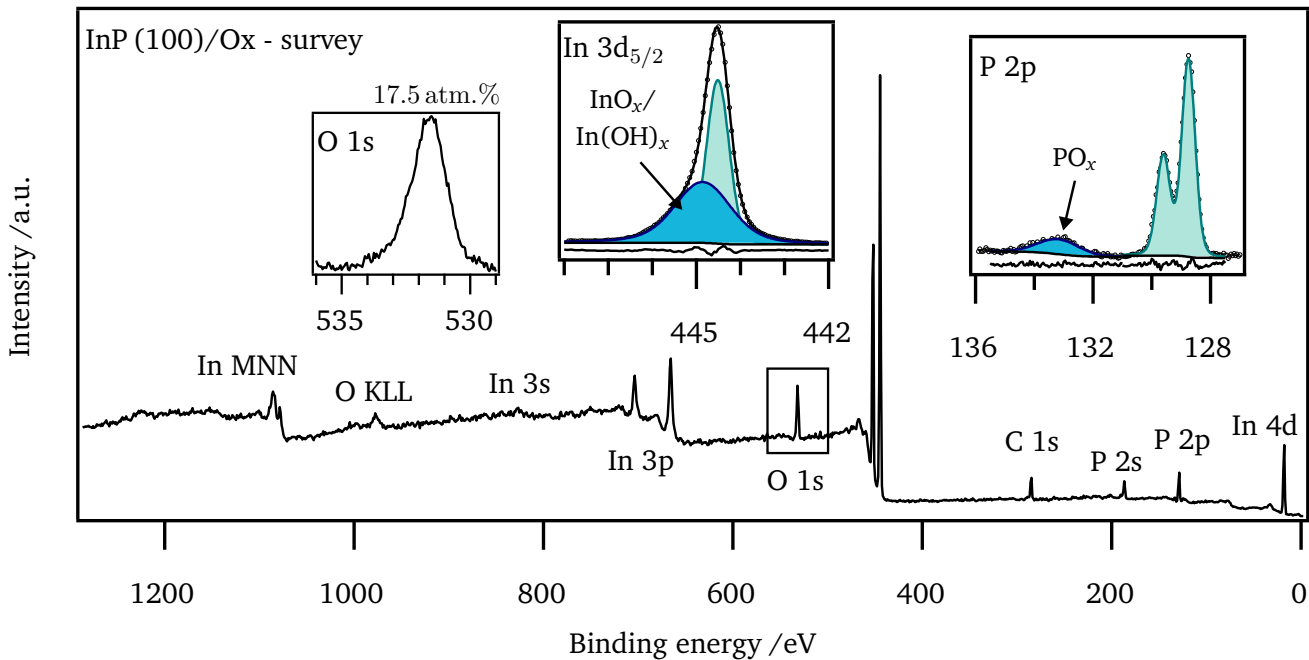


Figure 6.14: Survey XP spectra of a commercial native oxide terminated InP (100) with detailed spectra of O 1s, In 3d_{5/2} and P 2p core levels. The In 3d_{5/2} and P 2p core levels cannot be fitted with a single component. A top oxide layer leads to additional components in the In 3d and P 2p core levels.

Figure 6.14 shows the survey spectrum of an InP (100) wafer covered with a thin oxide layer. Beside their bulk components, the core level of In 3d_{5/2} and P 2p clearly reveal oxidized surface components at higher binding energies. According to Hofmann et al.²⁵⁹, these components mainly result from In(OH)₃ and InPO₄ species and are less of In₂O₃ character. Stoichiometry calculations reveal still an In:P ratio of $\approx 1 : 1$ (In:29.5 atm.% and P:28.3 atm.%) with an oxygen content of about 17.5 atm.%. However, as there is still a remarkable amount of adventitious carbon contamination with C 1s at $E_b = 285.05 \text{ eV}$ (24.7 atm.%), the analysis of O 1s with its maximum at 531.55 eV becomes difficult. The In 3d_{5/2} maximum of the wafer is located at 444.51 eV while the In related oxide species superimpose as a broad spectral contribution on the bulk related spectrum indicating different components. Interestingly, the main P 2p line consists of a very sharp bulk component at 128.75 eV, which can be fitted with the same line width as the clean P-rich surface (FWHM=0.54 eV) but does not show any subspecies. This is in good agreement to former investigations, that suggest a low temperature grown oxide forms an In-rich interlayer at the very InP/oxide interface.^{255,259} The oxidized phosphate species appear at about $\approx 133 \text{ eV}$ and can be separated fully from the main line.

The XPS VBM is found to be at 0.96 eV, indicating an inversion layer at the surface of the p-InP wafer due to the native oxide as similarly observed on oxide-passivated Si. The VB cut-off is therefore consistent with the higher core level binding energies in comparison to the reconstructed InP surfaces before. According to the doping concentration and Equation 6.1, the surface band bending is about 0.83 eV. Two years ago, Hajduk et al.²⁵⁸ found on the same wafer a surface band bending of 0.51 eV, indicating that wafer ageing leads to a further hole depletion at the surface. However, the VB offset between the crystalline InP and the top oxide layer, which is according to UPS measurements found at 3.85 eV, seems to be independent of ageing and is 2.91 eV. The WF from XPS SEE is 4.14 eV and therefore does not indicate any change in surface dipole due to ageing. In comparison, other studies found even higher core level binding energies for Zn doped p-InP with similar doping concentrations.^{256,257} It is still not fully clear, if these pinning levels result from intrinsic P or In vacancies,²⁶⁰ In_p anti-sites²⁶¹ or even from the shallow donor levels of In₂O₃ revealing a high charge carrier concentration.²⁶²

6.3.2 Electronic interaction of O-rich InP with water

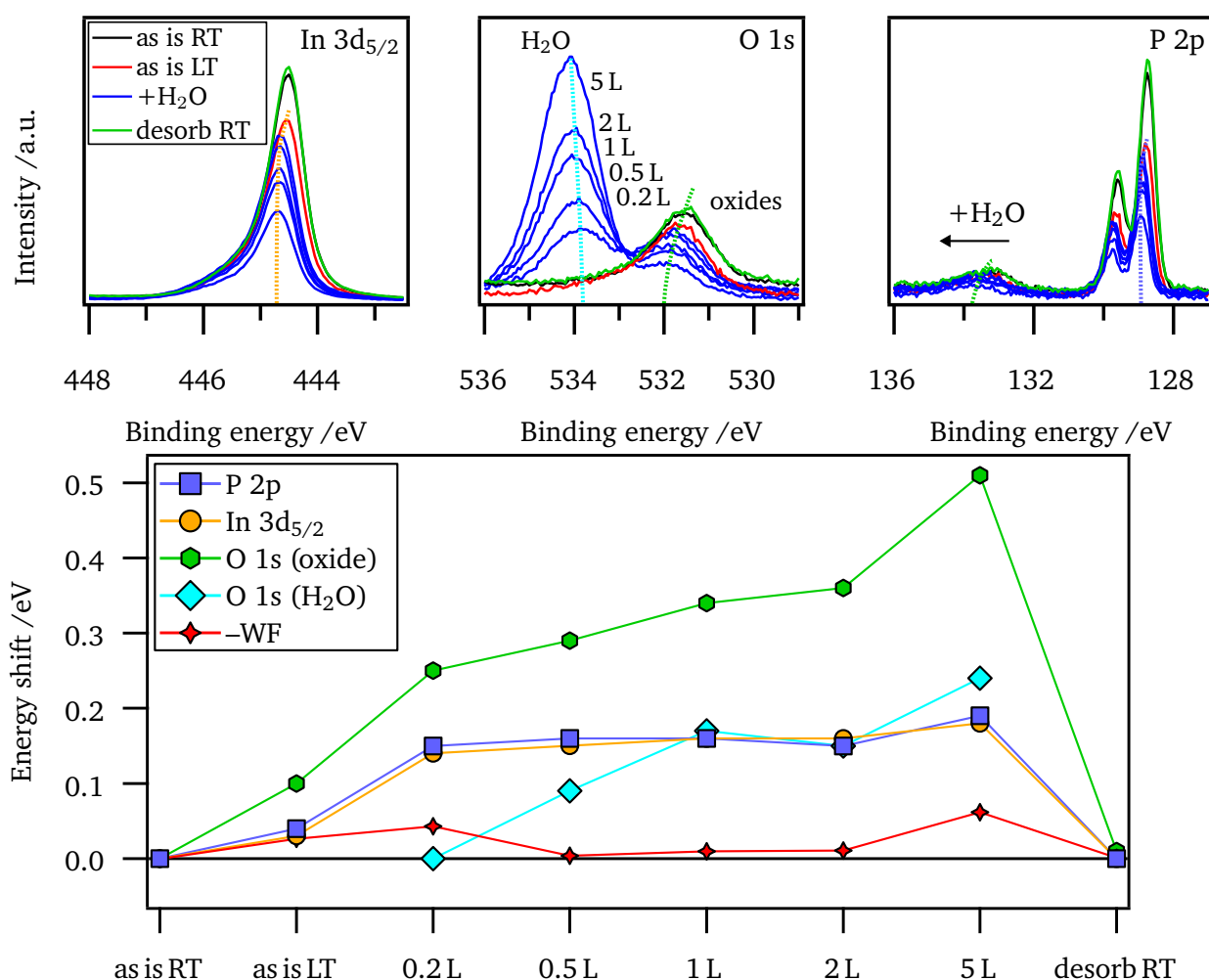


Figure 6.15: XP core level spectra of of low-temperature water adsorption on oxygen terminated InP (100) wafer (top) with core level shifts after each adsorption step (bottom).

In the following, the core levels of oxygen terminated InP upon water adsorption were analyzed (Fig-

ure 6.15). The adsorption experiment reveals clear differences in comparison to the reconstructed P- and In-rich surfaces above. After cooling, the In $3d_{5/2}$ and P 2p do not show the expected energy shift to lower binding energies due to source-induced SPV, which should lead to a more flat-band like situation. The lack of SPV due to the native oxide layer indicates a strong Fermi level pinning with a high recombination rate of excess charge carriers, which are expected to be separated at the strongly depleted p-InP surface. Rather than a decrease, an increase in binding energy during the cooling is observed (+30 meV). The HeII measurements show that a low amount of residual water already adsorbs during the sample cooling procedure (Figure 6.16). The first intentional adsorption step (0.2 L) shows a further shift in binding energy +120 meV of the main In $3d_{5/2}$ and P 2p level indicating that the water adsorption itself causes an increase in hole depletion at the InP surface. For further water coverage (>0.5 L), the InP substrate components seem to be constant in binding energy. In contrast to that, the oxide-related component in the O 1s line shows a continuous shift for higher water coverages following the O 1s shifts of the H₂O adsorbate, which is most probably related to adsorbate charging. The O 1s of the H₂O adsorbate on the oxidized InP reveals the highest binding energy of 533.85 eV in comparison to the reconstructed surfaces, therefore indicating an even stronger substrate interaction than on the In-rich InP surface. Interestingly, the SEE, which is proportional to $-\Phi$, not just simply follows the binding energy, therefore indicating a change in the ionization potential I_P due to a change in the surface dipole δ counteracting the Fermi level shift and keeping the WF almost constant for the whole experiment. The WF shift in the multi-layer regime (>2 L) confirms the charging in the adsorbate layer. The oxide-related component in the P 2p signal follows mostly the oxide related O 1s signal, which increases the distance to the main line with higher water coverages. Furthermore, the oxide-related shoulder of In $3d_{5/2}$ at about 455.5 eV also shifts from the main line. In both cases, it is assumed that the potential drop due to the charging ice layer causes the oxide shifts rather than a chemical surface reaction indicating a dielectric and capacitive character of the native oxide components. This assumption is also confirmed by the HeII spectra upon water adsorption in Figure 6.16. Apart from the molecular water features $1b_1$, $3a_1$, and $1b_2$, which start to appear at 7.0, 9.0 and 13.1 eV, no spectral changes can be observed. As expected for an *ex situ* sample, the spectra before and after the water adsorption experiment look the same.

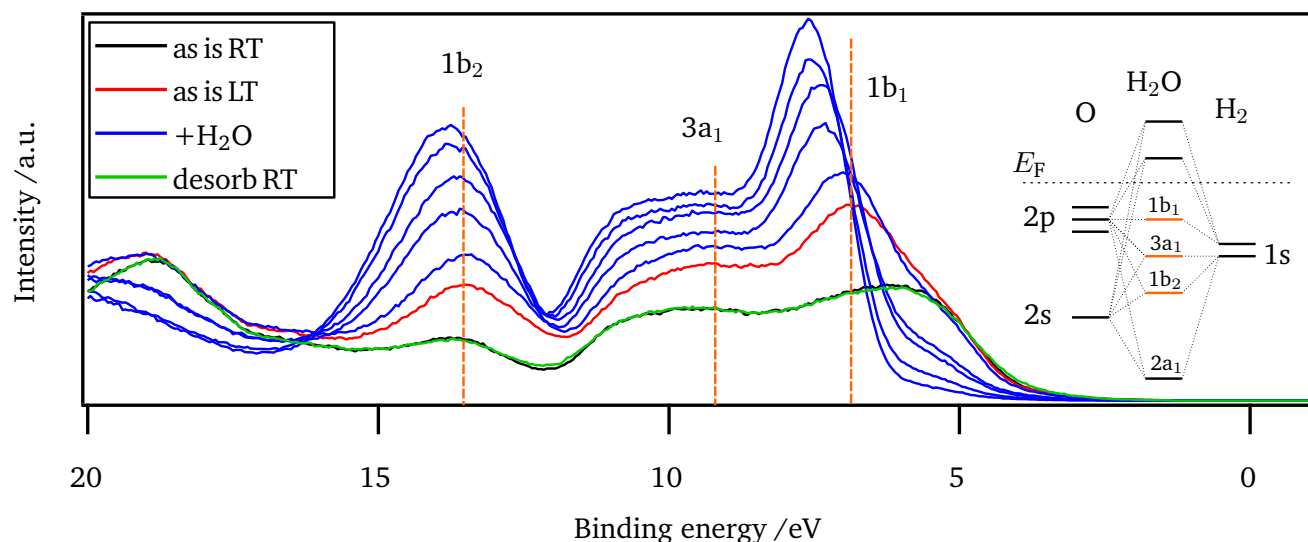


Figure 6.16: Monochromatic HeII spectra ($h\nu=40.81$ eV) of low-temperature water adsorption on oxygen terminated InP (100).

6.4 Final conclusion on InP surfaces in contact to water

In this chapter, the electronic surface properties of differently terminated InP surfaces were compared. In addition, possible charge transfers upon water adsorption were examined. The results are summarized in band energy diagrams without and with H₂O interaction shown in Figure 6.17.

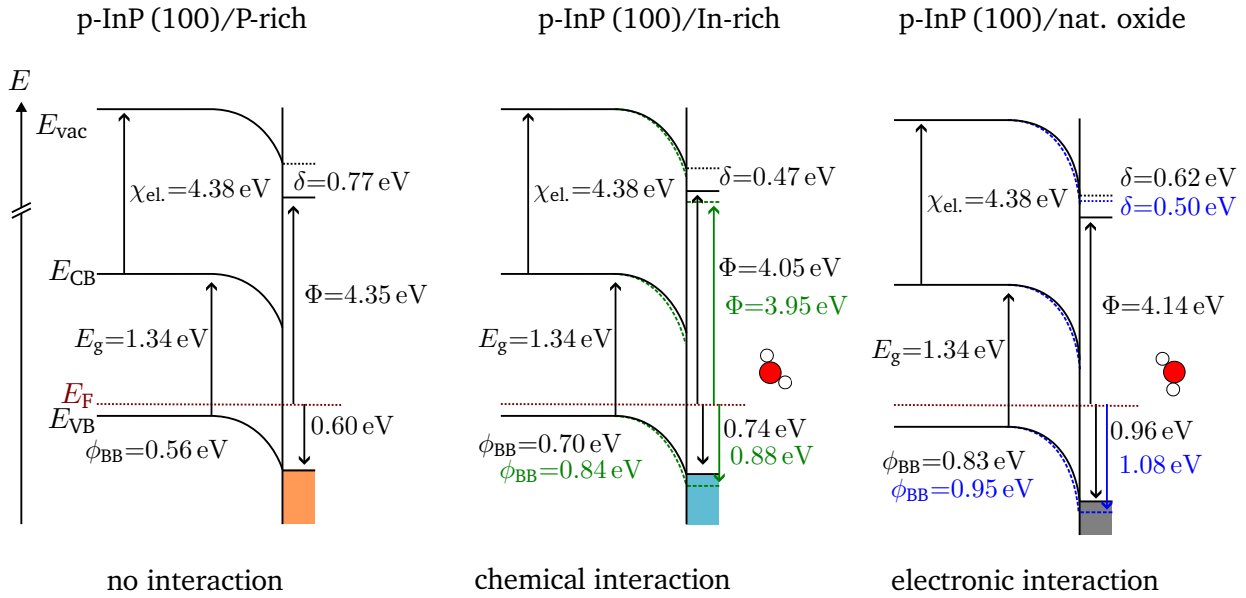


Figure 6.17: Electronic band energy diagrams of different p-InP (100) surfaces before and in contact with water. For P-rich InP, no interaction with H₂O could be identified. In-rich InP reveals a chemical surface reaction only at room temperature after H₂O exposure (green). Electronic interaction during low-temperature water adsorption (blue) was only observed on oxygen passivated surface. Values for E_g and $\chi_{el.}$ were taken from Schmidt³⁸.

The P-rich $2 \times 2 - 2D - 2H$ surface seems to be very stable during the UHV transport to Darmstadt. No surface contamination could be identified and the sample clearly revealed a 2×1 LEED pattern. In contrast to that, the In-rich sample showed to some extent surface oxidation. However, besides the clear 1×1 LEED pattern, the expected 2×4 surface reconstruction of the stable mixed-dimer surface could only be guessed from very weak spots in the LEED images after the sample transfer, indicating a higher tendency to surface oxidation. However, both surfaces showed a remarkable amount of surface band bending due to a hole depletion at the surface. For the P-rich InP, it is shown that the pinning level coincides with a P dangling bond defect level due to partial hydrogen desorption. Furthermore, it is shown that neither the clean surface reconstruction nor the defect itself interacts with molecular water. In case of the In-rich surface, it could not be clarified if the hole depletion results from the incorporation of oxygen causing donor levels or from other coexistent surface reconstructions. However, it is shown that upon low temperature water adsorption, no charge transfer could be identified. Only during cooling and warming Fermi level shifts could be identified as caused by chemical bond formation with oxygen that lead to further hole depletion. An *ex situ* InP wafer covered with a native oxide layer exhibited an even higher surface band bending caused by wafer ageing. However, upon low-temperature water adsorption, a clear electron injection of more than 100 meV is found, which is completely reversible after the desorption of molecular water and is associated with a change of the surface dipole moment δ .

7 TiO₂ as electrochemical buffer layer

In the previous two chapter model surfaces of Si and InP have been found to remain rather defective, leading to barrier formation and impede the charge transfer towards the surface. Furthermore, it was shown that the direct contact of the Pt-catalyst induces defects as well as Schottky barriers in photocathodes. This raises the question, if a suitable interlayer can improve the surface and interface properties investigated so far.

This chapter is dedicated to the investigation of TiO₂ as a passivation interlayer for photoelectrochemical interfaces. The requirements for an ideal passivation layer are quite challenging and often involve conflicting objectives. On one hand, the passivation layer has to protect the photoabsorber from corrosion and should ideally have minimal light absorption, which typically requires insulating optical properties. On the other hand, the passivation layer should facilitate efficient electronic charge transport without significant losses, which necessitates high charge carrier transfer rates.

In principle, one can follow two different design strategies, when considering TiO₂ as passivation layer on photoelectrochemical electrodes. On the one hand, a thick TiO₂ layer could ideally chemically passivate the semiconductor, which might enhance performance and life time of the photoelectrode. In this case, apart from the interfacial band alignment between the photoabsorber and the TiO₂, the conductance and optical properties of the TiO₂ bulk phase play a decisive role for the overall performance. On the other hand, a very thin and completely covering TiO₂ film composed of a few mono layers could also act as tunnel barrier for charge carriers, for which the Fermi level pinning mechanisms at the interface will dominate the overall performance. In this regard, TiO₂ deposited by atomic layer deposition (ALD) has been pointed out as promising passivation layer in terms of stability^{54,55} and efficiency optimization.^{21,263}

The chapter covers the electronic band alignment during interface formation between photoabsorber and ALD-TiO₂. Furthermore, the electronic bulk properties of sputter deposited TiO₂ is presented in dependence on oxygen stoichiometry.

7.1 Interfaces to ALD-TiO₂

ALD offers a distinct advantage in producing high-quality thin films if the alternating exposure of precursors is optimized by unique process controlling. It allows in principle the deposition of highly conformal thin films with precisely defined layer thicknesses. It can be used to coat not only flat substrates but also complex materials with a high aspect ratio such as nanostructures²⁶⁴ or three-dimensional surfaces.^{84,265} The ALD process used in this section was established and developed by Thorsten Cottre¹¹².

7.1.1 The p-Si/SiO₂/TiO₂ interface formation

During the step-wise ALD deposition of TiO₂ on a native oxide passivated p-Si/SiO₂ substrate, a growth rate of 0.8 Å/cycle is assumed,¹⁷⁷ which is about 25 % of a monolayer.⁸⁶

XPS core levels as well as core level shifts depending on the number of ALD cycles are depicted in Figure 7.1. The Ti 2p spectra exhibit clear peaks at approximately $E_b=459.7$ eV, which shift towards

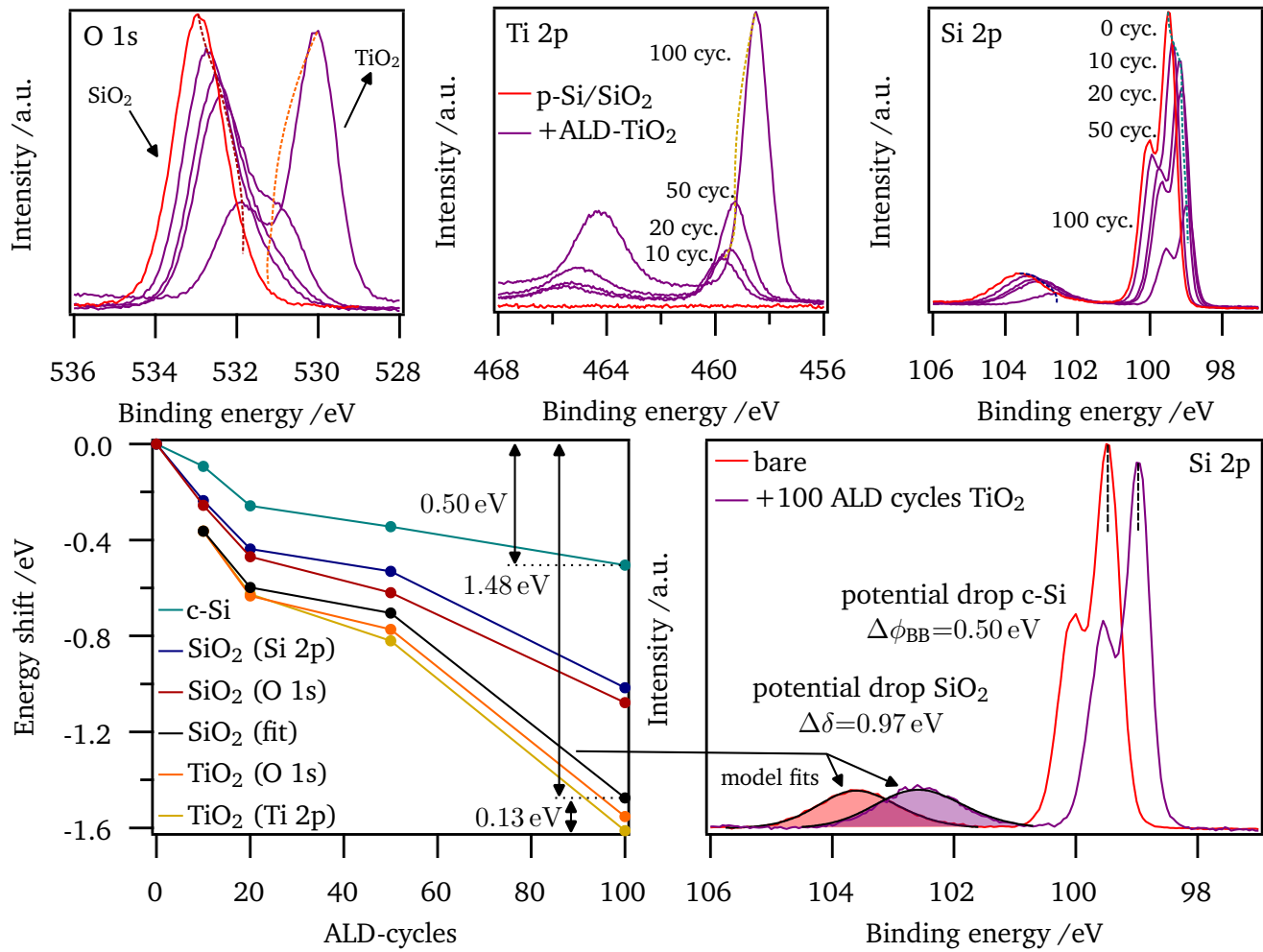


Figure 7.1: XPS core level spectra of ALD grown TiO₂ on top of native oxide terminated Si/SiO₂ (top). Energy shifts and potential drop models are shown at the bottom.

lower binding energies with increasing TiO₂ layer thickness, reaching 458.5 eV after 100 ALD cycles. The initially depleted p-Si/SiO₂ substrate also displays a shift towards lower binding energies, eventually reaching $E_b=98.98$ eV. The Si 2p and O 1s components related to SiO₂ show larger shifts of approximately -1.0 eV upon contact formation with TiO₂, and this shift is also evident in the emerging TiO₂ related O 1s signal being finally located at 530.0 eV. Applying the potential corrected line shape model to the SiO₂ related Si 2p contribution presented in Section 4.1.2, a dipolar potential drop of -0.97 eV is identified at the p-Si/SiO₂/TiO₂ interface. In contrast to the interface to platinum, the SiO₂ phase reveals no hints for a chemical reduction, thus there is no indication for the interdiffusion of both oxide phases. Furthermore, the fitted potential drops follow the TiO₂ related Ti 2p and O 1s energy shifts. All in all, an overall contact potential of 1.6 eV dropping at the p-Si/SiO₂/TiO₂ interface is detected. About 0.5 eV of the contact potential are dropping in the p-Si space charge region (SCR). However, the Fermi level is not coinciding with the valence band maximum (VBM), which would indicate an accumulation layer within the p-Si SCR. According to the Si 2p_{3/2} binding energy, the Fermi level position is located 0.24 eV above the Si VBM upon contact with ALD-TiO₂, indicating a pinning at that position. As already calculated for the interface to Pt, the potential drop of 1.0 eV over the SiO₂ layer, requires about $1.3 \times 10^{-13} \text{ cm}^{-2}$ ionized donors (Equation 5.7). As no additional defects are observed by the contact formation and the pinning level

coincides with the P_b dangling bond center, unoxidized dangling Si bonds are still the dominating defect remaining at the Si/SiO₂/TiO₂ interface. The high contact potential as well as the high work function (WF) of 6.3 eV shows a highly oxidized TiO₂ phase with a low charge carrier concentration.²⁶⁶ However, since at maximum 0.13 eV of the contact potential drops in the TiO₂ phase, almost no band bending is expected to form inside the thin TiO₂ layer. Significant amounts of chlorine found for these samples as well as the slight decrease in Ti 2p to O 1s energy difference of 71.54 eV compared to 71.29 eV,²⁶⁶ suggests that about 6 % of the TiO₂ layer contain unreacted TiCl₄ precursor, which increases for even lower layer thicknesses. This suggests a precursor accumulation at the very interface. Additionally, Bronneberg et al.²²³ found an increased content of Ti³⁺ at the very first TiO₂ interlayer indicating a different chemical environment at the very SiO₂/TiO₂ interface.

The results suggest that the reaction process is highly influenced by the pumping power utilized during the ALD process. In another p-Si/TiO₂ deposition, the TiCl₄ content in the TiO₂ layer could be reduced to about 2 %. As a result, the WF is found to be 4.78 eV. Accordingly, 0.23 eV are dropping in the p-Si SCR leaving to a pinned Fermi level 0.51 eV above the VBM which is located very closely (0.1 eV) below the charge neutrality level (CNL) of unoxidized P_b centers. Furthermore, about 0.53 eV are dropping in the SiO₂ phase, leaving to an overall potential drop of 0.76 eV which equals the measured differences in WF. The Ti 2p_{3/2} and O 1s emissions are found at 459.16 and 530.65 eV, which is associated to a valence band (VB) onset of 3.1 eV.²⁶⁶ With an optical bandgap of 3.1 eV,¹¹² the TiO₂ layer is highly n-doped while Mott-Schottky analysis reveals charge carrier concentrations of $1 \times 10^{-19} \text{ cm}^{-3}$.¹⁷⁷ The high charge carrier concentration is also the reason why almost no band bending is observed in the TiO₂ layer.

As a conclusion, it has to be mentioned that the processing condition of the ALD deposition is decisive for the interfacial band alignment of the TiO₂ covered photocathode. Unreacted TiCl₄ precursor leads to huge interface dipoles, that leads to an electron depletion of P_b centers. At the cathodic side, unoccupied P_b states will be highly active for the recombination of excess photoelectrons, as electrons can be captured at those empty states. The optimization of the ALD process leading to a complete reaction of precursors without severely affecting the substrate is therefore important for a considerable photoconversion efficiency of the electrode.

In order to oxidize remaining ALD precursor, the impact of an post-annealing treatment under oxygen atmosphere as well as the contact formation to Pt has been tested as presented in Section 8 in the Appendix. However, the interpretation of this data remain difficult due to multifactorial influences.

7.2 Band alignment of p-InP/ALD-TiO₂

In this Section the metal organic vapor phase epitaxy (MOVPE) prepared P- and In-rich InP (100) surfaces presented in Chapter 6 are used to investigate the ability of surface passivation by defined ALD-TiO₂ layer coatings. In the past, TiO₂ has been successfully used to improve device efficiency of InP photocathodes.^{55,263}

7.2.1 Initial ALD growth of TiO₂ P-rich InP (100)

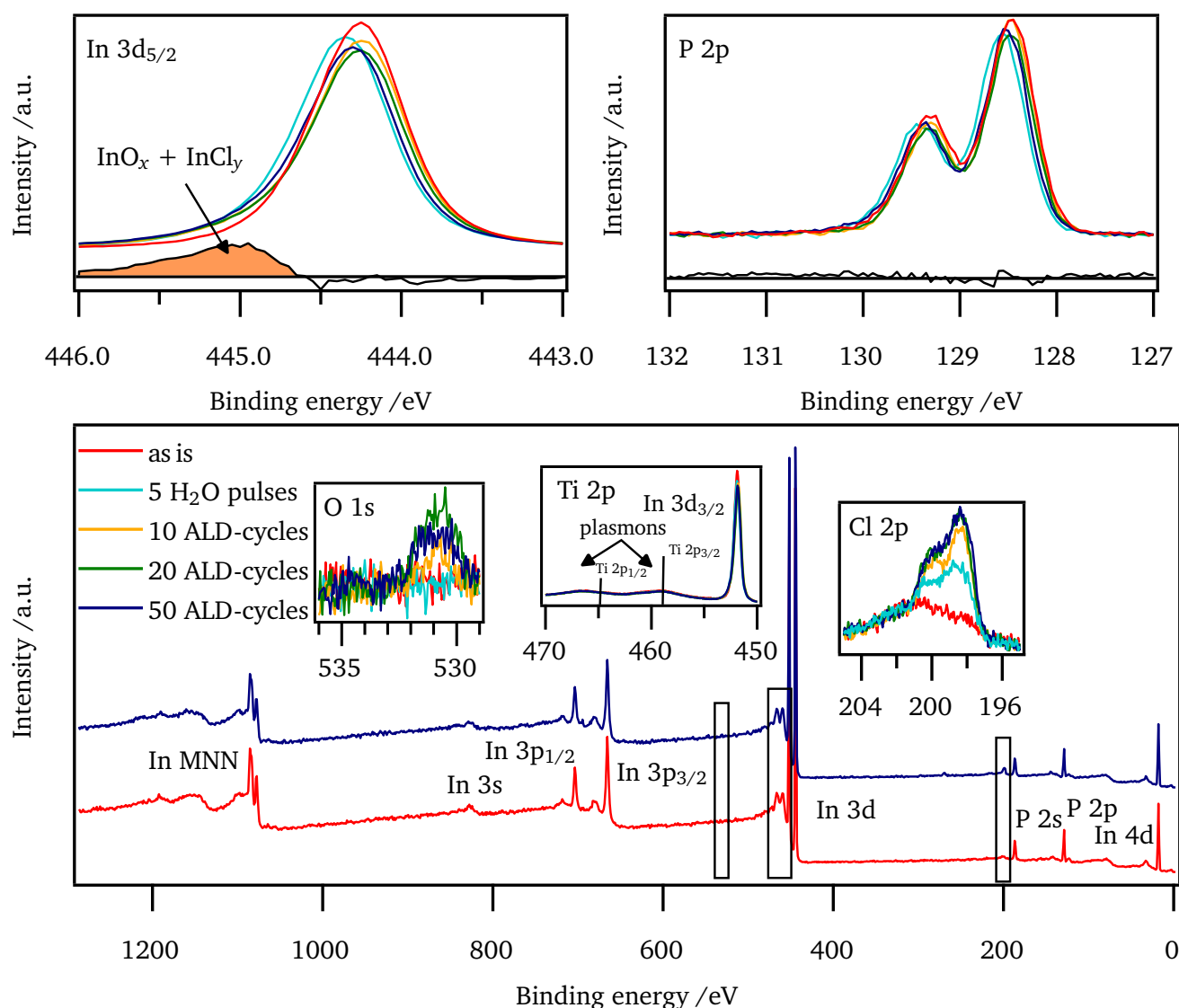


Figure 7.2: XPS In 3d_{5/2} and P 2p core levels (top) with survey spectra (bottom) after 5 ALD half, and 10, 20, and 50 ALD full cycles. Detail spectra of Ti 2p and O 1s insets do not indicate TiO₂ nucleation, although Cl contamination is observed.

The water adsorption experiment presented in Section 6.1 could show that the P-rich InP (100) surface is rather stable upon water adsorption up to partial water pressures of 10^{-7} mbar. The ALD process for TiO₂ deposition uses H₂O as oxygen agent to hydroxylate the surface in an initial step. In order to investigate the initial growth processes at the InP/TiO₂ interface, extensive water exposure as well as up to 50 ALD-cycles were analyzed (Figure 7.2). In a first step, 5 consecutive pulses of H₂O were investigated, which corresponds to 5 ALD half cycles. The exposure to water in the mbar range surprisingly did not lead to complete destruction of the 2×1 surface reconstruction as observed in the low-energy electron diffraction (LEED) pattern (Figure 7.3). Nevertheless, the LEED pattern becomes more indistinct and the diffuse streaks in the $\times 2$ half-order, which were characteristic for the $2 \times 2 - 2D-2H$ structure, can no longer be fully resolved. The water exposure leads to a weak shift of the In 3d and P 2p core levels to higher binding energies ($\Delta E_b \approx 0.1$ eV). According to the O 1s spectra however, there is no indication for surface oxidation, but there is a clear indication for Cl contamination coming from remaining ALD process products in the gas pipes. Nevertheless, as there is no Ti signal observed on the InP surface, it is expected that Cl results from HCl contamination. Even when starting the complete ALD process by running 10,

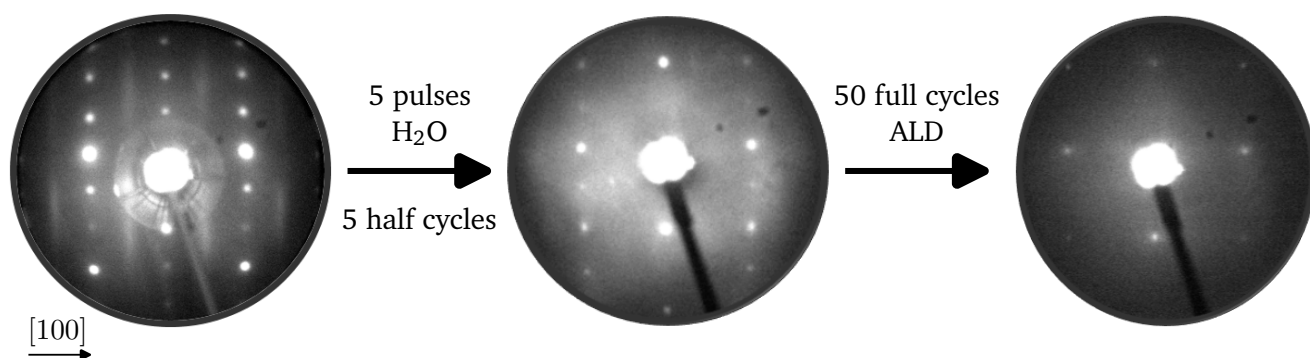
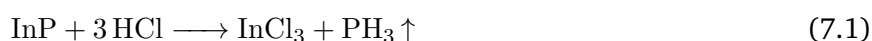


Figure 7.3: Evolution of P-rich InP (100) LEED images after 5 half cycles and 50 full cycles of ALD-TiO₂ deposition using TiCl₄ and H₂O as precursors.

20, and 50 full cycles, no notable nucleation of TiO₂ is observed in the Ti 2p and Ti 2s spectra. The Ti 2s is not disturbed by the In 3d plasmon shake-ups and therefore more sensitive on InP surfaces. At the same time, the Cl contamination increases but saturates at about 6 atm.%. Interestingly, the P content decreases by the same percentage, while the In content remains constant at about 50 atm.%. At the same time, the 2×1 LEED pattern turns into a 1×1 configuration (Figure 7.3), indicating a destruction of the well-defined P-rich InP surface reconstruction. This suggests that instead of TiO₂ nucleation, an etching process occurs during the ALD processing. It can not finally deduced if this etching process is attributed to the direct interaction with TiCl₄ precursor or to the formation of HCl, a side product of TiO₂ deposition. The ALD process is expected to occur on the exposed surfaces inside the reaction chamber, which could act as HCl source. The presence of HCl leads to a chemical etching process as confirmed by Notten²⁷⁵:



While the InCl₃ compound remains at the surface, PH₃ evaporates as a gas. However, since the Cl content is saturating, an adsorbed In–Cl_{ads} species is conceivable as well.²⁷⁶ Phosphorous depletion on cleaved InP surfaces have also been found by pure Cl₂ adsorption.^{242,277} The In 3d_{5/2} reveals a chlorinated (oxidized) species of about 7 % intensity at higher binding energies, which can be related to InCl and InCl₂ species.²⁷⁸ The presence of oxygen traces after full cycles might also indicate InO_x species in addition. The HeII valence band spectra clearly reveal chlorine features after the ALD treatment. The characteristic VB edge is damped after the treatment, while Cl 3p features rise up at about 4 to 6 eV. Furthermore, the In 4d

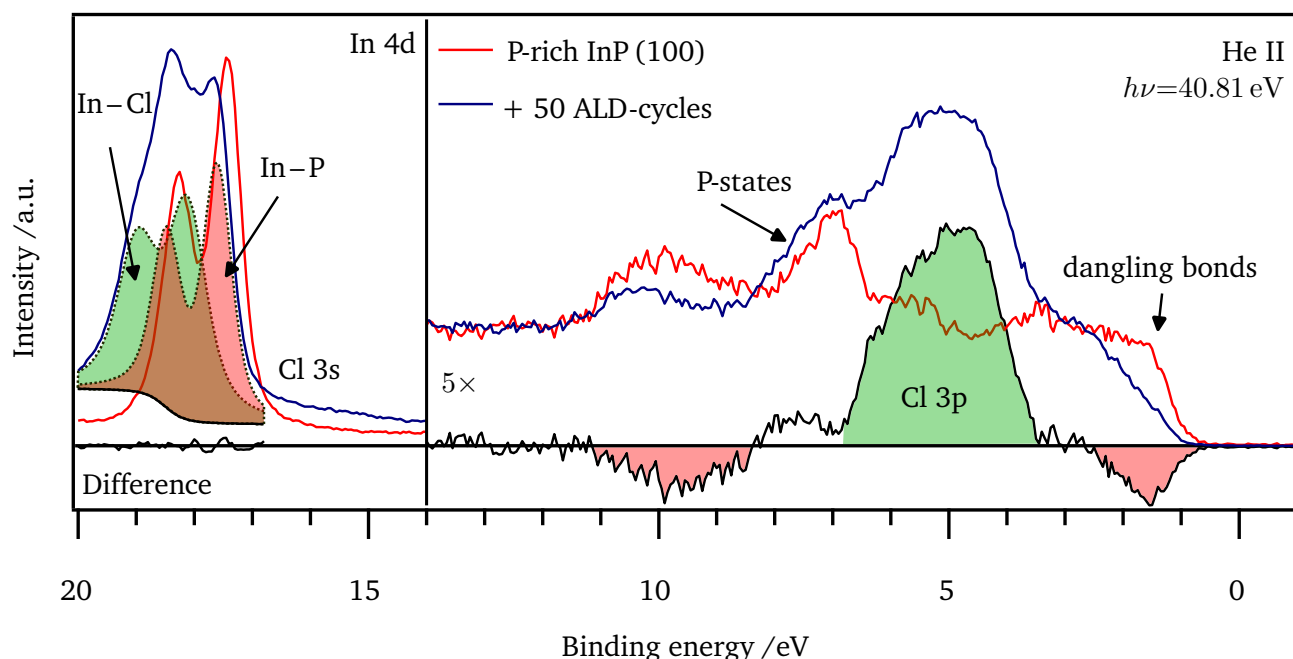


Figure 7.4: He II valence spectra before and after ALD treatment. Cl 3s features clearly arise up, while also the In 4d core level reveals a less ordered In – Cl surface species.

core level can be deconvoluted into the intact InP component and a less-ordered broader In–Cl surface species located at +0.44 eV.²⁷⁸ However, according to the VB spectrum there are still phosphorous states present at the surface¹¹¹ which might come from locally intact P-rich InP domains. This is also confirmed by pre-edge features in the XPS and UPS secondary electron edge (SEE), which might indicate lateral inhomogeneities (Figure A10 in the Appendix). However, the InCl_x surface layer forms a large surface dipole which increases the sample WF up to 5.9 eV. Interestingly, the bulk-related In 4d level shifts after the treatment by about 0.15 eV to higher binding energies, indicating an increase of the initial downward band bending due to additional electron donors which has to be therefore related to interfacial states. However, as the Fermi level shifts observed in XPS are smaller in comparison to UPS, source-induced surface photovoltage (SPV) cannot be ruled out in this case. But, as already observed on the In-rich surface when in contact to water, partial surface oxidation injects electrons into the p-InP SCR.

According to the experiment above, the P-rich InP (100) is not reactive enough to get hydroxylized in order to initially interact with the TiO_2 precursor. Rather than the interaction with H_2O , an etching process with TiCl_4 or HCl as a side product from the ALD process is observed, which leads to a phosphorous depletion and the formation of an InCl_x interlayer. However, the InCl_x interlayer apparently does not increase the reactivity of the surface to start the TiO_2 layer growth process. The ALD deposition of TiO_2 on rather perfect P-rich InP surfaces is therefore not possible.

7.2.2 Partially oxidized InP (100) as substrate for ALD- TiO_2

Due to the observations presented above, the experiments were repeated with the partially oxidized In-rich InP (100) surface after water adsorption as described in Section 6.2. In Figure 7.5, XP spectra of the In-rich InP surface are shown after different full cycles of ALD- TiO_2 deposition. It is clearly obvious that after 50 full cycles a clear Ti 2p signal arises at 459.20 eV binding energy and shifts to 459.10 eV

after 150 cycles. Interestingly, the InP substrate signals show a slight energy shift of about $\Delta E_b = 50$ meV towards higher binding energies, indicating an electron injection from the ALD-TiO₂ interface into the InP SCR. However, it is even more interesting that even after TiO₂ formation on the In-rich surface, the In and P core levels are found at the exact same binding energy as observed on the P-rich InP surface after non-deliberate etching during the ALD process. This indicates the same defect distribution causing Fermi level pinning on both the etched P-rich InP and the InP/ALD-TiO₂ interface. As already observed on the P-rich surface, the Cl content at the partially oxidized In-rich surface is in the initial deposition steps higher (≈ 5 atm.%) than observed for the thicker TiO₂ layer (≈ 2.5 %).

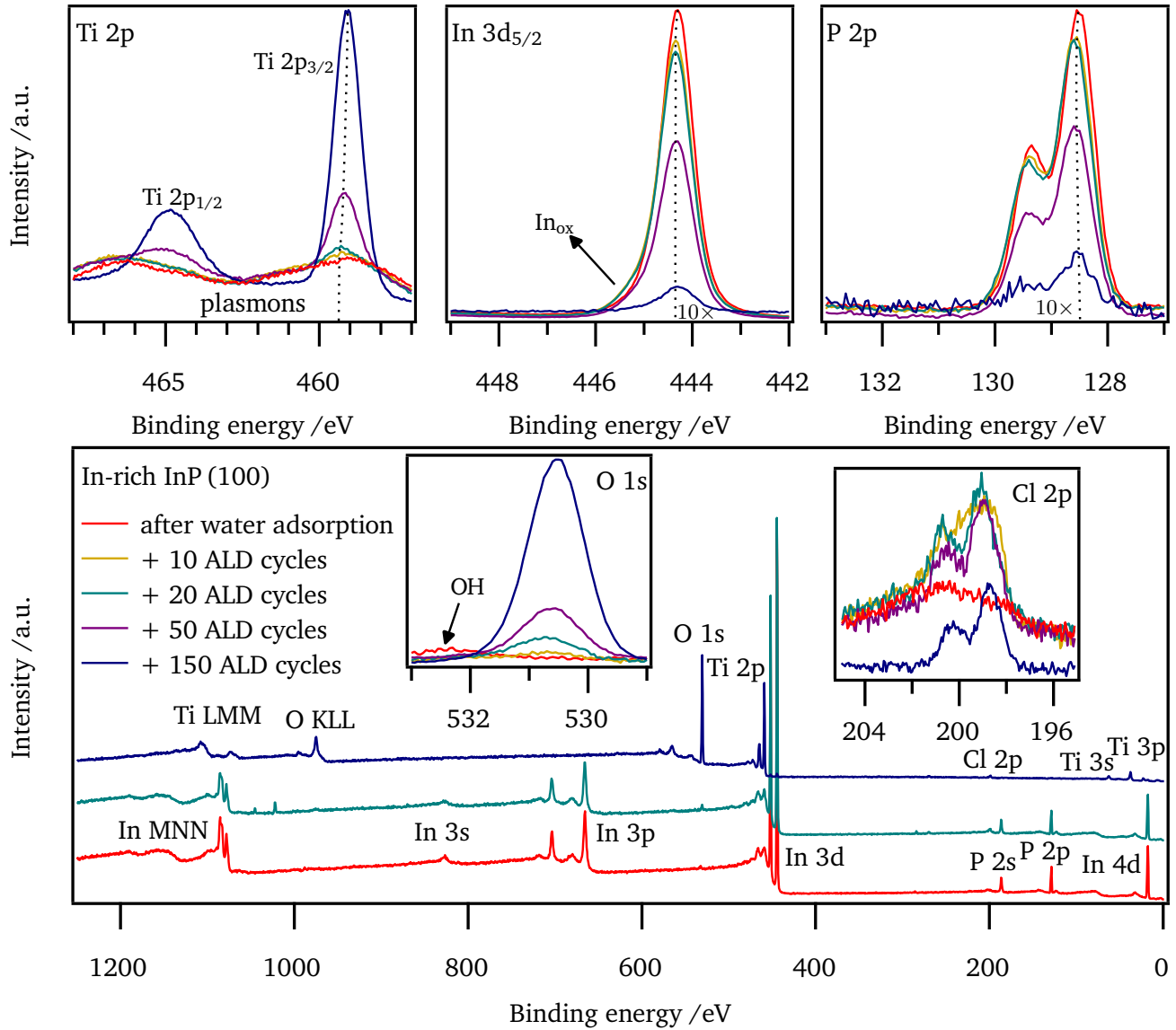


Figure 7.5: XP spectra of the In-rich InP (100) surface after water adsorption and different amounts of full ALD-TiO₂ cycles using H₂O and TiCl₄ as precursor gases.

The LEED images reveal that even for the partially oxidized InP (100) surface, showing no LEED pattern, an etching process occurs for the initial 10, 20, and 50 full cycles as indicated by the 1×1 -pattern already observed for the P-rich InP surface (Figure 7.6). After 150 full cycles of ALD-TiO₂ deposition, the LEED

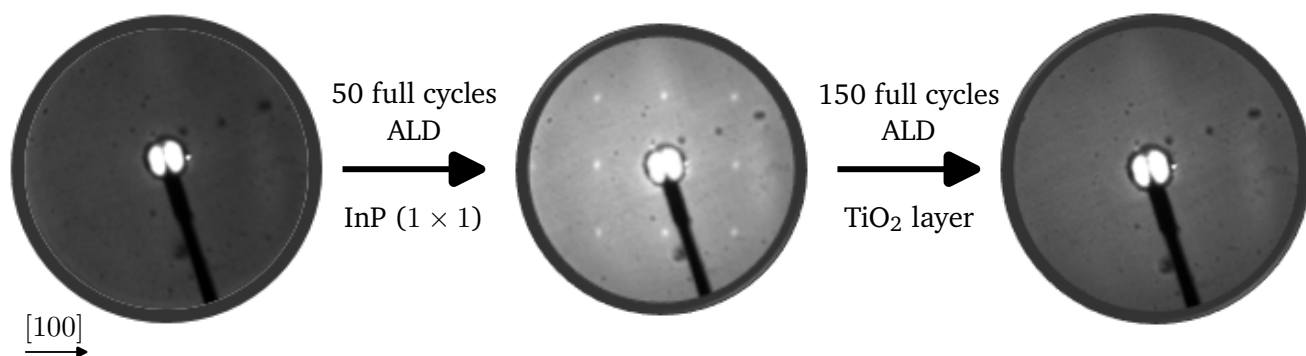


Figure 7.6: Evolution of oxidized In-rich InP (100) LEED images after 50 and 150 full cycles of ALD-TiO₂ deposition using TiCl₄ and H₂O as precursors.

pattern disappears again, as is expected for the X-ray amorphous TiO₂ layer. This suggests a closed layer of TiO₂ after 150 deposition cycles.¹¹² In contrast, the clear 1 × 1-pattern after 50 cycles suggests that the TiO₂ layer initially nucleates at a few nucleation centers, while the majority of the InP surface remains uncovered and etched by the evolving HCl as side product from the ALD process.

The etching process is also confirmed by the He II VB spectra showing that Cl 2p features appear at about 4 to 5 eV while at the same time, oxide and hydroxide species disappear after 10 full ALD cycles (Figure 7.7). In addition, the states at the VBM get quenched further and a sharp state 10.5 eV above E_F appears, which might be related to P 3s states^{279,280} and has been similarly observed by Lewerenz and Schulte²⁸¹. After 20 ALD cycles, TiO₂ is nucleating and forms the characteristic Ti 3d

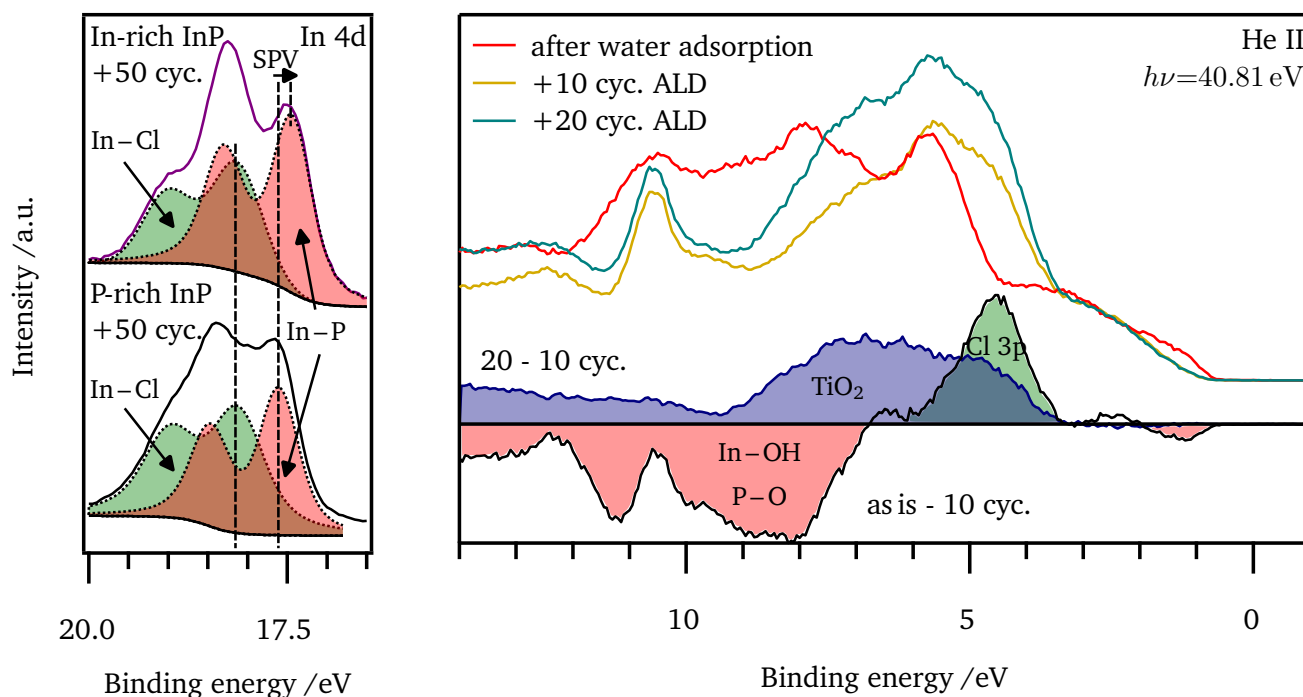


Figure 7.7: He II In 4d core level fits of In-rich and P-rich surface after 50 full ALD-TiO₂ cycles (left) and VB spectra before and after ALD treatment (right). HCl etching seems to be the initial treatment step. After 20 cycles, the TiO₂ VB appears.

– O 2p valence states of TiO₂.²⁸² However, according to the VB signal, the TiO₂ is still less than one monolayer after 20 cycles. It is an interesting observation that the HCl etching process attacks the oxide and hydroxide surface species as also observed in the O 1s XP spectra. It forms an InCl_x surface phase, which prevents the initial TiO₂ nucleation.

As already observed in XPS, the In 4d fits reveal slightly less amounts of chlorine contamination on the In-rich surface in comparison to the P-rich surface after 50 ALD cycles. In XPS, the In 3d and P 2p emissions of the In-rich and P-rich InP surface after 50 ALD cycles were observed on identical binding energies, indicating equal interfacial defect distribution. In UPS, the bulk-related In–P component differs in binding energy by about 0.15 eV while the surface related In–Cl component is found at identical binding energies of $E_b(\text{In } 4d_{5/2})=18.13$ eV. This fact suggests that again source-induced SPV shift the XP core level spectra to identical binding energies, while with He II illumination, the etched P-rich InP is less susceptible to SPV, indicating higher recombination rates for excess charge carriers. Light illumination of the In-rich surface leads to an additional shift towards lower binding energies of about 0.15 eV. In this case however, the In–Cl-related component is shifted by the same amount.

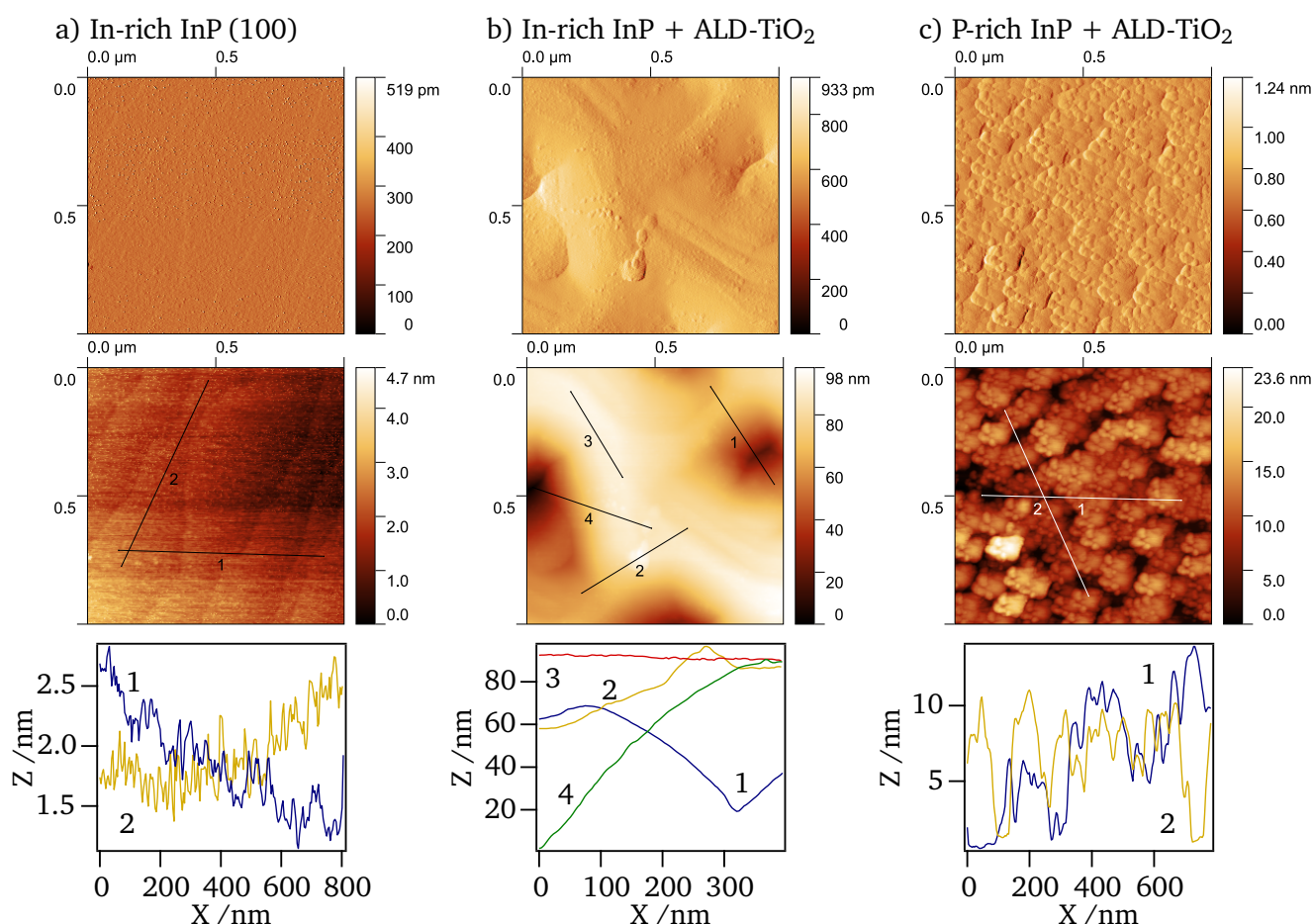


Figure 7.8: AFM images of a) In-rich InP after deposition, b) In-rich InP after 150 full ALD-TiO₂ cycles, and c) P-rich InP after 50 full ALD-TiO₂ cycles with amplitude image (top), topography image (middle), and Z-profiles along depicted paths (bottom).

In addition to spectroscopic analysis, the InP (100) surfaces were also investigated by *ex-situ* atomic force microscopy (AFM) (Figure 7.8). The untreated In-rich InP surface reveals a very flat surface, close to

the resolution limits of AFM. The topography image reveals the flat terraces with step edges in the sub-nm scale, confirming the epitaxial growth during the MOVPE process.²²⁰ After 150 cycles of ALD-TiO₂, the In-rich InP is fully covered with TiO₂. However, the topography image reveals a very undulated surface with height differences of up to 30 nm indicating island growth. Especially along path 1 and 4, deep crevices are observed that result from fusing islands. However, there are also very flat and homogeneous regions (along path 3) showing no height differences, while on other regions smaller nucleating islands are observed (along path 2) in the amplitude images. The P-rich surface confirms the etching process described above leading to a roughened surface with about 10 nm deep pinholes of about 50 nm in diameter.

As conclusion, the ALD process using TiCl₄ and H₂O as precursor leads on both surfaces, the P-rich and the partially oxidized In-rich surface to an etching process destroying the initial surface reconstructions. An In–Cl surface phase appears on both surfaces, leading to a Fermi level pinning about 0.7 ± 0.1 eV above the VBM, while the exact determination is difficult due to the reduction of effective density of states (DOS) at the VBM and due to source-induced SPV. However, even after etching both VB spectra look slightly different and also the recombination rates might differ on both surfaces. Apparently, the In–Cl surface phase limits TiO₂ nucleation, which finally only takes place on the partially oxidized In-rich surface. However, the ALD-TiO₂ process leads to an undulating surface with crevices along contact points of nucleation island, which might lead to pinhole corrosion during the photoelectrochemical operation.²⁸³

7.3 Low-temperature water adsorption on the p-InP/TiO₂ interface

As stated in literature, the p-InP/TiO₂ interface is an interesting device structure as photocathode for reasonable water splitting performances.^{55,263} Lin et al.²⁶³ found a gain in photovoltage of $\Delta eU_{\text{ph}} = 0.2$ eV under photoelectrochemical operation by the ALD deposition of an TiO₂ protection layer. They argued that this gain results from a further hole depletion of the p-InP substrate. However, according to the interface experiments above, the Fermi level remains pinned above midgap after the ALD deposition of TiO₂ accumulating residual chlorine at this interface. This raises the question if the electrolyte might change the analyzed interface energetics. In this Section, it is investigated how low-temperature water adsorption might change the interfacial band alignment of the p-InP/ALD-TiO₂ interface.

Interestingly, the largest changes of the energetic alignment are observed when storing the p-InP/TiO₂ sample for 5 days under ultra-high vacuum (UHV) with base pressures of $< 1 \times 10^{-9}$ mbar. The He II valence spectra in Figure 7.9 reveal a broad hydroxy feature arising between 8 to 11 eV binding energy^{272,284}.²⁸² Furthermore, an in-gap state arises 1 eV below E_{F} . These states are of Ti 3d character and represent Ti³⁺ states, even though the exact origin is still under debate.^{272,273} However, there are different studies on single crystals describing a deep gap state (DGS) at about 1.2 eV and a shallow gap state (SGS) which reaches from 0.6 eV up to the Fermi level.^{269,285} In addition, TiO₂ surface states resulting from dangling bonds might appear closely above the VBM as suggested by Lin et al.²⁶³. Recent studies verified the existence of this surface state experimentally.^{177,286} The adsorbed OH species seem to reduce the TiO₂ layer, which becomes evident on the one hand by Ti³⁺ formation, and on the other hand by the VBM shifts from 3.21 to 3.43 eV above E_{F} . This also shifts the Ti 2p XPS core level by about 0.1 eV towards higher binding energies, while an increasing shoulder towards lower binding energies also indicates Ti³⁺ states. The original core level spectra are shown in Figure A12 of the Appendix. Furthermore, the WF decreases from 5.89 eV straight after deposition to 4.33 eV. Even though these effects have been already observed on TiO₂,^{266,287} the exact nature of the adsorbate-induced reduction process is still not clear yet. Interestingly, the XP spectra reveal that the energy shifts result from a shift of the InP substrate core levels, although the about 12 nm TiO₂ overlayer significantly damps the substrate signals. This confirms

that a reduction of the TiO_2 overlayer might also lead to an electron accumulation in the photoabsorber substrate.

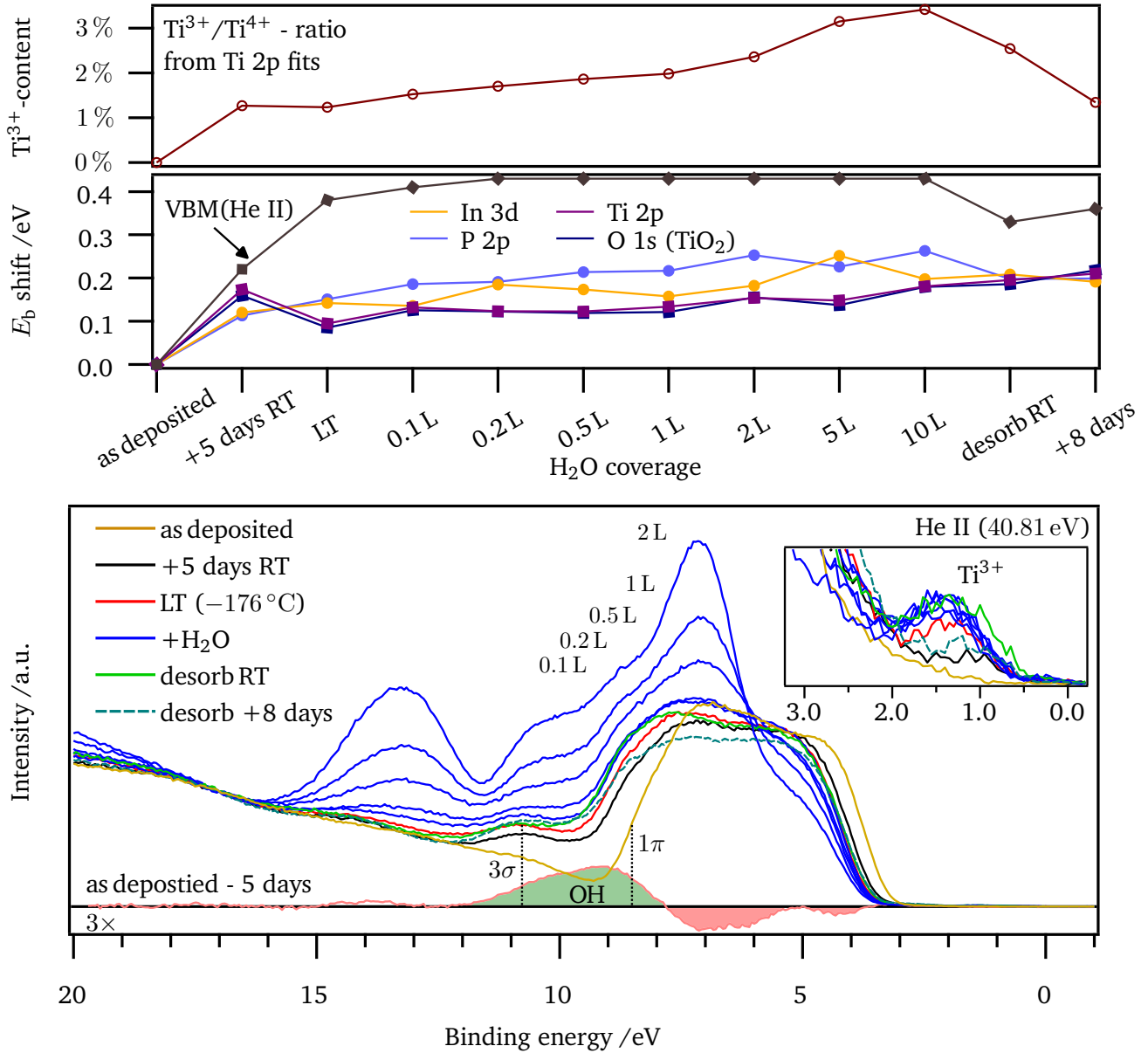


Figure 7.9: $\text{Ti}^{3+}/\text{Ti}^{4+}$ -ratio according to $\text{Ti } 2p_{3/2}$ fits (top), XPS core level shifts (middle), and He II spectra (bottom) of the p-InP/ TiO_2 low-temperature water adsorption experiment.

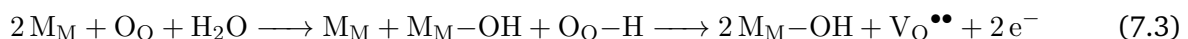
After cooling for low-temperature water adsorption, the TiO_2 -related core levels shift by about 50 meV towards flatband condition, indicating less source-induced SPV than observed on the uncovered In-rich InP surface. However, these shifts cannot be resolved in the substrate core levels due to the lack in intensity. Interestingly, the VB spectra from He II shift towards higher binding energies after cooling. However, the raising DGS at about 1.2 eV indicates a further reduction of the surface, which might be related to additional adsorbates, while difference spectra might indicate additional OH species. However, the effect of source-induced photoreduction might also affect these measurements.²⁶⁹ With adsorbing

water, XP core levels of TiO₂ shift towards higher binding energies by about 50 meV and remain constant in the monolayer regime. The small energy shifts cannot be resolved in the InP-related substrate signals. However, the He II spectra confirm the trend of binding energy shift in TiO₂ in the initial adsorption steps. Even though, the He II spectra are not normalized (Figure 7.9) and the valence features of TiO₂ get damped by the adsorbing water molecules, the DGS increases with additional H₂O coverage, suggesting a self-compensation mechanism limiting further Fermi level shifts. When normalizing the VB spectra at $E_b=4.8$ eV, the intensity of DGS increases continuously up to 10 L. This trend is also confirmed by the Ti³⁺/Ti⁴⁺-ratio derived from Ti 2p_{3/2} fits as shown in Figure A11 in the Appendix. After the H₂O desorption, the VBM shifts slightly back, but remains at a high level of 3.54 eV above E_F . Furthermore, the DGS slightly decreases after H₂O desorption but remains at a high level, too. Interestingly, after further 8 days of storage, the TiO₂ layer recovers and the Ti³⁺ content decreases again. Nevertheless, this recovery does not have any impact on the energetic band alignment of the p-InP/TiO₂ interface.

Such a surface reduction upon water adsorption has already been observed on different transition metal oxides such as BiVO₄,²⁸⁸ CuFeO₂,²⁸⁹ and NiO.²⁹⁰ According to Hermans et al.²⁸⁸, water adsorption leads to a release of O₂ or H₂O₂ that reduces the oxide surface chemically. They all observed a raising Fermi level and, an additional chemical reduction of lattice cations. Interestingly, before and after water adsorption the oxygen content decreases from 29.5 atm.% to 28.5 atm.%, although additional adsorbates should increase the oxygen signal. This indicates indeed to a loss of lattice oxygen:



However, the exact mechanism is not clear yet. If the vacancy formation either results from a chemical surface reaction upon water adsorption or if the vacancy forms spontaneously due to a self compensation mechanism counteracting further Fermi level shifts remains unclear.²⁹¹ Theoretical simulations suggest that H₂O adsorption may stabilize surface vacancies V_{O,surf} and lead to further migration of V_O towards the surface. Furthermore, V_{O,surf} might be the active site for H₂O dissociation.^{292–294} A considerable mechanism forming oxygen vacancies could be:



In any case, this reaction mechanism cannot explain the depletion of oxygen from the surface. Hermans et al.²⁸⁸ suggested that the OH groups at the surface might desorb as H₂O₂ or O₂, leaving M–H species at the surface. For a defect distribution of V_O close to the conduction band minimum (CBM), the free electrons could be released to the conduction band (CB) and raise the Fermi level in the TiO₂. Another option is the reduction of lattice cations by the localization of electrons due to polaron formation (Ti⁴⁺ + e[−] → Ti³⁺), which would limit further Fermi level shifts.^{289,295} There exists a lot of theoretical data about the effects of polaron formation in anatase,^{296–298} but also experimental proofs.^{299,300} However, free electrons are partially transferred into the p-InP substrate, while the formation of Ti³⁺ does not affect the InP Fermi energy. Accordingly, it can be concluded that the Ti³⁺-related defect state is located below the InP CB, since otherwise further hole depletion in the p-InP substrate would be expected with rising amounts of Ti³⁺ formation.

As conclusion, electron injection into the photoabsorber SCR is not only observed on native oxide passivated Si and InP, but also when covered with ALD-TiO₂. In this case however, a different injection mechanism is suggested, as oxygen vacancy formation is assumed while chemisorbed water dissociates. It is unlikely that molecular water interacts with InP related defect states through the ≈12 nm thick TiO₂ layer as suggested in Section 5.3. But, the TiO₂ surface chemistry upon water adsorption affects the interfacial band alignment at the p-InP/TiO₂ interface. The final energy band diagrams before and after contact to water including the suggested surface reactions is depicted in Figure 7.10.

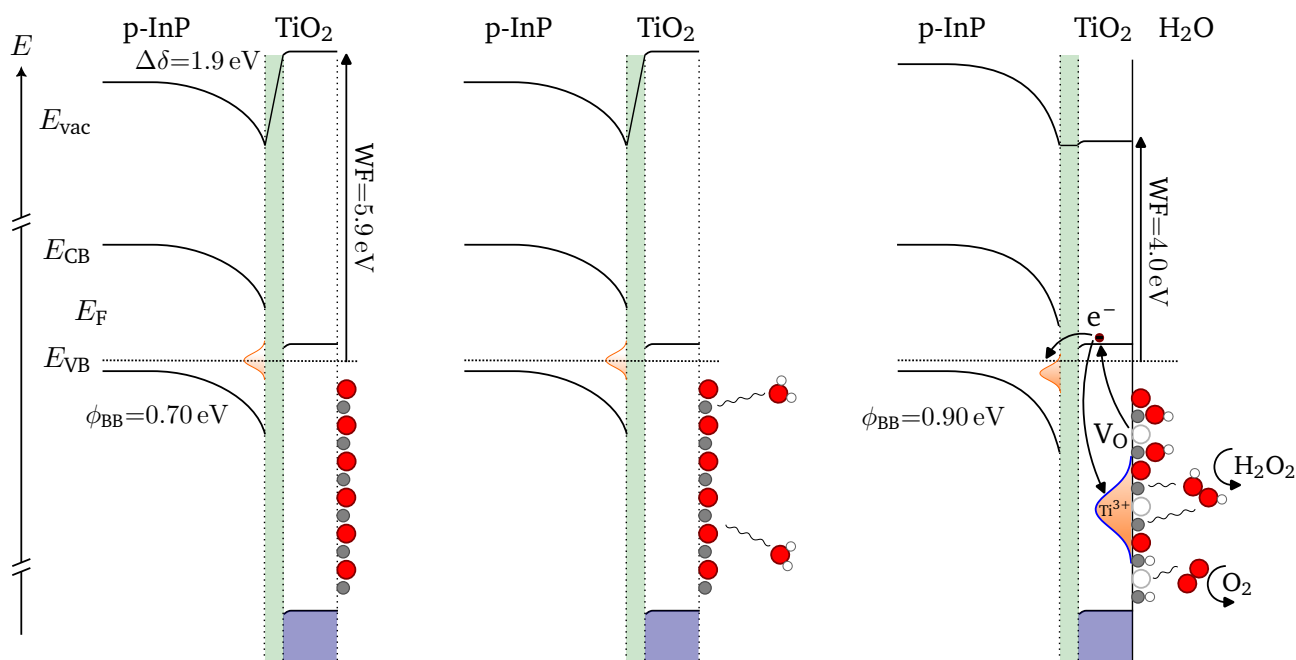


Figure 7.10: Energy band diagrams of p-InP/ALD-TiO₂ interface straight after deposition and in contact with water. Green areas represent double layer potential drops at the very interface. Possible reaction mechanism shown in which oxygen is leaving the surface and oxygen vacancies V_O act as electron donor.

7.4 Sputter deposition of TiO₂

The results of this section have been derived within the framework of a Bachelor thesis by Justus Carnap.

The results from the previous section show that the initial TiO₂ growth by an ALD process strongly depends on the surface chemistry of the substrate. As this lead to unwanted chemical reactions at the interface, TiO₂ deposition by reactive magnetron-sputtering has been investigated alternatively. The method allows modifying the electronic properties of TiO₂ thin films by varying the process parameter.

The physical vapour deposition (PVD) process allows to precisely control the defect concentration by varying the partial oxygen pressure during the sputter-process. In Figure 7.11, XP core level and He II VB spectra are shown for DC-sputter deposited TiO₂ films at room temperature (RT) with different oxygen contents in the process gas mixed with Ar (20 sccm total flow under 0.5 Pa working pressure) at 50 W DC-power. Apparently, the binding energy positions are very sensitive to the oxygen content in the process gas. Consequently, the defect distribution strongly depends on the oxygen content as observed for many other transition metal oxides.³⁰¹ Especially in the region for lower oxygen contents, between 2 and 3 %, the electronic shifts vary by about 1.0 eV. The oxygen deficient sample clearly shows a reduced oxygen to titanium ratio of 2:2, while for the other samples a ratio of about 2.3 is observed. The deviation from the expected 2:1-ratio is expected to come from OH adsorbates, which appear in samall amounts at around 10 eV in the He II VB. Furthermore, the oxygen deficient sample clearly shows a Ti³⁺-related subspecies at lower binding energies of about 13 % relative intensity. In addition, the Ti³⁺ related DGS state appears in the band gap as already observed in the hydroxilized ALD deposited TiO₂ films. Since the O 1s signal does not show a clear spectral change in the line shape, a phase segregation of an oxygen deficient sub-phase such as Ti₂O₃ is not assumed, but rather a self compensation effect as discussed above. The

observed binding energy ranges are in good agreement with energies found for single crystal surfaces.²⁶⁶ This indicates that the Fermi level is limited to the observed range from 2.24 to 3.57 eV above the VBM. According to the WF evaluated from XPS SEE, the values are ranging from 5.08 to 6.13 eV, which is larger than the c-Si ionization potential ($I_p(\text{c-Si})=5.1 \text{ eV}$ ²⁹). As a result, contact formation of c-Si with sputtered TiO_2 is expected to cause electron depletion in the Si substrate, even for the oxygen deficient TiO_2 film. As already investigated on the ALD- TiO_2 , the sputter-deposited TiO_2 films seem to be X-ray amorphous as only substrate reflexes are observed (see Figure A14 in the Appendix).

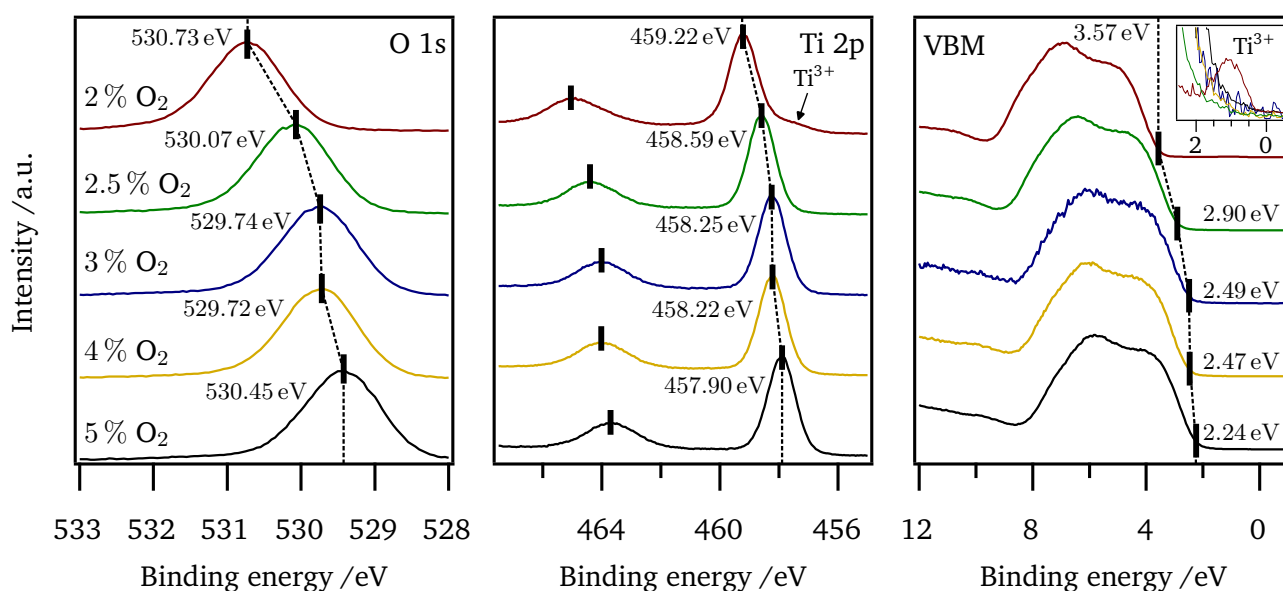


Figure 7.11: XP core level and He II VB spectra of sputtered TiO_2 films with different oxygen contents during deposition at room temperature. Ti^{3+} related bandgap states are depicted as inset in the VB spectra.

In addition to the oxygen content in the processing gas, the impact of substrate temperature on the TiO_2 film properties was investigated, as well. Elevated substrate temperatures during deposition led to crystalline TiO_2 films. For a substrate temperature of $T=296^\circ\text{C}$, an anatase related X-ray diffraction (XRD) pattern is observed, while for $T=440^\circ\text{C}$ rutile related reflexes can be assigned (see Figure A14 in the Appendix). The relative core level to VBM energy differences change for each modification. For the amorphous phase, an O 1s to Ti $2p_{3/2}$ difference of about $71.52 \pm 0.04 \text{ eV}$ is observed, which is reduced for the crystalline phases to 71.36 eV for anatase and to 71.27 eV for rutile. Interestingly, the energy difference $\Delta E(\text{Ti } 2p_{3/2}\text{-VBM})$ observed for the ALD- TiO_2 film from Section 7.2.2 is in between these values at 71.43 eV. According to the O-to-Ti signal ratio, which is found to be at about 2.3, the oxygen signal is not decreased. Furthermore, no Ti^{3+} related DGS are observed. Nevertheless, the VB onset is found to be at the same position of 3.14 eV above E_F for both the anatase and rutile phase, while the WF decreases on both samples to about 5.4 eV.

The optical properties of the amorphous and crystalline TiO_2 films are shown in Figure A15 in the Appendix. The oxygen deficient sample already show optical interband transitions below the expected band gap of $E_g=3.2 \text{ eV}$ due to optical transitions from Ti^{3+} related defect states located within the TiO_2 bandgap. This is typically observed in “black titania” as well.³⁰² There are 3 distinct transitions observable at about 1.5, 2.4 and 2.9 eV. According to direct and indirect Tauc-plots, the amorphous TiO_2 film, which was deposited at 2.5 % oxygen content, shows an indirect band gap of 3.28 eV, while a direct transition is observed at a similar energy and is close to values found in literature.^{302,303} Similar values are observed

for the anatase and rutile phase with 3.22 and 3.29 eV, respectively. Even though, for rutile a direct band transition is expected at about 3.0 eV,^{303,304} direct band transitions measured here, are only found at higher binding energy (3.33 eV for rutile and anatase film). However, the values are in good agreement as found on polycrystalline anatase and rutile films.³⁰³

Table 7.1: Properties of sputter-deposited TiO₂ films:

Sample	Deposition temperature	E_F -VBM	WF	Ti 2p _{3/2}	O 1s	O/Ti-ratio	E_g^\dagger
2 % O ₂	RT	3.57 eV	5.08 eV	459.22 eV	530.73 eV	2.20	3.26 eV
2.5 % O ₂	RT	2.9 eV	5.56 eV	458.59 eV	530.07 eV	2.30	3.28 eV
3 % O ₂	RT	2.49 eV	5.90 eV	458.25 eV	529.74 eV	2.33	–
4 % O ₂	RT	2.47 eV	6.05 eV	458.22 eV	529.72 eV	2.34	–
5 % O ₂	RT	2.24 eV	6.13 eV	457.90 eV	530.45 eV	2.29	–
2.5 % O ₂ anatase	296 °C	3.14 eV	5.39 eV	458.95 eV	530.31 eV	2.33	3.22 eV
2.5 % O ₂ rutile	440 °C	3.14 eV	5.36 eV	459.01 eV	530.28 eV	2.34	3.29 eV
ALD-TiO ₂ *	160 °C	3.24 eV	5.89 eV	459.09 eV	530.52 eV	2.17	3.1 eV ¹¹²

* ALD-TiO₂ from Section 7.2.2. † indirect optical band gaps from Tauc-plots (see Figure A15).

All relevant energy values for the prepared TiO₂ films are summarized in Table 7.1. Even though, the n-type doping effect strongly depends on the oxygen content in the process gas, almost all sputter-deposited samples show a constant O-to-Ti ratio of about 2.3. With free charge carrier concentrations of up to $2 \times 10^{-19} \text{ cm}^{-3}$,¹⁷⁷ the stoichiometry quantification by XPS is not evidential with respect to the doping effect. For the highly oxygen deficient sample deposited at 2 % O₂ in the processing gas, Ti³⁺ states appear, which might be assigned to trapped free electrons in the vicinity of oxygen vacancies. These electrons get localized in the lattice and reduce the surrounding lattice cations.³⁰⁵

Reasonable conductivity and mobility values could only be derived from the 2.5 % O₂ RT-deposited TiO₂ sample, with $\sigma = 1.0 \pm 0.1 \text{ S/cm}$. Hall measurements revealed an electron charge carrier concentration of $n_{el} = 1.4 \times 10^{18} \text{ cm}^{-3}$ with a mobility of $\mu_{el} = 4.4 \text{ cm}^2 \text{ V}^{-1} \text{ s}^{-1}$, which is in good agreement to other reactive magnetron-sputtered TiO₂ films.³⁰⁶ Interestingly, neither on the oxygen deficient nor the crystalline samples the conductivity could exceed values of $3 \times 10^{-5} \text{ S/cm}$.

Due to the good optical properties with sufficient electrical conductivity, RT sputter-deposited TiO₂ films with 2.5 % O₂ in the process gas is considered to be a good candidate for electrochemical buffer layer deposition when considering thick TiO₂ passivation layers at a sufficient deposition rate of 0.5 nm min^{-1} under these conditions.

However, the derived bulk conductivities ranging from 10^{-5} to 1 S/cm lead to neglectable ohmic overpotentials ($\leq 10 \text{ mV}$) when considering a 100 nm thick buffer layer at photocurrents of about 10 mA cm^{-2} . The overpotential losses due to interfacial barrier formation has accordingly a far higher impact on the overall performance of the photoelectrochemical device than the bulk conductance of the passivation layer.

8 pn⁺-Si model device structures

pn⁺-Si junctions used in this chapter have been supplied by Dr. Volker Häublein, Fraunhofer IISB, Erlangen.

In this chapter, a complete photoelectrochemical water splitting device structure is presented as demonstrator and the effect of contact formation to functional layers such as catalyst and bufferlayer on the electrochemical performance is investigated. The photocathode was produced by ion-implantation of As as n-dopant into the surface of a B-doped (100) wafer (p-type) with a conductivity σ of about 0.1 to 1 S cm⁻¹. The p-doped wafer therefore offers similar electronic properties to the p-doped wafer specified in Section 5.1 with charge carrier concentrations of $N_{ac} \approx 2 \times 10^{15}$ cm⁻³, corresponding to an expected Fermi level position in the bulk of $E_F - E_{VB} = 0.22 \pm 0.03$ eV. Before As implantation with a kinetic energy of 15 keV, a scattering oxide of 10 nm has been applied in order to control the As depth profile. After the implantation, the As dopant has been activated by an annealing process at 900 °C and the scattering oxide has been removed by wet-chemical etching. As a final step, 1 μ m of Al was sputtered on the wafer back side and the wafer were cut into 1 × 1 cm² chips before shipping to Darmstadt. Electrochemical capacitance–voltage profiling (CV profiling) show a thickness of the Si-n⁺ layer of about 50 nm with charge carrier concentrations of about 1 × 10²⁰ cm⁻³ (Figure 8.1).

Deeper inside, an abrupt transition to the wafers p-type region is reached, followed by a homogeneous

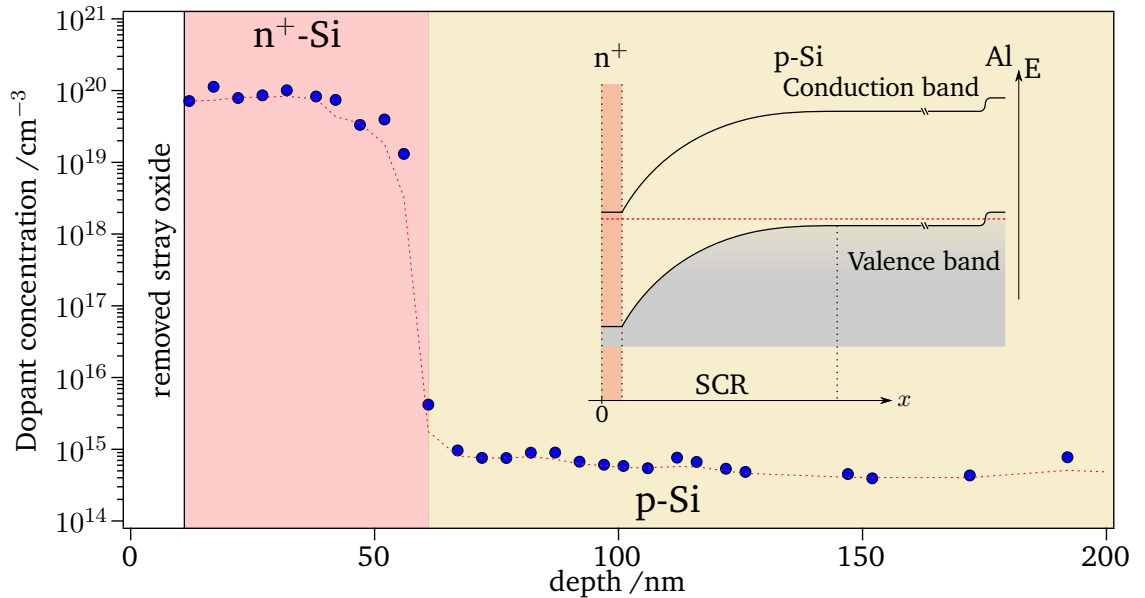


Figure 8.1: CV profiling of As-implanted p-Si wafer as-received from Fraunhofer IISB, Erlangen. As has been implanted by 15 keV and subsequent annealing at 900 °C. Inset shows ideal energy band diagram of pn⁺-junction after thermodynamic equilibrium.

dopant profile. Under thermodynamic electronic equilibrium, a charge transfer from the n⁺ layer into the p-substrate is expected, forming a hole depletion region inside the p-wafer as depicted in the inset of

Figure 8.1. With a maximum band bending ϕ_{BB} of 0.9 eV and $\epsilon=11.7$,²⁹ the width of the space charge region (SCR) W_{SCR} at which excess charge carriers are separated can be calculated with

$$W_{SCR} = \sqrt{\frac{2\epsilon\epsilon_0\phi_{BB}}{qN_{ac}}} = 7.6 \mu\text{m}. \quad (8.1)$$

Accordingly, the achieved cell provides the typical properties of an efficient Si photodiode.

8.1 Charge separation of the pn^+ -Si photoelectrode

To test the performance potential of the presented pn^+ -Si cell, the open circuit potential (OCP) was investigated in an electrochemical cell using a white light light emitting diode (LED) illumination of 1000 W m^{-2} simulating AM1.5 solar radiation. The OCP is measured versus the reversible hydrogen electrode (RHE) and shifts while illumination due to the induced photovoltage V_{OC} , which is expected to result from the buried pn^+ junction (Figure 8.2 a)). Even though the OCP tends to slightly shift over the measurement time of 5 min, the dark-illumination difference of 340 mV remain constant. When grounding the pn^+ wafer from the back side, those shifts can even be observed in XPS (Figure 8.2 b)). Illumination leads to a band flattening within the depleted p-type substrate shifting the core levels closer to the Fermi level reference.^{55,161} The amount of shift in XPS depends on source intensity. For 300 W intensity, the shift is $\Delta E_b=200 \text{ meV}$, while it increases to $\Delta E_b=325 \text{ meV}$ for 10 W intensity, almost reaching the total shift achieved from electrochemical measurements. Accordingly, the X-ray source even induces a certain amount of surface photovoltage (SPV) as already observed on very clean Si:H terminated surfaces as presented in Section 5.1. As an interesting fact, the SiO_2 related Si 2p and O 1s contribution only shift by 100 meV. The same behavior shows the XPS secondary electron edge (SEE), which might indicate that the

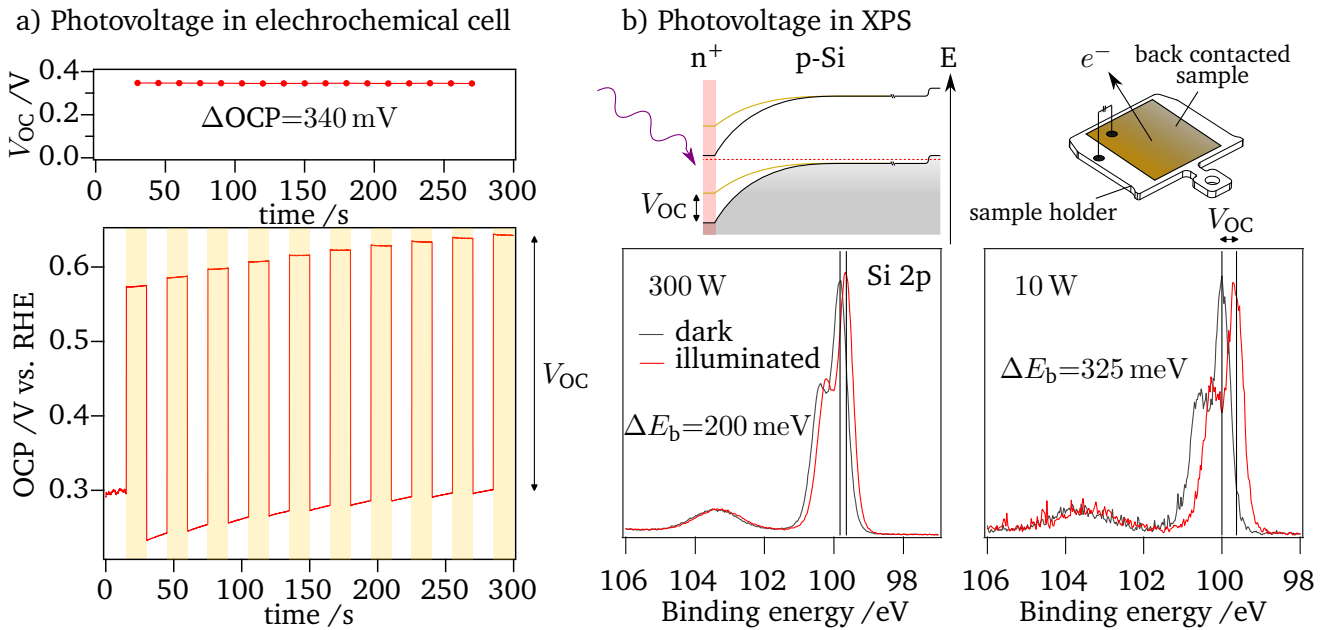


Figure 8.2: a) Chopped light OCP measurements in $0.1 \text{ M H}_2\text{SO}_4$ at 1000 W m^{-2} white light LED illumination. Shift in OCP while illumination is induced by the buried pn^+ junction and represents the photovoltage V_{OC} . b) XP-spectra of backside-grounded pn^+ wafer with and without illumination. Band flattening in p-Si substrate leads to reduction in binding energy.

photovoltage gets reduced at the interface to the native oxide due to surface recombination. Additional UV-bias light ($\lambda=365$ nm) did not lead to further energy shifts. Measuring at liquid nitrogen temperature leads to a shift of both, the dark and the illumination spectrum to lower binding energies due to enhanced source-induced SPV.

The total photovoltage V_{OC} at room temperature (RT) is far lower than expected for good pn^+ -junctions reported in literature, that range from 0.5 to 0.65 V.^{265,307–310} However, in all these studies the native oxide layer has been removed wet-chemically and a thin metallic Ti interlayer of about 5 nm has been applied. The role of the native oxide on the V_{OC} is therefore not fully clear in this case. It should be noted that the oxide thickness is with about 5.3 to 8.0 Å in the same range as observed on the bare wafers. An direct impact of the oxide thickness on the total V_{OC} could not be observed. Another reason for the low V_{OC} might be an improper back contact. Bae et al.⁴⁹ could show an increase of about 100 mV due to proper selective back and front contacts, while an p^+ -doped interlayer at the back contact could improve the V_{OC} by about 27 mV.

The current-voltage curve of the bare pn^+ -Si/SiO₂ wafer is shown in comparison to a p-Si/SiO₂ wafer in Figure A13 of the Appendix. The pn^+ homojunction reveals a slightly lower onset in the cathodic regime with twice the current density at -0.8 V vs. RHE in comparison to the pure p-Si wafer, even though the bare wafer barely reveal hydrogen evolution reaction (HER) activity.

8.2 The Pt covered pn^+ photocathode

As presented above, XPS provides the opportunity to measure the potential V_{OC} of a buried pn^+ -junction by illumination. In this Section, the contact formation of the Si photocell with metallic Pt as HER catalyst is investigated by performing interface measurements in the dark and under illumination. In this experiment Pt has been deposited by magnetron sputtering as presented in Section 5.4.1. For this experiment, a new sputtergun was used at an deposition angle of 30°. This lead to a reduction of the deposition rate to 7.2 Å min⁻¹. The drop in deposition rate might be furthermore related to progressing target consumption. In addition, the sputter deposited interface is compared to an *ex situ* thermal evaporation process by Jennifer Velázquez Rojas, Helmholtz-Zentrum Berlin.

The results of both interface experiments are shown in Figure 8.3. While the *in-situ* sputter-deposited Pt reveals a SEE at about $E_{kin}=6.0$ eV, the *ex-situ* thermal evaporated Pt shows the SEE at $E_{kin}=4.7$ eV which might be due to hydroxyl adsorbates as seen in the O 1s. All core levels show energy shifts under illumination, while the spectral shape does not seem to be affected by the white light LED. Similar as observed on the bare Si wafer in Section 5.4.1, all core levels show a shift to lower binding energies during contact formation, indicating an upwards band bending to the interface due to a high contact potential for the sputtered as well as the evaporated Pt layer. Due to the expected contact potential of ≈ 1.5 eV, the O 1s and Pt 4f spectra show continuous shifts of almost 1.0 eV with growing Pt layer. In contrast, the Si 2p line shows only minor shifts to lower binding energies of about 0.1 eV. The high charge carrier concentration of the top n^+ -layer of up to 10²⁰ cm⁻³, might lead to an ohmic contact behavior. The energy shifts induced by sputter deposited and thermal evaporated Pt are similar, even though the initial position of O 1s and with that also of Pt 4f differs. Since both set of samples are back side grounded as described above, the origin is not clear.

Due to the bias light induced shifts measured at X-ray intensities of 10 W, the SPV resulting from the buried pn^+ -junction can be measured during the interface formation with Pt. Interestingly, the contact formation to sputtered Pt clearly shows a reduction in photovoltage in all core levels, while the interface with evaporated Pt barely seems to influence the photovoltage and only decreases for film thicknesses >10 nm where the increasing reflectivity of the Pt film is expected to reduce the optical transmission into the buried junction. This raises the question if the sputter deposition process might form additional

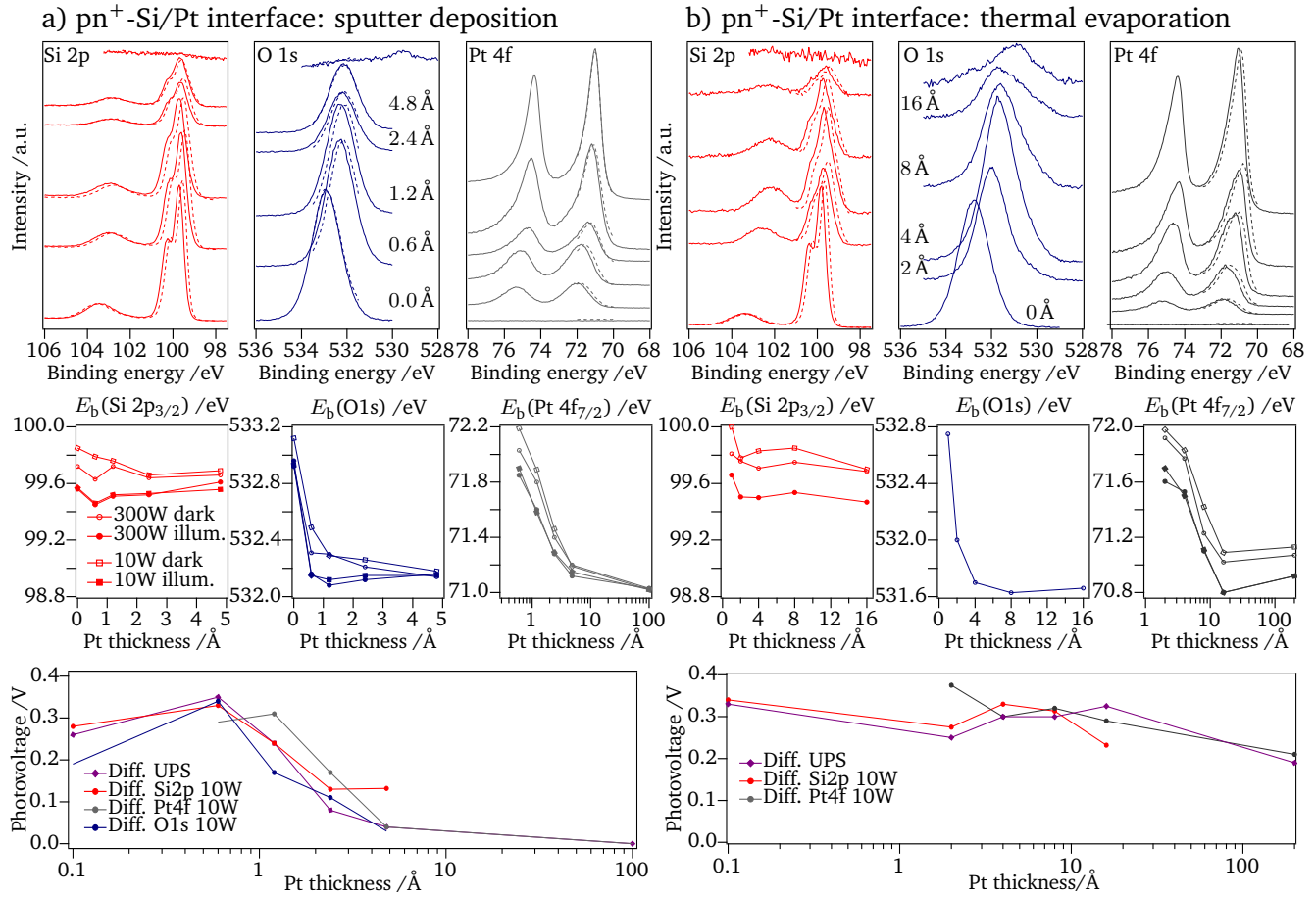
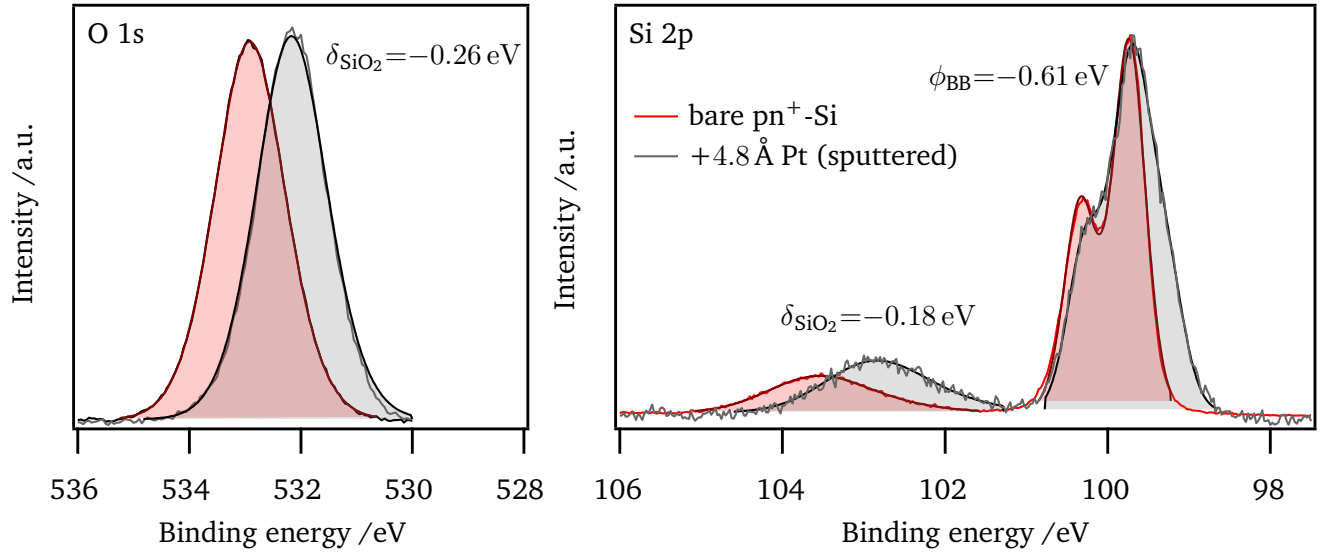


Figure 8.3: XP-spectra of a $\text{pn}^+\text{-Si/SiO}_2\text{/Pt}$ interface under dark and illuminated conditions. Pt was stepwise deposited by a) direct current (DC)-sputter deposition and b) thermal evaporation. Core level binding energy positions E_b are depicted over Pt thickness with 10 and 300 W X-ray source power.

recombination centers for photoelectrons at the $\text{n}^+\text{/SiO}_2\text{/Pt}$ interface, though this is on the other hand prevented by thermal evaporation.

In order to investigate the exact energetic alignment very close to the $\text{n}^+\text{-Si/Pt}$ interface, potential corrected peak shape analysis has been performed as described in Section 4.1.2, considering the bare $\text{pn}^+\text{-Si}$ as flat band potential reference (Figure 8.4). The c-Si contribution of a 4.8 Å thick sputtered Pt and a 4.0 Å thick evaporated Pt interface has been modeled using quadratic potential drops along the Si SCR with an information depth of $\lambda_{\text{IMFP}}(\text{Si } 2\text{p})_{\text{c-Si}} = 32 \text{ Å}$. The SiO_2 contribution has been modeled using a linear potential drop considering substrate related shifts according to the c-Si model using an information depth of $\lambda_{\text{IMFP}}(\text{Si } 2\text{p})_{\text{SiO}_2} = 38 \text{ Å}$ and $\lambda_{\text{IMFP}}(\text{O } 1\text{s})_{\text{SiO}_2} = 29 \text{ Å}$. When comparing the background subtracted Si 2p lines before and after contact formation to Pt, it is noted that with both deposition processes the native oxide thickness increases. This effect leads to an oxide thickness during sputtering of 9.1 Å. This is even more prominent during thermal evaporation, where the oxide increased to 13.5 Å. Furthermore, the Si 2p gets smeared out to lower binding energies, even though the main line only shows minor changes in energy position. When the reference fit of the bare $\text{pn}^+\text{-Si}$ is applied to the potential drop model as presented in Section 4.1.2, the raw data can be fitted very well to the interface related Si 2p core level. The results of the fitting model for both interfaces are summarized in Table 8.1. According to the fitting model, the top Si- n^+ layer forms a thin depletion layer of about $\approx 5 \text{ nm}$ as already observed on the bare Si

a) sputter deposition: $\text{pn}^+\text{-Si/Pt}$ (4.8 nm)



b) thermal evaporation: $\text{pn}^+\text{-Si/Pt}$ (4.0 nm)

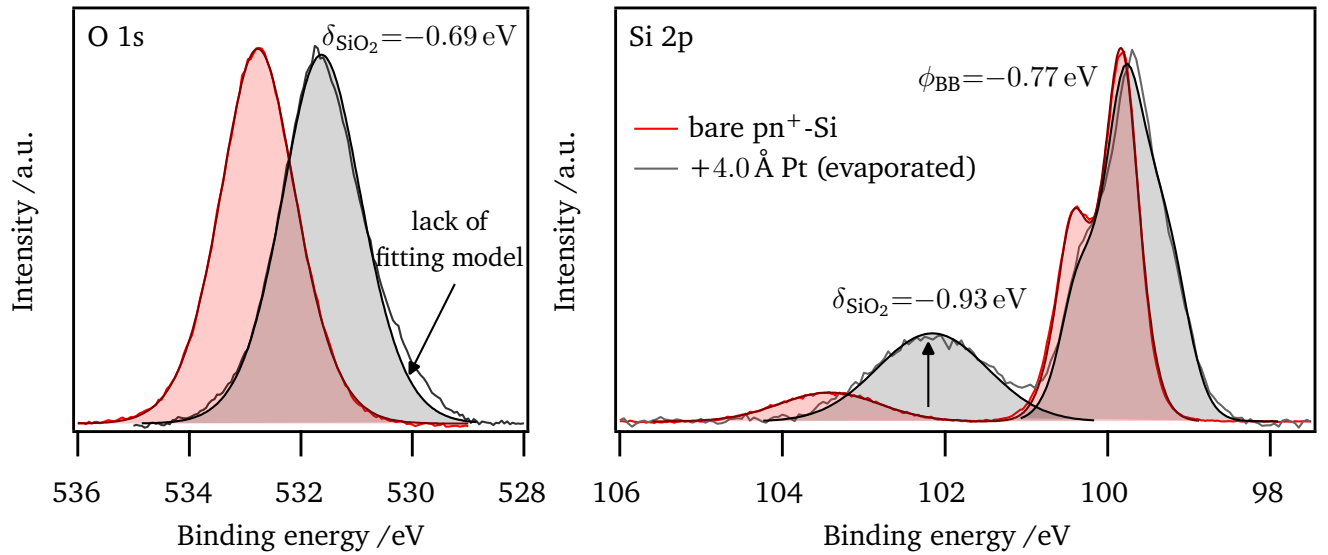


Figure 8.4: Background subtracted O 1s and Si 2p spectra of bare and Pt covered $\text{pn}^+\text{-Si}$. Potential drop corrected line shapes has been fitted and compared for a) sputter deposited b) thermal evaporated Pt. For energy resolution, Si 2p in a) was measured with 5 eV pass energy. All other spectra are measured with 10 eV pass energy.

Table 8.1: Fitting results of quadratic potential distributions inside the c-Si SCR, with E_0 as lowest Si 2p contribution at the very interface:

Deposition method	Pt layer thickness	Thickness of SCR	Potential drop	E_0	Doping concentration
sputtering	4.8 Å	3.9 nm	-0.61 eV	99.13 eV	$5.2 \times 10^{19} \text{ cm}^{-3}$
evaporation	4.0 Å	4.9 nm	-0.77 eV	99.05 eV	$4.1 \times 10^{19} \text{ cm}^{-3}$

wafers in contact to Pt. However, the band bending of the sputtered interface is with -0.61 eV slightly lower than -0.77 eV evaluated on the evaporated interface. The Si 2p contribution $E_{b,0}$ represents the Si 2p emission at the very interface, which is shifted from the bulk component by the total band bending. In this case, E_0 is found to be at $E_{b,0}=99.13$ eV, coinciding with the pinning level found on the Si wafers which was attributed to the interdiffusion of Pt. The higher band bending evaluated on the thermal evaporated interface might indicate that the Fermi level is not pinned due to interface states, but instead pins at the valence band maximum (VBM) caused by band gap narrowing in degenerated semiconductors ($E_g(N_{\text{don}}=2.5 \times 10^{20} \text{ cm}^{-3})=0.77$ eV).¹⁵⁹ Furthermore, the high doping concentrations of $5 \times 10^{19} \text{ cm}^{-3}$ confirm the CV profiling data, presented in the beginning of this chapter.

However, the fits shown here only consider potential related shifts and neglect any chemical related spectral changes, which might appear due to Pt_xSi formation and reduced SiO_x species. Furthermore, it is known that for highly doped semiconductors the *depletion approximation* is not valid since not all donors can be considered as ionized. Consequently, the charge distribution within the narrow SCR will not be constant but increases to the very interface. As a consequence, the potential distribution will be narrower as evaluated according to the model used here. However, this will rather overestimate the evaluated width of the SCR than the total potential drop which is dominated by the lower binding energy shoulder. Since the exact density of states (DOS)-distribution of the As-dopant is not known, the exact potential distribution inside the n^+ SCR could not be provided. Nevertheless, the fitting procedure leads to reasonable line shapes even with the used *depletion approximation* leading to reasonable physical fitting parameter. In this case, E_0 represents the SiO_2 contribution located at the very interface to the c-Si.

Table 8.2: Fitting results of potential drop within interfacial SiO_2 layer with E_0 as position of SiO_2 contribution at highest binding energies:

Deposition method	Spectral line	Oxide thickness	Depth correction λ_{IMFP}	Potential drop	E_0	IF charge
sputtering	Si 2p	9.1 Å	38 Å	-0.18 eV	102.97 eV	$1.9 \times 10^{12} \text{ cm}^{-2}$
sputtering	O 1s	9.1 Å	29 Å	-0.26 eV	531.63 eV	$2.7 \times 10^{12} \text{ cm}^{-2}$
evaporation	Si 2p	13.5 Å	38 Å	-0.93 eV	102.65 eV	$7.3 \times 10^{12} \text{ cm}^{-2}$
evaporation	O 1s	13.5 Å	29 Å	-0.69 eV	531.55 eV	$5.5 \times 10^{12} \text{ cm}^{-2}$

Apart from the c-Si line shapes, the linear potential drop within the interfacial SiO_2 layer has been fitted as well (Figure 8.4). Here, clear differences in the SiO_2 related Si 2p line are noted between the sputtered and evaporated Pt interfaces. With the considered substrate shifts according to Table 8.1, the potential drop has been evaluated from the Si 2p and O 1s line shapes (Table 8.2). The potential drops of the sputtered interfaces are only in the range of -0.2 eV, while in the evaporated interface, around -0.9 eV are dropping inside the SiO_2 layer. For both samples, the model fits of the O 1s signal lack for lower binding energies leading to a potential drop overestimation for the sputtered, and an underestimation for the evaporated surface which might result adsorbate related oxygen contributions on top of the Pt layer, which were neglected in this case. Furthermore, the effect of reduced SiO_x species remain unclear and cannot be covered by the presented fitting model.

After the deposition of 4 to 5 Å Pt, the total potential drop is about 0.8 eV along the sputtered pn^+ -Si/Pt interface, while about 1.7 eV are dropping at the evaporated interface. This might indicate, that the sputtering process leads to a more homogeneous and dense surface, while the thermally evaporated Pt film tends to form larger agglomerates that do not cover the whole Si surface, but fully evolves the Si/Pt contact potential.³¹¹

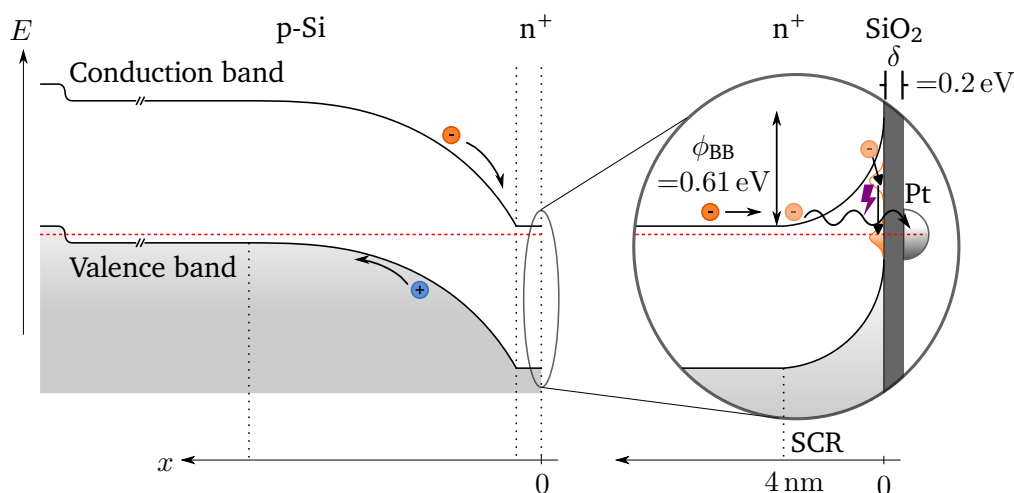


Figure 8.5: Band energy diagram of the Pt covered pn^+ -Si photocathode. Both, sputter deposited ($\phi_{BB}=0.61$ eV) and thermal evaporated Pt ($\phi_{BB}=0.77$ eV) induces a thin depletion layer of about 4 to 5 nm. Additional potential of $\delta \approx 0.2$ eV and $\delta \approx 0.9$ eV drops for the sputter and thermal deposited interface in the dielectric SiO_2 layer. Sputtered Pt might induce Pt related surface states which may act as recombination centers for excess charge carriers, reducing the photovoltage of the buried junction.

In any case, it is observed from the line shapes that both sputtered and evaporated Pt form a very thin depletion layer within the n^+ layer of the buried pn^+ -Si photocathode as schematically depicted in the band diagram in Figure 8.5. The sputtered interface shows slightly less depletion, which might indicate a Fermi level pinning due to Pt-related interface states. On the one hand, this would lead to a smaller potential barrier in comparison to the evaporated interface, but the Pt induced states might on the other hand act as recombination centers. Recombination could occur in two steps due to the amphoteric character of the Pt-related interface states. First, electrons could be captured by the fully unoccupied acceptor state. Then, the electron could recombine with a hole of the partially occupied donor state, which would finally lead to a loss of total photovoltage. This could explain why the SPV drops after the interface formation to sputtered Pt but not to the evaporated Pt, suggesting that Pt evaporation is the preferential physical vapour deposition (PVD) process to deposit Pt as HER-catalyst on Si photocathodes.

8.2.1 Electrochemical cell tests of pn^+ -Si/Pt photocathodes

In order to verify the experimental results deduced from the interface experiments, photoelectrochemical measurements have been performed. For this purpose, chopped light OCP measurements in 0.1 M H_2SO_4 have been conducted on the Pt covered samples using 1000 W cm^{-2} white light LED illumination. In Figure 8.6, the mean photovoltage of the evaporated and sputter deposited Pt samples is shown depending on the Pt thickness. In comparison to the *in situ* SPV analysis from XPS, chopped light OCP measurements do not show a clear relation to the Pt thickness and remains rather constant at about $V_{OC}=0.34$ V. The OCP data of the pn^+ -Si sample with about 20 nm evaporated Pt even seems to show an increase in V_{OC} by about 20 mV as shown in the chopped light measurements (compare right Figure in 8.6). At these film thicknesses, a reduction in photovoltage would be expected due to the increasing reflectivity of the metallic Pt film and has been observed in XPS. This suggests that the metallic Pt film delaminates in the 0.1 M H_2SO_4 solution, which was also observed by eye. In this context, the sputtered Pt films seemed to be a bit more stable indicating a higher mechanical sticking coefficient. However, XPS analysis after electrochemistry suggest that there remains a certain amount of Pt on the surface. It is not clear if the

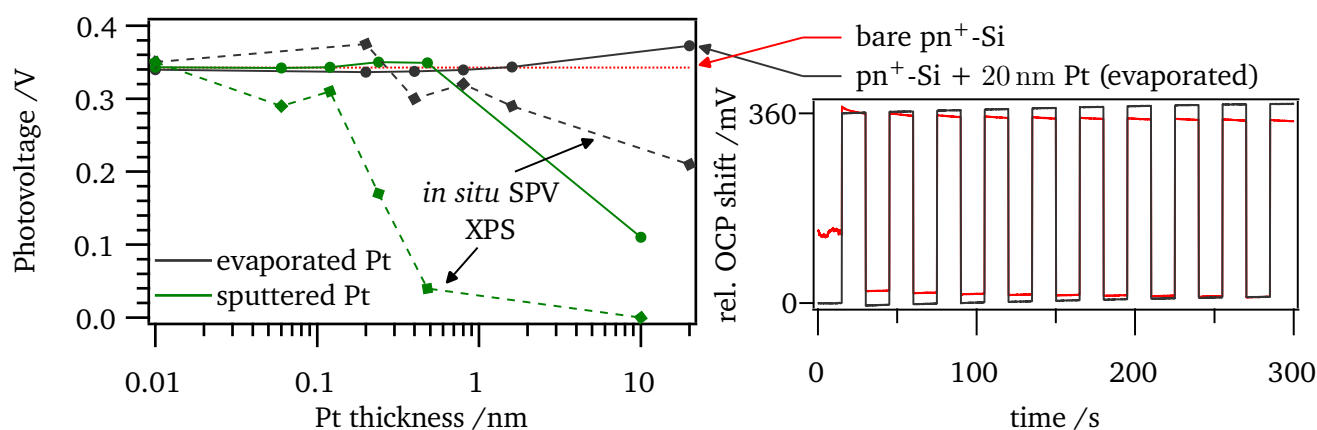


Figure 8.6: Photovoltage analysis of Pt-covered $\text{pn}^+\text{-Si}$ photocathodes by chopped light OCP measurements in a photoelectrochemical cell with $0.1 \text{ M H}_2\text{SO}_4$ under 1000 W m^{-2} white light LED illumination as shown for are bare and Pt covered pn^+ cell in comparison to *in situ* SPV analysis in XPS under vacuum.

increase in photovoltage is therefore related to an increased oxide thickness resulting from the evaporation process or from the contact of remaining Pt.

In addition to the chopped light OCP measurements, chopped light voltammetry experiments have been performed as well on the functionalized pn^+ Si wafers. In Figure 8.7 chopped light measurements of sputtered Pt with thicknesses of 1.2 and 4.8 \AA are shown. Even though delamination makes the evaluation difficult, reasonable current densities of up to -20 mA cm^{-2} can be achieved and are expected to result from HER. However, the native oxide impedes the charge transfer over the Si/Pt interface leading to very bad fill factors FF , while a clear saturation in current density could not be observed within the measurement potential window.³⁰⁹ Nevertheless, there are differences in the onset potential for the sputtered Pt samples. While the 4.8 \AA thick Pt sample shows an onset at 0.34 V vs. RHE which is equal to the photovoltage achieved from the chopped light OCP measurements, the 1.2 \AA thick Pt sample only shows the onset for HER at 0.16 V vs. RHE, indicating an additional charge transfer barrier, that leads

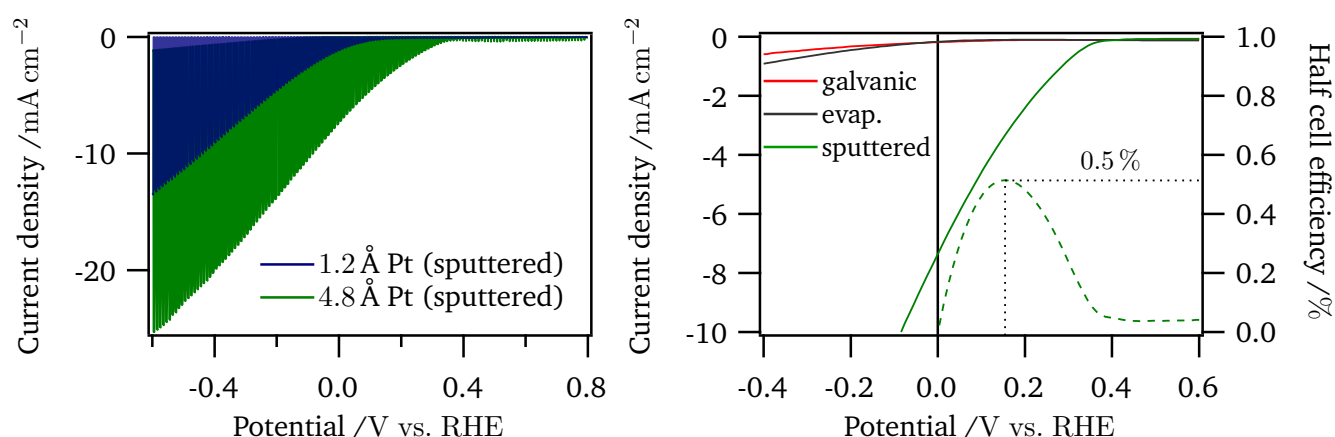


Figure 8.7: Chopped light voltammetry measurements in $0.1 \text{ M H}_2\text{SO}_4$ under 1000 W m^{-2} white light LED illumination (left), with steady state bright curves for differently deposited Pt on pn^+ Si (right). Only sputtered Pt shows a reasonable half cell efficiency of 0.5% at 0.15 V vs. RHE.

to a loss in usable photovoltage. It might be possible that Pt delamination leads to uncovered areas raising the overall photovoltage, while the homogeneous distribution before delamination leads to barrier formation as deduced from the interface experiments presented above. The 4.8 Å thick layer additionally reveals a considerable dark current, which indicates a short circuit current which might result from Pt covered sample edges. This might be also the reason, why the measured dark-light shifts in XPS or OCP measurements are dropping for the sputtered samples with increasing film thicknesses. However, the shifted onset of the HER from the RHE to anodic potentials should be independent from short circuits.

On the right hand side of Figure 8.7, the bright curves of the 4.8 Å sputter deposited Pt and the 4.0 Å thermal evaporated Pt sample are shown. These are the same samples from which the band energy diagram considerations have been achieved above. Furthermore, those samples were compared with a galvanostatic deposited Pt sample as described in Section 4.5.3. A half cell solar to hydrogen efficiency (STH) can be defined by considering the photocurrent density j_{ph} obtained under an applied bias of E_{RHE} , where E_{H^+/H_2} is the equilibrium redox potential of proton reduction ($=0.0$ V vs. RHE) and P_{sun} is the power density of the incident solar energy ($=1000$ W m⁻²):

$$\text{half cell STH} = |j_{ph}| \times \frac{E_{RHE} - E_{H^+/H_2}}{P_{sun}} \times 100 \% \quad (8.2)$$

Accordingly, only the sputter deposited Pt sample can achieve a reasonable half cell STH of about 0.5 %, which is still considerably lower than achieved on similar Si device structures in literature,^{265,309} while the evaporated as well as the galvanic deposited Pt sample cannot efficiently transfer the photovoltage from the buried junction to the Pt catalysts. At least on the galvanostatic deposited sample the Pt particle distribution did not change after the electrochemical characterization and a stable and homogeneous Pt particle distribution could be confirmed after the photoelectrochemical cell (PEC) measurements.

At these point it has to be conceded that the differences in electrochemical performance can not be fully elucidated by the interface model experiment, only considering interface energetics from a thin film approach. Accordingly, it is suggested that mechanical and electrochemical stability, as well as lateral homogeneities have to be considered as well to fully understand the differences in performances of the pn⁺-Si/Pt photocathode in dependence on the deposition technique.

8.3 The impact of TiO₂ on the device performance

It was shown that Pt on top of a single crystalline pn⁺-Si photocathode will lead to an electron depletion in the n⁺ layer. In many studies, TiO₂ as interlayer leads to an improvement in photoelectrochemical performance. In this section, the energetic alignment of the pn⁺-Si photocathode with TiO₂ is investigated comparing two different deposition techniques. An atomic layer deposition (ALD) process is used to deposit TiO₂ according to Section 7.1 and compared to sputter deposited TiO₂ as optimized in Section 7.4. For this experiment, ALD-TiO₂ layers have been deposited by *Jennifer Velázquez Rojas, Helmholtz-Zentrum Berlin* with three different TiO₂ film thicknesses that were confirmed by ellipsometry. Furthermore, two different Ti precursors TiCl₄ and titan(IV)isopropoxid (TTIP) have been compared.

For the sputter deposition process, the conductivity optimized parameter from Section 7.4 were used with 2.5 % oxygen mixed with Ar.

The ALD samples have been transferred *ex situ* in air for the analysis, while the sputter deposited samples could be analyzed straight after deposition in DAISY-FUN without breaking vacuum.

In Figure 8.8, the core level spectra of a) the ALD-deposited and b) the DC-sputter deposited TiO₂ films on top of the pn⁺-Si photocathode are depicted including the binding energy position under dark and

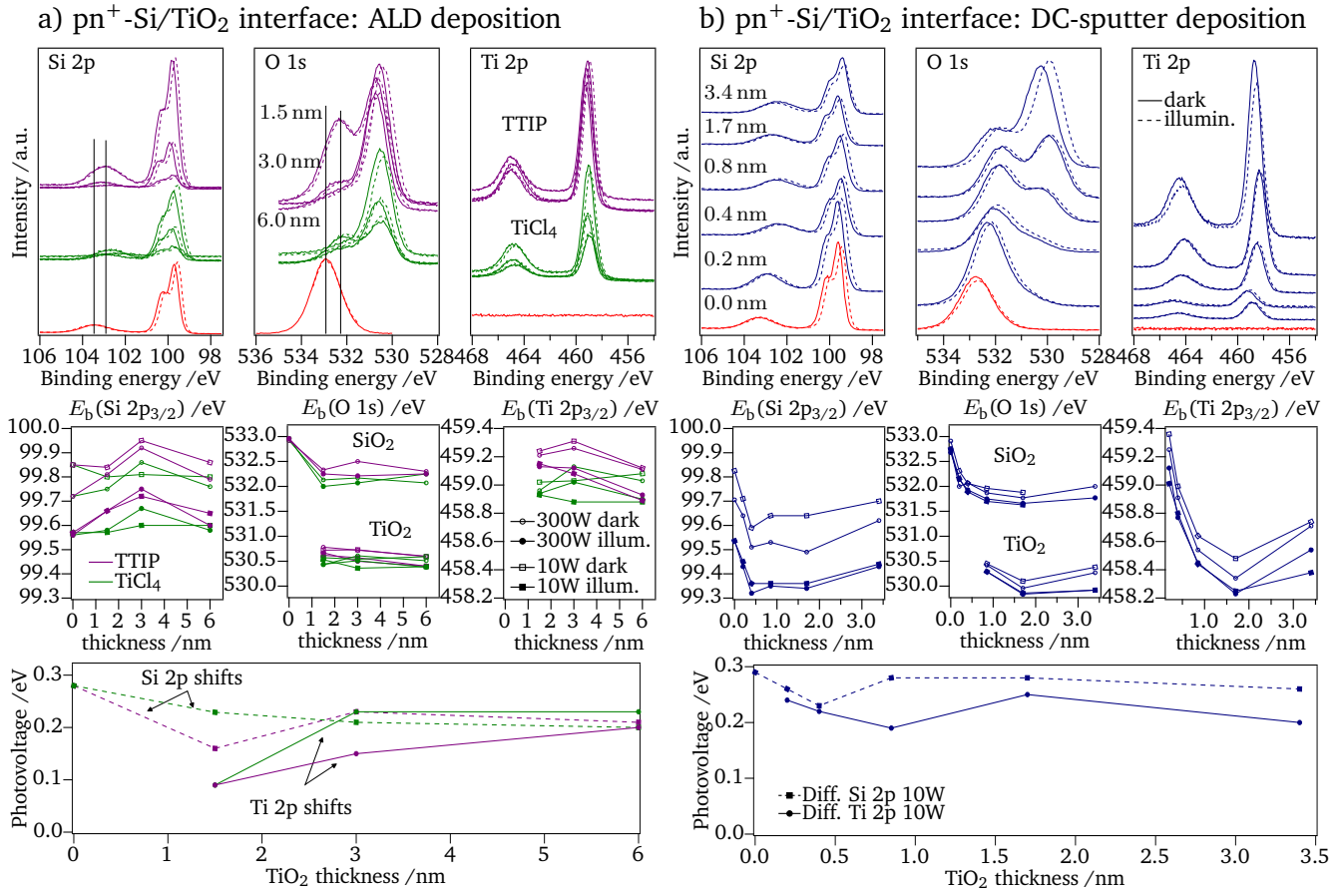


Figure 8.8: XP-spectra of $\text{pn}^+\text{-Si/SiO}_2/\text{TiO}_2$ interface under dark and illuminated conditions. TiO_2 step-wise deposited by a) an ALD process using TiCl_4 (green) and TTIP (purple) as different Ti precursors and b) a DC-sputter deposition process (blue). Core level binding energy positions E_b is depicted over TiO_2 layer thickness with 10 and 300 W X-ray source power.

illuminated conditions with 10 and 300 W X-ray intensity. In contrast to the Pt-Schottky interface, the Si 2p_{3/2} binding energy does not show a clear tendency when forming the contact to ALD- TiO_2 , even though a shift of the SiO_2 related Si 2p and O 1s components can be observed, indicating a potential drop of about -0.8 eV, which is significantly lower than observed with the in-house developed ALD process from Section 7.1. The two precursors seem to have a little influence on the binding energy of all core levels, even though the Ti 2p spectra seem to shift to lower binding energies with increasing coverage, while the Ti 2p binding energy of the TiCl_4 precursor remains rather constant with increasing film thickness. All in all the samples treated with TTIP show slightly higher binding energies in all core levels of about 0.2 eV compared to the TiCl_4 treated samples. However, the grounding of the samples seem to be an crucial point in this type of experiments when comparing absolute binding energy values on these samples while the relative shifts during illumination do not seem to be so different. When sample edges get covered with TiO_2 , the TiO_2 layer could be shortend directly to the back contact. This might be even more critical for the ALD process, while the sputter deposition is more recitified and edges are protected via shadowing. In this case however, the photovoltages in the Ti 2p should decrease with increasing film thickness, which is not observed in this case.

In case of both different ALD-covered samples, the potential corrected line shape fitting routines as presented in Section 8.2 cannot provide unambiguous results for the c-Si, which might indicate flat band

conditions in the n^+ -Si layer. Also, the less defined SiO_2 component reveals a maximum electron depletion of <0.2 eV within the n^+ layer. Interestingly, the *in situ* photovoltage analysis provided from dark and bright measurements at 10 W source-intensity shows a slight decrease on the top TiO_2 layer for lower film thicknesses of 1.5 nm, while the pn^+ related Si shifts remain constant. For higher film thicknesses the TiO_2 -related shifts approach the substrate shifts again.

The contact of the pn^+ -Si photocathode to a sputter deposited TiO_2 layer shows a slightly different picture. Even though the potential drop observed on the SiO_2 -related Si 2p and O 1s components is in the similar range of about -0.8 eV as the ALD deposited films, the c-Si line shows a shift to lower binding energies, indicating an electron depletion layer as observed at the Pt-Schottky interface. Furthermore, the Ti 2p is located at lower binding energies compared to the ALD process, which might indicate a more reduced TiO_2 species than achieved by the ALD process, indicating a lower doped TiO_2 layer than achieved with ALD and with that a higher contact potential at the Si/ TiO_2 interface. In contrast to that, the *in situ* photovoltage does not change significantly upon the sputtered TiO_2 layer and remains constant with increasing film thickness.

In summary, the interface data suggest that the ALD- TiO_2 -covered photocathodes do not reveal a significant electron depletion in contrast to the sputtered TiO_2 covered sample. This would suggest that the concentration of defects and the electron transfer properties differ significantly for both deposition types. However, the difference in interface energetics cannot be confirmed in the dark-bright data, where the open circuit photovoltage does not seem to be significantly affected by the contact layer.

8.3.1 Electrochemical cell tests of pn^+ -Si/ TiO_2 photocathodes

To verify the interface energetics deduced above, photoelectrochemical tests have been performed as final characterization of the device performance of the demonstrator cell.

When analyzing the photovoltage in the photoelectrochemical cell (Figure 8.9), the sputter-deposited TiO_2 does not show any impact on the V_{OC} under white light LED illumination, confirming the SPV analysis using XPS. For the ALD-deposited TiO_2 one notes drastic differences in the photovoltage. For both precursors, a drop in photovoltage is observed first (left image in Figure 8.9). This drop is also indicated by *in situ* XPS analysis (right image in Figure 8.9), where SPV shifts of the n^+ related Si 2p are not transferred over the interfacial oxide layer. As a result, SPV shifts are only measured in the substrate, but not in the TiO_2 related core levels which might indicate interface-induced recombination centers. There are no significant differences between the different Ti precursors visible. Interestingly, after 100 ALD-cycles (3.0 nm), the photovoltage increases significantly to 0.41 V, which is an improvement of more than 50 mV compared to the bare pn^+ -Si photocathode indicating here, a passivation of interfacial recombination centers. The gain in photovoltage, however, cannot result from the photocatalytic activity of the TiO_2 , since the electron depletion of the TiO_2 in contact to the electrolyte would counteract the HER.³¹²

However, to test if this gain in photovoltage can be really converted to the HER onset needs to be tested using linear sweep voltammetry.

In Figure 8.10a), the photoelectrochemical performance of the TiO_2 covered photocathodes is shown in comparison to the bare pn^+ -Si cell. On all samples Pt has been deposited galvanostatically at 0.5 mA cm^{-2} for 2 min (see Section 4.5.3 for details). The Pt deposition did not lead to significant changes in the OCP shifts under illumination. The sample with only 50 ALD-cycles (1.5 nm) showed the lowest V_{OC} in the OCP measurements. As expected, it also shows the worst photoelectrochemical performance. The best

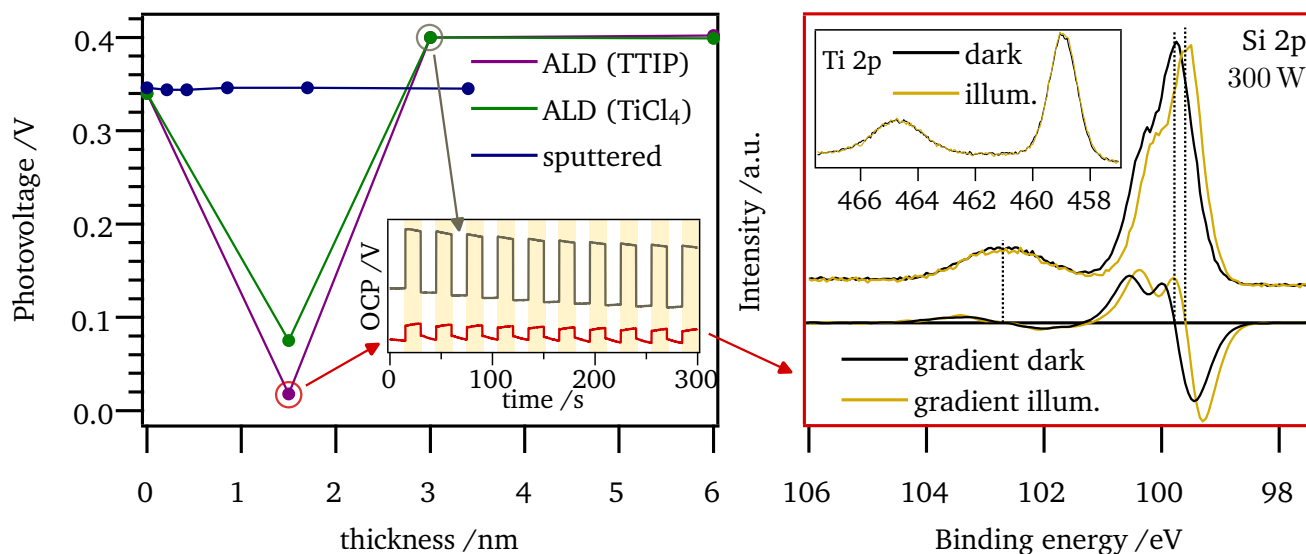


Figure 8.9: Photovoltage analysis of TiO₂-covered pn⁺-Si photocathodes in photoelectrochemical cell with 0.1 M H₂SO₄ under 1000 W m⁻² white light LED illumination (left). ALD-TiO₂ leads to a significant improvement in V_{OC} for film thicknesses >3 nm/100 cycles. For 1.5 nm/50 cycles, the potential drop is confirmed in XPS, where c-Si reveals shifts under illumination, which do not occur on the interfacial oxide layer indicating recombination of excess charge carriers (right).

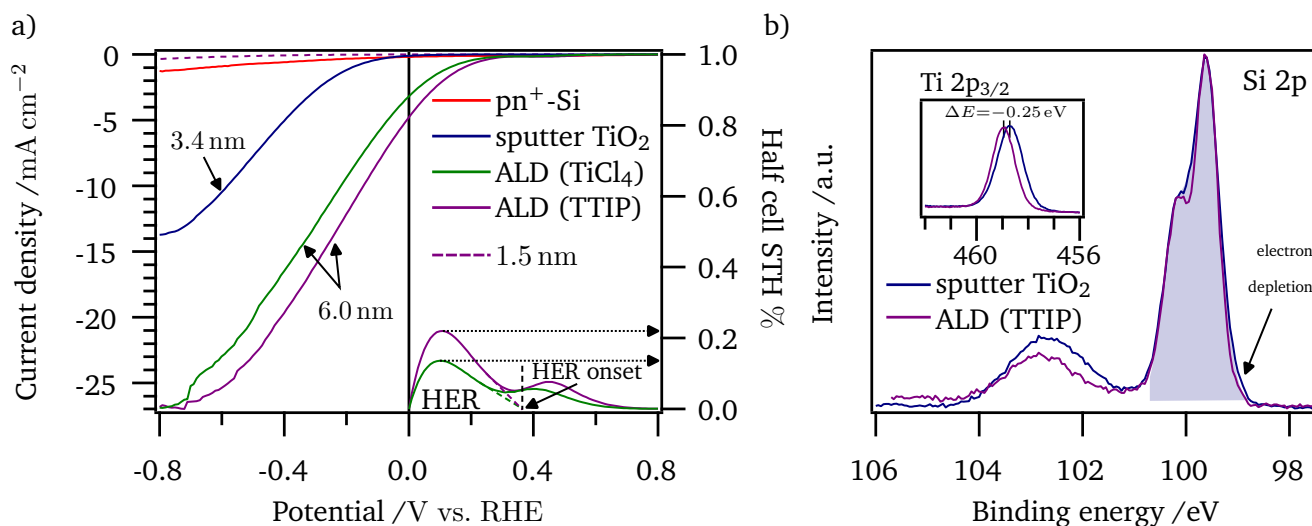


Figure 8.10: a) Linear voltage curves of bare (red) and TiO₂-covered pn⁺-Si photocathodes with galvanostatic Pt as HER catalyst. Photovoltage loss for sputtered TiO₂ results from depletion of n⁺-layer as indicated by line shape analysis of Si 2p line in b).

performances are shown for thicker ALD-deposited films, while the differences between 3 and 6 nm film thickness is negligible. The sample deposited with TTIP shows a slightly better performance and with that a maximum half cell efficiency of 0.22 % in comparison to the sample deposited with TiCl_4 , whose half cell efficiency of 0.13 % might be related to a better conductivity. The efficiency waves have been derived according to Equation 8.2 and show an increase at about 0.6 V vs. RHE, which is not related to the HER but a reduction wave that might be related to a chemical reduction of the TiO_2 or proton adsorption on the Pt particles.³¹³ Since the reduction wave is more pronounced on the thicker TiO_2 films, it might be also related to a reduction of the TiO_2 surface. However, the onset for the HER is observed at about 0.34 V vs. RHE, coinciding with the photovoltage of the bare pn^+ -Si cell. Consequently, the gain in photovoltage observed with the shifted OCP does not lead to a gain in the onset of the HER. Interestingly, the onset of the sputtered TiO_2 sample is at about 0.05 V vs. RHE, indicating no usable gain in photovoltage for the HER. When comparing the Si 2p line shapes of the sputtered and ALD-deposited sample, one notes that the sputtered Si 2p line is less structured. By applying the potential corrected line shape fitting routine presented above (Figure 8.10b)), a depleted n^+ is confirmed at the sputtered interface, while an electron depletion cannot be proved at the ALD interface. According to the fitting model which are not that evidential than observed on the Pt, the sputter-deposited TiO_2 interface leads to an electron depletion in the n^+ layer of about -0.28 eV . This is confirmed by the SiO_2 -related component and the Ti $2\text{p}_{3/2}$ signal, which are shifted by $\Delta E = -0.25 \text{ eV}$ in comparison to the ALD deposited interface. As a result, the charge transfer at the sputtered Si/ TiO_2 interface shows a diode-like behavior leading to a shifted onset of the HER which leads to a loss in usable photovoltage and finally requires additional overpotentials. In addition, the increased thickness of interfacial SiO_2 will also affect the charge transfer and might be responsible for the reduced slope in current density in comparison to the ALD- TiO_2 covered samples.

8.4 Conclusions on pn^+ -Si device structure performances

In this chapter, photoelectrochemical model structures have been designed and tested with respect to their photoelectrochemical cell performance. At first, Pt covered photoelectrodes and their band alignment under dark and illuminated conditions were investigated. For both deposition methods, an electron depletion layer was observed to form when forming the interface to Pt. With that, a loss in photovoltage was observed in XPS. Subsequent photoelectrochemical measurements in the electrolyte could not confirm the drop in photovoltage. Contradicting to the energetic band alignment, which was similar for evaporated and sputtered Pt, sputter deposited Pt showed by far the best photoelectrochemical HER performance. This suggests that apart from the energetic band alignment, also other parameters such as charge transfer rates, electrochemical stability, and mechanical sticking are essential for a good substrate-catalyst coupling. On both sample Pt delamination was observed suggesting a lateral inhomogeneous electrode surface. The interfacial band alignment models, such as peak shape analysis require homogeneous surfaces. The impact of lateral potential distributions can therefore not be considered, but may play a decisive role to understand the differences in the photoelectrochemical performance.

When adding TiO_2 as buffer layer between the photocell and electrodeposited Pt as HER catalyst, the total current densities could be increased by at least a factor of 10 indicating a “better” electric contact in comparison to the non-covered pn^+ -Si photocathode. One aspect in that sense is related to the better sticking of the Pt catalyst on top of TiO_2 in contrast to SiO_2 , which might also enhance the charge transfer properties as well as the overall stability. However, reasonable half cell efficiencies can only be derived when using ALD as deposition method. XPS peak shape analysis suggests that the ALD process prevents the substrate photoelectrode from forming an electron depletion layer and with that from barrier formation which is observed when using a sputter method. Barrier formation requires additional overpotentials for

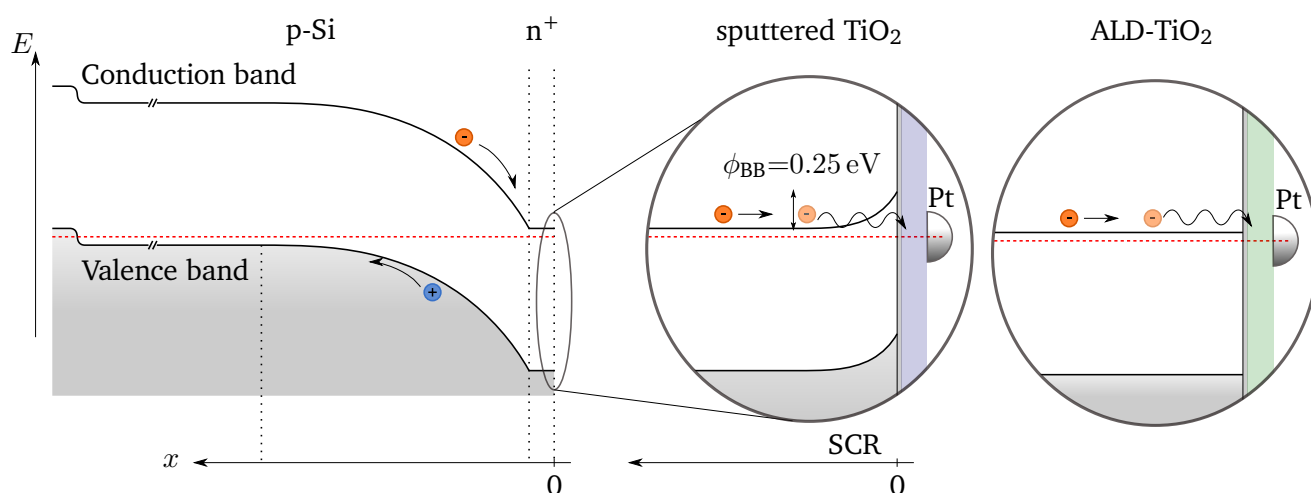


Figure 8.11: Schematic band energy diagram of pn^+ -Si photocathodes covered with TiO_2 as electrochemical buffer layer. Sputter deposition leads to an electron depletion forming a charge transfer barrier, while no depletion is observed when using ALD.

the charge transfer processes across the functional layers to run the HER as summarized in Figure 8.11. However, the presence of SCR at the functional interfaces does not seem to have an influence on the V_{OC} measured by chopped light OCP or XPS-SPV measurements. In contrast, for thin ALD- TiO_2 of about 1.5 nm which forms after 50 ALD cycles, the V_{OC} drops drastically, which is more related to the formation of recombination centers rather than electronic barriers. In this case, the charge carrier recombination might be related to a not fully TiO_2 covered photocathode surface where lateral inhomogeneities form recombination centers.

In summary, the energetic role of TiO_2 on Si-based photocathodes could be elucidated. However, the deposition technique and its processing condition and with that the electronic film properties of the TiO_2 layers play a decisive role when trying to prevent electronic barrier formation and to finally improve photoconversion efficiencies.

There remains still a need of optimizing the treatment and deposition process e.g. controlling SiO_2 and TiO_2 properties, which could also include post-deposition treatments.

9 Conclusions and outlook

The main goal of this thesis was to elucidate the electronic structure and energy band diagrams for photoelectrochemical water splitting devices. This included the systematic investigation of energy band diagrams in the vicinity of a liquid electrolyte and the coupling of the photoabsorbers to chemical and electronic passivation layers as well as co-catalysts. To address this goal, model surfaces and device structures were designed with respect to surface and interface states and their influence on interfacial charge distribution were monitored.

As a first set of experiments on these questions, the band energy diagrams of differently prepared single crystalline Si surfaces were investigated by photoemission spectroscopy (PES). With X-ray photoemission spectroscopy (XPS), it is shown that the Fermi level position at the prepared Si surfaces differs from the value expected from bulk doping concentrations, indicating surface band bending. Surface band bending is induced by the charge transfer from surface states into the Si bulk. The impact of the different surface preparation procedures on surface band bending was analyzed. In addition, ultraviolet photoemission spectroscopy (UPS) and near edge X-ray absorption fine structure (NEXAFS) were performed in order to identify occupied and unoccupied defect levels within the Si bandgap. An occupied and an unoccupied defect level was found at the lower and upper half of the Si bandgap with a charge neutrality level (CNL) very close to midgap, showing that the simple picture of a gaussian electronic surface state distribution around the CNL is too much simplified in the case of Si surfaces. These states coincide very well to unsaturated dangling bond defects on Si surfaces, which were so far only unequivocally established as P_b centers by spin resonance spectroscopy. With that, Si dangling bonds are the dominating surface defects on Si surfaces, which can even be found on very well-defined surface reconstructions.

Furthermore, the experiments showed that the energetic position of the dangling bond defect bands strongly depends on the chemical environment of the defect center. If the $\equiv Si \cdot$ atom, which localizes a dangling bond, gets oxidized by a backbonding to 1,2 or 3 oxygen atoms ($R_3 \equiv Si \cdot$ with $R = Si$ or O), all defect levels shift towards the vacuum level, moving the unoccupied defect band above the conduction band minimum (CBM). As a result, only occupied donor-like states remain within the Si bandgap and are electronically active, which characterizes the dominating defect at not completely oxidized surfaces or Si/SiO₂ interfaces.

It turned out that the results of such studies, especially with respect to the defect related band bending depend not only on the electronic distribution of charge at the surface, but also on the non-equilibrium condition when measuring using illumination sources, which induces a surface photovoltage (SPV). The SPV in that case can either be induced by the excitation of the probing light, or also by deliberate bias light illumination.

Repeating those studies at cryogenic temperatures could even more pronounce source-induced SPV due to the thermally inhibited recombination. These measurements indicated that the recombination of excess charge carriers depend on the minority charge carriers due to the difference in capture cross-sections of holes and electrons as well as the oxidation state of the defect center.

It is crucial to emphasize that even with the most effective surface termination treatments, there will still be residual concentrations of the active $R_3 \equiv Si \cdot$ dangling bond states due to entropy reasons of defect

formation.

Subsequently, the reactivity of the Si dangling bonds was explored and the electronic interaction of the Si surfaces with H₂O was deduced by applying a “frozen electrolyte” adsorption method. The dissociation of H₂O is only observed on unreconstructed surfaces, forming Si–OH_{ads} and Si–H_{ads} states after flashing. For all other passivated surfaces, a direct dissociative reaction with the remaining Si dangling bonds is not observed. However, the adsorption of molecular H₂O on adsorbate modified surfaces leads to a slight change of band bending. It is suggested that the change in band bending is related to an electron transfer from the dangling bond state into the bulk due to the interaction of the unsaturated Si bond with the H₂O oxygen lone pair, lifting the dangling bond electron above CBM.

Dangling bond defects at the Si/SiO₂ surface also play a crucial role in the electronic coupling to the Pt catalyst. The contact formation to Pt led to an electron depletion layer at the Si/SiO₂ interface due to the high work function (WF) of Pt. The contact potential is expected to partially deplete Si dangling bond states. However, there are spectral indications that the sputter deposition of Pt on top of the native SiO₂ substrate partially reduces the oxide, which further increases the number of unsaturated Si states. In addition, Fermi level pinning occurs at the lower half of the Si bandgap due to the deep level impurity traps resulting from a SiPt_x interface phase.

In any case, the electronic contact formation of Si/Pt is not beneficial for photoelectrochemical cells (PECs), since either additional defect formation or electron depletion will limit cathodic charge transfers at this specific interface, which leads to a photovoltage loss when using it as photocathode.

In comparison to Si as elemental semiconductor, similar investigations were performed on the binary III-V model system InP, which is known to show even better photovoltaic properties than Si. Here, the InP was prepared with highly pure and controlled surface reconstructions, which were characterized by UPS and low-energy electron diffraction. Unsaturated phosphorous dangling bonds have been proven to cause midgap Fermi level pinning at P-rich surfaces when loosing their bond saturation to H, which was confirmed by DFT calculations. These unsaturated defects did not interact with molecular water, even though they seem to bind to the dissociation products H_{ads} and OH_{ads} if available.

In-rich surfaces are much more reactive, since they could not be transferred contaminant-free to Darmstadt. The partially oxidized surface reacted chemically to molecular water, leading to further surface oxidation, which shifted the Fermi level to the upper half of the band gap. Evidently, this surface oxidation process leads to a newly formed surface layer, which is able to inject electrons into the semiconductor. The origin of this charge transfer process remains unclear and has to be calculated computationally.

On a native oxide passivated InP layer, an electronic interaction of the surface with molecular water was observed, leading to an electron injection as seen in oxide passivated Si surfaces. This fact suggests a similar reaction mechanism in which a dangling bond interacts with the H₂O oxygen lone pair.

The ability of TiO₂ to electronically passivate the semiconductor surfaces was tested using an in-house developed ALD process. With this process, a large contact potential drop is observed between a p-Si/SiO₂ wafer and the TiO₂, leading to electron depletion in the semiconductor. Furthermore, when investigating the atomic layer deposition (ALD) growth on InP, the TiCl₄ precursor did not absorb sufficiently on oxygen-free unpolar InP surfaces, which prevented the efficient TiO₂ layer growth. HCl, assumed as by-product in the process, led to surface etching instead, destroying the surface structure. The nucleation of TiO₂ required the oxidized surface species of the water exposed In-rich InP surface, at which the TiO₂ grows in an island mode.

Once TiO₂ is covering the InP, the Fermi level remains pinned at the interface. When adsorbing additional water, a chemical reduction of lattice Ti⁴⁺ to Ti³⁺ is observed, indicating again an electron injection upon water adsorption, even though the reaction mechanisms on transition metal oxides with water may be

different compared to Si and InP. These electrons might even be injected into the InP substrate, changing the energetics of the entire InP/TiO₂ interface.

In the last phase of interface experiments, Si pn⁺ model-junctions were studied to elucidate the band alignment at the functional device interfaces and the samples were transferred to an electrolyte solution to test its photoelectrochemical device performance. Modeling potential corrected XPS line shapes could identify a strong inversion layer at the topmost Si-n⁺ layer in contact to Pt, which is independent of the applied deposition technique. This inversion layer is expected to act as a barrier when using the device as photocathode and remains during illumination under operation. In contrast to that, the photoelectrochemical device tests showed a strong impact of the deposition technique on the measured device performance, where sputter-coated photocathodes revealed much higher photocurrents than thermal evaporated or galvanically deposited Pt samples. These effects cannot solely be described with band energy diagrams derived from the model interfaces, suggesting that stability-related effects and lateral inhomogeneities play a decisive role when designing efficient devices.

A clear relation between the energetic band alignment and the device performance could be observed when using TiO₂ as interlayer. It was shown experimentally that the sputter deposition of TiO₂ leads also to an electron depletion in the Si-n⁺ layer, which is not that prominently observed in ALD-deposited TiO₂. Here, only the ALD-TiO₂ covered photocathodes show a reasonable photoconversion efficiency, while for sputtered TiO₂ the inner photovoltage is consumed completely to overcome the electron transfer barrier at the n⁺-Si/TiO₂ interface.

In summary, this work shows that even highly defined and reconstructed elemental or binary semiconductor surfaces reveal Fermi level pinning due to a significant amount of still existing surface states. Those surface states typically remain due to entropy reasons. In literature, band structure calculations are mostly discussed for the most stable surface reconstructions. But less probable surface reconstructions have to be considered as well, since they coexist depending on their energy in different concentrations with the majority configuration. Even in the sub-percent regime, these sub-phases might dominate the electronic properties of the overall surface or interface. To reduce the entropy-driven amount of sub-phases, optimizing the cooling procedures after growing Si and III-V tandem structures at high temperatures is extremely important. Nevertheless, the presented studies here suggest that it seems almost impossible to completely passivate these surface states electronically, neither by surface preparation nor by contact formation to adsorbates or passivation layers. In an additional study with project partners from TU Ilmenau, we could show that even an epitaxial contact formation of ternary III-V systems does not lead to a complete depinning of the Fermi level at the interface.³¹⁴

In addition, at pinned surfaces the total amount of surface defects acting as recombination sites will still limit the maximum photocurrents.

According to the experiments, it is possible to deplete and occupy defect states without fully passivating them. Apart from defect passivation, also a flooding or complete depletion of surface states could become an efficient engineering strategy when designing complex interface structures for energy conversion.

Following that strategy in photocathodes, photoelectrons excited in a buried junction will accumulate at an n⁺ emitter layer. If all surface states are occupied (flooded) with electrons localized at these states, the photoelectron cannot be captured by a hole state, which will impede recombination. The electronic flooding of surface states might be either implemented by additional doping or by the contact formation to an appropriate, e.g. an extremely thin low-WF contact layer. According to the shown results, optimized TiO₂ layers can prevent the electron depletion of the emitter layer in contact to the catalyst. Better results can even be achieved, by adding thin metallic interlayers of Ti or Al on top of the emitter layer as shown in literature.^{265,309}

According to the results presented in this thesis, the contact potential of two materials is given by the thermodynamic difference in electrochemical potential and is independent from surface and interface preparation. However, the potential distribution over the whole interface can be strongly influenced by surface treatments, interfacial layers and chemistry. For instance, the contact of the noble-metal catalyst directly to the photoabsorber always leads to an electron depletion of the emitter layer due to the high contact potential with those materials, enhancing charge carrier recombination and barrier formation. This has to be prevented for highly efficient PEC devices, suggesting that electronic and chemical passivation has to be achieved in different layer arrangement i.e. metallic and oxidic layers, introducing an additional interface and with that increase device complexity. This will finally require much more research efforts in interface engineering.

This work could show in addition that surface defects play a decisive role when interacting with liquid electrolytes, modeled here with water as adsorbed molecule. However, since these defects are in the minority when analyzing well-prepared surfaces, it becomes almost impossible to resolve the chemistry at these defects. The Fermi level seems to be the only measure to follow electron transfer reactions, even though the involved electronic states and their origin remain unknown.

To further increase the understanding of interface energetics in PEC devices, a detailed analysis before and after sample preparation is not sufficient. In a future study a detailed analysis before and after operation in the liquid electrolyte is required, focusing on the electronic states involved in degradation and corrosion mechanisms. In fact, interface energetics may strongly differ when facing operation conditions since electronic potentials are redistributed and charge carriers will cross the interfaces under non-equilibrium conditions. With classical surface science approaches, we come to a limit since the ultra-high vacuum gap in the experimental setup can not cover the whole complexity of the investigated device structure. Fortunately, there are new developments in the field of surface science techniques such as operando near-ambient pressure XPS (NAP-XPS), which enable more realistic device-related experimental set-ups.³¹⁵ In addition, the combination of electron and vibrational spectroscopies such as infrared spectroscopy might be helpful in order to couple electron transfer reactions with surface bound intermediates. Furthermore, the use of hard X-rays from synchrotron radiation can additionally help to analyze buried multi-layer junctions or even electrochemical interfaces, when controlling the information depth by modifying inelastic mean free path of electrons.

As a conclusion, there remains a lot to do in the fascinating world of PEC device interfaces. Even though this thesis cannot fully cover the complex interface energetics at such buried multi-junction devices, the surface science approach presented here seems a promising way to close the knowledge gap in the future to bring these devices closer to their physical limits and making them competitive for the mass market.

Bibliography

- (1) Intergovernmental Panel on Climate Change (IPCC), Ed. *Climate Change 2022 - Mitigation of Climate Change*; Cambridge University Press, 2023.
- (2) Bundeszentrale für politische Bildung: Primärenergie-Versorgung. 2023; <https://www.bpb.de/kurz-knapp/zahlen-und-fakten/globalisierung/52741/primaerenergie-versorgung/>, accessed on September 7, 2023.
- (3) AGEE-Stat; AGEb: Bruttostromerzeugung 2022 - Statistisches Bundesamt. 2023; https://www.destatis.de/DE/Themen/Branchen-Unternehmen/Energie/_Grafik/_Interaktiv/bruttostromerzeugung-erneuerbare-energien.html, accessed on September 7, 2023.
- (4) McGlade, C.; Ekins, P. The geographical distribution of fossil fuels unused when limiting global warming to 2 °C. *Nature* **2015**, *517*, 187–190.
- (5) Höök, M.; Tang, X. Depletion of fossil fuels and anthropogenic climate change—A review. *Energy Policy* **2013**, *52*, 797–809.
- (6) Van de Krol, R.; Grätzel, M. In *Photoelectrochemical Hydrogen Production*; van de Krol, R., Grätzel, M., Eds.; Electronic Materials: Science & Technology; Springer US: Boston, MA, 2012; Vol. 102.
- (7) Barton, J.; Infield, D. Energy Storage and Its Use With Intermittent Renewable Energy. *IEEE Transactions on Energy Conversion* **2004**, *19*, 441–448.
- (8) Lewis, N. S.; Nocera, D. G. Powering the planet: Chemical challenges in solar energy utilization. *Proceedings of the National Academy of Sciences* **2006**, *103*, 15729–15735.
- (9) Sazali, N. Emerging technologies by hydrogen: A review. *International Journal of Hydrogen Energy* **2020**, *45*, 18753–18771.
- (10) Shockley, W.; Queisser, H. J. Detailed Balance Limit of Efficiency of p-n Junction Solar Cells. *Journal of Applied Physics* **1961**, *32*, 510–519.
- (11) Bolton, J. R.; Strickler, S. J.; Connolly, J. S. Limiting and realizable efficiencies of solar photolysis of water. *Nature* **1985**, *316*, 495–500.
- (12) Jaegermann, W.; Kaiser, B.; Ziegler, J.; Klett, J. *Photoelectrochemical Solar Fuel Production*; Springer International Publishing: Cham, 2016; pp 199–280.
- (13) Jaegermann, W.; Kaiser, B.; Finger, F.; Smirnov, V.; Schäfer, R. Design Considerations of Efficient Photo-Electrosynthetic Cells and its Realization Using Buried Junction Si Thin Film Multi Absorber Cells. *Zeitschrift für Physikalische Chemie* **2020**, *234*, 549–604.

-
- (14) Pinaud, B. A.; Benck, J. D.; Seitz, L. C.; Forman, A. J.; Chen, Z.; Deutsch, T. G.; James, B. D.; Baum, K. N.; Baum, G. N.; Ardo, S.; Wang, H.; Miller, E.; Jaramillo, T. F. Technical and economic feasibility of centralized facilities for solar hydrogen production via photocatalysis and photoelectrochemistry. *Energy & Environmental Science* **2013**, *6*, 1983.
- (15) Xiao, M.; Luo, B.; Wang, Z.; Wang, S.; Wang, L. Recent Advances of Metal-Oxide Photoanodes: Engineering of Charge Separation and Transportation toward Efficient Solar Water Splitting. *Solar RRL* **2020**, *4*, 1900509.
- (16) Hu, S.; Xiang, C.; Haussener, S.; Berger, A. D.; Lewis, N. S. An analysis of the optimal band gaps of light absorbers in integrated tandem photoelectrochemical water-splitting systems. *Energy & Environmental Science* **2013**, *6*, 2984.
- (17) Moritz, D. C.; Calvet, W.; Zare Pour, M. A.; Paszuk, A.; Mayer, T.; Hannappel, T.; Hofmann, J. P.; Jaegermann, W. In *Encyclopedia of Solid-Liquid Interfaces*; Wandelt, K., Bussetti, G., Eds.; Elsevier, 2024; pp 93–119.
- (18) Rocheleau, R. E. Photoelectrochemical production of hydrogen: Engineering loss analysis. *International Journal of Hydrogen Energy* **1997**, *22*, 771–782.
- (19) Urbain, F.; Smirnov, V.; Becker, J. P.; Lambert, A.; Yang, F.; Ziegler, J.; Kaiser, B.; Jaegermann, W.; Rau, U.; Finger, F. Multijunction Si photocathodes with tunable photovoltages from 2.0 v to 2.8 v for light induced water splitting. *Energy and Environmental Science* **2016**, *9*, 145–154.
- (20) Abdi, F. F.; Han, L.; Smets, A. H. M.; Zeman, M.; Dam, B.; van de Krol, R. Efficient solar water splitting by enhanced charge separation in a bismuth vanadate-silicon tandem photoelectrode. *Nature Communications* **2013**, *4*, 2195.
- (21) Cheng, W.-H.; Richter, M. H.; May, M. M.; Ohlmann, J.; Lackner, D.; Dimroth, F.; Hannappel, T.; Atwater, H. A.; Lewerenz, H.-J. Monolithic Photoelectrochemical Device for Direct Water Splitting with 19% Efficiency. *ACS Energy Letters* **2018**, *3*, 1795–1800.
- (22) May, M. M.; Döscher, H.; Turner, J. A. *Integrated Solar Fuel Generators*; The Royal Society of Chemistry, 2018; Vol. 2019-Janua; pp 454–499.
- (23) May, M. M.; Jaegermann, W. Combining experimental and computational methods to unravel the dynamical structure of photoelectrosynthetic interfaces. *Current Opinion in Electrochemistry* **2022**, *34*, 100968.
- (24) Thiel, P. A.; Madey, T. E. The interaction of water with solid surfaces: Fundamental aspects. *Surface Science Reports* **1987**, *7*, 211–385.
- (25) Jaegermann, W. In *Modern Aspects of Electrochemistry*; White, R. E., Conway, B. E., Bockris, J. O., Eds.; Plenum Press, 1996; Vol. 30; pp 1–185.
- (26) Mönch, W. *Semiconductor Surfaces and Interfaces*; Springer Series in Surface Sciences; Springer Berlin Heidelberg: Berlin, Heidelberg, 1995; Vol. 26; p 550.
- (27) Memming, R. *Semiconductor Electrochemistry*; Wiley-VCH Verlag GmbH & Co. KGaA: Weinheim, Germany, 2015.
- (28) Hamann, C. H.; Vielstich, W. *Elektrochemie*, 4th ed.; Wiley-VCH: Weinheim, 2005.

-
- (29) Levinshtein, M. E.; Rumyantsev, S. L. In *Handbook Series on Semiconductor Parameters*; Levinshstein, M., Rumyantsev, S., Shur, M., Eds.; World Scientific Publishing Co. Pte. Ltd., 1996; Vol. 1; pp 1–32.
- (30) Sze, S.; Ng, K. K. *Physics of Semiconductor Devices*; Wiley, 2006.
- (31) Bardeen, J. Surface States and Rectification at a Metal Semi-Conductor Contact. *Physical Review* **1947**, *71*, 717–727.
- (32) Cowley, A. M.; Sze, S. M. Surface States and Barrier Height of Metal-Semiconductor Systems. *Journal of Applied Physics* **1965**, *36*, 3212–3220.
- (33) Würfel, P. The chemical potential of radiation. *Journal of Physics C: Solid State Physics* **1982**, *15*, 3967–3985.
- (34) Shockley, W.; Read, W. T. Statistics of the Recombinations of Holes and Electrons. *Physical Review* **1952**, *87*, 835–842.
- (35) Marcus, R. A. On the Theory of Electron-Transfer Reactions. VI. Unified Treatment for Homogeneous and Electrode Reactions. *The Journal of Chemical Physics* **1965**, *43*, 679–701.
- (36) Gerischer, H. Über den Ablauf von Redoxreaktionen an Metallen und an Halbleitern. *Zeitschrift für Physikalische Chemie* **1961**, *27*, 48–79.
- (37) Willig, F.; Gundlach, L. *Encyclopedia of Applied Electrochemistry*; Springer New York: New York, NY, 2014; pp 1786–1798.
- (38) Shmidt, N. M. In *Handbook Series on Semiconductor Parameters*; Levinshstein, M., Rumyantsev, S., Shur, M., Eds.; World Scientific Publishing Co. Pte. Ltd., 1996; pp 169–190.
- (39) Raj, V.; Haggren, T.; Wong, W. W.; Tan, H. H.; Jagadish, C. Topical review: pathways toward cost-effective single-junction III–V solar cells. *Journal of Physics D: Applied Physics* **2022**, *55*, 143002.
- (40) Liang, D.; Bowers, J. E. Recent progress in lasers on silicon. *Nature Photonics* **2010**, *4*, 511–517.
- (41) Levinshstein, M.; Rumyantsev, S.; Shur, M. *Handbook Series on Semiconductor Parameters*; WORLD SCIENTIFIC, 1996; Vol. 1.
- (42) Zandvliet, H. J. The Ge(001) surface. *Physics Reports* **2003**, *388*, 1–40.
- (43) Chadi, D. J. Atomic and Electronic Structures of Reconstructed Si(100) Surfaces. *Physical Review Letters* **1979**, *43*, 43–47.
- (44) Nikolaychuk, P. A. The Revised Pourbaix Diagram for Silicon. *Silicon* **2014**, *6*, 109–116.
- (45) Weinrich, H.; Durmus, Y. E.; Tempel, H.; Kungl, H.; Eichel, R.-A. Silicon and Iron as Resource-Efficient Anode Materials for Ambient-Temperature Metal-Air Batteries: A Review. *Materials* **2019**, *12*, 2134.
- (46) Chung, Y.; Lee, C.-W. Electrochemical behaviors of Indium. *Journal of Electrochemical Science and Technology* **2012**, *3*, 1–13.
- (47) Pourbaix, M.; Zhang, H.; Pourbaix, A. Presentation of an Atlas of Chemical and Electrochemical Equilibria in the Precence of a Gaseous Phase. *Materials Science Forum* **1997**, *251-254*, 143–148.

-
- (48) Fujishima, A.; Honda, K. Electrochemical Photolysis of Water at a Semiconductor Electrode. *Nature* **1972**, *238*, 37–38.
- (49) Bae, D.; Pedersen, T.; Seger, B.; Iandolo, B.; Hansen, O.; Vesborg, P. C.; Chorkendorff, I. Carrier-selective p- and n-contacts for efficient and stable photocatalytic water reduction. *Catalysis Today* **2017**, *290*, 59–64.
- (50) Tang, H.; Prasad, K.; Sanjinès, R.; Schmid, P. E.; Lévy, F. Electrical and optical properties of TiO₂ anatase thin films. *Journal of Applied Physics* **1994**, *75*, 2042–2047.
- (51) Hitosugi, T.; Yamada, N.; Nakao, S.; Hirose, Y.; Hasegawa, T. Properties of TiO₂-based transparent conducting oxides. *physica status solidi (a)* **2010**, *207*, 1529–1537.
- (52) da Silva, A. L.; Hotza, D.; Castro, R. H. Surface energy effects on the stability of anatase and rutile nanocrystals: A predictive diagram for Nb₂O₅-doped-TiO₂. *Applied Surface Science* **2017**, *393*, 103–109.
- (53) Minhas, B.; Dino, S.; Qian, H.; Zuo, Y. An approach for high stability TiO₂ in strong acid environments at high temperature. *Surface and Coatings Technology* **2020**, *395*, 125932.
- (54) Hu, S.; Shaner, M. R.; Beardslee, J. A.; Lichterman, M.; Brunschwig, B. S.; Lewis, N. S. Amorphous TiO₂ coatings stabilize Si, GaAs, and GaP photoanodes for efficient water oxidation. *Science* **2014**, *344*, 1005–1009.
- (55) Gao, L.; Cui, Y.; Vervuurt, R. H. J.; van Dam, D.; van Veldhoven, R. P. J.; Hofmann, J. P.; Bol, A. A.; Haverkort, J. E. M.; Notten, P. H. L.; Bakkers, E. P. A. M.; Hensen, E. J. M. High-Efficiency InP-Based Photocathode for Hydrogen Production by Interface Energetics Design and Photon Management. *Advanced Functional Materials* **2016**, *26*, 679–686.
- (56) Wang, S.; Lu, A.; Zhong, C.-J. Hydrogen production from water electrolysis: role of catalysts. *Nano Convergence* **2021**, *8*, 4.
- (57) Li, C.; Baek, J.-B. Recent Advances in Noble Metal (Pt, Ru, and Ir)-Based Electrocatalysts for Efficient Hydrogen Evolution Reaction. *ACS Omega* **2020**, *5*, 31–40.
- (58) Hansen, J. N.; Prats, H.; Toudahl, K. K.; Mørch Secher, N.; Chan, K.; Kibsgaard, J.; Chorkendorff, I. Is There Anything Better than Pt for HER? *ACS Energy Letters* **2021**, *6*, 1175–1180.
- (59) Neuberger, F.; Baranyai, J.; Schmidt, T.; Cottre, T.; Kaiser, B.; Jaegermann, W.; Schäfer, R. From Bulk to Atoms: The Influence of Particle and Cluster Size on the Hydrogen Evolution Reaction. *Zeitschrift für Physikalische Chemie* **2020**, *234*, 847–865.
- (60) Schweinberger, F. F.; Berr, M. J.; Döblinger, M.; Wolff, C.; Sanwald, K. E.; Crampton, A. S.; Ridge, C. J.; Jäckel, F.; Feldmann, J.; Tschurl, M.; Heiz, U. Cluster Size Effects in the Photocatalytic Hydrogen Evolution Reaction. *Journal of the American Chemical Society* **2013**, *135*, 13262–13265.
- (61) Hüfner, S., Ed. *Very High Resolution Photoelectron Spectroscopy*; Lecture Notes in Physics; Springer Berlin Heidelberg: Berlin, Heidelberg, 2007; Vol. 715.
- (62) de Groot, F.; Kotani, A. *Core Level Spectroscopy of Solids*; CRC Press, 2008; pp 1–491.
- (63) Bubert, H.; Rivière, J. C. *Surface and Thin Film Analysis*; Wiley-VCH Verlag GmbH: Weinheim, FRG, 2003; pp 6–32.

-
- (64) Lenard, P. Erzeugung von Kathodenstrahlen durch ultraviolettes Licht. *Annalen der Physik* **1900**, 307, 359–375.
- (65) Einstein, A. Über einen die Erzeugung und Verwandlung des Lichtes betreffenden heuristischen Gesichtspunkt. *Annalen der Physik* **1905**, 322, 132–148.
- (66) Bohr, N. The Spectra of Helium and Hydrogen. *Nature* **1913**, 92, 231–232.
- (67) Klein, A.; Mayer, T.; Thissen, A.; Jaegermann, W. *Methods in Physical Chemistry*; Wiley: Weinheim, Germany, 2012; pp 477–512.
- (68) Powell, C. J. Practical guide for inelastic mean free paths, effective attenuation lengths, mean escape depths, and information depths in x-ray photoelectron spectroscopy. *Journal of Vacuum Science & Technology A: Vacuum, Surfaces, and Films* **2020**, 38.
- (69) Reilman, R. F.; Msezane, A.; Manson, S. T. Relative intensities in photoelectron spectroscopy of atoms and molecules. *Journal of Electron Spectroscopy and Related Phenomena* **1976**, 8, 389–394.
- (70) Held, G. *Surface and Thin Film Analysis*; Wiley-VCH Verlag GmbH: Weinheim, FRG, 2003; pp 71–82.
- (71) Van Hove, M. A.; Weinberg, W. H.; Chan, C.-M. *Low-Energy Electron Diffraction*; Springer Series in Surface Sciences; Springer Berlin Heidelberg: Berlin, Heidelberg, 1986; Vol. 6.
- (72) De Broglie, L. Waves and Quanta. *Nature* **1923**, 112, 540–540.
- (73) Niu, S.; Li, S.; Du, Y.; Han, X.; Xu, P. How to Reliably Report the Overpotential of an Electrocatalyst. *ACS Energy Letters* **2020**, 5, 1083–1087.
- (74) Chen, Z.; Jaramillo, T. F.; Deutsch, T. G.; Kleiman-Shwarsstein, A.; Forman, A. J.; Gaillard, N.; Garland, R.; Takanabe, K.; Heske, C.; Sunkara, M.; McFarland, E. W.; Domen, K.; Miller, E. L.; Turner, J. A.; Dinh, H. N. Accelerating materials development for photoelectrochemical hydrogen production: Standards for methods, definitions, and reporting protocols. *Journal of Materials Research* **2010**, 25, 3–16.
- (75) van der Pauw, J. L. A method of measuring the resistivity and Hall coefficient on lamellae of arbitrary shape. *Philips Technical Review* **1958**, 20, 220–224.
- (76) Oliveira, F. S.; Cipriano, R. B.; da Silva, F. T.; Romão, E. C.; dos Santos, C. A. M. Simple analytical method for determining electrical resistivity and sheet resistance using the van der Pauw procedure. *Scientific Reports* **2020**, 10, 16379.
- (77) Moorthy, S. B. K. In *Thin Film Structures in Energy Applications*; Babu Krishna Moorthy, S., Ed.; Springer International Publishing: Cham, 2015; pp 1–292.
- (78) Tauc, J. Optical properties and electronic structure of amorphous Ge and Si. *Materials Research Bulletin* **1968**, 3, 37–46.
- (79) Zanatta, A. R. Revisiting the optical bandgap of semiconductors and the proposal of a unified methodology to its determination. *Scientific Reports* **2019**, 9, 11225.
- (80) Behera, A.; Aich, S.; Theivasanthi, T. *Design, Fabrication, and Characterization of Multifunctional Nanomaterials*; Elsevier, 2022; pp 177–199.

-
- (81) Safi, I. Recent aspects concerning DC reactive magnetron sputtering of thin films: a review. *Surface and Coatings Technology* **2000**, *127*, 203–218.
- (82) Nafarizal, N. Precise Control of Metal Oxide Thin Films Deposition in Magnetron Sputtering Plasmas for High Performance Sensing Devices Fabrication. *Procedia Chemistry* **2016**, *20*, 93–97.
- (83) Leskelä, M.; Ritala, M. Atomic layer deposition (ALD): from precursors to thin film structures. *Thin Solid Films* **2002**, *409*, 138–146.
- (84) George, S. M. Atomic Layer Deposition: An Overview. *Chemical Reviews* **2010**, *110*, 111–131.
- (85) Puurunen, R. L. Surface chemistry of atomic layer deposition: A case study for the trimethylaluminum/water process. *Journal of Applied Physics* **2005**, *97*, 121301.
- (86) Puurunen, R. Growth Per Cycle in Atomic Layer Deposition: Real Application Examples of a Theoretical Model. *Chemical Vapor Deposition* **2003**, *9*, 327–332.
- (87) Fang, Q.; Hodson, C.; Xu, C.; Gunn, R. Nucleation and Growth of Platinum Films on High-k/Metal Gate Materials by Remote Plasma and Thermal ALD. *Physics Procedia* **2012**, *32*, 551–560.
- (88) Endres, F.; Abbott, A.; MacFarlane, D., Eds. *Electrodeposition from Ionic Liquids*; Wiley-VCH Verlag GmbH & Co. KGaA: Weinheim, Germany, 2017.
- (89) Gurrappa, I.; Binder, L. Electrodeposition of nanostructured coatings and their characterization—A review. *Science and Technology of Advanced Materials* **2008**, *9*, 043001.
- (90) Shi, Y.; Lee, C.; Tan, X.; Yang, L.; Zhu, Q.; Loh, X.; Xu, J.; Yan, Q. Atomic-Level Metal Electrodeposition: Synthetic Strategies, Applications, and Catalytic Mechanism in Electrochemical Energy Conversion. *Small Structures* **2022**, *3*, 2100185.
- (91) Liu, Y.; Gokcen, D.; Bertocci, U.; Moffat, T. P. Self-Terminating Growth of Platinum Films by Electrochemical Deposition. *Science* **2012**, *338*, 1327–1330.
- (92) Tengeler, S. Cubic Silicon Carbide For Direct Photoelectrochemical Water Splitting. Ph.D. thesis, Technische Universität, Darmstadt, 2017.
- (93) Klett, J. Interface and catalyst investigation for solar water splitting. Ph.D. thesis, Technische Universität, Darmstadt, 2016.
- (94) Hannappel, T.; Visbeck, S.; Töben, L.; Willig, F. Apparatus for investigating metalorganic chemical vapor deposition-grown semiconductors with ultrahigh-vacuum based techniques. *Review of Scientific Instruments* **2004**, *75*, 1297.
- (95) Seah, M. P. Simple universal curve for the energy-dependent electron attenuation length for all materials. *Surface and Interface Analysis* **2012**, *44*, 1353–1359.
- (96) Tanuma, S.; Powell, C. J.; Penn, D. R. Calculations of electron inelastic mean free paths. III. Data for 15 inorganic compounds over the 50–2000 eV range. *Surface and Interface Analysis* **1991**, *17*, 927–939.
- (97) Seah, M. P.; Spencer, S. J. Ultrathin SiO₂ on Si II. Issues in quantification of the oxide thickness. *Surface and Interface Analysis* **2002**, *33*, 640–652.

-
- (98) Scofield, J. Hartree-Slater subshell photoionization cross-sections at 1254 and 1487 eV. *Journal of Electron Spectroscopy and Related Phenomena* **1976**, 8, 129–137.
- (99) Ohashi, N.; Yoshikawa, H.; Yamashita, Y.; Ueda, S.; Li, J.; Okushi, H.; Kobayashi, K.; Haneda, H. Determination of Schottky barrier profile at Pt/SrTiO₃:Nb junction by x-ray photoemission. *Applied Physics Letters* **2012**, 101, 251911.
- (100) Frericks, M.; Pflumm, C.; Mankel, E.; Mayer, T.; Jaegermann, W. Space Charge Regions at Organic p-i-Homointerfaces from Advanced Modeling of In Situ-Prepared Interfaces Analyzed by Photoelectron Spectroscopy. *ACS Applied Electronic Materials* **2021**, 3, 1211–1227.
- (101) Rangan, S.; Kalyanikar, M.; Duan, J.; Liu, G.; Bartynski, R. A.; Andrei, E. Y.; Feldman, L.; Garfunkel, E. Nanoscale Internal Fields in a Biased Graphene–Insulator–Semiconductor Structure. *The Journal of Physical Chemistry Letters* **2016**, 7, 3434–3439.
- (102) Copuroglu, M.; Aydogan, P.; Polat, E. O.; Kocabas, C.; Süzer, S. Gate-tunable photoemission from graphene transistors. *Nano Letters* **2014**, 14, 2837–2842.
- (103) Givon, A.; Piao, H.; McMahon, J.; Zorn, G.; Cohen, H. Contactless derivation of inner fields in gate-oxide layers: SiO₂ on SiC. *Applied Physics Letters* **2015**, 107, 10–15.
- (104) Döscher, H.; Supplie, O.; Brückner, S.; Hannappel, T.; Beyer, A.; Ohlmann, J.; Volz, K. Indirect in situ characterization of Si(100) substrates at the initial stage of III–V heteroepitaxy. *Journal of Crystal Growth* **2011**, 315, 16–21.
- (105) Brückner, S.; Döscher, H.; Kleinschmidt, P.; Supplie, O.; Dobrich, A.; Hannappel, T. Anomalous double-layer step formation on Si(100) in hydrogen process ambient. *Physical Review B* **2012**, 86, 195310.
- (106) Brückner, S.; Supplie, O.; Dobrich, A.; Kleinschmidt, P.; Hannappel, T. Control Over Dimer Orientations on Vicinal Si(100) Surfaces in Hydrogen Ambient: Kinetics Versus Energetics. *physica status solidi (b)* **2018**, 255, 1700493.
- (107) Aspnes, D. E.; Studna, A. A. Anisotropies in the Above—Band-Gap Optical Spectra of Cubic Semiconductors. *Physical Review Letters* **1985**, 54, 1956–1959.
- (108) Angermann, H.; Henrion, W.; Rebien, M.; Zettler, J.-T.; Röseler, A. Characterization of chemically prepared Si-surfaces by uv-vis and IR spectroscopic ellipsometry and surface photovoltage. *Surface Science* **1997**, 388, 15–23.
- (109) Hannappel, T.; Töben, L.; Möller, K.; Willig, F. In-situ monitoring of InP(100) and GaP(100) interfaces and characterization with RDS at 20 K. *Journal of Electronic Materials* **2001**, 30:11, 1425–1428.
- (110) Letzig, T.; Schimper, H. J.; Hannappel, T.; Willig, F. P-H bonds in the surface unit cell of P-rich ordered InP(001) grown by metalorganic chemical vapor deposition. *Physical Review B - Condensed Matter and Materials Physics* **2005**, 71, 033308.
- (111) Hannappel, T.; Töben, L.; Visbeck, S.; Crawack, H.-J.; Pettenkofer, C.; Willig, F. UPS and 20 K reflectance anisotropy spectroscopy of the P-rich and In-rich surfaces of InP(100). *Surface Science* **2000**, 470, L1–L6.

-
- (112) Cottre, T. Photoelektrochemische Wasserspaltung mittels adaptierter siliziumbasierter Halbleiter-Mehrfachstapelstrukturen. Ph.D. thesis, Technische Universität Darmstadt, Darmstadt, 2020.
- (113) Becker, J.-P.; Urbain, F.; Smirnov, V.; Rau, U.; Ziegler, J.; Kaiser, B.; Jaegermann, W.; Finger, F. Modeling and practical realization of thin film silicon-based integrated solar water splitting devices. *physica status solidi (a)* **2016**, *213*, 1738–1746.
- (114) Kayes, B. M.; Atwater, H. A.; Lewis, N. S. Comparison of the device physics principles of planar and radial p-n junction nanorod solar cells. *Journal of Applied Physics* **2005**, *97*, 114302.
- (115) Moritz, D. C.; Calvet, W.; Zare Pour, M. A.; Paszuk, A.; Mayer, T.; Hannappel, T.; Hofmann, J. P.; Jaegermann, W. Dangling Bond Defects on Si Surfaces and Their Consequences on Energy Band Diagrams: From a Photoelectrochemical Perspective. *Solar RRL* **2023**, *7*, 2201063.
- (116) Grundner, M.; Jacob, H. Investigations on hydrophilic and hydrophobic silicon (100) wafer surfaces by X-ray photoelectron and high-resolution electron energy loss-spectroscopy. *Applied Physics A Solids and Surfaces* **1986**, *39*, 73–82.
- (117) Boland, J. J. Structure of the H-saturated Si(100) surface. *Physical Review Letters* **1990**, *65*, 3325–3328.
- (118) May, M. M.; Lewerenz, H.-J.; Lackner, D.; Dimroth, F.; Hannappel, T. Efficient direct solar-to-hydrogen conversion by in situ interface transformation of a tandem structure. *Nature Communications* **2015**, *6*, 8286.
- (119) Tengeler, S.; Fingerle, M.; Calvet, W.; Steinert, C.; Kaiser, B.; Mayer, T.; Jaegermann, W. The Impact of Different Si Surface Terminations in the (001) n-Si/NiO_x Heterojunction on the Oxygen Evolution Reaction (OER) by XPS and Electrochemical Methods. *Journal of The Electrochemical Society* **2018**, *165*, H3122–H3130.
- (120) Schlaf, R.; Hinogami, R.; Fujitani, M.; Yae, S.; Nakato, Y. Fermi level pinning on HF etched silicon surfaces investigated by photoelectron spectroscopy. *Journal of Vacuum Science & Technology A: Vacuum, Surfaces, and Films* **1999**, *17*, 164–169.
- (121) Poindexter, E. H.; Caplan, P. J. Characterization of Si/SiO₂ interface defects by electron spin resonance. *Progress in Surface Science* **1983**, *14*, 201–294.
- (122) Jupina, M.; Lenahan, P. A spin dependent recombination study of radiation induced defects at and near the Si/SiO₂/sub 2/ interface. *IEEE Transactions on Nuclear Science* **1989**, *36*, 1800–1807.
- (123) Angermann, H.; Henrion, W.; Rebien, M.; Fischer, D.; Zettler, J.-T.; Röseler, A. H-terminated silicon: spectroscopic ellipsometry measurements correlated to the surface electronic properties. *Thin Solid Films* **1998**, *313-314*, 552–556.
- (124) Altermatt, P. P.; Schenk, A.; Geelhaar, F.; Heiser, G. Reassessment of the intrinsic carrier density in crystalline silicon in view of band-gap narrowing. *Journal of Applied Physics* **2003**, *93*, 1598–1604.
- (125) Himpsel, F. J.; Hollinger, G.; Pollak, R. A. Determination of the Fermi-level pinning position at Si(111) surfaces. *Physical Review B* **1983**, *28*, 7014–7018.
- (126) Poindexter, E. H.; Gerardi, G. J.; Rueckel, M.; Caplan, P. J.; Johnson, N. M.; Biegelsen, D. K. Electronic traps and P b centers at the Si/SiO₂ interface: Band-gap energy distribution. *Journal of Applied Physics* **1984**, *56*, 2844–2849.

-
- (127) Uren, M. J.; Stathis, J. H.; Cartier, E. Conductance measurements on P b centers at the (111) Si:SiO₂ interface. *Journal of Applied Physics* **1996**, *80*, 3915–3922.
- (128) Füssel, W.; Schmidt, M.; Angermann, H.; Mende, G.; Flietner, H. Defects at the Si/SiO₂ interface: Their nature and behaviour in technological processes and stress. *Nuclear Instruments and Methods in Physics Research Section A: Accelerators, Spectrometers, Detectors and Associated Equipment* **1996**, *377*, 177–183.
- (129) Johnson, N. M.; Biegelsen, D. K.; Moyer, M. D.; Chang, S. T.; Poindexter, E. H.; Caplan, P. J. Characteristic electronic defects at the Si-SiO₂ interface. *Applied Physics Letters* **1983**, *43*, 563–565.
- (130) Northrup, J. E. Effective correlation energy of a Si dangling bond calculated with the local-spin-density approximation. *Physical Review B* **1989**, *40*, 5875–5878.
- (131) Broqvist, P.; Alkauskas, A.; Pasquarello, A. Defect levels of dangling bonds in silicon and germanium through hybrid functionals. *Physical Review B* **2008**, *78*, 075203.
- (132) Himpsel, F. J.; McFeely, F. R.; Taleb-Ibrahimi, A.; Yarmoff, J. A.; Hollinger, G. Microscopic structure of the SiO₂/Si interface. *Physical Review B* **1988**, *38*, 6084–6096.
- (133) Aberle, A. G.; Glunz, S.; Warta, W. Impact of illumination level and oxide parameters on Shockley–Read–Hall recombination at the Si-SiO₂ interface. *Journal of Applied Physics* **1992**, *71*, 4422–4431.
- (134) Robinson, S. J.; Wenham, S. R.; Altermatt, P. P.; Aberle, A. G.; Heiser, G.; Green, M. A. Recombination rate saturation mechanisms at oxidized surfaces of high-efficiency silicon solar cells. *Journal of Applied Physics* **1995**, *78*, 4740–4754.
- (135) Schmeisser, D.; Himpsel, F. J.; Hollinger, G. Chemisorption of H₂O on Si(100). *Physical Review B* **1983**, *27*, 7813–7816.
- (136) Hollinger, G.; Sferco, S. J.; Lannoo, M. Deviation from the classical 4:2 coordination in very thin SiO₂ films grown on silicon. *Physical Review B* **1988**, *37*, 7149–7152.
- (137) Engel, T. The interaction of molecular and atomic oxygen with Si(100) and Si(111). *Surface Science Reports* **1993**, *18*, 93–144.
- (138) Alay, J. L.; Hirose, M. The valence band alignment at ultrathin SiO₂/Si interfaces. *Journal of Applied Physics* **1997**, *81*, 1606–1608.
- (139) Miyazaki, S.; Nishimura, H.; Fukuda, M.; Ley, L.; Ristein, J. Structure and electronic states of ultrathin SiO₂ thermally grown on Si(100) and Si(111) surfaces. *Applied Surface Science* **1997**, *113-114*, 585–589.
- (140) Takahashi, K.; Seman, M. B.; Hirose, K.; Hattori, T. Energy Barrier for Valence Electrons at SiO₂/Si(111) Interface. *Japanese Journal of Applied Physics* **2002**, *41*, L223–L225.
- (141) DiStefano, T.; Eastman, D. The band edge of amorphous SiO₂ by photoinjection and photoconductivity measurements. *Solid State Communications* **1971**, *9*, 2259–2261.
- (142) Flietner, H. Passivity and electronic properties of the silicon/silicondioxide interface. *Materials Science Forum* **1995**, *185-188*, 73–82.
-

-
- (143) Lewerenz, H. J.; Aggour, M.; Murrell, C.; Kanis, M.; Jungblut, H.; Jakubowicz, J.; Cox, P. A.; Campbell, S. A.; Hoffmann, P.; Schmeisser, D. Initial Stages of Structure Formation on Silicon Electrodes Investigated by Photoelectron Spectroscopy Using Synchrotron Radiation and In Situ Atomic Force Microscopy. *Journal of The Electrochemical Society* **2003**, *150*, E185.
- (144) Uhrberg, R. I. G.; Hansson, G. V.; Nicholls, J. M.; Flodström, S. A. Experimental studies of the dangling- and dimer-bond-related surface electron bands on Si(100) (2×1). *Physical Review B* **1981**, *24*, 4684–4691.
- (145) Hricovini, K.; Günther, R.; Thiry, P.; Taleb-Ibrahimi, A.; Indlekofer, G.; Bonnet, J. E.; Dumas, P.; Petroff, Y.; Blase, X.; Zhu, X.; Louie, S. G.; Chabal, Y. J.; Thiry, P. A. Electronic structure and its dependence on local order for H/Si(111)-(1×1) surfaces. *Physical Review Letters* **1993**, *70*, 1992–1995.
- (146) Pandey, K. C. Realistic tight-binding model for chemisorption: H on Si and Ge (111). *Physical Review B* **1976**, *14*, 1557–1570.
- (147) Blase, X.; Zhu, X.; Louie, S. G. Self-energy effects on the surface-state energies of H-Si(111) 1×1 . *Physical Review B* **1994**, *49*, 4973–4980.
- (148) Gallego, S.; Avila, J.; Martin, M.; Blase, X.; Taleb, A.; Dumas, P.; Asensio, M. C. Electronic structure of the ideally H-terminated Si(111)-(1×1) surface. *Physical Review B* **2000**, *61*, 12628–12631.
- (149) Harp, G. R.; Saldin, D. K.; Tonner, B. P. Finite-size effects and short-range crystalline order in Si and SiO₂ studied by X-ray absorption fine structure spectroscopy. *Journal of Physics: Condensed Matter* **1993**, *5*, 5377–5388.
- (150) Harp, G. R.; Han, Z.-L.; Tonner, B. P. Spatially-resolved X-ray Absorption Near-edge Spectroscopy of Silicon in Thin Silicon-oxide Films. *Physica Scripta* **1990**, *T31*, 23–27.
- (151) Harp, G. R.; Han, Z. L.; Tonner, B. P. X-ray absorption near edge structures of intermediate oxidation states of silicon in silicon oxides during thermal desorption. *Journal of Vacuum Science & Technology A: Vacuum, Surfaces, and Films* **1990**, *8*, 2566–2569.
- (152) Gerlach, W.; Schlangenotto, H.; Maeder, H. On the radiative recombination rate in silicon. *Physica Status Solidi (a)* **1972**, *13*, 277–283.
- (153) Arnold, E.; Abowitz, G. Effect of surface states on electron mobility in silicon surface-inversion layers. *Appl. Phys. Lett* **1966**, *9*, 344.
- (154) Donchev, V. Surface photovoltage spectroscopy of semiconductor materials for optoelectronic applications. *Materials Research Express* **2019**, *6*, 103001.
- (155) Kronik, L.; Shapira, Y. Surface photovoltage phenomena: Theory, experiment, and applications. *Surface Science Reports* **1999**, *37*, 1–206.
- (156) Alonso, M.; Cimino, R.; Horn, K. Surface photovoltage effects in photoemission from metal-GaP(110) interfaces: Importance for band bending evaluation. *Physical Review Letters* **1990**, *64*, 1947–1950.
- (157) Klein, A.; Tomm, Y.; Schlaf, R.; Pettenkofer, C.; Jaegermann, W.; Lux-Steiner, M.; Bucher, E. Photovoltaic properties of WSe₂ single-crystals studied by photoelectron spectroscopy. *Solar Energy Materials and Solar Cells* **1998**, *51*, 181–191.

-
- (158) Stevenson, D. T.; Keyes, R. J. Measurements of the recombination velocity at germanium surfaces. *Physica* **1954**, *20*, 1041–1046.
- (159) Van Overstraeten, R. J.; Mertens, R. P. Heavy doping effects in silicon. *Solid-State Electronics* **1987**, *30*, 1077–1087.
- (160) Çopuroğlu, M.; Sezen, H.; Opila, R. L.; Suzer, S. Band-Bending at Buried SiO₂/Si Interface as Probed by XPS. *ACS Applied Materials & Interfaces* **2013**, *5*, 5875–5881.
- (161) Sezen, H.; Suzer, S. XPS for chemical- and charge-sensitive analyses. *Thin Solid Films* **2013**, *534*, 1–11.
- (162) Himpsel, F. J.; Eastman, D. E. Photoemission studies of intrinsic surface states on Si(100). *Journal of Vacuum Science and Technology* **1979**, *16*, 1297.
- (163) Boland, J. J. Evidence of pairing and its role in the recombinative desorption of hydrogen from the Si(100)-2×1 surface. *Physical Review Letters* **1991**, *67*, 1539–1542.
- (164) Ren, X.-Y.; Kim, H.-J.; Niu, C.-Y.; Jia, Y.; Cho, J.-H. Origin of Symmetric Dimer Images of Si(001) Observed by Low-Temperature Scanning Tunneling Microscopy. *Scientific Reports* **2016**, *6*, 27868.
- (165) Raza, H. Theoretical study of isolated dangling bonds, dangling bond wires, and dangling bond clusters on a : H:Si(001)-(2×1) surface. *Physical Review B* **2007**, *76*, 045308.
- (166) Yu, S.-Y.; Kim, H.; Koo, J.-Y. Extrinsic Nature of Point Defects on the Si(001) Surface: Dissociated Water Molecules. *Physical Review Letters* **2008**, *100*, 036107.
- (167) Lee, J.-Y.; Cho, J.-H. Two Dissociation Pathways of Water and Ammonia on the Si(001) Surface. *The Journal of Physical Chemistry B* **2006**, *110*, 18455–18458.
- (168) Himpsel, F. J.; Heimann, P.; Eastman, D. E. Surface states on Si(111)-(2×1). *Physical Review B* **1981**, *24*, 2003–2008.
- (169) Chadi, D. J. Origins of (111) surface reconstructions of Si and Ge. *Journal of Vacuum Science and Technology* **1980**, *17*, 989–992.
- (170) Layet, J. M.; Hoarau, J. Y.; Lüth, H.; Derrien, J. Dispersion of the dangling-bond surface states of Si(111)-(7×7). *Physical Review B* **1984**, *30*, 7355–7357.
- (171) Hansson, G. V.; Uhrberg, R. I. G.; Flodström, S. A. Electronic structure of the Si(111) 7×7 surface studied by angle-resolved photoelectron spectroscopy. *Journal of Vacuum Science and Technology* **1979**, *16*, 1287–1289.
- (172) Chadi, D. J.; Bauer, R. S.; Williams, R. H.; Hansson, G. V.; Bachrach, R. Z.; Mikkelsen, J. C.; Houzay, F.; Guichar, G. M.; Pinchaux, R.; Pétróff, Y. Atomic and Electronic Structure of the 7 × 7 Reconstructed Si (111) Surface. *Physical Review Letters* **1980**, *44*, 799–802.
- (173) Uhrberg, R. I. G.; Hansson, G. V.; Nicholls, J. M.; Flodström, S. A. Experimental Evidence for One Highly Dispersive Dangling-Bond Band on Si(111) 2 × 1. *Physical Review Letters* **1982**, *48*, 1032–1035.
- (174) Houzay, F.; Guichar, G.; Pinchaux, R.; Thiry, P.; Petroff, Y.; Dagneaux, D. Angle-resolved photoemission of the Si(111) 7 × 7 surface. *Surface Science* **1980**, *99*, 28–33.
-

-
- (175) McGrath, R.; Cimino, R.; Braun, W.; Thornton, G.; McGovern, I. A photoemission study of H₂O adsorption on a vicinal Si(100) surface. *Vacuum* **1988**, 38, 251–255.
- (176) Borkowska, Z.; Cappadonia, M.; Stimming, U. Interfacial and bulk electrolyte properties in frozen electrolyte studies. *Electrochimica Acta* **1992**, 37, 565–568.
- (177) Cottre, T.; Fingerle, M.; Kranz, M.; Mayer, T.; Kaiser, B.; Jaegermann, W. Interaction of Water with Atomic Layer Deposited Titanium Dioxide on p-Si Photocathode: Modeling of Photoelectrochemical Interfaces in Ultrahigh Vacuum with Cryo-Photoelectron Spectroscopy. *Advanced Materials Interfaces* **2021**, 8, 2002257.
- (178) Moritz, D. C.; Ruiz Alvarado, I. A.; Zare Pour, M. A.; Paszuk, A.; Frieß, T.; Runge, E.; Hofmann, J. P.; Hannappel, T.; Schmidt, W. G.; Jaegermann, W. P-Terminated InP (001) Surfaces: Surface Band Bending and Reactivity to Water. *ACS Applied Materials & Interfaces* **2022**, 14, 47255–47261.
- (179) Jaegermann, W.; Mayer, T. In *Landolt-Börnstein*; Bonzel, H., Ed.; Landolt-Börnstein - Group III Condensed Matter; Springer-Verlag: Berlin/Heidelberg, 2005; Vol. 42A4; pp 226–298.
- (180) Henderson, M. The interaction of water with solid surfaces: fundamental aspects revisited. *Surface Science Reports* **2002**, 46, 1–308.
- (181) Wendt, S.; Frerichs, M.; Wei, T.; Chen, M.; Kempter, V.; Goodman, D. The interaction of water with silica thin films grown on Mo(112). *Surface Science* **2004**, 565, 107–120.
- (182) Nishijima, M.; Edamoto, K.; Kubota, Y.; Tanaka, S.; Onchi, M. Vibrational electron energy loss spectroscopy of the Si(111)(7×7)-H₂O(D₂O) system. *The Journal of Chemical Physics* **1986**, 84, 6458–6465.
- (183) Krischok, S.; Höfft, O.; Günster, J.; Stultz, J.; Goodman, D.; Kempter, V. H₂O interaction with bare and Li-precovered TiO₂: studies with electron spectroscopies (MIES and UPS(HeI and II)). *Surface Science* **2001**, 495, 8–18.
- (184) Klett, J.; Elger, B.; Krähling, S.; Kaiser, B.; Jaegermann, W.; Schäfer, R. Water dissociation on silica in the presence of atomic platinum. *Applied Surface Science* **2016**, 375, 85–89.
- (185) Takagi, N.; Minami, N.; Furukawa, T.; Nishijima, M. The growth of ice clusters on the Si(100)(2 × 1)-H(D) surface: Electron energy loss spectroscopy and thermal desorption studies. *Surface Science* **1993**, 297, L43–L47.
- (186) Mayer, T.; Pettenkofer, C.; Jaegermann, W. Synchrotron-Induced Photoelectron Spectroscopy of Semiconductor/Electrolyte Model Interfaces: Coadsorption of Br₂ and H₂O on WSe₂ (0001). *The Journal of Physical Chemistry* **1996**, 100, 16966–16977.
- (187) Fingerle, M.; Tengeler, S.; Calvet, W.; Mayer, T.; Jaegermann, W. Water Interaction with Sputter-Deposited Nickel Oxide on n-Si Photoanode: Cryo Photoelectron Spectroscopy on Adsorbed Water in the Frozen Electrolyte Approach. *Journal of The Electrochemical Society* **2018**, 165, H3148–H3153.
- (188) Lebedev, M. V.; Savchenko, G. M.; Averkiev, N. S.; Hajduk, A.; Kaiser, B.; Jaegermann, W. Surface potential in n- and p-GaInP₂ (100): temperature effect. *Journal of Physics D: Applied Physics* **2021**, 54, 185104.

-
- (189) Moulder, J. F.; Stickle, W. F.; Sobol, P. E.; Bomben, K. D. In *Handbook of X-ray photoelectron spectroscopy: a reference book of standard spectra for identification and interpretation of XPS data*; Chastain, J., Ed.; Perkin-Elmer Corporation, 1992.
- (190) Sun, Y.; Wang, Y.; Pan, J. S.; Wang, L.-L.; Sun, C. Q. Elucidating the 4f Binding Energy of an Isolated Pt Atom and Its Bulk Shift from the Measured Surface- and Size-Induced Pt 4f Core Level Shift. *The Journal of Physical Chemistry C* **2009**, *113*, 14696–14701.
- (191) Danyluk, S.; McGuire, G. E. Platinum silicide formation: Electron spectroscopy of the platinum-platinum silicide interface. *Journal of Applied Physics* **1974**, *45*, 5141–5144.
- (192) Peuckert, M.; Bonzel, H. Characterization of oxidized platinum surfaces by X-ray photoelectron spectroscopy. *Surface Science* **1984**, *145*, 239–259.
- (193) Hammond, J.; Winograd, N. XPS spectroscopic study of potentiostatic and galvanostatic oxidation of Pt electrodes in H_2SO_4 and HClO_4 . *Journal of Electroanalytical Chemistry and Interfacial Electrochemistry* **1977**, *78*, 55–69.
- (194) da Silva, L.; Alves, V.; de Castro, S.; Boodts, J. XPS study of the state of iridium, platinum, titanium and oxygen in thermally formed $\text{IrO}_2 + \text{TiO}_2 + \text{PtO}_x$ films. *Colloids and Surfaces A: Physicochemical and Engineering Aspects* **2000**, *170*, 119–126.
- (195) Michaelson, H. B. The work function of the elements and its periodicity. *Journal of Applied Physics* **1977**, *48*, 4729–4733.
- (196) Derry, G. N.; Kern, M. E.; Worth, E. H. Recommended values of clean metal surface work functions. *Journal of Vacuum Science & Technology A: Vacuum, Surfaces, and Films* **2015**, *33*, 060801.
- (197) Slavcheva, E.; Ganske, G.; Topalov, G.; Mokwa, W.; Schnakenberg, U. Effect of sputtering parameters on surface morphology and catalytic efficiency of thin platinum films. *Applied Surface Science* **2009**, *255*, 6479–6486.
- (198) Kojima, D.; Makihara, K.; Shi, J.; Hashimoto, M. Structure and electrical property of platinum film biased dc-sputter-deposited on silicon. *Applied Surface Science* **2001**, *169–170*, 320–324.
- (199) Robertson, J. High dielectric constant oxides. *The European Physical Journal Applied Physics* **2004**, *28*, 265–291.
- (200) Allen, F. G.; Gobeli, G. W. Work Function, Photoelectric Threshold, and Surface States of Atomically Clean Silicon. *Physical Review* **1962**, *127*, 150–158.
- (201) Deal, B. E.; Sklar, M.; Grove, A. S.; Snow, E. H. Characteristics of the Surface-State Charge (Q_{ss}) of Thermally Oxidized Silicon. *Journal of The Electrochemical Society* **1967**, *114*, 266.
- (202) Shi, J.; Kojima, D.; Hashimoto, M. The interaction between platinum films and silicon substrates: Effects of substrate bias during sputtering deposition. *Journal of Applied Physics* **2000**, *88*, 1679–1683.
- (203) Pant, A. K.; Murarka, S. P.; Shepard, C.; Lanford, W. Kinetics of platinum silicide formation during rapid thermal processing. *Journal of Applied Physics* **1992**, *72*, 1833–1836.

-
- (204) Thomas, J. H.; Hofmann, S. Ion bombardment induced changes in silicon dioxide surface composition studied by x-ray photoelectron spectroscopy. *Journal of Vacuum Science & Technology A: Vacuum, Surfaces, and Films* **1985**, 3, 1921–1928.
- (205) Hofmann, S. An XPS study of the influence of ion sputtering on bonding in thermally grown silicon dioxide. *Journal of Vacuum Science & Technology B: Microelectronics and Nanometer Structures* **1983**, 1, 43.
- (206) Crider, C. A.; Poate, J. M.; Rowe, J. E.; Sheng, T. T. Platinum silicide formation under ultrahigh vacuum and controlled impurity ambients. *Journal of Applied Physics* **1981**, 52, 2860–2868.
- (207) Schibli, E.; Milnes, A. Deep impurities in silicon. *Materials Science and Engineering* **1967**, 2, 173–180.
- (208) Mantovani, S.; Nava, F.; Nobili, C.; Ottaviani, G. In-diffusion of Pt in Si from the PtSi/Si interface. *Physical Review B* **1986**, 33, 5536–5544.
- (209) Woodbury, H. H.; Ludwig, G. W. Spin Resonance of Pd and Pt in Silicon. *Physical Review* **1962**, 126, 466–470.
- (210) Lowther, J. E. Structural bonding of deep level defects and the nature of amphoteric centres in silicon. *Journal of Physics C: Solid State Physics* **1980**, 13, 3665–3679.
- (211) Brotherton, S. D.; Bradley, P.; Bicknell, J. Electrical properties of platinum in silicon. *Journal of Applied Physics* **1979**, 50, 3396–3403.
- (212) Miller, M. D.; Schade, H.; Nuese, C. J. Lifetime-controlling recombination centers in platinum-diffused silicon. *Journal of Applied Physics* **1976**, 47, 2569–2578.
- (213) Derry, G. N.; Ross, P. N. A work function change study of oxygen adsorption on Pt(111) and Pt(100). *The Journal of Chemical Physics* **1985**, 82, 2772–2778.
- (214) Mayer, T.; Klein, A.; Lang, O.; Pettenkofer, C.; Jaegermann, W. H₂O adsorption on the layered chalcogenide semiconductors WSe₂, InSe and GaSe. *Surface Science* **1992**, 269–270, 909–914.
- (215) Nakato, Y.; Ueda, K.; Yano, H.; Tsubomura, H. Effect of microscopic discontinuity of metal overlayers on the photovoltages in metal-coated semiconductor-liquid junction photoelectrochemical cells for efficient solar energy conversion. *The Journal of Physical Chemistry* **1988**, 92, 2316–2324.
- (216) Rossi, R. C.; Tan, M. X.; Lewis, N. S. Size-dependent electrical behavior of spatially inhomogeneous barrier height regions on silicon. *Applied Physics Letters* **2000**, 77, 2698–2700.
- (217) Lombardi, I.; Marchionna, S.; Zangari, G.; Pizzini, S. Effect of Pt Particle Size and Distribution on Photoelectrochemical Hydrogen Evolution by p-Si Photocathodes. *Langmuir* **2007**, 23, 12413–12420.
- (218) Nunez, P.; Cabán-Acevedo, M.; Yu, W.; Richter, M. H.; Kennedy, K.; Villarino, A. M.; Brunschwig, B. S.; Lewis, N. S. Origin of the Electrical Barrier in Electrolessly Deposited Platinum Nanoparticles on p-Si Surfaces. *The Journal of Physical Chemistry C* **2021**, 125, 17660–17670.
- (219) Schmidt, W. G.; Hahn, P. H.; Bechstedt, F.; Esser, N.; Vogt, P.; Wange, A.; Richter, W. InP(001)-(2 x 1) Surface: A Hydrogen Stabilized Structure. *Physical Review Letters* **2003**, 90, 4.

-
- (220) Vogt, P.; Frisch, A. M.; Hannappel, T.; Visbeck, S.; Willig, F.; Jung, C.; Follath, R.; Braun, W.; Richter, W.; Esser, N. Atomic structure and composition of the P-rich InP(001) surfaces. *Applied Surface Science* **2000**, *166*, 190–195.
- (221) May, M. M.; Lewerenz, H.-J.; Hannappel, T. Optical in Situ Study of InP(100) Surface Chemistry: Dissociative Adsorption of Water and Oxygen. *The Journal of Physical Chemistry C* **2014**, *118*, 19032–19041.
- (222) Hajduk, A.; Lebedev, M. V.; Kaiser, B.; Jaegermann, W. Interaction of liquid water with the p-GaInP₂(100) surface covered with submonolayer oxide. *Physical Chemistry Chemical Physics* **2018**, *20*, 21144–21150.
- (223) Bronneberg, A. C.; Höhn, C.; Van De Krol, R. Probing the Interfacial Chemistry of Ultrathin ALD-Grown TiO₂ Films: An In-Line XPS Study. *Journal of Physical Chemistry C* **2017**, *121*, 5531–5538.
- (224) Li, L.; Han, B.-K.; Fu, Q.; Hicks, R. F. Example of a Compound Semiconductor Surface that Mimics Silicon: The InP(001)-(2 × 1) Reconstruction. *Physical Review Letters* **1999**, *82*, 1879–1882.
- (225) Kleinschmidt, P.; Döscher, H.; Vogt, P.; Hannappel, T. Direct observation of dimer flipping at the hydrogen-stabilized GaP(100) and InP(100) surfaces. *Physical Review B* **2011**, *83*, 155316.
- (226) Frisch, A.; Vogt, P.; Visbeck, S.; Hannappel, T.; Willig, F.; Braun, W.; Richter, W.; Bernholz, J.; Schmidt, W.; Esser, N. Angle Resolved Photoemission Spectroscopy of the InP(001) surface. *Applied Surface Science* **2000**, *166*, 224–230.
- (227) Hahn, P. H.; Schmidt, W. G. Surface Ordering of P-rich InP(001): Hydrogen Stabilization vs Electron Correlation. *Surface Review and Letters* **2003**, *10*, 163–167.
- (228) Mishra, R.; Restrepo, O. D.; Kumar, A.; Windl, W. Native point defects in binary InP semiconductors. *Journal of Materials Science* **2012**, *47*, 7482–7497.
- (229) Larsson, C.; Flodström, A. Dissociative H₂O adsorption on the Si (100) 2 × 1 and Ge (100) 2 × 1 surfaces. *Vacuum* **1991**, *42*, 297–300.
- (230) Henrion, O.; Klein, A.; Jaegermann, W. Water adsorption on UHV cleaved InP(110) surfaces. *Surface Science* **2000**, *457*, L337–L341.
- (231) Alvarado Ruiz, I. A.; Schmidt, W. G. Water/InP(001) from Density Functional Theory. *ACS Omega* **2022**, *7*, 19355–19364.
- (232) Wood, B. C.; Schwegler, E.; Choi, W. I.; Ogitsu, T. Surface chemistry of GaP(001) and InP(001) in contact with water. *Journal of Physical Chemistry C* **2014**, *118*, 1062–1070.
- (233) Llewellyn, P. *Adsorption by Powders and Porous Solids*, 2nd ed.; Elsevier, 2014; pp 529–564.
- (234) Schmidt, W. G.; Bechstedt, F.; Esser, N.; Pristovsek, M.; Schultz, C.; Richter, W. Atomic structure of InP(001) – (2 × 4): A dimer reconstruction. *Physical Review B* **1998**, *57*, 14596–14599.
- (235) Zhang, X.; Ptasinska, S. Distinct and dramatic water dissociation on GaP(111) tracked by near-ambient pressure X-ray photoelectron spectroscopy. *Physical Chemistry Chemical Physics* **2015**, *17*, 3909–3918.

-
- (236) Feng, Z. A.; El Gabaly, F.; Ye, X.; Shen, Z.-X.; Chueh, W. C. Fast vacancy-mediated oxygen ion incorporation across the ceria–gas electrochemical interface. *Nature Communications* **2014**, *5*, 4374.
- (237) Zhang, X.; Ptasinska, S. Heterogeneous Oxygen-Containing Species Formed via Oxygen or Water Dissociative Adsorption onto a Gallium Phosphide Surface. *Topics in Catalysis* **2016**, *59*, 564–573.
- (238) Schmidt, W. G.; Esser, N.; Frisch, A. M.; Vogt, P.; Bernholc, J.; Bechstedt, F.; Zorn, M.; Hannappel, T.; Visbeck, S.; Willig, F.; Richter, W. Understanding reflectance anisotropy: Surface-state signatures and bulk-related features in the optical spectrum of InP(001)(2 × 4). *Physical Review B* **2000**, *61*, R16335–R16338.
- (239) Hannappel, T.; Visbeck, S.; Knorr, K.; Mahrt, J.; Zorn, M.; Willig, F. Preparation of P-rich InP surfaces via MOCVD and surface characterization in UHV. *Applied Physics A: Materials Science & Processing* **1999**, *69*, 427–431.
- (240) Pahlke, D.; Kinsky, J.; Schultz, C.; Pristovsek, M.; Zorn, M.; Esser, N.; Richter, W. Structure of InP (001) surfaces prepared by decapping and by ion bombardment and annealing. *Physical Review B* **1997**, *56*, R1661–R1663.
- (241) Tereshchenko, O.; Paget, D.; Chiaradia, P.; Placidi, E.; Bonnet, J.; Wiame, F.; Taleb-Ibrahimi, A. Chemically prepared well-ordered InP(001) surfaces. *Surface Science* **2006**, *600*, 3160–3166.
- (242) Murrell, A.; Price, R.; Jackman, R.; Foord, J. Surface studies of the interaction of Cl₂ with InP(100)(4 × 2); an investigation of adsorption, thermal etching and ion beam assisted processes. *Surface Science* **1990**, *227*, 197–207.
- (243) Töben, L. Untersuchungen zur Energetik und Dynamik von Elektronen an MOCVD-gewachsenen III-V-Halbleiter-Oberflächen. Ph.D. thesis, TU Berlin, 2002.
- (244) Schmidt, W.; Bechstedt, F. Geometry and electronic structure of InP(001)(2 × 4) reconstructions. *Surface Science* **1998**, *409*, 474–484.
- (245) Schmidt, W. G.; Briggs, E. L.; Bernholc, J.; Bechstedt, F. Structural fingerprints in the reflectance anisotropy spectra of InP(001)(2 × 4) surfaces. *Physical Review B* **1999**, *59*, 2234–2239.
- (246) Hollinger, G.; Bergignat, E.; Joseph, J.; Robach, Y. On the nature of oxides on InP surfaces. *Journal of Vacuum Science & Technology A: Vacuum, Surfaces, and Films* **1985**, *3*, 2082–2088.
- (247) Hollinger, G. On the chemistry of passivated oxide–InP interfaces. *Journal of Vacuum Science & Technology B: Microelectronics and Nanometer Structures* **1987**, *5*, 1108.
- (248) Ruiz Alvarado, I. A.; Karmo, M.; Runge, E.; Schmidt, W. G. InP and AlInP(001)(2 × 4) Surface Oxidation from Density Functional Theory. *ACS Omega* **2021**, *6*, 6297–6304.
- (249) Le Lay, G.; Mao, D.; Kahn, A.; Hwu, Y.; Margaritondo, G. High-resolution synchrotron-radiation core-level spectroscopy of decapped GaAs(100) surfaces. *Physical Review B* **1991**, *43*, 14301–14304.
- (250) Wilke, W. G.; Hinkel, V.; Theis, W.; Horn, K. Surface core-level shifts on InP(110): Experiments and Madelung energy calculations. *Physical Review B* **1989**, *40*, 9824.
- (251) Pashley, M. D. Electron counting model and its application to island structures on molecular-beam epitaxy grown GaAs(001) and ZnSe(001). *Physical Review B* **1989**, *40*, 10481–10487.

-
- (252) Santosh, K. C.; Wang, W.; Dong, H.; Xiong, K.; Longo, R. C.; Wallace, R. M.; Cho, K. First principles study on InP (001)-(2 × 4) surface oxidation. *Journal of Applied Physics* **2013**, *113*, 103705.
- (253) Barr, T. L.; Ying Li Liu An x-ray photoelectron spectroscopy study of the valence band structure of indium oxides. *Journal of Physics and Chemistry of Solids* **1989**, *50*, 657–664.
- (254) Chye, P.; Su, C.; Lindau, I.; Garner, C.; Pianetta, P.; Spicer, W. Photoemission studies of the initial stages of oxidation of GaSb and InP. *Surface Science* **1979**, *88*, 439–460.
- (255) Noboru Shibata, N. S.; Hideaki Ikoma, H. I. X-Ray Photoelectron Spectroscopic Study of Oxidation of InP. *Japanese Journal of Applied Physics* **1992**, *31*, 3976.
- (256) Nelson, A.; Geib, K.; Wilmsen, C. W. Composition and structure of thermal oxides of indium phosphide. *Journal of Applied Physics* **1983**, *54*, 4134–4140.
- (257) Faur, M.; Faur, M.; Jayne, D. T.; Goradia, M.; Goradia, C. XPS investigation of anodic oxides grown on p-type InP. *Surface and Interface Analysis* **1990**, *15*, 641–650.
- (258) Hajduk, A.; Zare Pour, M. A.; Paszuk, A.; Guidat, M.; Löw, M.; Ullmann, F.; Moritz, D. C.; Hofmann, J. P.; Krischok, S.; Runge, E.; Schmidt, W. G.; Jaegermann, W.; May, M. M.; Hannappel, T. In *Encyclopedia of Solid-Liquid Interfaces*; Wandelt, K., Bussetti, G., Eds.; Elsevier, 2024; pp 120–156.
- (259) Hofmann, A.; Streubel, P.; Meisel, A. XPS investigation of oxide films on InP(100). *Surface and Interface Analysis* **1988**, *12*, 315–319.
- (260) Daw, M. S.; Smith, D. L. Surface vacancies in InP and GaAlAs. *Applied Physics Letters* **1980**, *36*, 690–692.
- (261) Dow, J. D.; Allen, R. E. Surface defects and Fermi-level pinning in InP. *Journal of Vacuum Science and Technology* **1982**, *20*, 659–661.
- (262) Bertness, K. A.; Kendelewicz, T.; List, R. S.; Williams, M. D.; Lindau, I.; Spicer, W. E. Fermi level pinning during oxidation of atomically clean n-InP(110). *Journal of Vacuum Science & Technology A: Vacuum, Surfaces, and Films* **1986**, *4*, 1424–1426.
- (263) Lin, Y.; Kapadia, R.; Yang, J.; Zheng, M.; Chen, K.; Hettick, M.; Yin, X.; Battaglia, C.; Sharp, I. D.; Ager, J. W.; Javey, A. Role of TiO₂ Surface Passivation on Improving the Performance of p-InP Photocathodes. *The Journal of Physical Chemistry C* **2015**, *119*, 2308–2313.
- (264) Greene, L. E.; Law, M.; Yuhas, B. D.; Yang, P. ZnO–TiO₂ Core–Shell Nanorod/P3HT Solar Cells. *The Journal of Physical Chemistry C* **2007**, *111*, 18451–18456.
- (265) Bae, D.; Seger, B.; Vesborg, P. C. K.; Hansen, O.; Chorkendorff, I. Strategies for stable water splitting via protected photoelectrodes. *Chemical Society Reviews* **2017**, *46*, 1933–1954.
- (266) Kashiwaya, S.; Morasch, J.; Streibel, V.; Toupance, T.; Jaegermann, W.; Klein, A. The Work Function of TiO₂. *Surfaces* **2018**, *1*, 73–89.
- (267) Diebold, U. The surface science of titanium dioxide. *Surface Science Reports* **2003**, *48*, 53–229.

-
- (268) Thomas, A. G.; Flavell, W. R.; Mallick, A. K.; Kumarasinghe, A. R.; Tsoutsou, D.; Khan, N.; Chatwin, C.; Rayner, S.; Smith, G. C.; Stockbauer, R. L.; Warren, S.; Johal, T. K.; Patel, S.; Holland, D.; Taleb, A. et al. Comparison of the electronic structure of anatase and rutile TiO₂ single-crystal surfaces using resonant photoemission and X-ray absorption spectroscopy. *Physical Review B* **2007**, *75*, 035105.
- (269) Reckers, P.; Dimamay, M.; Klett, J.; Trost, S.; Zilberberg, K.; Riedl, T.; Parkinson, B. A.; Brötz, J.; Jaegermann, W.; Mayer, T. Deep and Shallow TiO₂ Gap States on Cleaved Anatase Single Crystal (101) Surfaces, Nanocrystalline Anatase Films, and ALD Titania Ante and Post Annealing. *J. Phys. Chem. C* **2015**, *119*, 20.
- (270) Mackrodt, W.; Simson, E.-A.; Harrison, N. An ab initio Hartree-Fock study of the electron-excess gap states in oxygen-deficient rutile TiO₂. *Surface Science* **1997**, *384*, 192–200.
- (271) Di Valentin, C.; Pacchioni, G.; Selloni, A. Reduced and n-Type Doped TiO₂ : Nature of Ti 3+ Species. *The Journal of Physical Chemistry C* **2009**, *113*, 20543–20552.
- (272) Wendt, S.; Sprunger, P. T.; Lira, E.; Madsen, G. K. H.; Li, Z.; Hansen, J. Ø.; Matthiesen, J.; Blekinge-Rasmussen, A.; Lægsgaard, E.; Hammer, B.; Besenbacher, F. The Role of Interstitial Sites in the Ti 3d Defect State in the Band Gap of Titania. *Science* **2008**, *320*, 1755–1759.
- (273) Yim, C. M.; Pang, C. L.; Thornton, G. Oxygen Vacancy Origin of the Surface Band-Gap State of TiO₂(110). *Physical Review Letters* **2010**, *104*, 036806.
- (274) Deskins, N. A.; Du, J.; Rao, P. The structural and electronic properties of reduced amorphous titania. *Physical Chemistry Chemical Physics* **2017**, *19*, 18671–18684.
- (275) Notten, P. H. L. The Etching of InP in HCl Solutions: A Chemical Mechanism. *Journal of The Electrochemical Society* **1984**, *131*, 2641–2644.
- (276) Caneau, C.; Bhat, R.; Koza, M.; Hayes, J.; Esagui, R. Etching of InP by HCl in an OMVPE reactor. *Journal of Crystal Growth* **1991**, *107*, 203–208.
- (277) Montgomery, V.; Williams, R. H.; Varma, R. R. The interaction of chlorine with indium phosphide surfaces. *Journal of Physics C: Solid State Physics* **1978**, *11*, 1989–2000.
- (278) Hung, W.-H.; Hsieh, J.-T.; Hwang, H.-L.; Hwang, H.-Y.; Chang, C.-C. Surface etching of InP(100) by chlorine. *Surface Science* **1998**, *418*, 46–54.
- (279) Jiao, Z.-Y.; Ma, S.-H.; Guo, Y.-L. Simulation of optical function for phosphide crystals following the DFT band structure calculations. *Computational and Theoretical Chemistry* **2011**, *970*, 79–84.
- (280) Proix, F.; Sébenne, C. A.; El Hafsi, B.; Hricovini, K.; Pinchaux, R.; Bonnet, J. E. Ultraviolet-photoemission-spectroscopy study of the interaction of atomic hydrogen with cleaved InP: A valence-band contribution. *Physical Review B* **1991**, *43*, 14581–14588.
- (281) Lewerenz, H.; Schulte, K. Combined photoelectrochemical conditioning and surface analysis of InP photocathodes. *Electrochimica Acta* **2002**, *47*, 2639–2651.
- (282) Heise, R.; Courths, R.; Witzel, S. Valence band densities-of-states of TiO₂(110) from resonant photoemission and photoelectron diffraction. *Solid State Communications* **1992**, *84*, 599–602.

-
- (283) Ronge, E.; Cottre, T.; Welter, K.; Smirnov, V.; Ottinger, N. J.; Finger, F.; Kaiser, B.; Jaegermann, W.; Jooss, C. Stability and Degradation Mechanism of Si-based Photocathodes for Water Splitting with Ultrathin TiO₂ Protection Layer. *Zeitschrift für Physikalische Chemie* **2020**, *234*, 1171–1184.
- (284) Kurtz, R. L.; Stock-Bauer, R.; Msdey, T. E.; Román, E.; De Segovia, J. Synchrotron radiation studies of H₂O adsorption on TiO₂(110). *Surface Science* **1989**, *218*, 178–200.
- (285) Schwanitz, K.; Weiler, U.; Hunger, R.; Mayer, T.; Jaegermann, W. Synchrotron-Induced Photoelectron Spectroscopy of the Dye-Sensitized Nanocrystalline TiO₂ /Electrolyte Interface: Band Gap States and Their Interaction with Dye and Solvent Molecules. *The Journal of Physical Chemistry C* **2007**, *111*, 849–854.
- (286) Kashiwaya, S.; Toupance, T.; Klein, A.; Jaegermann, W. Fermi Level Positions and Induced Band Bending at Single Crystalline Anatase (101) and (001) Surfaces: Origin of the Enhanced Photocatalytic Activity of Facet Engineered Crystals. *Advanced Energy Materials* **2018**, *8*, 1802195.
- (287) Reckers, P. Electronic properties of titania (and AZO) and its interface to organic acceptor materials. Ph.D. thesis, Technische Universität, Darmstadt, 2019.
- (288) Hermans, Y.; Murcia-López, S.; Klein, A.; Jaegermann, W. BiVO₄ Surface Reduction upon Water Exposure. *ACS Energy Letters* **2019**, *4*, 2522–2528.
- (289) Hermans, Y.; Klein, A.; Sarker, H. P.; Huda, M. N.; Junge, H.; Toupance, T.; Jaegermann, W. Pinning of the Fermi Level in CuFeO₂ by Polaron Formation Limiting the Photovoltage for Photochemical Water Splitting. *Advanced Functional Materials* **2020**, *30*, 1910432.
- (290) Poulain, R.; Rohrer, J.; Hermans, Y.; Dietz, C.; Brötz, J.; Proost, J.; Chatenet, M.; Klein, A. Origin of Surface Reduction upon Water Adsorption on Oriented NiO Thin Films and Its Relation to Electrochemical Activity. *The Journal of Physical Chemistry C* **2022**, *126*, 1303–1315.
- (291) Li, H.; Guo, Y.; Robertson, J. Calculation of TiO₂ Surface and Subsurface Oxygen Vacancy by the Screened Exchange Functional. *The Journal of Physical Chemistry C* **2015**, *119*, 18160–18166.
- (292) Li, Y.; Gao, Y. Interplay between Water and TiO₂ Anatase (101) Surface with Subsurface Oxygen Vacancy. *Physical Review Letters* **2014**, *112*, 206101.
- (293) Oyekan, K. A.; Van de Put, M.; Tiwari, S.; Rossi, C.; Esteve, A.; Vandenberghe, W. Re-examining the role of subsurface oxygen vacancies in the dissociation of H₂O molecules on anatase TiO₂. *Applied Surface Science* **2022**, *594*, 153452.
- (294) Schaub, R.; Thostrup, P.; Lopez, N.; Lægsgaard, E.; Stensgaard, I.; Nørskov, J. K.; Besenbacher, F. Oxygen Vacancies as Active Sites for Water Dissociation on Rutile TiO₂ (110). *Physical Review Letters* **2001**, *87*, 266104.
- (295) Lohaus, C.; Klein, A.; Jaegermann, W. Limitation of Fermi level shifts by polaron defect states in hematite photoelectrodes. *Nature Communications* **2018**, *9*, 4309.
- (296) Elmaslmane, A. R.; Watkins, M. B.; McKenna, K. P. First-Principles Modeling of Polaron Formation in TiO₂ Polymorphs. *Journal of Chemical Theory and Computation* **2018**, *14*, 3740–3751.
- (297) Reticcioli, M.; Diebold, U.; Franchini, C. Modeling polarons in density functional theory: lessons learned from TiO₂. *Journal of Physics: Condensed Matter* **2022**, *34*, 204006.

-
- (298) De Lile, J. R.; Bahadoran, A.; Zhou, S.; Zhang, J. Polaron in TiO₂ from First-Principles: A Review. *Advanced Theory and Simulations* **2022**, *5*, 2100244.
- (299) Sezen, H.; Buchholz, M.; Nefedov, A.; Natzeck, C.; Heissler, S.; Di Valentin, C.; Wöll, C. Probing electrons in TiO₂ polaronic trap states by IR-absorption: Evidence for the existence of hydrogenic states. *Scientific Reports* **2014**, *4*, 3808.
- (300) Verdi, C.; Caruso, F.; Giustino, F. Origin of the crossover from polarons to Fermi liquids in transition metal oxides. *Nature Communications* **2017**, *8*, 15769.
- (301) Klein, A.; Körber, C.; Wachau, A.; Säuberlich, F.; Gassenbauer, Y.; Schafranek, R.; Harvey, S.; Mason, T. Surface potentials of magnetron sputtered transparent conducting oxides. *Thin Solid Films* **2009**, *518*, 1197–1203.
- (302) Liu, X.; Zhu, G.; Wang, X.; Yuan, X.; Lin, T.; Huang, F.; Liu, X. Y.; Wang, X.; Yuan, X. T.; Huang, F. Q.; Zhu, G. L.; Lin, T. Q. Progress in Black Titania: A New Material for Advanced Photocatalysis. *Advanced Energy Materials* **2016**, *6*, 1600452.
- (303) Tanemura, S.; Miao, L.; Wunderlich, W.; Tanemura, M.; Mori, Y.; Toh, S.; Kaneko, K. Fabrication and characterization of anatase/rutile–TiO₂ thin films by magnetron sputtering: a review. *Science and Technology of Advanced Materials* **2005**, *6*, 11–17.
- (304) Mo, S.-D.; Ching, W. Y. Electronic and optical properties of three phases of titanium dioxide: Rutile, anatase, and brookite. *Physical Review B* **1995**, *51*, 13023–13032.
- (305) Amano, F.; Nakata, M.; Yamamoto, A.; Tanaka, T. Effect of Ti 3+ Ions and Conduction Band Electrons on Photocatalytic and Photoelectrochemical Activity of Rutile Titania for Water Oxidation. *The Journal of Physical Chemistry C* **2016**, *120*, 6467–6474.
- (306) Jeong, B.-S.; Norton, D.; Budai, J. Conductivity in transparent anatase TiO₂ films epitaxially grown by reactive sputtering deposition. *Solid-State Electronics* **2003**, *47*, 2275–2278.
- (307) Seger, B.; Pedersen, T.; Laursen, A. B.; Vesborg, P. C. K.; Hansen, O.; Chorkendorff, I. Using TiO₂ as a Conductive Protective Layer for Photocathodic H₂ Evolution. *Journal of the American Chemical Society* **2013**, *135*, 1057–1064.
- (308) Seger, B.; Tilley, D. S.; Pedersen, T.; Vesborg, P. C. K.; Hansen, O.; Grätzel, M.; Chorkendorff, I. Silicon protected with atomic layer deposited TiO₂: durability studies of photocathodic H₂ evolution. *RSC Advances* **2013**, *3*, 25902.
- (309) Ros, C.; Andreu, T.; Hernández-Alonso, M. D.; Penelas-Pérez, G.; Arbiol, J.; Morante, J. R. Charge Transfer Characterization of ALD-Grown TiO₂ Protective Layers in Silicon Photocathodes. *ACS Applied Materials & Interfaces* **2017**, *9*, 17932–17941.
- (310) Bae, D.; Shayestehaminzadeh, S.; Thorsteinsson, E. B.; Pedersen, T.; Hansen, O.; Seger, B.; Vesborg, P. C.; Ólafsson, S.; Chorkendorff, I. Protection of Si photocathode using TiO₂ deposited by high power impulse magnetron sputtering for H₂ evolution in alkaline media. *Solar Energy Materials and Solar Cells* **2016**, *144*, 758–765.
- (311) Wildhaber, I.; Gross, H.; Moor, H. Comparative studies of very thin shadowing films produced by atom beam sputtering and electron beam evaporation. *Ultramicroscopy* **1985**, *16*, 321–330.

-
- (312) Hashimoto, K.; Irie, H.; Fujishima, A. TiO_2 Photocatalysis: A Historical Overview and Future Prospects. *Japanese Journal of Applied Physics* **2005**, *44*, 8269.
- (313) Karlberg, G. S.; Jaramillo, T. F.; Skúlason, E.; Rossmeisl, J.; Bligaard, T.; Nørskov, J. K. Cyclic Voltammograms for H on Pt(111) and Pt(100) from First Principles. *Physical Review Letters* **2007**, *99*, 126101.
- (314) Zare Pour, M. A.; Romanyuk, O.; Moritz, D. C.; Paszuk, A.; Maheu, C.; Shekarabi, S.; Hanke, K. D.; Ostheimer, D.; Mayer, T.; Hofmann, J. P.; Jaegermann, W.; Hannappel, T. Band energy diagrams of n-GaInP/n-AlInP(100) surfaces and heterointerfaces studied by X-ray photoelectron spectroscopy. *Surfaces and Interfaces* **2022**, *34*, 102384.
- (315) Guo, J.; Jaegermann, W. Special issue on “Spectroscopy of liquid/Solid interfaces: Detailed insights into electrochemical energy converters”. *Journal of Electron Spectroscopy and Related Phenomena* **2017**, *221*, 1.

Appendix

1 Prepared Si surfaces

Table A1: Sample list of prepared Si surfaces.

Idx	Name	Wafer/orientation	Treatment	LEED pattern	Si 2p _{3/2}
i _a	flash	p-(100)	flashed / deoxidized	None	99.33 eV
i _b	flash	n-(100)	flashed / deoxidized	None	99.56 eV
ii _a	flash-2 × 1	p-(100)	Annealed after flushing	2 × 1	99.46 eV
iii _a	nat. Ox	p-(100)	native oxide / no treatment	None	99.48 eV
iii _b	nat. Ox	n-(100)	native oxide / no treatment	None	99.74 eV
iv _a	therm. Ox	p-(100)	sputter-annealed oxide	None	99.25 eV
iii _a	therm. Ox	n-(100)	sputter-annealed oxide	None	99.59 eV
v _a	dry-H	p-(100)*	H ₂ -annealed H-terminated	2 × 2	99.23 eV
v _b	dry-H	n-(100)*	H ₂ -annealed H-terminated	2 × 2	99.68 eV
vi _a	111-H	p-(111)	Wet-chemical H-terminated	–	99.35 eV
vi _b	111-H	n-(111)	Wet-chemical H-terminated	1 × 1	99.88 eV
vi _c	111-H def.	p-(111)	H-terminated surface stored for 4 weeks in UHV	–	99.40 eV
vii _a	100-H	p-(100)	Wet-chemical H-terminated	–	99.34 eV
vii _b	100-H	n-(100)	Wet-chemical H-terminated	1 × 1	99.81 eV

* Wafer with different doping concentration.

Table A2: Oxide stoichiometry c_X of native SiO₂ layer with Shirley subtracted raw areas I_X .

Sample	I_{Si}	I_{O}	c_{Si}	c_{O}
p-Si (therm. Ox)	2155.72 kcps eV	4391.02 kcps eV	33.9 %	66.1 %
n-Si (therm. Ox)	1433.29 kcps eV	2743.03 kcps eV	34.3 %	65.7 %
p-Si (nat. Ox)	1519.53 kcps eV	2980.78 kcps eV	33.8 %	66.2 %
n-Si (nat. Ox)	2885.85 kcps eV	5483.23 kcps eV	34.5 %	65.5 %

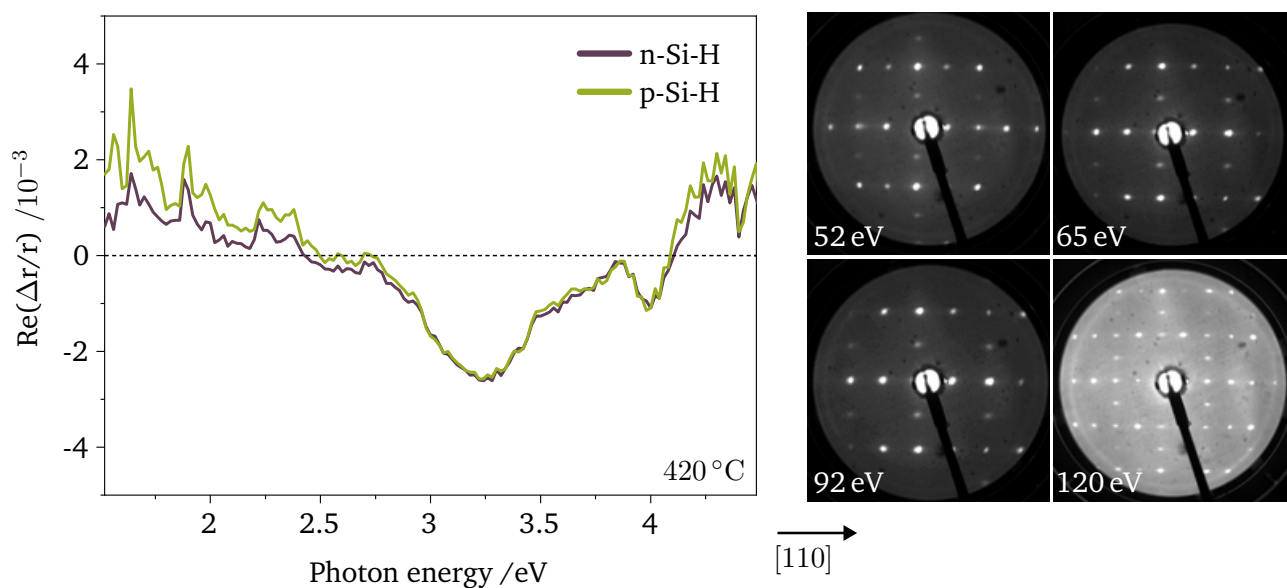


Figure A1: reflection anisotropy spectroscopy (RAS)-signal (left) and low-energy electron diffraction (LEED) pattern at different electron energies (right) indicate formation of mixed A- and B-type dimer orientation domains according to Brückner et al.¹⁰⁵. RAS spectra have been measured by M.A. Zare Pour, TU Ilmenau

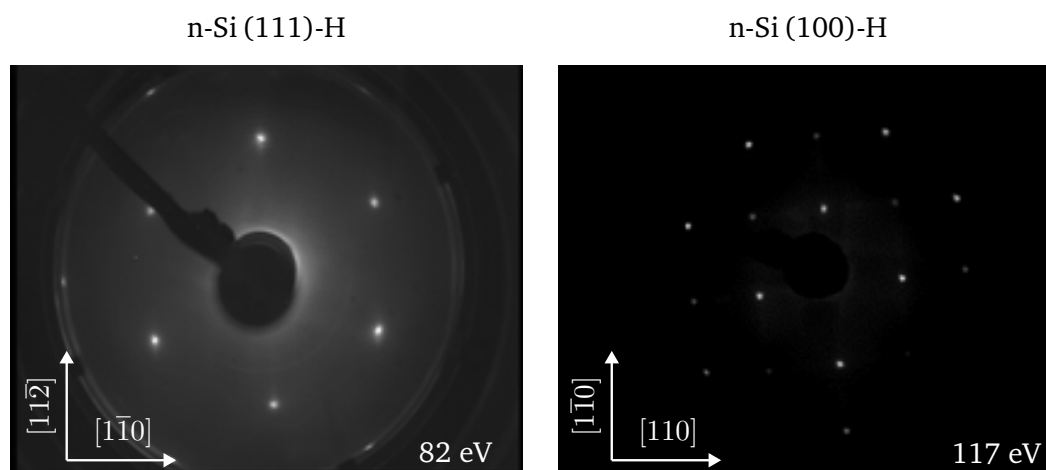


Figure A2: LEED pattern of hydrogen terminated Si (111) (left) and (100) (right) surfaces.

2 Water adsorption on Si(100)-H

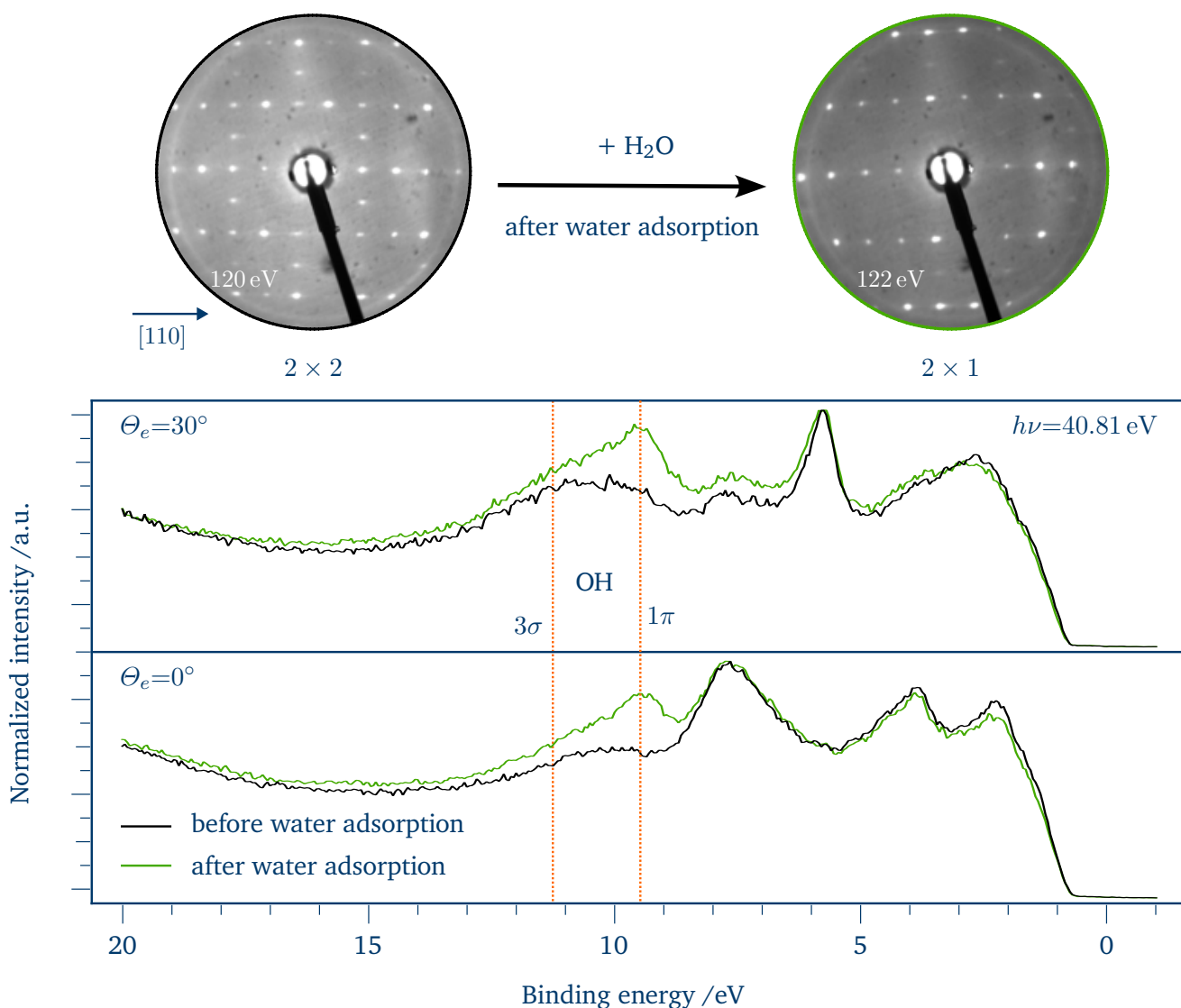


Figure A3: LEED pattern of dry-H terminated Si(100) surface before and after water adsorption. The clear initial 2×2 pattern transforms to a 2×1 surface after low-temperature water adsorption (top). HeII UP spectra reveal a broad feature from 9.4 to 11.2 eV showing no energy dispersion along the $\Gamma - J$ direction, which might be related to adsorbed OH species.

After the desorption of molecular water on the monohydride Si(100)-H surface, transforms from a 2×2 LEED pattern into a 2×1 LEED pattern, indicating a loss in surface order in some of the 2×1 monohydride domain. At the same time surface features appear in the HeII UP valence spectra, which might be assigned to adsorbed OH species (Figure A3). These features showing no angular dispersion, confirming the adsorbate-related loss in surface order. However, the H-resonance at 6.0 eV does not loose in intensity, which suggests that the monohydride Si surface remains intact in contact to the H₂O adsorbates, while reactions and H₂O dissociation might occur at surface defects along step edges at the surface, which do not significantly change the electronic structure of the overall surface.

3 Impact of bias light on low-temperature adsorption experiment

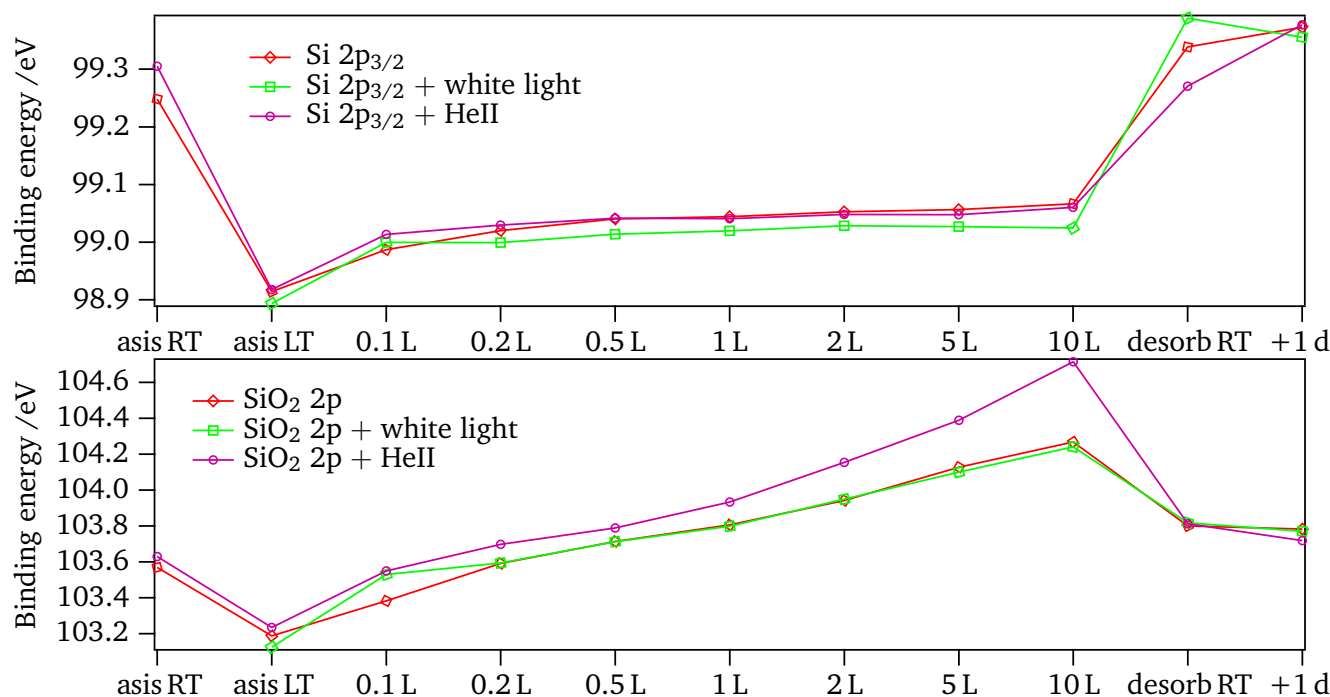


Figure A4: Low-temperature water adsorption on p-Si/SiO₂ surface: Binding energy of metallic Si 2p_{3/2} (top) and of SiO₂ component (bottom) depending on water dosage. Additional bias light excitation only affects the dielectric SiO₂ layer (charging effect). The semiconducting Si 2p component does not reveal a charging effect.

To analyze the impact of additional bias light intensity, different light sources like white light LED and HeII UV light have been used on p-Si/SiO₂ surfaces. In the semiconducting c-Si substrate, the additional HeII illumination does not seem to have a significant impact on the binding energy. The white light LED shifts by about 30 meV, which is related to additional surface photovoltage (SPV). In the SiO₂ component, the HeII light shifts the binding energy to higher values, which is therefore related to a charging effect in the dielectric oxide, due to the high intensity and photoionization cross section of the HeII source. Furthermore, it is observed, that the charging effect increases with an increasing ice layer on top.

4 n-Si/SiO₂/Pt interface

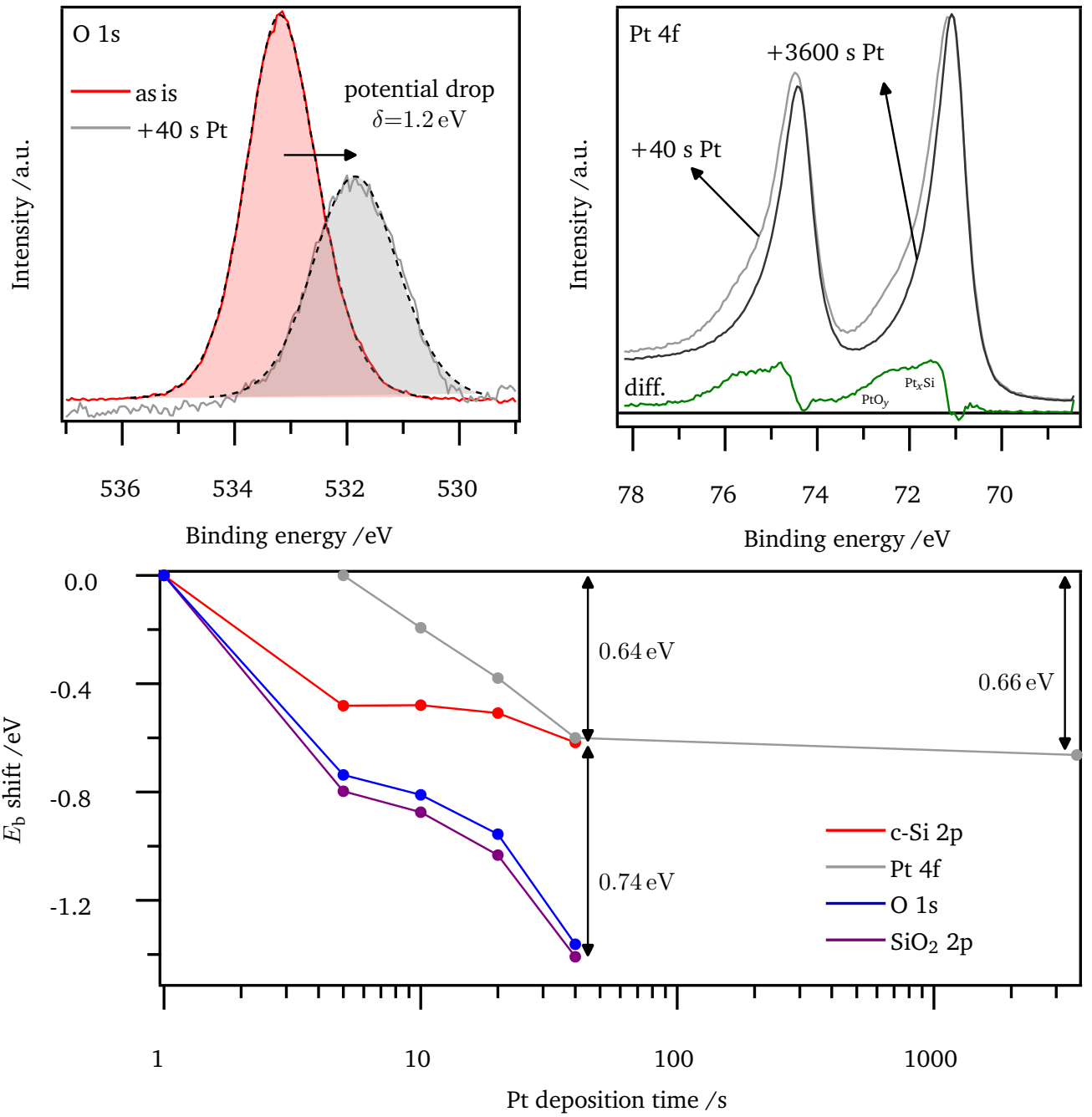


Figure A5: n-Si/SiO₂/Pt interface experiment: DC-sputtered Pt is step-wise deposited. O 1s fits represent interfacial potential drop with and without Pt as presented in Section 5.4.1. Comparison of initial Pt layer show Pt – Si and Pt – O species. E_b shifts represent potential drop in each interface layer.

5 Water adsorption on Pt and Pd foil

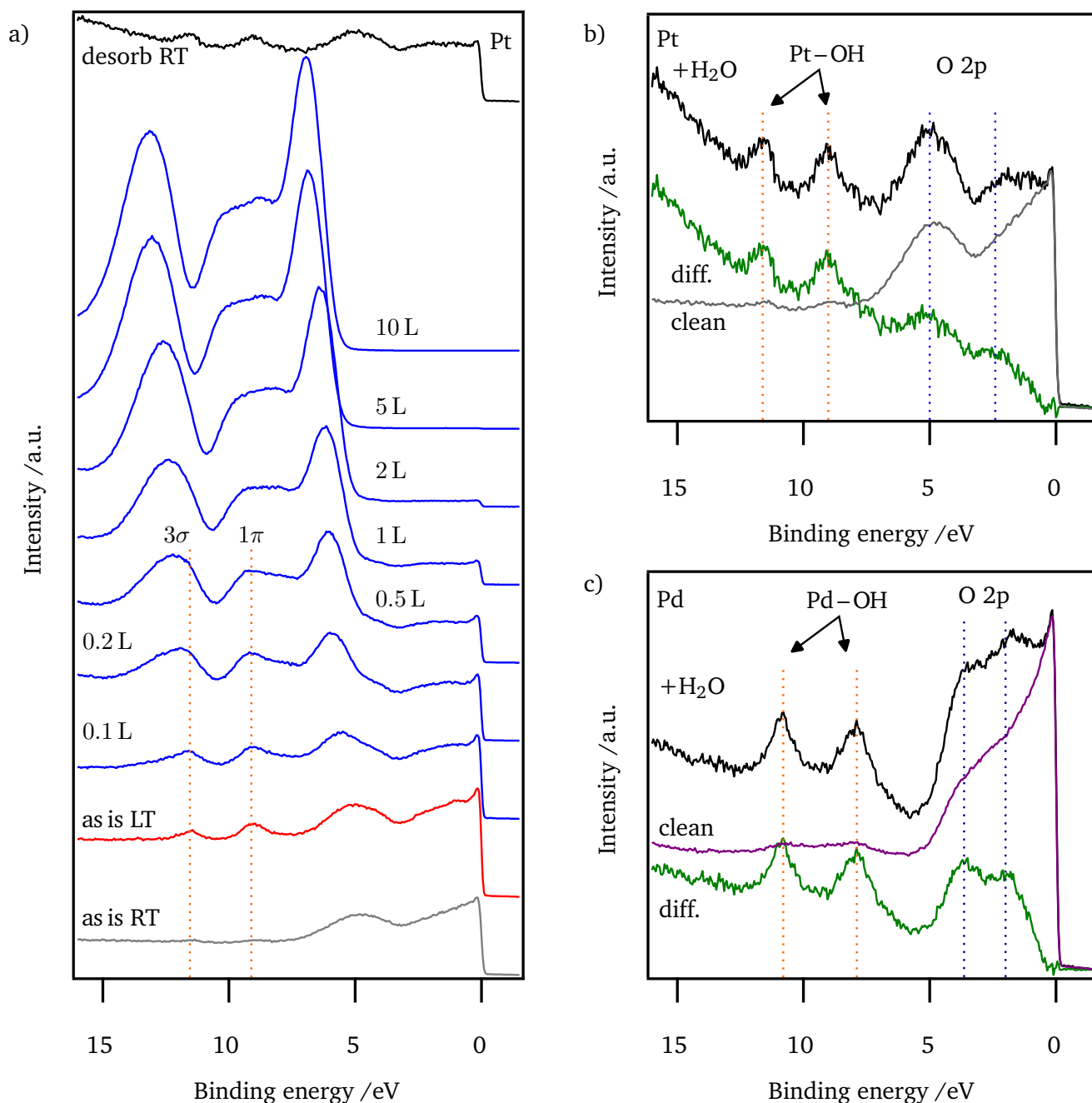


Figure A6: HELL spectra ($h\nu=40.81$ eV) of low temperature water adsorption experiment on sputter cleaned Pt foil (a). Difference spectra before and after adsorption experiment on Pt and Pd-foil are shown in (b) and (c). Clear indication for OH adsorption is observed on both metal foils. However, the 1π and 3σ states appear not only at slightly different binding energy positions at 9.05 and 11.6 eV (Pt) and 7.56 and 12.08 eV (Pd), but also with slightly different relative distances (2.55 vs. 2.90 eV). The OH features overlap with the $3a_1$ and $1b_2$ states of molecular water, which impedes the evaluation of water dissociation during multi-layer adsorption.

6 Hell spectra of p-Si/SiO₂/Pt interfaces upon water adsorption

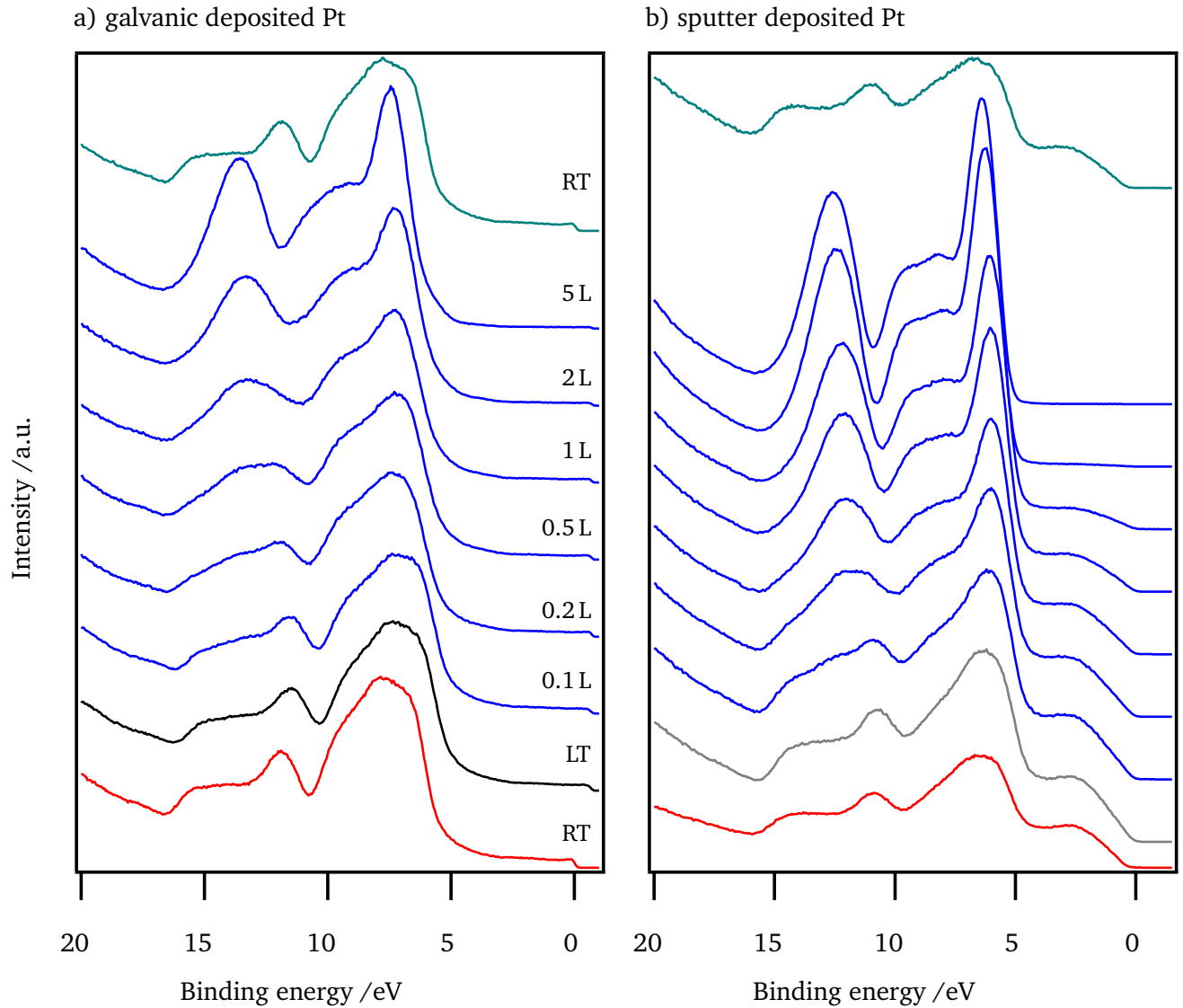


Figure A7: Hell spectra ($h\nu=40.81$ eV) of Si/SiO₂/Pt interfaces upon low-temperature water adsorption. Pt was deposited by a) electrochemical deposition and b) a sputter deposition technique. Most of the features are related to SiO₂ states in comparison to Figure A6 as well as H₂O adsorbate states. A Fermi edge is only observed for a) due to metallic particle formation, while in case of b) a Pt monolayer approach is assumed. Mostly molecular H₂O adsorption is observed while OH cannot be detected.

7 Chopped light current voltage scans of p-Si/SiO₂/Pt

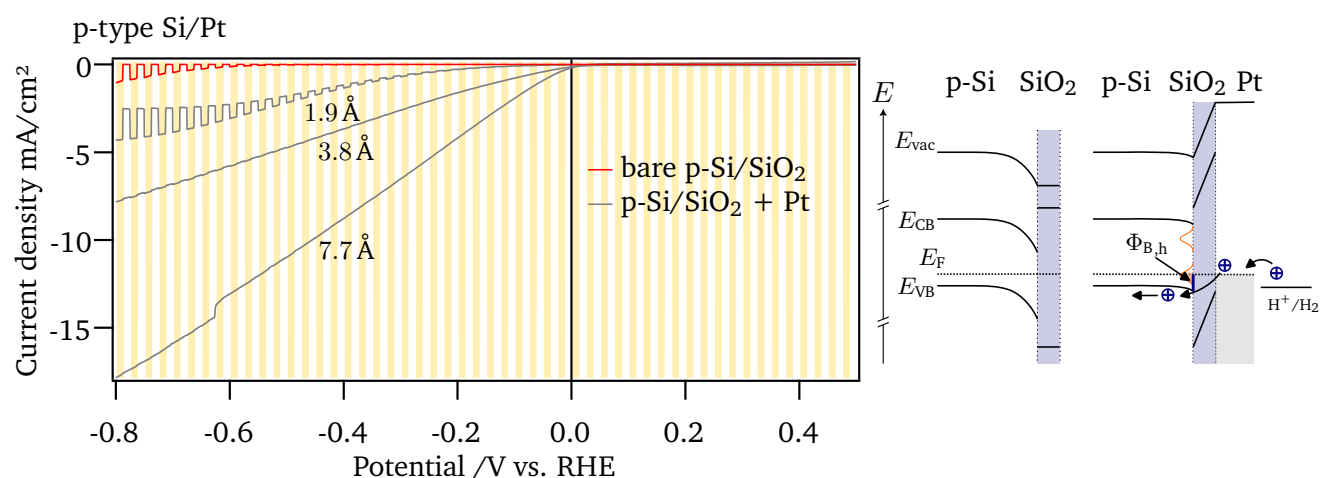


Figure A8: Linear chopped light sweeps in 0.1 M H₂SO₄ for bare (red) and Pt covered p-Si/SiO₂ surfaces (5 mV s⁻¹). Pt was deposited by DC-sputtering with thicknesses as given in the graph. Yellow and light bars, represent dark and white light illumination (1000 W m⁻²), respectively. Energy band diagram for bare and covered p-Si/SiO₂ are shown on the right as deduced from the interface experiment.

In Figure A8, chopped light sweeps were performed on sputter-deposited p-Si/SiO₂/Pt interfaces. The bare p-Si/SiO₂ surface without the Pt catalyst barely shows any hydrogen evolution reaction (HER) activity¹⁴³ with a cathodic photoresponse only visible below -0.4 V vs. RHE. With Pt, the cathodic currents are rising in the HER region. For a thickness of 1.9 Å (about 50 % of a monolayer), a photo response is observed, showing slightly higher currents under illumination. For the charge-transfer, the holes as majority charge carriers have to overcome the measured Schottky barrier Φ_{B,h} of 0.4 eV. For higher Pt coverages however, the dependency on illumination diminishes, which might indicate a short-circuit between the Pt-layer and the back contact plate of the photoelectrochemical cell.

8 Photoreduction of p-Si/SiO₂/TiO₂ interfaces

In order to further understand the impact of post-annealing treatments on the p-Si/SiO₂/TiO₂ interface as well as additional contact formation to Pt, synchrotron based XPS measurements have been conducted. However, a possible disfunction of the spectrometer as well as beam damage occurring on the samples during measurement impede a decisive interpretation, and the presented data has to be treated with caution.

By modifying the electronic properties of the TiO₂ layer, the interface to Si might be affected as well. Differently prepared p-Si/SiO₂/TiO₂ interfaces were investigated (Figure A9). In a first step, the impact of a reduced atomic layer deposition (ALD)-TiO₂ passivation layer straight after deposition on the energetic band alignment is compared to an oxidized one after 5 h of annealing at 270 °C in 0.5 Pa O₂ atmosphere. On a third sample, a monolayer of Pt is deposited ($\approx 10^{15}$ atoms/cm²) using DC-magnetron sputtering at 10 W on top of the oxidized TiO₂ passivation layer. The top row of spectra in Figure A9 illustrates the O 1s, Ti 2p, and Si 2p spectra obtained immediately after preparation using the lab-based X-ray photoemission spectroscopy (XPS) system in DAISY-FUN. The oxidation of the ALD-TiO₂ layer by a thermal post-treatment results in an increase in contact potential, as the TiO₂ work function (WF) rises due to the chemical reduction of oxygen vacancies.^{267,268} Consequently, the Si 2p peak shifts downward by approximately 0.15 eV to a binding energy of $E_b = 98.95$ eV. When Pt is deposited on top of the oxidized surface, the Si 2p peak shifts back, indicating a Fermi level of approximately 0.51 eV above the valence band maximum (VBM). The exact reason for this effect is not entirely clear and could be related to the slightly varying oxide thicknesses. It should be noted that all spectra were acquired from different samples and not consecutively after each treatment step. However, for all samples, the Fermi level falls within the range of 0.51 to 0.22 eV above the VBM within the p-Si space charge region (SCR).

In addition, significant spectral differences are observed when the samples are transported via a dedicated ultra-high vacuum (UHV) transfer to the BESSY II synchrotron. The exposure to highly intense synchrotron radiation results in the reduction of the ALD-TiO₂ layer as previously reported by Reckers et al.²⁶⁹. This X-ray-induced reduction is clearly evident in the Ti 2p core level lines as well as in resonant VB spectra forming Ti³⁺ gap states,^{270,271} even though their exact origin is still under debate.^{272,273} Interestingly, the reduction of TiO₂ leads to a depletion of the p-Si substrate, as all Si 2p core levels are observed at the same binding energy of 99.65 ± 0.10 eV. Nevertheless, it should be noted that the total energy calibration might be less reliable than that of the lab-based XPS machine, and the high X-ray intensity could also result in local charging effects. Nevertheless, it is observed that all Ti 2p spectra shift to the same binding energy. In contrast, the amount of Ti³⁺ strongly varies. The highest amounts are found in the as deposited sample, while almost no Ti³⁺ forms in contact to metallic Pt. Here, the high-WF of Pt prevents the reduction of lattice Ti by transferring free electrons into the metal instead of trapping them at Ti³⁺ lattice sites. This is an interesting observation, as it suggests that instead of the photoabsorber, the buffer layer experiences electron depletion without a significant shift in E_F . Additionally, the prevention of Ti³⁺ formation could potentially limit charge transfer, optical or stability properties of the TiO₂ buffer layer.^{270,274} The about 4 nm thick TiO₂ layer is capable to screen the contact potential of Pt which might prevent electron depletion in the photoabsorber.

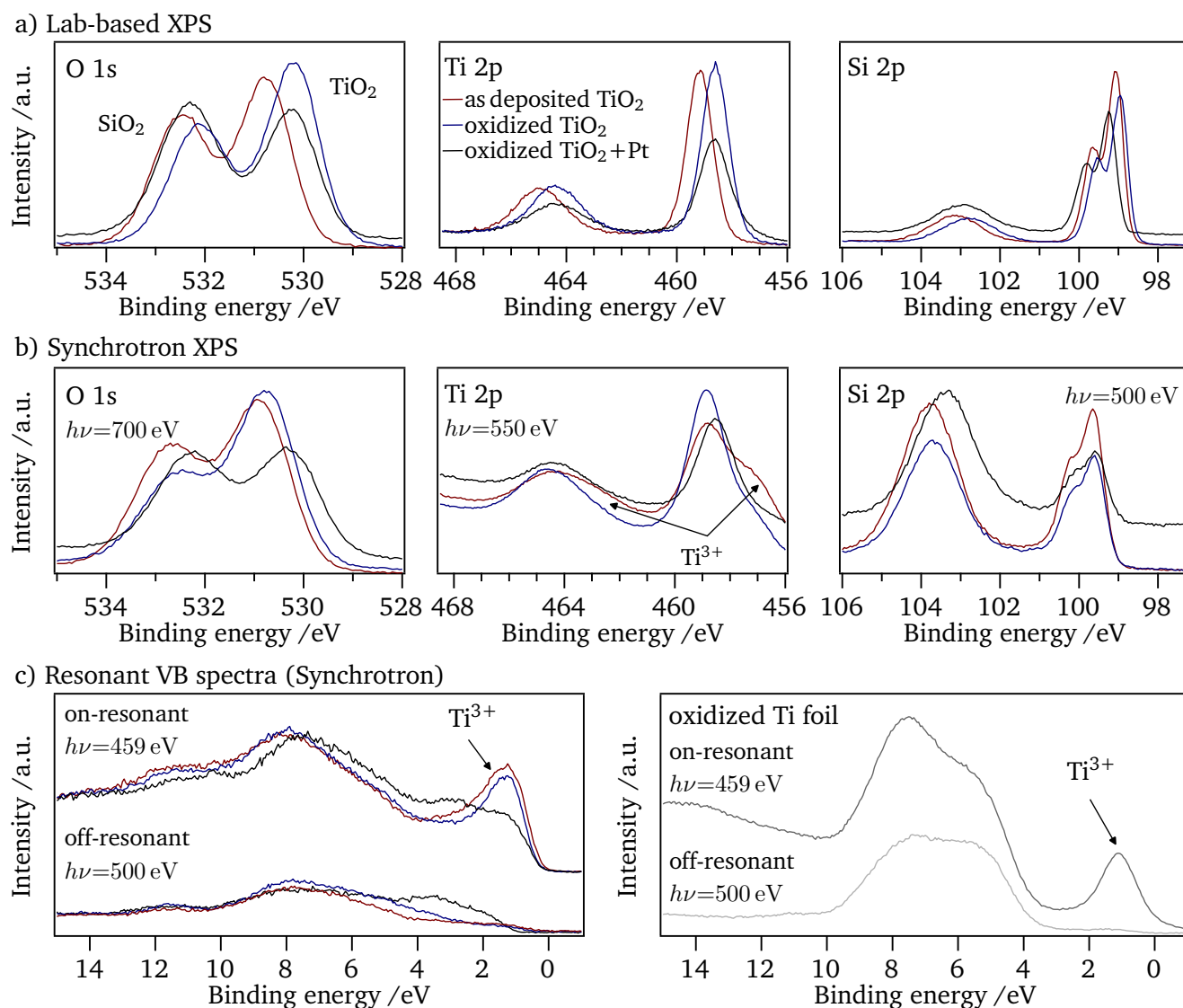


Figure A9: a) XPS spectra of p-Si/SiO₂/ALD-TiO₂ surfaces in different modifications: as deposited (red), oxidized by annealing for 5 h at 270 °C in 0.5 Pa O₂ atmosphere (blue), oxidized plus one monolayer sputtered Pt. Synchrotron beam reads TiO₂ phase b). Resonant valence band (VB) measurements reveal Ti³⁺ gap state in comparison to native oxide Ti foil c). Pt inhibits reduction of lattice site.

9 InP (100) after ALD treatment

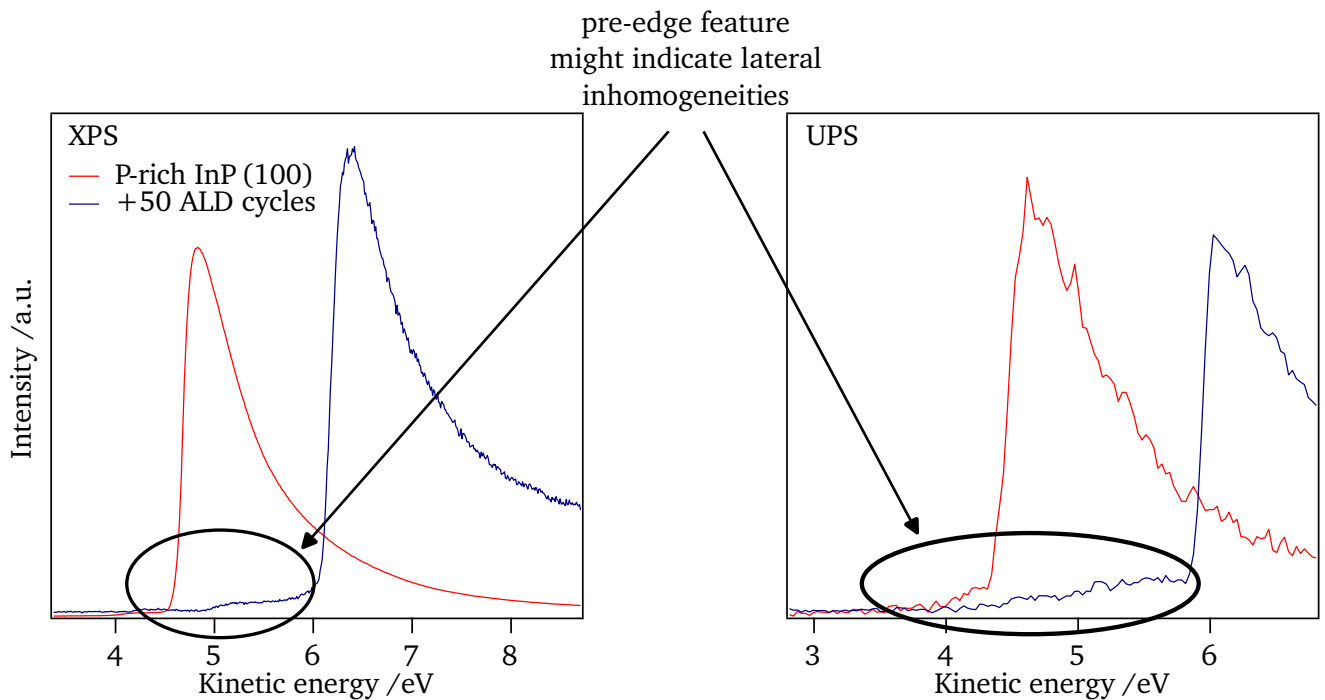


Figure A10: XPS (left) and UPS (right) secondary electron edge (SEE) of P-rich InP (100) before and after 50 full cycles of ALD-TiO₂. Pre-edge features might indicate lateral inhomogeneities with still intact P-rich InP domains.

After chlorination within the ALD process, the InP phase shows a little pre-edge feature, which might be related to intact surface domains with a lower WF. However, these domains might only remain in very small quantity after the process, since SEE in photoemission spectroscopy are mainly dominated by the surface domain with the lowest WF.

10 Low-temperature water adsorption on p-InP/ALD-TiO₂ interface

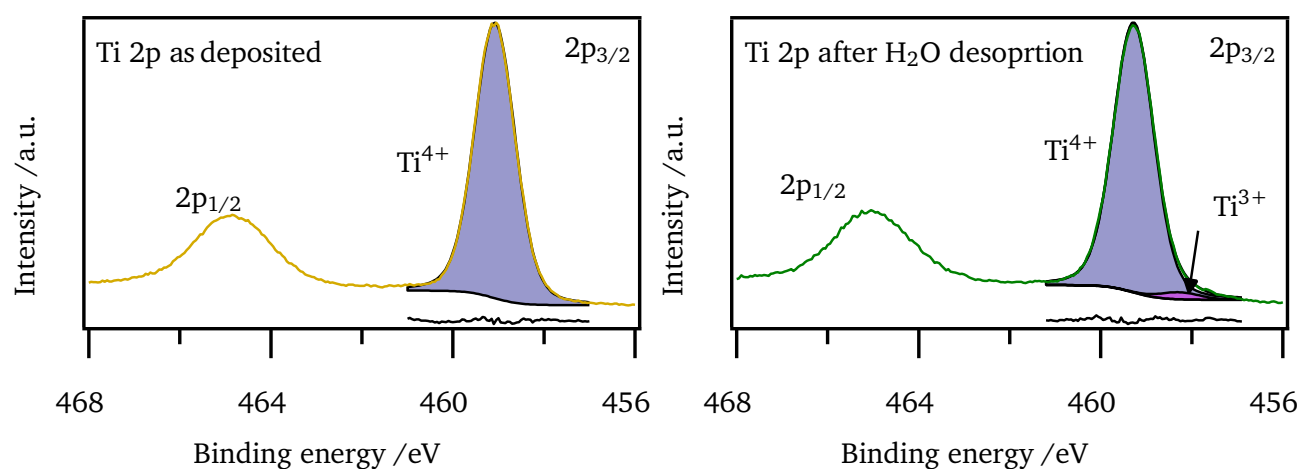


Figure A11: Ti 2p spectra of InP/TiO₂ interface with Ti⁴⁺ and Ti³⁺ components fitted with Voigt-lines and after Shirley background subtraction. Fitting parameter: FWHM(Lorentzian)=0.214 eV, FWHM(Gaussian)=0.93 eV, and Shirley parameter=0.046 eV⁻¹.

The contact of the ALD-TiO₂ covered p-InP surface with water, leads to a chemical reduction of Ti⁴⁺ to Ti³⁺ cations as shown in Ti 2p_{3/2} XPS-fits (Figure A11). After the desorption of 10 L H₂O, an additional feature shifted by -1.00 eV of 2.5 atm.% is detected by confining line shapes, which is attributed to the Ti³⁺-species.

All core level spectra of the low-temperature water adsorption experiment are shown in Figure A12. Even though the In 3d and P 2p substrate signals are very low, the substrate core levels show a clear shift to higher binding energy after the desorption, which indicates an electron injection due to the contact of remaining adsorbates.

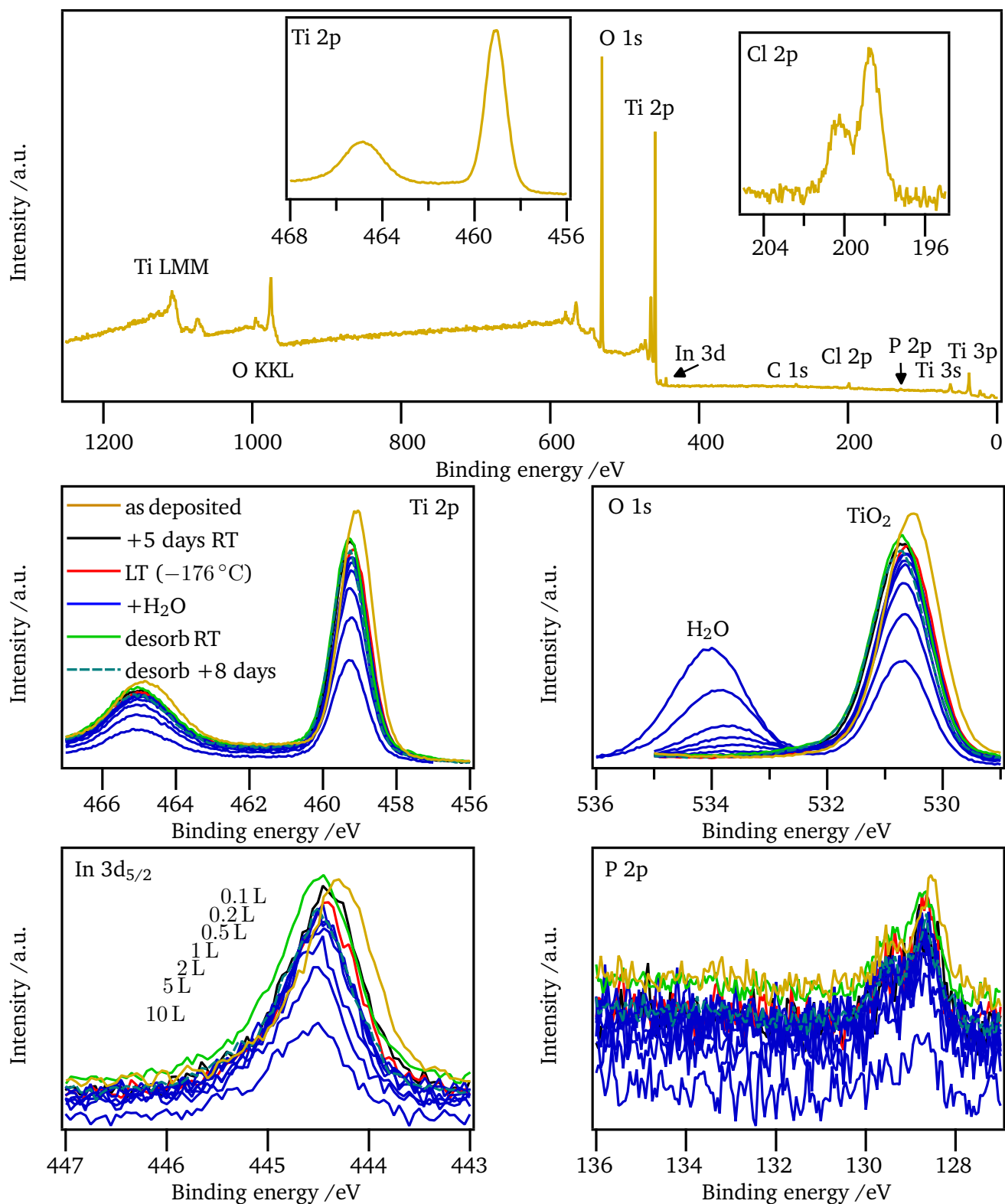


Figure A12: XPS survey and core level spectra of p-InP/ALD-TiO₂ interface under low-temperature water adsorption.

11 Current-voltage curves of p-Si and pn⁺-Si

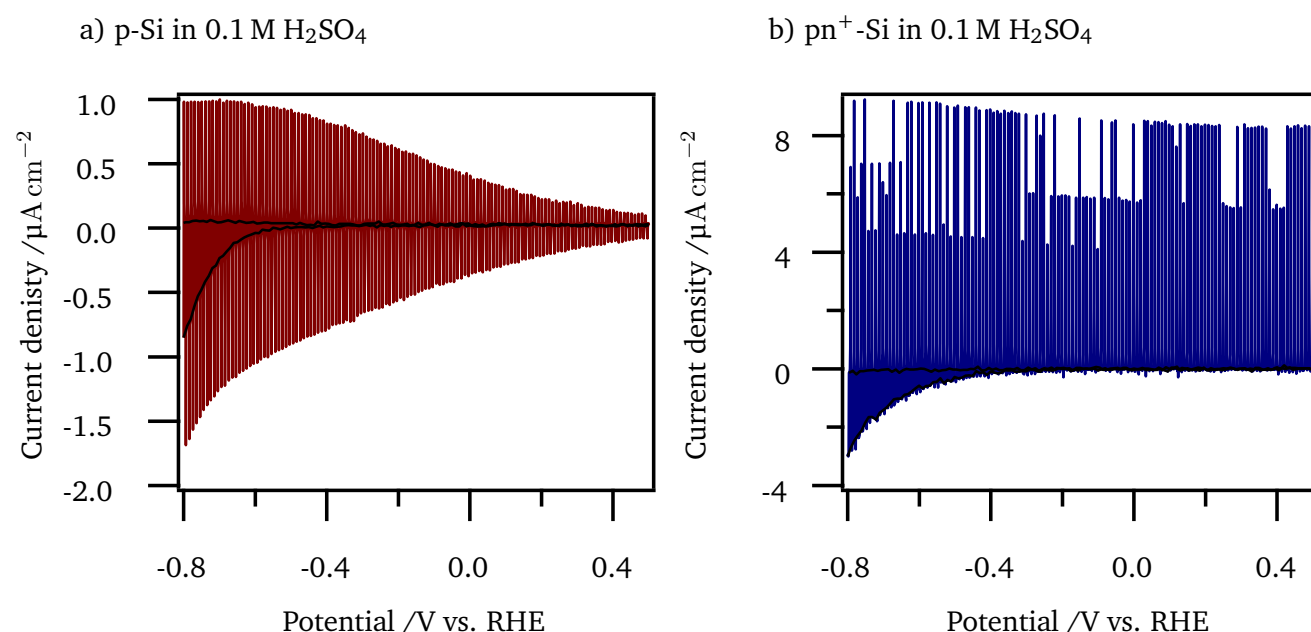


Figure A13: Chopped light current-voltage curves of a) a p-Si/SiO₂ b) a pn⁺-Si/SiO₂ wafer und 1000 W m⁻² white light illumination. The steady-state curves under dark and illuminated condition are depicted in black.

Chopped light current-voltage curves of native oxide covered p-Si and a pn⁺-Si homo-junction in contact to 0.1 mol H_2SO_4 . Both wafer do not show significant HER activity, since the show very low current densities in the cathodic regime. Cathodic currents are expected to result from SiO₂ reduction to silanes (Si_nH_{2n}). The currents are blocked under dark conditions, due to the reversed biasing of the rectifying junctions. No significant shift in the reaction onset is observed for the pn⁺ buried junction in comparison to the pure p-Si wafer.

12 Sputter-deposited TiO₂

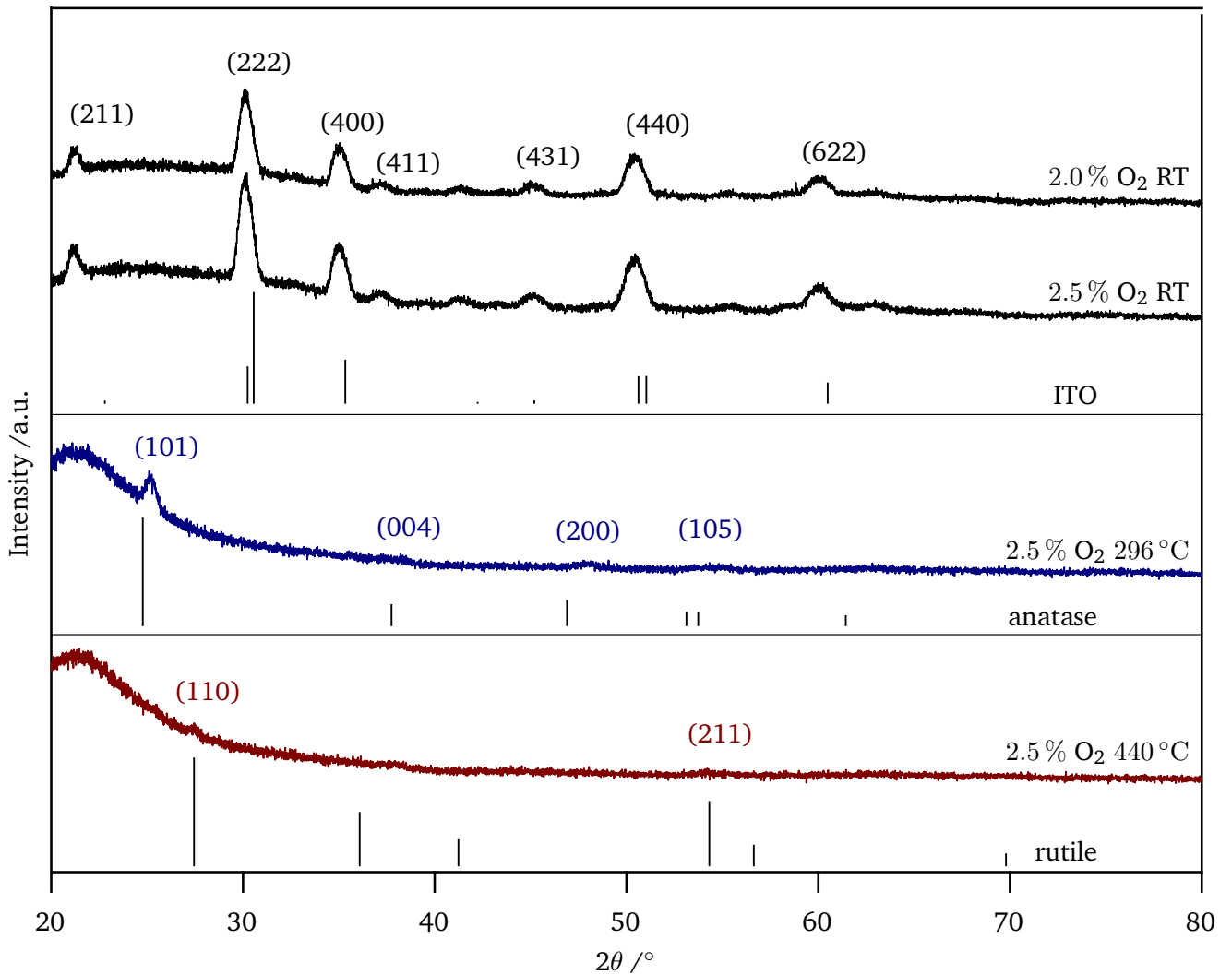


Figure A14: X-ray diffraction (XRD) patterns measured at a fixed incident angle of 5° of direct current (DC)-magnetron sputtered TiO₂ films. Room temperature (RT) deposition does not lead to TiO₂ related reflexes. Only reflexes of the indium tin oxide (ITO) substrate are observed (top). Deposition at 296 °C lead to anatase-related reflexes (middle, quartz glass substrate). For substrate temperatures of 440 °C during deposition, rutile related reflexes are observed (bottom, quartz glass substrate). Reference reflexes up to a relative intensity of 10 % are depicted according to PDF-2 card 01-088-0773 (ITO), 04-011-0664 (anatase), and 00-021-1276 (rutile).

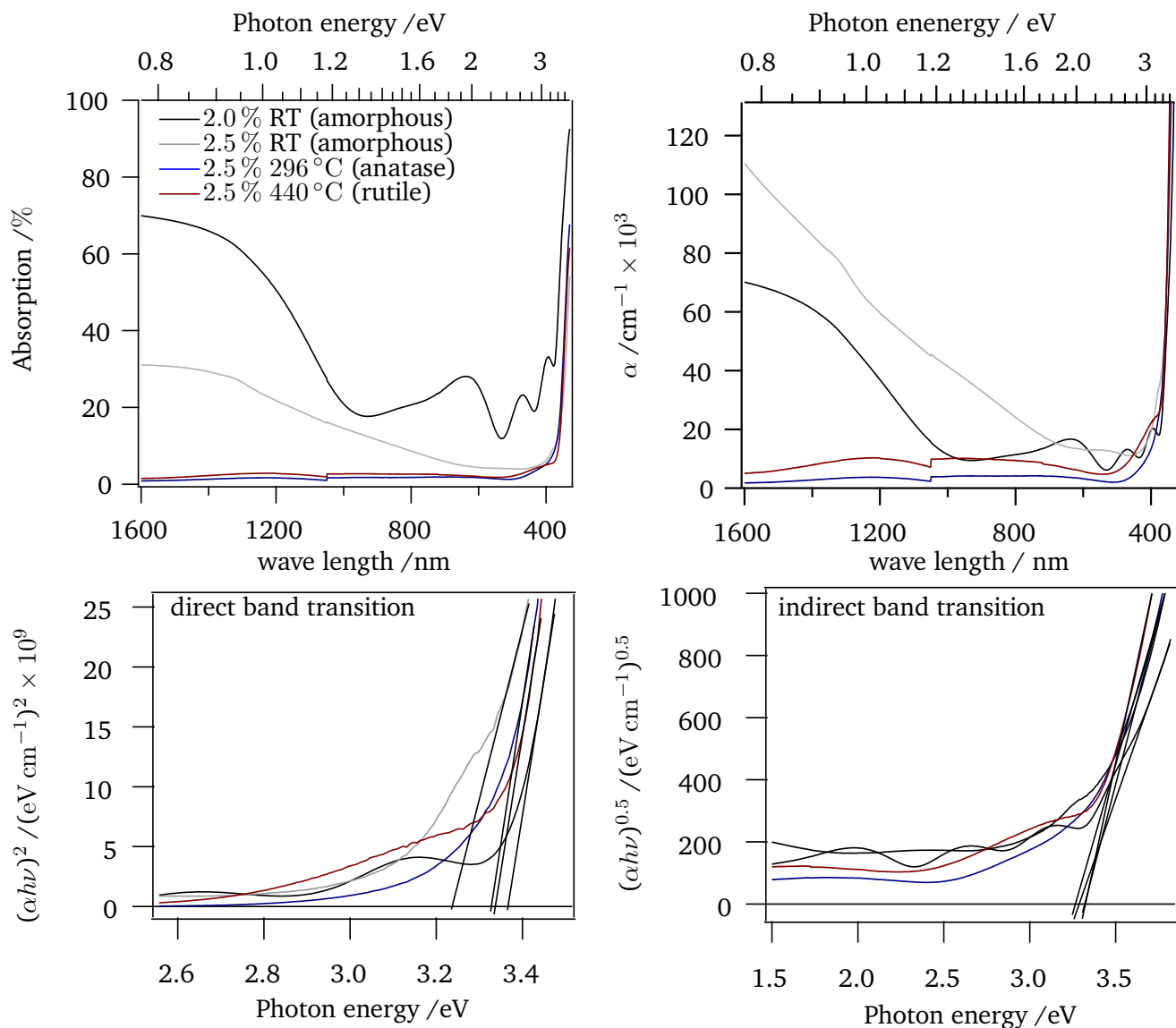


Figure A15: Ultraviolet-visible-near-infrared (UV-Vis-NIR) absorption spectra with resulting absorption coefficient α (top) and Tauc-plots for direct and indirect band transitions (bottom). ITO has been used as substrate for the RT deposited TiO₂, whereas quartz glass has been used for the annealed samples. Absorption intensity below the bandgap are related to different transition into TiO_{2-x} related defect states within the bandgap.³⁰²

Danksagung

An dieser Stelle möchte ich die Möglichkeit nutzen, denjenigen einen besonderen Dank auszurichten, die mir diese Arbeit ermöglicht haben.

Zuallererst möchte ich mich bei Herrn Prof. Dr. Wolfram Jaegermann bedanken, der mir nicht nur die Möglichkeit meiner Promotion unter seiner Aufsicht gab, sondern sich auch Zeit für Diskussionen, Korrekturen sowie hilfreiche Anregungen nahm.

Einen weiteren Dank möchte ich auch Herrn Prof. Dr. Jan Philipp Hofmann aussprechen, der mich nach der Übernahme des Fachgebietes ebenso unterstützte und mir die Fertigstellung des Forschungsprojektes ermöglichte.

Bei Herrn Prof. Dr. Andreas Klein möchte ich mich für die Übernahme des Zweitgutachtens bedanken, sowie die fachlichen und handwerklichen Fertigkeiten, die ich im Laufe des Studiums in seinem Fachbereich erlangen durfte. Ebenso möchte ich mich bei Herrn Prof. Dr. Thomas Hannappel sowie Prof. Dr. Oliver Gutfleisch bedanken, die sich bereiterklärt haben, meiner Disputation als Prüfer beizuwohnen.

Ein besonderes Dankeschön geht an das Team der Wasserspaltungsgruppe unter der Leitung von Dr. Bernhard Kaiser für die interessanten und hilfreichen wöchentlichen Diskussionen rund um unsere Forschung. Ebenso, möchte ich mich bei jenen bedanken, die mich gerade zu Beginn meiner Promotion in das DAISY-FUN eingearbeitet haben. Namentlich sind hier im Besonderen Dr. Wolfram Calvet, Dr. Yannick Hermans sowie meine Büronachbarn Jona und Paula zu nennen, die mich gerade in der Umstrukturierungsphase des Fachgebietes an die Hand genommen haben. Ich möchte mich außerdem bei allen bedanken, die tatkräftig bei der Wartung und Instandhaltung des Systems mitgeholfen haben und somit ihren Beitrag zu meiner Arbeit geleistet haben. In gleicher Weise bedanke ich mich bei jenen, die für die Instandhaltung aller verwendeter Geräte verantwortlich waren. Dies gilt insbesondere auch für verwendete Gerätschaften anderer Fachgebiete.

Ein besonderer Dank gilt ebenso meinen Projektpartnern der TU Ilmenau, die mir unter der Leitung von Prof. Dr. Thomas Hannappel sehr definierte Proben präparieren konnten und deren Diskussionen mich stets weiter gebracht haben. In dieser Hinsicht danke ich vorallem Dr. Agnieszka Paszuk für die hilfreichen Diskussionen sowie die tolle Koordination des Projektes. Der größte Dank gilt Mohammad Amin Zare Pour, für die zahlreichen wissenschaftlichen und organisatorischen Diskussionen, die für die Umsetzung meiner Forschungsziele maßgeblich waren. Danke auch für deinen Einsatz während der Zeit am BESSY II.

Für ihren Einsatz bei den sehr intensiven und stets von Problem geplagten Messzeiten möchte ich mich ebenso bei Tim, Chris, Wolfram, Harol, Freddy und Oleksandr bedanken.

Ein Dank gilt auch meinen Studenten Sumanth, Justus und Tilo, die erfolgreich ihre Forschungsprojekte abschließen konnten und somit einen wertvollen Beitrag zu wichtigen Fragestellungen dieser Thesis liefern konnten. Ebenso bedanken möchte ich mich bei Chuanmu und Kerstin, die mit ihren Messungen zu dieser Arbeit beitrugen.

Vielen Dank an alle weiteren Mitglieder des **Surface Science Lab** nicht nur für die fachliche, sondern vor allem auch für die soziale Unterstützung während der Pandemiezeit. Dank unserer Laufgruppe sowie dem ein oder andere Feierabendbier werde ich diese Zeit in schöner Erinnerung behalten. Danke an unsere Dauerläufer **Tim, Max, Clément, Andi** und **Jona**.

Darüber hinaus gilt ein ganz besonderer Dank meiner Verlobten **Anna**, die viel Zeit in die sprachliche Korrektur meiner Arbeit gesteckt hat und mir die Zuversicht gab, diese Arbeit erfolgreich zu beenden.

Dieser Dank richtet sich außerdem auch an meine Eltern **Kornelia** und **Armin**, meine Schwester **Isabel** und meine Freunde für den stärkenden Rückhalt und die stets motivierenden Worte nicht nur während dieser Arbeit, sondern auch während meines gesamten Studiums.

Curriculum vitae

Dominik Christian Moritz

Academic Education

- 2019 – 2023** **PhD studies at Technical University of Darmstadt**
Surface Science Laboratory (Prof. W. Jaegermann / Prof. J. P. Hofmann)
PhD Thesis:
Electronic Structure of Functionalized Semiconductor Surfaces and Interfaces for Photo-electrochemical Water Splitting
- 2017 – 2019** **Master of Science in Materials Science (M.Sc.)**
at Technical University of Darmstadt
Electronic Structure of Materials (Prof. A. Klein)
Master Thesis: *Fermi Level Limitations in Copper Oxides for Solar Cell Applications*
- 2013 – 2016** **Bachelor of Science in Materials Science (B.Sc.)**
at Technical University of Darmstadt
Surface Science (Prof. A. Klein)
Bachelor Thesis: *Characterization of Magnetron-Sputtered $\text{La}_{1-x}\text{Sr}_x\text{MnO}_3$ Thin Films*

External Experience

- 2018** **Advanced Research Lab at Grenoble Institute of Technology**
Laboratoire des Matériaux et du Génie Physique (Prof. D. Bellet)
Project report: *Stability of Silver Nanowire Networks Under Electrical and Thermal Stress*

School Education

- 2013** **Abitur at Goetheschule Wetzlar**
Oberstufengymnasium

List of Publications

1. **Moritz, D. C.**; Calvet, W.; Zare Pour, M. A.; Paszuk, A.; Mayer, T.; Hannappel, T.; Hofmann, J. P.; Jaegermann, W. Dangling Bond Defects on Si Surfaces and Their Consequences on Energy Band Diagrams: From a Photoelectrochemical Perspective. *Solar RRL* **2023**, *7*, 2201063
2. **Moritz, D. C.**; Ruiz Alvarado, I. A.; Zare Pour, M. A.; Paszuk, A.; Frieß, T.; Runge, E.; Hofmann, J. P.; Hannappel, T.; Schmidt, W. G.; Jaegermann, W. P-Terminated InP (001) Surfaces: Surface Band Bending and Reactivity to Water. *ACS Applied Materials & Interfaces* **2022**, *14*, 47255–47261
3. Maheu, C.; Zare Pour, M. A.; Damestoy, I.; Ostheimer, D.; Mellin, M.; **Moritz, D. C.**; Paszuk, A.; Jaegermann, W.; Mayer, T.; Hannappel, T.; Hofmann, J. P. Tapered Cross Section Photoelectron Spectroscopy Provides Insights into the Buried Interfaces of III-V Semiconductor Devices. *Advanced Materials Interfaces* **2023**, *10*, 2201648
4. Einert, M.; Waheed, A.; **Moritz, D. C.**; Lauterbach, S.; Kundmann, A.; Daemi, S.; Schlaad, H.; Osterloh, F. E.; Hofmann, J. P. Mesoporous CuFe₂O₄ Photoanodes for Solar Water Oxidation: Impact of Surface Morphology on the Photoelectrochemical Properties**. *Chemistry – A European Journal* **2023**, *29*, e202300277
5. Zare Pour, M. A.; Romanyuk, O.; **Moritz, D. C.**; Paszuk, A.; Maheu, C.; Shekarabi, S.; Hanke, K. D.; Ostheimer, D.; Mayer, T.; Hofmann, J. P.; Jaegermann, W.; Hannappel, T. Band energy diagrams of n-GaInP/n-AlInP(100) surfaces and heterointerfaces studied by X-ray photoelectron spectroscopy. *Surfaces and Interfaces* **2022**, *34*, 102384
6. Glahn, L. J.; Ruiz Alvarado, I. A.; Neufeld, S.; Zare Pour, M. A.; Paszuk, A.; Ostheimer, D.; Shekarabi, S.; Romanyuk, O.; **Moritz, D. C.**; Hofmann, J. P.; Jaegermann, W.; Hannappel, T.; Schmidt, W. G. Clean and Hydrogen-Adsorbed AlInP(001) Surfaces: Structures and Electronic Properties. *physica status solidi (b)* **2022**, *259*, 2200308
7. Boer, D. D.; Siberie, Q.; Siegler, M. A.; Ferber, T. H.; **Moritz, D. C.**; Hofmann, J. P.; Hetterscheid, D. G. On the Homogeneity of a Cobalt-Based Water Oxidation Catalyst. *ACS Catalysis* **2022**, *12*, 4597–4607
8. Resende, J.; Papanastasiou, D. T.; **Moritz, D. C.**; Fontanals, N.; Jiménez, C.; Muñoz-Rojas, D.; Bellet, D. Time of Failure of Metallic Nanowire Networks under Coupled Electrical and Thermal Stress: Implications for Transparent Electrodes Lifetime. *ACS Applied Nano Materials* **2022**, *5*, 2102–2112

Book Chapter

1. **Moritz, D. C.**; Calvet, W.; Zare Pour, M. A.; Paszuk, A.; Mayer, T.; Hannappel, T.; Hofmann, J. P.; Jaegermann, W. In *Encyclopedia of Solid-Liquid Interfaces*; Wandelt, K., Bussetti, G., Eds.; Elsevier, 2024; pp 93–119
2. Hajduk, A.; Zare Pour, M. A.; Paszuk, A.; Guidat, M.; Löw, M.; Ullmann, F.; **Moritz, D. C.**; Hofmann, J. P.; Krischok, S.; Runge, E.; Schmidt, W. G.; Jaegermann, W.; May, M. M.; Hannappel, T. In *Encyclopedia of Solid-Liquid Interfaces*; Wandelt, K., Bussetti, G., Eds.; Elsevier, 2024; pp 120–156